Investigation on Some Metal Phthalocyanine Nanostructures and Their Composites for Multifunctional Applications

Thesis submitted by

Madhupriya Samanta

Doctor of Philosophy (Engineering)

Department of Electronics and Telecommunication Engineering
Faculty Council of Engineering & Technology
Jadavpur University
Kolkata, India
2022

JADAVPUR UNIVERSITY

KOLKATA-700 032, INDIA

INDEX NO.: 219/18/E

1. **Title of the thesis:** Investigation on Some Metal Phthalocyanine Nanostructures and Their Composites for Multifunctional Applications

2. **Name, Designation & Institution of the Supervisor/s:**

Prof. (Dr.) Chayanika Bose (Supervisor)
Professor
Department of Electronics and Telecommunication Engineering
Jadavpur University
188, Raja S.C. Mallik Road, Jadavpur, Kolkata-700032

Prof. (Dr.) Kalyan Kumar Chattopadhyay (Co-Supervisor)
Professor
Department of Physics
Jadavpur University
188, Raja S.C. Mallik Road, Jadavpur, Kolkata-700032

3. List of Publications:

❖ **International journals:**

i. Ultrasound assisted catalytic degradation of textile dye under the presence of reduced Graphene Oxide enveloped Copper Phthalocyanine nanotube
M. Samanta, M. Mukherjee, U. K. Ghorai, S. Sarkar, C. Bose and K. K. Chattopadhyay, Applied Surface Science 449 (2018) 113–121.

ii. Solution processed Copper Phthalocyanine nanowires: A promising supercapacitor anode material
M. Samanta, P. Howli, U. K. Ghorai, M. Mukherjee, C. Bose and K. K. Chattopadhyay, Physica E: Low-dimensional Systems and Nanostructures, 114 (2019) 113654.

iii. Room temperature processed copper phthalocyanine nanorods: A potential sonophotocatalyst for textile dye removal
M. Samanta, M. Mukherjee, U. K. Ghorai, C. Bose and K. K. Chattopadhyay, Materials Research Bulletin 123 (2020) 110725.

iv. Role of various transport layer and electrode materials in enhancing performance of stable environment-friendly Cs_2TiBr_6 solar cell
M. Samanta, Sk I. Ahmed, K. K. Chattopadhyay and C. Bose, Optik 217 (2020) 164805

v. Enhanced electrocatalytic oxygen reduction reaction from organic-inorganic heterostructure
M. Samanta, M. Mukherjee, S. Ghosh, B. Das, C. Bose and K. K. Chattopadhyay, Int. J. of hydrogen energy 47 (2022) 6710-6720

vi. Graphene wrapped organic nanotube: A promising material for Oxygen Reduction Reaction
M. Mukherjee, **M. Samanta**, S. Sarkar, G. P. Das and K. K. Chattopadhyay, Materials Letter 248 (2019) 8-11.

vii. Facile synthesis of ZnPc nanoflakes for cold cathode emission
M. Samanta, U. K. Ghorai, B. Das, P. Howli, S. Das, D. Sen and K. K. Chattopadhyay, RSC Adv. 2016, 6, 42739.

viii. Copper (II) Phthalocyanine (CuPc) Based Optoelectronic Memory Device with Multilevel Resistive Switching for Neuromorphic Application
B. Das, **M. Samanta**, P. Sarkar, U. K. Ghorai, A. Mallik and K. K. Chattopadhyay, Adv. Electron. Mater. 2021, 2001079

ix. Shape-Shifting via Salt Crystallization: Conversion of a Nanostructured Polymer into a Site-Selective Nitrogen-Doped Carbon Sheet with Enhanced Supercapacitive Performance

P. Bairi, K. Sardar, K. Chanda, **M. Samanta**, K. K. Chattopadhyay *et al.,* ACS Appl. Energy Mater. 2020, 3, 5984−5992

x. $MoSe_2$-Amorphous CNT Hierarchical Hybrid Core−Shell Structure for Efficient Hydrogen Evolution Reaction
S. Maity, B. Das**, M. Samanta**, B. K. Das, S. Ghosh and K. K. Chattopadhyay, ACS Appl. Energy Mater. 2020, 3, 5067−5076

xi. Hexagonal nickel selenide nanoflakes decorated carbon fabric: An efficient binder-free water loving electrode for electrochemical water splitting
S. Ghosh, **M. Samanta**, B. Das, S. Maity, P. Howli, S. Sarkar and K.K. Chattopadhyay, Solid State Sciences 116 (2021) 106613

xii. Investigation of electrochemical performances of ceramic oxide $CaCu_3Ti_4O_{12}$ nanostructures
S. Maity, **M. Samanta**, A. Sen and K. K. Chattopadhyay, Journal of Solid State chemistry 269 (2019) 600-607.

xiii. Graphene wrapped Copper Phthalocyanine nanotube: Enhanced photocatalytic activity for industrial waste water treatment
M. Mukherjee, U. K. Ghorai, **M. Samanta** and K. K. Chattopadhyay *et al.* Applied Surface Science 418 (2017) 156–162.

xiv. One pot solvothermal synthesis of ZnPc nanotube and its composite with RGO: A high performance ORR catalyst in alkaline medium
M. Mukherjee, **M. Samanta** and K. K. Chattopadhyay *et al.* Applied Surface Science, 449 (2018) 144-151.

xv. Novel Quaternary Chalcogenide / rGO Based Asymmetric Supercapacitor with High Energy Density
S. Sarkar, **M. Samanta** and K. K. Chattopadhyay *et al*. ACS Appl. Mater. Interfaces, 9 (2017) 22652-22664.

xvi. Band Edge Tuned $Zn_xCd_{1-x}S$ Solid Solution Nanopowders for Efficient Solar Photocatalysis
S. Ghosh, **M. Samanta** and K. K. Chattopadhyay *et al*. Phys. Chem. Chem. Phys. 19 (2017) 29998-30009.

xvii. Co_3O_4 nanowires on flexible carbon fabric as a binder free electrode for all solid state symmetric supercapacitor
P. Howli, **M. Samanta** and Kalyan K. Chattopadhyay *et al.* ACS Omega 2 (2017) 4216-4226.

xviii. Flower-like Cu_2NiSnS_4 microspheres for application as electrodes of asymmetric supercapacitors endowed with high energy density

S. Sarkar, P. Howli, **M. Samanta** and K. K. Chattopadhyay *et al.* CrystEngComm., 20, (2018), 1443-1454.

xix. Endorsement of Manganese Phthalocyanine microstructures as electrocatalyst in ORR: experimental and computational study
M. Mukherjee, **M. Samanta** and K. K. Chattopadhyay *et al.* Electrochimica Acta, 296 (2019) 528-534.

xx. Investigation of ORR performances on graphene/Phthalocyanine nanocomposite in neutral medium
M. Mukherjee, **M. Samanta** and K. K. Chattopadhyay *et al.* Microscopy and Microanalysis, 2019, 1-6.

xxi. Co incorporated Ni_3S_2 hierarchical nano/micro cactus for electrochemical water splitting
R. Khan, **M. Samanta** and K. K. Chattopadhyay *et al.* International journal of hydrogen energy 44 (2019) 21315-21323.

xxii. Photocatalytic and sonocatalytic dye degradation by sulfur vacancy rich ZnS nanopowder
S. Ghosh, **M. Samanta** and K. K. Chattopadhyay *et al*. Journal of Nanoparticle Research 23 (2021), 160

xxiii. Resistive Switching in a $MoSe_2$ Based Memory Device Investigated Using Conductance Noise Spectroscopy
B. Das, A. Bera, **M. Samanta** and K. K. Chattopadhyay *et al*. ACS Applied Electronic Materials 2021, 3, 7, 3096–3105

xxiv. Nanoporous nitrogen-doped graphitic carbon hollow spheres with enhanced electrochemical properties
P. Bairi, K. Sardar, **M. Samanta**, Kausik Chanda and K. K. Chattopadhyay, Materials chem. Frontiers, Mater. Chem. Front., 5 (2021), 7645-7653

xxv. Boron Vacancy: A strategy to boost the Oxygen Reduction Reaction of hexagonal boron nitride nanosheet in hBN-MoS_2 heterostructure
D. Roy, K. Panigrahi, B. K. Das, U. K. Ghorai, S. Bhattacharjee, **M. Samanta**, S. Sarkar and K. K. Chattopadhyay, Nanoscale Adv. 3 (2021), 4739

❖ **International conference proceedings:**

i. "A Simulation Based Comparative Study of P3HT: PCBM and OC_1C_{10}PPV: PCBM Organic Solar Cells", IEEE digital Xplore, 2018, EISBN-978-1-5386-6415-5 [IEEE EDKCON, Kolkata, 2018].

ii. "Sonocatalytic activity of solution processed Zinc oxide nanowires: Efficient remediation of organic pollutants" IEEE digital Xplore, EISBN-9781509047246, 277-280 [IEEE DeVIC, Kalyani, 2017].

iii. "Facile Synthesis of ZnPc Nanocubes: An Electron Emitting Material for Field Emission Display Devices" AIP Conf. Proc. 1832, 050032-1–050032-3[DAE SSPS, Bhubaneswar, 2016].

iv. "Recent advancement of metal phthalocyanine as electrode material in supercapacitor applications" Advances in Industrial Engineering and Management, Vol. 5, No. 2 (2016), 214-217 [IEEE VLSI DCS, Kolkata, 2016].

4. List of Patents: Nil

5. List of Presentations in National/International/Conferences/Workshops:

❖ **International conferences:**

i. Facile synthesis and visible photocatalytic study of self-assembled copper phthalocyanine nanowires
M. Samanta, U. K. Ghorai and K. K. Chattopadhyay *et al.* **ICEFN 2016 (Oral presentation)**

ii. Recent advancement of metal phthalocyanine as electrode material in supercapacitor applications
M. Samanta, U. K. Ghorai and K. K. Chattopadhyay *et al.* **IEEE VLSI DCS 2016 (Oral presentation)**

iii. Facile Synthesis of ZnPc Nanocubes: An Electron Emitting Material for Field Emission Display Devices
M. Samanta, U. K. Ghorai and K. K. Chattopadhyay *et al.* **DAE SSPS 2016 (Oral & Poster presentation)**

iv. Ultrasound assisted catalytic activity of solution processed Zinc oxide nanowires: Efficient remediation of organic pollutants
M. Samanta, M. Mukherjee, U. K. Ghorai and K. K. Chattopadhyay, IEEE DeVIC 2017 **(Oral presentation)**

v. Ultrasound Assisted Catalytic Removal of Textile Effluent: An Efficient Remediation for Waste Water Treatment
M. Samanta, M. Mukherjee, C. Bose and K. K. Chattopadhyay, ICONN 2017 **(Oral presentation)**

vi. Improved electrochemical performances of copper ferrite modified amorphous carbon nanotubes in neutral electrolyte
M. Samanta, S. Maity, K. K. Chattopadhyay *et al*. ICCMP 2017 (**Poster presentation)**

vii. One step facile synthesis of Copper Phthalocyanine nanowires: a potential candidate for positive electrode in supercapacitor application
M. Samanta, C. Bose and K. K. Chattopadhyay *et al.* EMSI 2018 (**Poster presentation)**

viii. Sonocatalytic dye degradation by RGO wrapped Copper Phthalocyanine nanotube
M. Samanta, C. Bose and K. K. Chattopadhyay *et al.* ICONSEA 2018 (**Poster presentation)**

ix. A Simulation Based Comparative Study of P3HT: PCBM and $OC_1C_{10}PPV$: PCBM Organic Solar Cells
M. Samanta, K. K. Chattopadhyay and C. Bose *et al.* IEEE EDKCON 2018 **(Oral presentation**)

x. One pot synthesis of MoS_2 nanoflakes decorated CuPc rod and its electrocatalytic activity towards oxygen reduction reaction
M. Samanta, M. Mukherjee, C. Bose and K. K. Chattopadhyay *et al.* ICNAN 2019 **(Oral presentation)**

xi. A comparative study of textile dye removal by advanced oxidation process under the presence of RGO enveloped CuPc nanotube
M. Samanta, K. K. Chattopadhyay and C. Bose *et al.* IWPSD 2019 **(Poster presentation**)

"Statement of Originality"

I, ***Madhupriya Samanta,*** registered on ***27.03.2018*** do hereby declare that this thesis entitled "***Investigation on Some Metal Phthalocyanine Nanostructures and Their Composites for Multifunctional Applications***" contains literature survey and original research work done by the undersigned candidate as part of Doctoral studies.

All information in this thesis have been obtained and presented in accordance with existing academic rules and ethical conduct. I declare that, as required by these rules and conduct, I have fully cited and referred all materials and results that are not original to this work.

I also declare that I have checked this thesis as per the "Policy on Anti Plagiarism, Jadavpur University, 2019", and the level of similarity as checked by iThenticate software is 6 %.

Signature of Candidate: Madhupriya Samanta.

Date: 23.05.22

Certified by Supervisor(s):

(Signature with date, seal)

1. Chayanika Bose
23.05.2022

Dr. Chayanika Bose
Professor
Dept. of Electronics & Telecomm. Engg.
Jadavpur University
Kolkata- 700032, India

2.

23.5.22

Prof. Kalyan Kr. Chattopadhyay
Professor and Head
Department of Physics
Jadavpur University
Kolkata – 700 032

CERTIFICATE FROM THE SUPERVISOR/S

This is to certify that the thesis entitled **"Investigation on Some Metal Phthalocyanine Nanostructures and Their Composites for Multifunctional Applications"** submitted by Smt. **Madhupriya Samanta**, who got her name registered on **27.03.2018** for the award of Ph. D. (Engg.) degree of Jadavpur University is absolutely based upon her own work under the supervision of **Prof. (Dr.) Chayanika Bose and Prof. (Dr.) Kalyan Kumar Chattopadhyay** and that neither her thesis nor any part of the thesis has been submitted for any degree/diploma or any other academic award anywhere before.

1. Chayanika Bose 23.05.2022

Signature of the Supervisor
and date with Office Seal

Dr. Chayanika Bose
Professor
Dept. of Electronics & Telecomm. Engg.
Jadavpur University
Kolkata- 700032, India

2. 23.5.22

Signature of the Supervisor
and date with Office Seal

Prof. Kalyan Kr. Chattopadhyay
Professor and Head
Department of Physics
Jadavpur University
Kolkata – 700 032

Acknowledgements

This research work presented in the dissertation entitled ***"Investigation on Some Metal Phthalocyanine Nanostructures and Their Composites for Multifunctional Applications"*** would not have been successfully completed without constant support, guidance and efforts from a lot of people.

The person who guides not only to resolve the technical issues regarding the research work but also provides adequate flexibility and wise advice to overcome any kind of difficulties during my entire research duration is my supervisor, ***Prof. Chayanika Bose***. I do express my heartiest gratitude and immense respect to her. Next, I would like to express deep gratitude to my joint supervisor, ***Prof. Kalyan Kumar Chattopadhyay*** for granting me the opportunity to work in ***Thin film and Nanoscience lab*** with his research group. His infectious enthusiasm and unlimited support in the field of experimental work have been the major driving forces throughout my journey at Jadavpur University.

Being a member of Prof. Chattopadhyay's research group, I am truly fortunate to work with so many wonderful people. Initially, I would like to convey special thanks to Dr. Uttam Kumar Ghorai, for helping me with the initial stage of experimental process handling as well as his ideas and support for further progress of my research work. Specially, I would like to thank my seniors Moumita Mukherjee, Biswajit Das and one of my favourite juniors, Shrabani Ghosh for their extreme co-operation as well as friendly support in all situations during the entire research period. Also, I would like to extend my heartiest gratitude to other members; Supratim Maity, Nirmalya Sankar Das, Promita Howli, Karamjyoti Panigrahi and all other seniors and juniors for extending their helping hands towards the fulfillment of my research work.

My special gratitude goes to all my family members for their encouragement and full support to accomplish my research works. I must acknowledge my husband, Mr. Prithu Dey, for his constant cooperation and moral support during my entire journey.

Finally, the support provided by Department of Science and Technology (through INSPIRE fellowship scheme), Govt. of India, Department of Electronics and Telecommunication Engineering, and Jadavpur University are thankfully acknowledged.

Madhupriya Samanta

Contents

Abbreviations	Description
MPc	**M**etal **P**hthalocyanine
2D	**T**w**o**-**D**imensional
UV	**U**ltra**v**iolet
AOP	**A**dvanced **O**xidation **P**rocess
SC	**S**uper**c**apacitor
CuPc	**C**opper **P**hthalo**c**yanine
ZnPc	**Z**inc **P**hthalo**c**yanine
rGO	**R**educed **G**raphene **O**xide
MoS_2	**Mo**lybdenum di**s**ulfide
XRD	**X**-**R**ay **D**iffraction
FESEM	**F**ield **E**mission **S**canning **E**lectron **M**icroscopy
HRTEM	**H**igh **R**esolution **T**ransmission **E**lectron **M**icroscopy
XPS	**X**- ray **P**hotoelectron **S**pectroscopy
ORR	**O**xygen **R**eduction **R**eaction
Pb	**L**ead
TI	**T**opological **I**nsulators
TMDC	**T**ransition **M**etal **D**ichal**c**ogenides
h- BN	**H**exagonal-**B**oron **N**itride
MOFs	**M**etal-**O**rganic **F**rameworks
GO	**G**raphene **O**xide
ZnO	**Z**inc **O**xide
TiO_2	**T**itanium di**o**xide
Bi_2O_3	**Bi**smuth oxide
CeO_2	**C**erium oxide
RB	**R**hodamine **B**
AB92	**A**cid **B**lue **92**
RO29	**R**eactive **O**range **29**
AO7	**A**cid **O**range **7**
MO	**M**ethyl **O**range
BG	**B**rilliant **G**reen
RB69	**R**eactive **B**lue **69**

AR17	**A**cid **R**ed **17**
MB	**M**ethylene **B**lue
CV	**C**rystal **V**iolet
AY23	**A**cid **Y**ellow **23**
NBB	**N**aphthol **B**lue **B**lack
PC	**P**ropylene **C**arbonate
EDLC	**E**lectrical **D**ouble **L**ayer **C**apacitor
TNFePc	**T**etra**n**itro Iron **P**hthalocyanine
TFA	**T**ri-**F**luoro **A**cetic acid
HOR	**H**ydrogen **O**xidation **R**eaction
H_2O_2	Hydrogen Peroxide
Pt	**P**la**t**inum
Pd	**P**alla**d**ium
CNTs	**C**arbon **N**ano**t**ubes
FePc	Iron **P**hthalo**c**yanine
MnPc	**M**a**n**ganese **P**hthalo**c**yanine
HTL or EBL	**H**ole **T**ransport or **E**lectron **B**locking **L**ayer
ETL or HBL	**E**lectron **T**ransport or **H**ole **B**locking **L**ayer
TCO	**T**ransparent **C**onducting **O**xide
ITO or FTO	**I**ndium **T**in **O**xide or **F**luorine Doped **T**in **O**xide
FF	**F**ill **F**actor
PCE	**P**ower **C**onversion **E**fficiency
OSC	**O**rganic **S**olar **C**ell
PPV	**P**oly(P-**P**henylene**v**inylene)
P3HT	**P**oly-**3**-**H**exyl**t**hiophene
PCBM	**P**henyl-**C**61-**B**utyric acid **M**ethyl Ester
BHJ	**B**ulk **H**etero**j**unction
HOMO	**H**ighest **O**ccupied **M**olecular **O**rbital
LUMO	**L**owest **U**noccupied **M**olecular **O**rbital
CT	**C**harge **T**ransfer
WF	**W**ork-**F**unction
$OC_1C_{10}PPV$	Poly[2-Methoxy- 5-(3´,7´-Dimethyloctyloxy)-P Phenylene Vinylene]

MDMO-PPV	Poly[2-Methoxy-5-(3′,7′-Dimethyloctyloxy)-1,4-Phenylenevinylene]
V_2O_5	**V**anadium dioxide
NiO	**N**ickel oxide
PEDOT:PSS	Poly(3,4-Ethylenedioxythiophene) Polystyrene Sulfonate
Ag	Silver
PSC	**P**erovskite **S**olar **C**ell
HP	**H**alide **P**erovskite
OIHP	**O**rganic-**I**norganic **H**alide **P**erovskite
IHP	**I**norganic **H**alide **P**erovskite
EDX	**E**nergy **D**ispersive **X**-Ray
UV-Vis	**U**ltra**v**iolet-**Vis**ible Spectroscopy
FTIR	**F**ourier **T**ransform **I**nfra**r**ed Spectroscopy
EM	**E**lectro**m**agnetic
SAED	**S**elected **A**rea **E**lectron **D**iffraction
CV	**C**yclic **V**oltammetry
RDE	**R**otating **D**isk **E**lectrode
GC	**G**lassy **C**arbon
LSV	**L**inear **S**weep **V**oltammetry
GCD	**G**alvanostatic **C**harge **D**ischarge
EIS	**E**lectrochemical **I**mpedance **S**pectroscopy
D.I	**D**e-**I**onized
PVDF	**P**oly**v**inyli**d**ene **F**luoride
DMF	N, N-**D**i**m**ethyl**f**ormamide
NMP	**N**–**M**ethyl **P**yrrolidone
RHE	**R**eversible **H**ydrogen **E**lectrode
SDS	**S**odium **D**odecyl **S**ulfate
SyI	**Sy**nergy **I**ndex
APS	**A**mmonium **P**er**s**ulfate
ISC	**I**nter**s**ystem **C**rossing
CPE	**C**onstant **P**hase **E**lement
K-L	**K**outecky–**L**evich
ECSA	**E**lectro**c**hemically Active **S**urface **A**rea

Au	Gold
Al	**Al**uminium
PTAA	Polytriarlyamine
PL	**P**hoto**l**uminescence
ZnS	**Z**i**n**c **S**ulphide
CB	**C**onduction **B**and
VB	**V**alence **B**and

Abstract

In recent times, nanoscience and nanotechnology are widely considered as one of the most promising areas of scientific and technological development. They evolve as an important multidisciplinary research field combining various areas of physics, chemistry, biology and engineering. Interestingly, nano-sized materials exhibit significantly enhanced features with respect to their bulk counterparts as a result of their reduced dimension(s) lying in nanometer length scale. In general, nanostructured materials can be categorized as two-dimensional (2D), one-dimensional (1D) and zero-dimensional (0D) materials. In the present dissertation, synthesis and characterization of few 2D and 1D nanostructured materials, and their heterostructures are investigated. The morphological and dimensional modifications of nanomaterials are achieved by varying the synthesis routes. The suitability of synthesized materials in some environment and energy related fields is also examined.

Nanostructures of one class of organic semiconductors, namely metal phthalocyanine (MPc) in its pristine form and their heterostructures with various two dimensional (2D) layered materials *viz.* reduced graphene oxide (*rGO*) and molybdenum disulfide (MoS_2) are first investigated. The reason behind the choice of MPc is that MPcs possess advantages like ease of preparation, low temperature synthesis, low cost, mechanical flexibility, and many more. Thus, a simple room / low temperature chemical route for the synthesis of zinc phthalocyanine (*ZnPc*) and copper phthalocyanine (*CuPc*), and their hybrids is adopted here. The nanostructures of *ZnPc* (nanoflake) and those of *CuPc* (nanowire, nanotube, microrod) are synthesized, and subsequently characterized to find their structural, morphological and compositional descriptions.

As for application of the above synthesized materials in the environmental field, wastewater remediation offers one of the most important prospects. It aims at reduction in water pollution through the color contaminants removal from the industrial wastewater. Organic dyes present in textile wastewater, hamper aquatic animal life as well as human health. For the purpose of dye removal, conventional methods like ultraviolet (UV)/visible light assisted catalysis, ozonation, Fenton are employed using different catalytic materials. The special feature of pristine *CuPc* without any functional group (sulfo, nitro, etc.) is its high hydrophobicity, which makes it unsuitable for catalytic dye degradation through its tendency of lack of mixing in aqueous medium. Thus, performance of the heterostructure synthesized from *CuPc* with r*GO*, as a catalyst in dye removal is examined here. However, in recent years,

dye degradation follows new kinds of efficient advanced oxidation processes (AOP) that use the powerful effect of ultrasonic irradiation. Among various AOPs, sonophotocatalysis and sonocatalysis of one textile dye namely, rhodamine B (*RB*) are investigated here respectively using *CuPc* nanowire and *rGO-CuPc*. The influences of different operational parameters *viz.* initial dye concentration, catalyst dosage, dissolved gas, pH, on these processes are also studied. Results establish the superiority of *rGO-CuPc* in the field of ultrasound based catalysis.

Energy has always played a promising role in human survival and civilization. Survey of worldwide energy resources and their consumption indicate that fossil fuels are the primary energy source and take the dominant role in the overall energy consumption. In last few decades, issues related to fossil fuel depletion and uneven distribution of energy resources are of prime environmental concerns. Such ever-increasing energy demand, all over the world, makes exploring alternative renewable natural energy resources like hydro, solar, air, etc. very much essential. Thus, energy conversion, storage and harvesting become the most attractive field of contemporary research. In this dissertation, study of electrochemical supercapacitors (SCs), fuel cells and solar cells based on MPc nanostructures and their hybrids are explored. In case of energy storage, electrochemical performances of some inorganic transition metal oxides as supercapacitor electrode have been well studied, as revealed from existing literature. Electrochemical activities of some substituted MPcs reported so far, have been studied in acidic electrolyte. The activity of unsubstituted MPcs as electrode material is not yet explored. In this dissertation, performances of pristine *CuPc* and *ZnPc* as supercapacitor electrode materials are investigated in alkaline medium. In the context of energy conversion, sluggish nature of oxygen reduction reaction (ORR) in fuel cells calls for the development of efficient electrocatalyst materials. Noble metals such as *Pt*, *Pd* are standard ORR catalysts, but poor stability, high cost and resource scarcity hinder their commercialization. As an alternative, r*GO* and MoS_2 based *CuPc* heterostructures are examined here as ORR electrocatalyst in alkaline medium. MoS_2-*CuPc* heterostructure emerges as more efficient catalyst compared to *rGO-CuPc* hybrid.

Solar cell is one of the important solar energy harvesting systems. Here, organic solar cells (OSCs) with two different absorber materials ($OC_1C_{10}PPV$:*PCBM* and *P3HT:PCBM*) are simulated using ATLAS Device Simulator (SILVACO). Layers of appropriate materials, termed as transport layers, added to the basic solar cell structure facilitate effective segregation of photo-generated electrons and holes, and improve the cell performance. Thus, role of various transport layer materials, including *CuPc*, and that of carrier mobility in the absorber materials in controlling the cell performance are investigated here. Employing *CuPc* as the hole transport

material along with another electron transport layer yields a photo conversion efficiency (PCE) as high as 3 times of that of the basic solar cell. Perovskite based solar cells (PSCs) have already been established as much more efficient compared to OSCs. From some *Pb*-based PSCs, record efficiency of ~ 23% has been reported. But their performance degrades over time under the atmospheric exposure and prevents their commercialization. More importantly, the environmental issues associated with the hazardous effects raised from *Pb*-based materials urge for exploring new *Pb*-free perovskite material as absorber. Thus, simulation of solar cell of cesium based double-perovskite (Cs_2TiBr_6) with various inorganic / organic transport materials are carried out for the first time and presented here. In this case, the PCE of the basic cell gets doubled with the use of *CuPc* as HTL along with another ETL material. The obtained PCE is still low as compared to *Pb*-based PSCs, but much higher than polymer based OSCs. Most importantly, highly hydrophobic nature of *CuPc* makes it popular for the design of moisture stable solar cells, which in turn, enhances the life of solar devices. In addition, the environment friendly nature of such *Pb*-free PSCs is expected to turn them as emerging absorber materials for next generation solar cell.

1.1 Overview:

Nanoscience is an 'Interdisciplinary Science' involving concepts of more than one discipline, such as chemistry, physics, biology and others. It thus suits for the study of *Nanoscale Materials***,** in the general sense, materials with at least one dimension below 0.1 micron but larger than one nanometer [1 *nm* = 10^{-9} *m*]. Figure 1.1 may be helpful for visualization of nanometer length scale. As one or more dimensions of such materials are comparable to the electron wavelength, the quantum mechanical effects appear and manifest novel features as compared to their bulk counterparts. The important properties such as electrical, optical, thermal, mechanical, etc. of a nanoscale material can be modulated by the way of molecular and atomic arrangements along its nanoscale dimension.

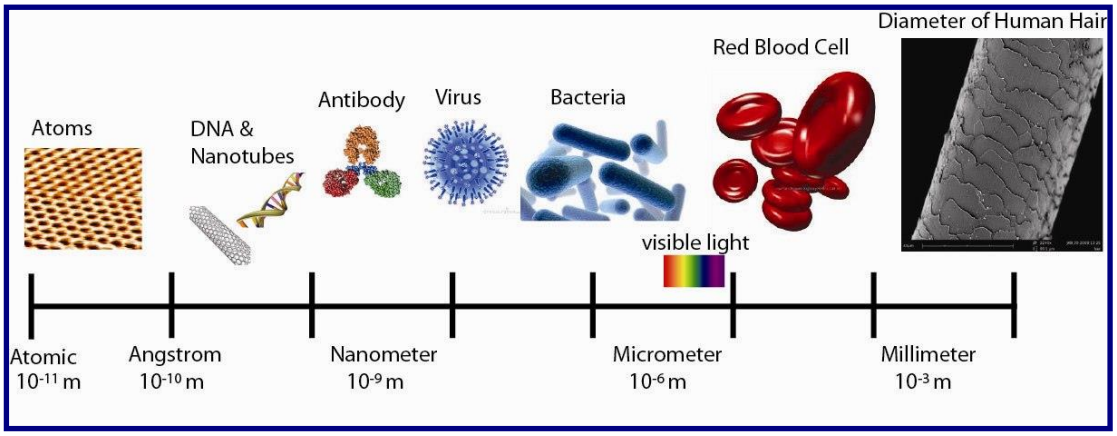

Figure 1.1: *Example of common objects lying in various length scales [1]*

Engineering with atomic precision [2] is a simple definition of Nanotechnology. It is based on the manipulation, control and integration of atoms and molecules to yield materials, structures, components, devices and systems at the nanoscale. Nanotechnology may also be associated with the technological application of nanoscience that makes the use of new nano-dimensional materials feasible in various disciplines of engineering like metallurgy, electrical, electronics, etc. Nanotechnology furnishes us with the design ability of different customized materials and products with their features enhanced significantly, and are expected to do so in future with greater flexibility. This newborn discipline is employed at the interface between physics, chemistry, material science, microelectronics, biochemistry and biotechnology. The overview of nanoscience and nanotechnology is pictorially represented in Figure 1.2.

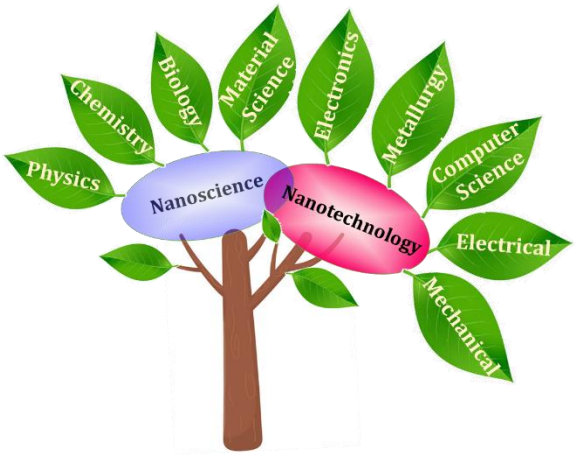

Figure 1.2: *Fields of nanoscience and nanotechnology*

Various applications of nanoscale materials involve a number of processing steps including their synthesis and characterizations. The suitability of nanomaterials for few applications in the field of environment and energy sector will be investigated in this dissertation. Nanostructures of one type of organic semiconductor, namely metal phthalocyanine (MPc) in its pristine form and its heterostructures with various two-dimensional (2D) layered materials will be synthesized and characterized here for the above purposes.

An extensive classification divides the synthesis methods into two categories: *top-down* and *bottom-up* approach. In top-down approach, bulk materials are broken to form nano-sized particles, while in bottom-up approach nanomaterial has been prepared by aggregation of small clusters of atoms of their constituent precursor materials. The bottom-up approach yields a better chance of producing nanostructures with fewer defects and more homogenous chemical composition in a relatively simple way as compared with the top-down approach. Therefore, a simple low temperature chemical route for the synthesis of MPc nanostructures and their hybrids, following bottom-up approach, is more popular. In order to characterize such synthesized nanomaterials to find their structural, morphological and other related descriptions, various techniques should be adopted.

In the present scenario, energy and environmental sustainability are of utmost importance. For the environmental aspects, wastewater remediation is one of the important issues to address. Previously, conventional methodologies like ultraviolet (UV)/visible light assisted catalysis, ozonation, Fenton, etc. were used for the remediation of textile wastewater. In recent times, dye degradation is investigated through new kinds of efficient advanced

oxidation processes (AOP) that use the powerful effect of ultrasonic irradiation. Among various AOPs, sonocatalysis and sonophotocatalysis are usually explored using probe and bath sonicators. Sonocatalysis can be defined as the catalytic degradation of organic hazardous substances by ultrasonic irradiation. When the same process is carried out with visible light, it is called sonophotocatalysis. Recently, ultrasound irradiation has gained major attention for the removal of organic and inorganic substances, such as pesticides [3, 4], textile dyes [5, 6] and pharmaceutical drugs [7, 8], present in industrial wastewater. Various kinds of synergistic effects *viz.* sono-Fenton, sono-photo, sono-ozonation, sono-catalysis, etc. may play important roles in removing the organic pollutants. To choose an appropriate process, one must have adequate knowledge about the mechanisms of such processes as well as the influence of several operational parameters on processes. Detailed investigations on sonocatalysis and sonophotocatalysis using MPc and their hybrids will be carried out and presented in this dissertation.

Issues related to fossil fuel depletion and non-uniform energy resource distribution are of grave environmental concerns due to huge non-renewable energy consumption. The ever-increasing demand of energy, all over the world, makes exploring alternative renewable natural energy resources like sunlight, tide and wind, very much essential. Thus, energy conversion, storage and harvesting have been turned into the most attractive field of contemporary research. Utilization of the natural energy resources urgently necessitates the development of reliable and efficient energy storage and conversion systems. Among numerous efficient energy systems, electrochemical supercapacitors (SCs), fuel cells and solar cells based on MPc nanostructure and their hybrids will be explored in this dissertation.

1.2 Aims and Objectives:

The major aims and objectives of this dissertation are sketched below:

i. To study various synthesis routes of two members of MPc family *viz.* copper phthalocyanine (*CuPc*) and zinc phthalocyanine (*ZnPc*) nano / microstructures and their heterostructures with reduced graphene oxide (*rGO*) and molybdenum disulfide (MoS_2).
ii. To investigate detailed morphology of as-synthesized pristine *CuPc*, *ZnPc* and *CuPc* hybrids through field emission scanning electron microscopy (FESEM) and high resolution transmission electron microscopy (HRTEM), structural characterizations by X-ray diffraction (XRD) and HRTEM, and compositional analysis and optical

properties respectively will be studied by Energy Dispersive X-Ray (EDX) and Ultraviolet-Visible (UV-vis) spectroscopy.

iii. To explore the ultrasound assisted catalytic activity of *CuPc* and r*GO-CuPc* towards textile dye removal for the purpose of wastewater treatment.

iv. To examine the suitability of *ZnPc* and *CuPc* nanostructures as anode materials in electrochemical supercapacitor and *CuPc* hybrids as oxygen reduction reaction (ORR) electrocatalysts in fuel cell.

v. Lastly, to find the influences of synthesized *CuPc* as transport layer material on the performance of organic and lead free (*Pb*) perovskite solar cells.

1.3 Organization of the thesis:

The entire research work carried out is reported in the form of different chapters. The thesis is thus organised as below:

Chapter 1 introduces the background of this entire research work, the aims and objectives, and organization of the thesis.

Chapter 2 describes the overall introductory review of MPc and their hybrid materials, and their possible areas of applications identified on the basis of existing literature.

Chapter 3 elaborates the methodologies adopted to carry out the synthesis, characterizations and applications of *CuPc, ZnPc* and their hybrids. Various processes involved in synthesis and different characterization tools will be briefly described. Also, the experimental set up for their multiple functionalities [as mentioned in Chapter 2] will be discussed thoroughly in this chapter.

The synthesis procedures and characterizations of *CuPc*, *ZnPc* and their hybrids with *rGO* and MoS_2 are described in **Chapter 4**.

Chapter 5 describes the sonophotocatalysis by *CuPc* nanowires and sonocatalysis using *rGO* enveloped *CuPc* tube for the removal of textile dye.

Chapter 6 elaborates the electrochemical activity of *CuPc* and *ZnPc* nanostructures as supercapacitor electrode, in addition the suitability of *rGO-CuPc* and *MoS_2-CuPc* as electrocatalyst towards ORR in alkaline media.

Chapter 7 presents the simulation based study of organic polymer as well as lead (*Pb*) free perovskite based solar cells, along with their performance improvement through use of various transport layer materials, including *CuPc*.

Finally, the concluding **Chapter 8** includes a brief summary of investigations carried out and results obtained that have been compiled in the present dissertation. Possible extensions of the studies made here are also discussed.

2.1 Introduction:

The overall review of nanostructured organic semiconductor materials and their hybrids with 2D layered materials *viz. rGO* and MoS_2 is dealt in this chapter. Multiple functionalities of the synthesized nanostructures in the fields of energy as well as the environmental sector are also surveyed through study of existing literature. Among various organic semiconductors, here transition metal based phthalocyanine material is primarily focused due to their advantages of ease of preparation, low temperature synthesis route, low cost, mechanical flexibility, and others. Surveying the past relevant literature helps us to steer the intended work in the right direction along which any novel approach or appropriate modifications of the existing synthesis routes can be made to tune the morphological structures of MPcs as well as their hybrids. The suitability of such synthesized samples in the fields of ultrasound assisted catalysis, electrochemistry and photovoltaic cells can be examined only after a thorough study of the published literature on these areas.

2.2 Nanostructured semiconductors:

2.2.1 Organic semiconductors:

The term 'organic semiconductor' implies that (i) the materials are mostly made up of carbon and hydrogen atoms (with a few hetero atoms such as sulfur, oxygen, and nitrogen), and (ii) they show properties typically those associated with a semiconductor material. The main building block of many functional organic semiconducting molecules is the benzene ring. Benzene is formed by six sp^2 hybridized carbon atoms. There is a σ bond between each atom of the ring, whereas each carbon makes a π bond with either of the neighbouring atoms. The configurations of alternating single and double (or triple) bonds between carbon atoms are a typical example of conjugation in organic systems; every organic molecule having these series of bonds is considered as a conjugated system.

The molecular structure with a conjugated π electron system formed by the p_z orbitals of sp^2-hybridized carbon atoms is shown in Figure 2.1. As compared to the σ bonds forming the backbone of the molecules, the π bonds are significantly weaker. Therefore, the lowest electronic excitations of conjugated molecules are the π-π^* transitions with an energy gap lying within 1.5 and 3 *eV*, leading to light absorption or emission in the visible spectral range [9]. Thus there is a wide range of possibilities to tune the optoelectronic properties of organic semiconducting materials.

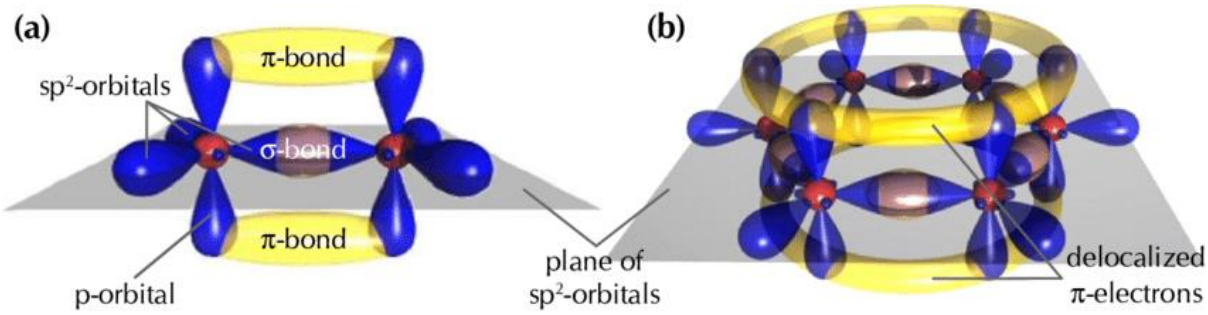

Figure 2.1: *(a) Conjugated π electron system and (b) electron delocalization in sp^2-hybridized carbon atoms [10]*

2.2.1.1 Metal Phthalocyanine (MPc):

The name phthalocyanine (Pc) is derived from two Greek terms '*naphtha*' (rock oil) and '*cyanine*' (dark blue). Although discovered long years back, in 1907 phthalocyanine was first reported as a by-product of a chemical reaction between acetic acid and phthalimide [11]. This blue by-product was metal-free phthalocyanine (H_2Pc). But the chemical stability of this material was under question. Following this, copper phthalocyanine was accidentally synthesized at Scottish Dyes Ltd. (later became Imperial Chemical Industries) with high chemical stability. The basic structure of a phthalocyanine molecule is composed of a metal centre having redox couple capability, and a large planar conjugated ring structure that binds the metal center via four nitrogen (N) moieties. Pcs are π-conjugated systems where 18 π-electrons are delocalized and free to move around the aromatic structure. Due to 2^- oxidation state of the organic ring, the central region is capable of accommodating H^+ ions or any other distinct metal ions such as Cu^{2+}, Fe^{2+}, Ni^{2+}, Zn^{2+} and Co^{2+}. The molecular formula of *Cu* based *Pc* is $C_{32}H_{16}CuN_8$ and its molecular arrangement is shown in Figure 2.2.

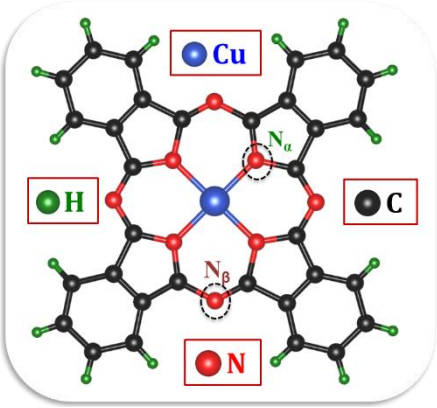

Figure 2.2: *Molecular structure of CuPc*

MPcs exist in three different polymorphic forms depending on their molecular stacking arrangements designated as α, β, γ phases. The β form has the monoclinic structure,

whereas the α-form has been reported to be tetragonal, orthorhombic or monoclinic. Among various MPcs, mainly *CuPc* and *ZnPc* are studied in this dissertation.

In solid state, more than 10 different phases including α and β phases have been reported for *CuPc*. α and β phases are most common when deposited in the form of thin films over the substrate. Such thin film preparation requires mainly physical vapor deposition i.e. thermal evaporation process. Works on *CuPc* and *ZnPc* thin films deposited on various substrates exist in literature [12-15]. The α phase, however, undergoes a transition to the β phase when deposited at higher substrate temperatures or post annealed in a controlled environment [16]. On the other hand, β phase *CuPc* is thermodynamically more stable and generally found in larger needle-shaped crystals [17]. Table 2.1 summarizes the chemical synthesis protocols for the growth of *CuPc* and *ZnPc* micro/nanostructures as prepared by several research groups. Based on these, low temperature chemical synthesis of both α and β phases of *CuPc* and only β phases of *ZnPc* will be explored in the present dissertation.

Table 2.1: *Various synthesis protocols for MPcs nanostructures*

Materials	**Synthesis protocol**	**Morphology**	**Ref.**
CuPc	Self-assembly	Nanowire	[18]
	Hydrothermal	Nanotube	[18]
CuPc	Hydrothermal	Nanobelt	[19]
CuPc	Solvothermal (Quinoline)	Crystal	[20]
CuPc	Solvothermal (Quinoline)	Needle like crystal	[21]
CuPc	Solvothermal (ethanol)	Needle like crystal	[22]
ZnPc	Solvothermal (ethylene glycol)	Flaky nanotube	[23]

At first, Jung *et al.* reported the self-assembly synthesis process for the growth of *CuPc* nanowires from commercially available *CuPc* powder in room temperature. These wires are subsequently transformed into rectangular nanotubes by hydrothermal process [18]. The same process is adopted with some modifications in molar ratio in the precursor materials. One step solvothermal synthesis of needle-like *CuPc* crystal using Quinoline and ethanol solvents were reported by some research groups [21, 22]. *CuPc* microrod is synthesized by following the route as reported by Li *et al.* [19], but reaction time is diminished from 5 days to 1 day in our case. *ZnPc* flaky nanotubes were solvothermally synthesized by Guo and his co-workers using ethylene glycol solvent. In a similar way, green synthesis of *ZnPc* using water solvent is also carried out for the first time by our group.

2.2.2 Layered 2D materials:

In the last decades, various 2D layered materials acquired significant interest among the scientific community. They possess different properties like large surface area, enormous active sites and enhanced electron mobility that facilitates good transport medium for electrons. In 2004, graphene was first discovered by two researchers of Manchester University named A. Geim and K. Novoselov, who employed scotch tape method [24]. In the year of 2010, they won the Nobel Prize in Physics for their revolutionary discovery of this disrupted material that has opened a whole new 2D world. By the success of graphene, other 2D layered materials *viz.*, topological insulators (TIs) [25, 26], transition metal dichalcogenides (TMDCs) [27-29], hexagonal-boron nitride (h- BN) [30-32], MXenes [33, 34], graphitic carbon nitride (g-C_3N_4) [35-37], metal-organic frameworks (MOFs) [38-40] as presented in Figure 2.3 are evolved, thus reinforcing the family of 2D layered materials. They also find potential applications in numerous fields of science and technology [41].

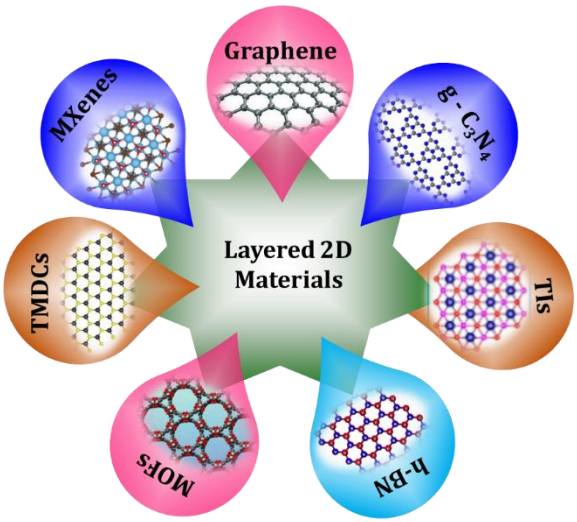

Figure 2.3: *Various classes of layered 2D materials*

Among those, graphene and TMDC based layered materials are chosen for the formation of heterostructure with MPcs, followed by examining their potential for various possible applications.

2.2.2.1 Graphene:

The discovery of graphene and its composites has revealed a whole new area with numerous opportunities. Graphene is a flat monolayer of sp^2 bonded carbon atoms tightly packed into a 2D honeycomb lattice. It is acting as a basic building block for all other dimensional graphitic materials. It can be wrapped up into 0D fullerenes, rolled into 1D nanotube or stacked into 3D graphite. Isolation of monolayer graphite or graphene from bulk graphite in large scale and usable form remained as a challenge to material scientists and

chemists for a decade. The scotch tape method [24] was unique but had limitations towards large scale applications. Other than that, several methods including chemical exfoliation, intercalation, surface functionalization, etc. to obtain modified graphene /graphene oxide (*GO*) in suitable form also exist. *rGO* nanosheets exhibit some unique physical and electrical properties. In addition to that, their easy preparation process gives rise to a greater hope towards the revolutionary move from scientific research to exciting practical applications. The planar geometry of graphene makes it useful in diverse applications e.g. electronic devices [42, 43], catalysis [44], energy storage [45] and conversion [46, 47].

2.2.2.2 Transition metal dichalcogenides (TMDCs):

Analogous to graphene, another type of 2D materials i.e. TMDC also possesses layered structure. The general stoichiometric formula is MX_2, where transition metal and chalcogens are denoted by M and X, respectively. M can be chosen from group IVB (Ti, Zr, Hf and so on), group VB (V, Nb or Ta) or group VIB (Mo, W and others), and X is the elements from group VIA (S, Se or Te) [48]. These classes of materials exhibit layered structures in the form of X-M-X in which two hexagonal planes made of chalcogen are isolated by a plane of metal atoms as shown in Figure 2.4.

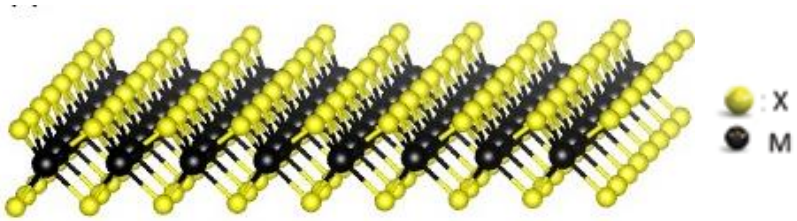

Figure 2.4: *Molecular arrangements of monolayer of MX_2 [48]*

The intralayer bonds are covalent in nature, whereas two adjacent MX_2 layers are typically bonded by van der Waals interaction to form the bulk crystal. In case of graphene, the electronic properties are based on the hybridization of *s* and *p* orbitals, whereas the electronic structure of TMDCs are governed by the electron filling of d orbitals of the transition metals. Transition metals and chalcogens in MX_2 [MoS_2, $MoSe_2$ etc.] compounds have an oxidation state of +4 and -2, respectively. By the combinations of various transition metals and chalcogens, TMDCs with a variety of electronic structures can be engineered. The electronic properties of TMDCs can be tuned in the range from metallic to semiconducting. Due to the two dimensional electron movement and the absence of strong interlayer coupling, layered TMDCs possess a direct bandgap as compared to indirect bandgap exhibited by their bulk counterparts. More importantly, presence of unsaturated coordination as well as dangling bonds at the edges of exfoliated layers of TMDCs make them potential candidates for many

contemporary research fields *viz.* catalysis [49, 50], transistor [51, 52], energy storage [53, 54] and sensor [55]. Out of different 2D TMDCs, MoS_2 is specifically chosen for investigations in the present dissertation.

❖ **Molybdenum disulfide (MoS_2):**

MoS_2 is one of the promising layered materials in the class of 2D TMDCs. Exfoliation of bulk MoS_2 proceeds via various means of facile chemical synthesis route to obtain single layer or stacked layers of 2D MoS_2. The cost of 2D MoS_2 preparation is lower as compared to other 2D TMDCs due to ease of processing. 2D MoS_2 reveals semiconducting nature with a direct band-gap, which in turn, makes them suitable for electrical and more so for optoelectronic applications [56].

Crystal structure plays an important role in determining the properties of 2D MoS_2. In the molecular structure of MoS_2, the S-Mo-S of each unit is treated as single layer comprising of two layers of S atoms with an intervening layer of Mo atoms. The presence of weak van der Waals interaction in between two S-Mo-S layers makes the exfoliation of layers facile towards the synthesis of single-layer / multiple layered MoS_2. Depending on the atomic arrangements, two most common crystal structures i.e. 1T and 2H have been observed where T and H indicate the tetragonal and hexagonal structure, respectively and the numbers denote the number of S-Mo-S layers present in one unit cell [57]. These two configurations are pictorially shown in Figure 2.5. From the figure, it is seen that in 1T phase, one Mo atom and six S atoms are interconnected in a twisted octahedral configuration whereas in 2H crystal structure, six S atoms are covalently bonded with every Mo atom, positioned in the centre of hexagonal prism. These 1T and 2H phases, respectively exhibit metallic and semiconducting properties. When thickness of 2D MoS_2 layer is reduced to nanometer range, lot of edges get exposed leading to an increase in the vacancy defects thereby, lowering the coordination number of surface atoms.

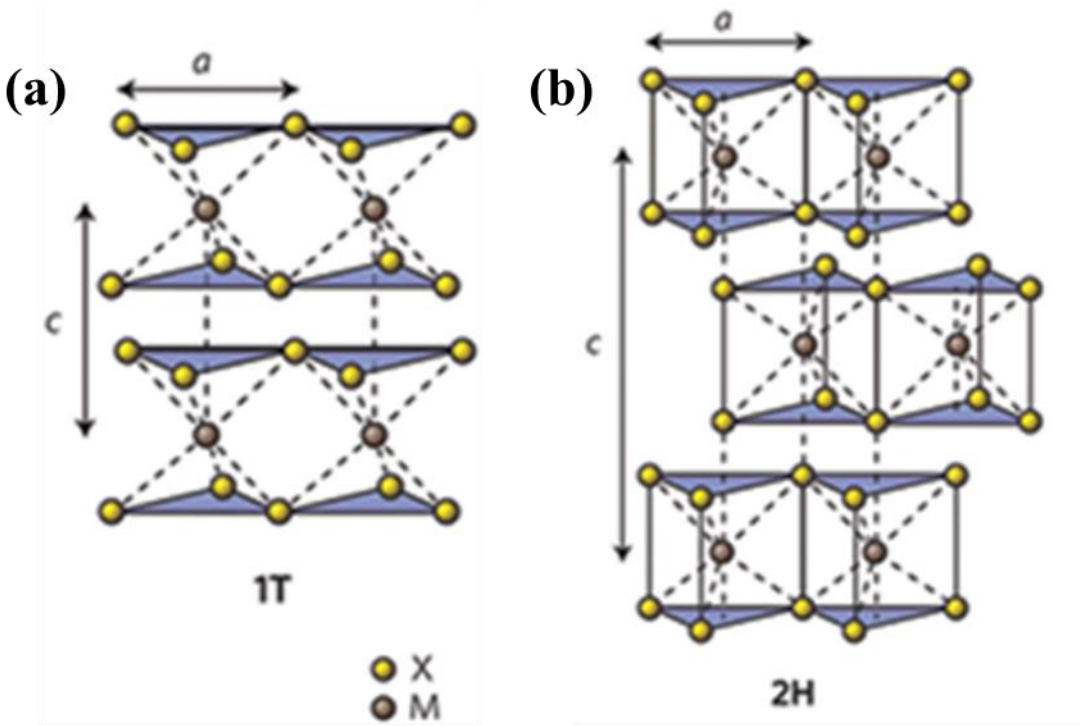

Figure 2.5: *Two common crystal structures of MoS_2: (a)1T and (b)2H [48]*

2.2.3 Hybrid nanostructures:

Hybrid nanostructures can be defined as the combination of two or more distinct materials in which at least one dimension of each material should be in the range of nanometer [58]. Potential integration of advantages along with suppression of limitations of the constituent elements make the overall structures outperforming over the individual components in any field of applications [59, 60]. Factors like composition, structure, crystal phase, exposed facet, spatial organization, the interface between constituents and others determine the properties and functionalities of a hybrid nanostructure. Thus, controlled synthesis and realistic design of such structures play crucial role in extracting the functional properties varying over a broad range with improved performances. From a morphological point of view, various types of hybrids are possible: core shell, Janus type nanostructures, etc. In hybrid materials, association of different components not only exhibits the additive effects of individual components, but also proclaims some new properties as a result of synergistic effect in between them.

According to the existing literature [Table 2.2], there are very few reports on the synthesis of MPc hybrid with carbon and TMDC based materials. Thus, wrapping/ hierarchical growth of *rGO* and *MoS_2* over *CuPc* surface will be synthesized in which pristine *GO* and *MoS_2* can be prepared by following conventional procedures.

Table 2.2: *Various synthesis protocols for MPc hybrids*

Materials	Synthesis protocol	Morphology	Ref.
ACNT-CuPc	Solution process	CuPc particles decorated ACNT	[61]
rGO/CuPc	Solution process	rGO wrapped CuPc nanotube	[62]
MoS_2/CNF	Hydrothermal	MoS_2 decorated CNF	[63]
FePc-MoS_2	Hydrothermal	FePc molecule attached in MoS_2 nanosheet	[64]
ZnPc-MoS_2	Solution process	Particle	[65]
MoS_2–ZnTTBPc	Hydrothermal- solution	Particle	[66]

Pristine MPcs substituted with functional groups (sulfo, nitro, etc.) are highly water soluble, but unsubstituted MPcs are partially soluble in organic solvents and highly insoluble in water [67]. Therefore, potential applications of unsubstituted MPcs in the field of catalytic dye degradation are limited due to proper mixing in aqueous medium. This is one of the major problems that MPcs are still facing in conventional ways of dye degradation. This problem can be eliminated in different ways: either by heterostructure formation of MPcs with *rGO* and *MoS_2* possessing inherent partial/high hydrophilicity [68, 69] or by the introduction of some new approach in the conventional degradation mechanism of dyes.

2.3 Multifunctional applications:

2.3.1 Environmental:

In recent times, significant attention is to be paid on the colour contaminants removal from the industrial wastewater aiming to reduce water pollution. Many industries i.e. textile, pharmaceutical, printing, etc. release different kinds of organic pollutants that in turn hampers aquatic animal life as well as human health. Dyes, used in textile colouring and printing purposes, remain in the wastewater and finally cause water contamination. To eliminate these problems, sonocatalysis and sonophotocatalysis are being explored recently rather than conventional photocatalysis.

2.3.1.1 Sonocatalysis:

❖ **Basic theory:**

Ultrasonic irradiation is an acoustic wave with frequencies more than 20 *kHz* i.e. the highest frequency of human hearing. The phenomenon of acoustic cavitation is caused by the propagation of the ultrasonic waves through aqueous medium. Acoustic cavitation comprises of three phases- formation of cavitation bubbles, bubble growth during negative pressure cycle and their explosive collapse during positive pressure cycle. The acoustic cavitation can be

classified into two stages: stable cavitation and transient cavitation. Stable cavitation is predominant at high frequency, in which only bubble oscillations can occur and no other implosion can take place. In this case, a small amount of agitation can be imparted due to micro-streaming caused by the motion of cavitation bubbles in their surrounding area. On the other hand, at low frequency, transient cavitation bubbles are generated by ultrasound that can sustain for few acoustic cycles and within a period of cycles, bubbles rapidly grow to a critical size until the violent implosion occurs [70]. Figure 2.6 illustrates the schematic of stable and transient cavitation.

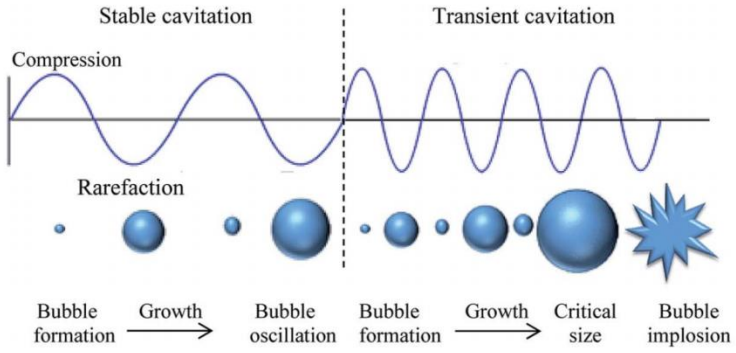

Figure 2.6: *Schematic representation of stable and transient cavitation [71]*

❖ **Mechanisms:**

Some hydrodynamic phenomena e.g. shock waves and micro-jets with high velocity are produced by the violent implosion of the transient bubble [72-74]. In addition to that, such implosions of cavitation bubbles produce a very high local temperature (~ 5000 *K*) and pressure (~100 *MPa*) that can guide the pyrolysis of organic pollutants as well as water inside the bubbles [70, 75]. This process is termed as '*hot spot*' by which different highly reactive species like $H^{\cdot}$, $HO_2^{\cdot}$ and $OH^{\cdot}$ are generated. These radicals react with dissolved organic and inorganic substances through hydroxylation and oxidation reactions [76, 77]. The reaction mechanism for the formation of radicals during the thermal dissociation of water vapor is as follows [71]:

$$H_2O + us \overset{)))}{\rightarrow} OH^{\cdot} + H^{\cdot} \quad (2.1)$$

$$O_2 + us \overset{)))}{\rightarrow} 2O^{\cdot} \quad (2.2)$$

$$O^{\cdot} + H_2O \rightarrow 2OH^{\cdot} \quad (2.3)$$

$$H^{\cdot} + O_2 \rightarrow OH^{\cdot} + O \quad (2.4)$$

$$H^{\cdot} + O_2 \rightarrow HO_2^{\cdot} \quad (2.5)$$

❖ **Sonoluminescence:**

Sonoluminescence is an interesting phenomenon observed in ordinary cold water due to the application of ultrasonic vibration. Initially, cavitation bubbles are formed which are filled up by water and dissolved gases in water. Due to the presence of surface tension, cavitation bubbles are shaped in the form of spheres in order to achieve minimum surface area as compared to other shapes of the same volume. With the increase in pressure of the sound wave, there is a decrease in bubble diameter gradually; thereby gases within the bubbles are compressed. As a result of this adiabatic compression of gases, the temperature of the gases increases. These cavitation bubbles collapse very violently under some conditions. After this violent collapse, a broad band visible spectrum of faint light with picosecond width is emitted from the bubble [78].

Plasma formation is an alternate explanation of light emission from bubbles [79-81]. At low temperatures, atoms of gases remain neutral, but as temperature increases within the collapsed bubble due to *'hot spot'*, atoms get ionized. These ionized atoms form plasma and take part in the emission of light through various ways [82].

2.3.1.2 Sonophotocatalysis:

Similar to sonocatalysis, sonophotocatalysis is another type of AOPs in which ultrasound and UV/Visible light are simultaneously applied to semiconductor catalysts in aqueous dye solution. The combination of ultrasound and light with catalyst effectively creates a synergy mechanism due to which more efficient removal of pollutants can be achieved. As a result of sonoluminescence, emitted light creates some charge carriers within the catalyst. In addition to that, external light also excites the catalyst and generates charge carriers. These generated carriers, in turn, help to generate a greater number of highly reactive $OH^{\cdot}$ radicals, enhancing the efficiency of dye degradation. There are various parameters that can influence the rate of dye degradation in both types of catalysis.

❖ **Influences of various factors on sono (sonophoto) catalysis:**

There are several operational variables as shown in the following flowchart by which the generation of reactive radicals can be influenced, thereby affecting the decomposition of dissolved dyes in wastewater.

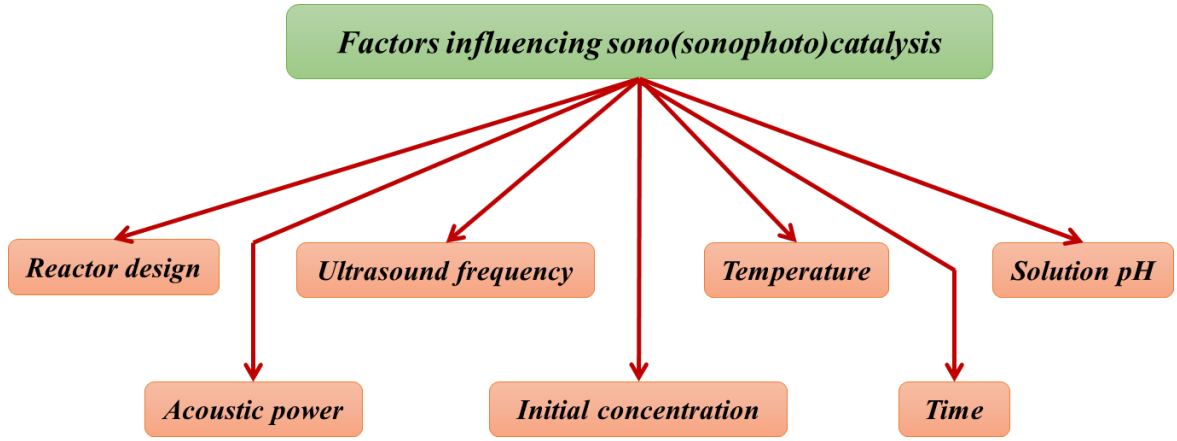

Some factors are briefly explained one by one in the following sections:

✹ **Design of reactor:**

There are four types of ultrasonic reactors that are most commonly used in research laboratories. These are bath, probe/horn, cup-horn and whistle sonochemical reactors. Among them, bath and probe sonicators are used in my work.

- The most commonly used ultrasonic device for carrying out sonocatalytic experiments is the ultrasonic bath. This is a device with low ultrasonic intensity and low cost. However, it is not that easy to maintain the temperature in this system and also the power of ultrasound is limited by various factors *viz.* water, bath size, wall thickness and bath position.
- On account of the above reasons, the bath sonicator is utilized for the purpose of cleaning; therefore the surface of the catalyst is also cleaned by removing the adsorbed molecules.
- Now, in the case of the probe or horn sonicator, the ultrasonic probe is directly immersed in the solution and intense cavitation is observed. Such horn provides efficient power control. Furthermore, there is a chance of cavitational erosion of the probe tip that leads to some kinds of chemical contamination within the system. It is evident from most of the published reports that horn type ultrasonic system is widely used because of highly intense ultrasonic vibration and optimal performance at particular amplitude for the decomposition of pesticides, textile dye, antibiotic drugs, etc.
- But the main limitation is that a small cavitation zone is produced around the transducer that limits the treatment of large volume of liquid and also consumes high-energy [71].

✹ **Frequency:**

There are important impacts of ultrasonic frequency on sonocatalytic degradation of textile dyes. Experimental results from several research groups also proclaim the prominent effect of frequency on the generation rate of $OH^{\cdot}$ radicals by the process of cavitation.

- With the increase in the ultrasonic frequency, the generated cavitation bubbles are of small size and shorter lifetime. Thus cavitation intensity as well as the maximum attainable temperature during collapse process are reduced causing a lower rate of $OH^{\cdot}$ radical generation.
- In case of hydrophobic materials, the optimum frequency for degradation is not only decided by the generation rate of $OH^{\cdot}$ radicals but also the mass transfer of molecules towards the interfacial region within the cavitation bubbles. Finally, 20 *KHz* is recommended for the optimum cavitation effects along with mass transfer rate [71]. Ultrasonic frequency may vary depending on the nature of the catalyst and type of contaminants.

✹ **Time:**

Time plays an important role in order to know about the reaction kinetics and the optimum reaction time for the removal of textile dyes. Sono-assisted degradation profile can be divided into three phases:

- Initially, when the concentration of dye molecules in the solution is very high, ultrasound is significantly utilized for rapid removal of dyes, thereby accelerating the reaction kinetics. So, a sharp rise in degradation efficiency is observed.
- Then, with the increase in reaction time, degradation occurs slowly as the concentration of dyes is reduced as compared to initial conditions that in turn exhibits slower reaction kinetics.
- At the end of the sonochemical degradation process, the removal efficiency reaches its maximum value and it remains saturated with prolonging reaction time.

The standard range of ultrasound assisted degradation times would be anywhere in between 5 *min* to 1 *h* [71].

✹ **pH:**

Another important factor in determining the degradation efficiency of pollutants is solution pH. During the sono-degradation process, the rate of formation of $OH^{\cdot}$ radicals is controlled by initial solution pH that in turn, affects the ultimate extent of textile dye degradation. The mechanism of degradation under acidic and alkaline condition is described as follows:

- Acidic environment inside the sonochemical reactor helps to generate huge number of $OH^{\cdot}$ radicals formation as well as accumulation by preventing the recombination reaction between $OH^{\cdot}$ that produces H_2O_2. So, efficient reactivity of $OH^{\cdot}$ radicals is observed in the acidic medium.
- In case of solution with high pH, ultimate available $OH^{\cdot}$ radicals for degradation is diminished due to the recombination of $OH^{\cdot}$ that produces H_2O_2 [83, 84]. Generated H_2O_2 will act as free radical scavenger which lowers the $OH^{\cdot}$ concentration [85, 86].
- Apart from that, there is one physicochemical property i.e. pK_a value of ionizable organic pollutants that in relation with solution pH ultimately controls the degradation performance [71].

As a newly developed efficient method, ultrasound-based remediation processes have the unique following advantages over the existing conventional strategies:

1. Ultrasound based processes can be operated at ambient temperature and pressure conditions.
2. This process is environment friendly as it does not introduce any hazardous elements into the water as by products.
3. As there is no need for extra chemicals, this method is cost effective.
4. This is easy to implement and faster remediation rate can be achieved as compared to other techniques.

Current status of ultrasound assisted dye degradation of various catalyst materials are discussed here. There are some associated parameters by which performances of catalyst materials are compared. Efficiency of dye degradation depends on concentration of dye, dose of catalyst, reaction time, type of dye molecules, etc.

Khataee and his co-workers investigated the sonochemical degradation of different dye molecules using various lanthanide element doped zinc oxide (*ZnO)* nanoparticles and corresponding results are listed in Table 2.3.

Table 2.3: *Sonodegradation performances of dyes using doped ZnO as catalyst*

Catalyst	Dye	C_{dye} (*mg/L*)	$C_{catalyst}$ (*g/L*)	Efficiency (%)	Time (*min*)	Ref.
Sm-doped ZnO	AB92	10	1	90.10	150	[87]
Ho-doped ZnO	RO29	10	1	88.30	150	[88]
Er-doped ZnO	RO29	5	1	88.09	150	[88]
Gd-doped ZnO	AO7	10	1	90	90	[89]
Ho-doped ZnO	RO29	10	1	88.3	180	[90]
Nd-doped ZnO	AB92	10	1	86.2	150	[91]

Apart from doped *ZnO*, many oxide materials *viz.* titanium dioxide (TiO_2), bishmuth oxide (Bi_2O_3), cerium oxide (CeO_2), etc. and their combinations were explored as sonocatalyst for the removal of different textile dyes done by several research groups. The performances of these catalyst materials are summarized in the following Table 2.4.

Table 2.4: *Sonodegradation performances of dyes using various catalysts*

Catalyst	Dye	C_{dye} (*mg/L*)	$C_{catalyst}$ (*g/L*)	Efficiency (%)	Time (*min*)	Ref.
Porous trigonal TiO_2 nanoflakes (p-TiO_2)	RB	10	0.5	81	180	[92]
β-Bi_2O_3	RB	5	3	98.7	90	[93]
	MO			81.12	30	
NiO@CeO_2	BG	10	0.3	46.1	240	[94]
Bi_2WO_6	MO	10	1	80	30	[95]
$LuFeO_3$	RB	5	4	82.9	90	[96]

Besides the sonodegradation of textile dyes by oxides and ferrites-based catalysts, focuses are given to the carbon-based hybrid materials. Incorporation of carbon-based materials enhances the catalytic degradation efficiency as compared to its bare counterparts due to high carrier mobility within carbon network, promotes the large separation of generated charge carriers (e^--h^+ pair), and thereby, ultimately reduces the carrier recombination. Table 2.5 summarizes the comparative study of catalytic activity of some carbon-based composite catalysts for dye removal.

Table 2.5: *Sonodegradation performances of dyes using carbon composite-based catalysts*

Catalyst	Dye	C_{dye} (*mg/L*)	$C_{catalyst}$ (*g/L*)	Efficiency (%)	Time (*min*)	Ref.
TiO_2-biochar	RB69	20	1.5	97.5	80	[97]
PbSe–graphene–TiO_2	RB	14	4	93	150	[98]
ZnO/graphene/TiO_2	MB	20	1	70.30	120	[99]
CdS-C_{60}/TiO_2	RB	4.8	0.2	~ 66	150	[100]
Fe_3O_4-CHC	AR17	10	1	100	80	[101]

Survey of the existing literature, as far as I know, reveals that no such report on ultrasound assisted catalytic activity of MPc nanostructures and their carbon-based heterostructures exists. Incorporation of *rGO* with MPc may offer an effective way to enhance the above activity by suppressing recombination of the charge carriers and can also modulate the hydrophobicity of MPc. In addition to that, the influence of some process parameters on catalytic degradation of textile dye will also be probed in this dissertation. Applications of *CuPc* and its hybrid in this field are expected to open up some new directions in wastewater remediation.

Initially, in case of dye degradation through a conventional photocatalysis process, certain limitations such as prolonged reaction time and high catalyst dosage may restrict their applications. Therefore, photocatalysis can be combined with some new techniques *viz.* electrochemical, sonication, microwave, etc. in order to achieve remarkably efficient water remediation. In this dissertation, ultrasound coupled visible light driven catalysis process is specifically focused. Some sorts of synergistic effect in between light and ultrasound help to uplift the overall performances. Advantages of this combination include the uniform dispersion of catalyst into the aqueous medium, cleaning of catalyst surface, enhanced mass transfer, generation of enormous active radicals, and many others.

ZnO and TiO_2 are wide bandgap semiconductors (3.1-3.3 *eV*) and behave as efficient photocatalysts when irradiated with UV light. They also exhibit visible light assisted catalytic activity only when their bandgap is tuned to lie within the visible region through various means *viz.* doping, composite formation with other materials, etc. Such sonophotocatalytic degradation of different dyes using *ZnO* and TiO_2 based materials with UV/Visible irradiation is summarized in Table 2.6.

Table 2.6: *Sonophotodegradation performances using various catalysts*

Catalyst	Pollutant	Source	C_{dye} (*mg/L*)	$C_{catalyst}$ (*g/L*)	Efficiency (%)	Time (*min*)	Ref.
F-TiO₂(B)	CV	US+Vis	30	0.1	46.15	120	[102]
F-TiO₂(B)	MG	US+Vis	30	0.1	58.61	120	[103]
ZnO	MO	US+UV	20	0.3	63	40	[104]
Fe/ZnO	AY23	US+UV	9.2	0.2	98	60	[105]
Fe-TiO₂	NBB	US+UV	10	2.2	96	60	[106]

The parameters involved in conventional photocatalytic activity of MPc and its composite towards dye degradation under visible light illumination is listed in Table 2.7. As MPc materials inherently exhibit visible bandgap, they get excited readily by the visible irradiation. From literature mentioned in Table 2.7, it is evident that ~ 1.5 - 5 *h* reaction time is recommended for all the cases. This is one of the limitations of the photocatalysis process.

Table 2.7: *Photodegradation of pollutants using phthalocyanine based catalysts*

Catalyst	Pollutant	Light	C_{dye} (*mg/L*)	$C_{catalyst}$ (*g/L*)	Efficiency (%)	Time (*min*)	Ref.
TNCuPc	RB	Visible	10	0.5	91	300	[107]
BiOCl/CuTNPc/PAN	RB	UV-Vis	10	1	75	180	[108]
CuPc-rGO	RB	Visible	4.8	0.25	96.2	210	[62]
TiO₂/FePc	MB	Visible	12.8	1	100	90	[109]
CuFePc-PAN/H₂O₂	RB	Visible	9.6	4	80	180	[110]

Based on the existing literature discussed so far, it can be clearly proclaimed that till now there is no such report on ultrasound assisted visible photocatalytic activity of MPcs

towards the textile dye removal. Synergistic effect of ultrasound and visible light combination and other factors on dye degradation under the presence of *CuPc* nanostructures will be explored in this dissertation.

2.3.2 Energy:

2.3.2.1 Storage: Supercapacitor (SC)

The ever increasing demand of energy in modern society makes a new class of energy storage systems, very essential. Efficient systems are required in order to store and release excess energy according to the purpose. Many forms of energies *viz.* chemical, electrical, electrochemical can be stored by several means of energy storage systems. Depending on that, they are classified into four categories: mechanical, chemical, electrical, and electrochemical storage [111, 112]. Among these, electrochemical energy storage in terms of SCs designed by MPc nanostructures is chosen as the area of investigation. SCs are electrochemical energy storage devices that have very fast charge discharge characteristics, high power density with excellent cycling retentivity. Power density vs. energy density plot is termed as Ragone plot that is shown in Figure 2.7. It can be seen that SCs have moderate energy density as compared to conventional batteries. The power density actually dictates the rapidness with which energy can be delivered whereas energy density proclaims how far the energy can be delivered after a single charging process. In recent times, serious and sustained efforts are devoted by the research community to improve the energy density by adopting new classes of materials, electrolytes, device design, etc.

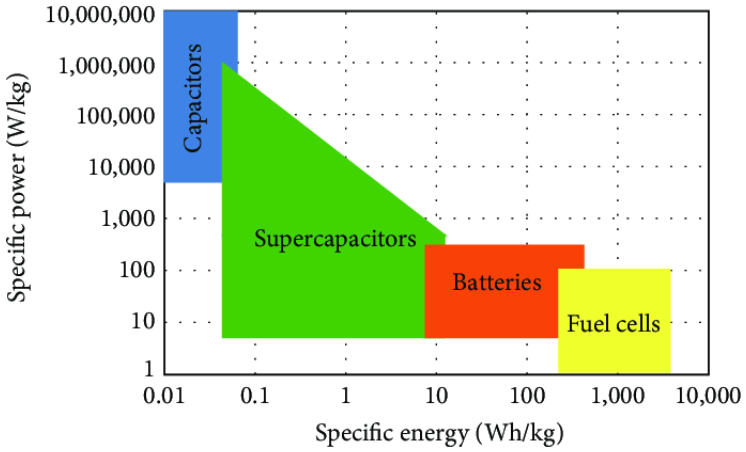

Figure 2.7: *Ragone plot for various energy storage and conversion systems [113]*

SCs furnish the existing gap in between normal capacitors and batteries as they offer higher power-density than batteries, larger capacitance value than normal capacitors, and rapid

charge/discharge process. Ideal supercapacitor electrode should offer features like high electrochemically active sites for improved charge transfer and ionic transport that lead to rapid surface redox reaction [114].

❖ **Advantages**:

- Nearly unlimited cycle life of SC device (millions of times) than battery (~ 500 times)
- High power density as compared to battery
- Charging process is very fast (takes a few seconds).
- Ability to power portable electronic systems.

❖ **Limitations:**

- Low energy density as compared to conventional battery
- Higher self-discharge than most of the batteries
- Low voltage from a single cell that necessitates a number of devices to be connected in appropriate fashion to achieve the required voltage.
- High cost per watt than regular battery

On the basis of the energy storage mechanism and electrical charge distribution over the two electrode surfaces, supercapacitors can be classified into three categories:

Electrical double layer capacitor (EDLC)

Pseudocapacitor

Hybrid capacitor

Among them, pseudocapacitor is our area of interest. Pseudocapacitors, shown in Figure 2.8, comprise mainly two oxide-based electrode materials, separator and an electrolyte. Here, charge storage mechanism proceeds via Faradaic process where charge is transferred in between electrode and the electrolyte. Due to the application of potential, reduction and oxidation reactions take place that result in the flow of Faradaic current through the pseudocapacitor cell. The limitations of pseudocapacitors are that they suffer from stability issue after long term operation as well as low power density as compared to EDLCs.

Examples of well-established inorganic pseudocapacitor electrode materials are transition metal oxides *viz*. Co_3O_4, VO_2, MnO_2, redox polymers e.g. polyaniline, polypyrrole, RuO_2, IrO_2. Other than all inorganic materials, current research interest is directed towards establishing organic MPcs as pseudocapacitor material.

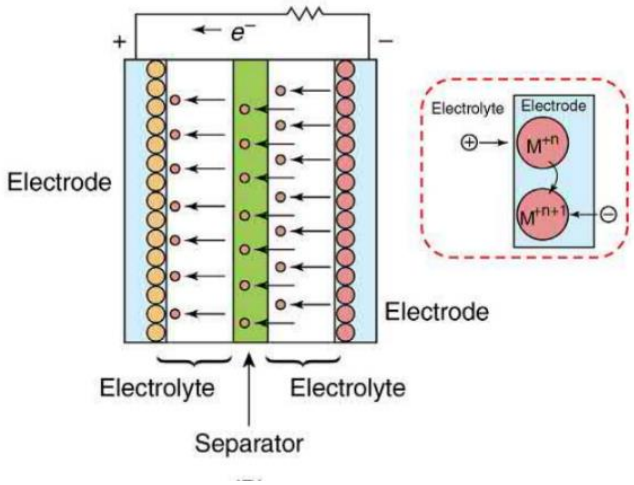

Figure 2.8: *Construction of pseudocapacitor [115]*

Transition metal based binary, ternary oxides, ferrites and their combinations were well studied by various researcher groups since the last few years. Table 2.8 shows performances of such supercapacitor electrode materials. Specific capacitance, retention after long duration of charge-discharge cycles and electrolytes are considered here for performance analysis. Some metal oxides *viz. Co_3O_4, NiO,* etc., offer high specific capacitance and are abundant in nature, but their poor electrical conductivity and high processing temperature become their major drawbacks.

Table 2.8: *Performances of conventional oxide-based supercapacitor electrodes*

Materials	**Electrolyte**	**Specific Capacitance (*F/g*)**	**Retention (%) @ # cycles**	**Ref.**
V_2O_5 flakes	$LiClO_4$/PC	510 @ 0.2 A/g	110 @ 1000	[116]
Cr_2O_3	1 M KOH	130 @ 1 A/g	96.2 @ 3000	[117]
CuO/ZnO	2 M KOH	579.5 @ 1 A/g	83 @ 2000	[118]
MnO_2 nanosheet	1 M Na_2SO_4	379 @ 0.5 A/g	87.3 @ 5000	[119]
$CoFe_2O_4$	6 M KOH	429 @ 0.5 A/g	98.8 @ 6000	[120]
$BiFeO_3$	2 M NaOH	72.2 @ 1 A/g	82.8 @ 1500	[121]

With the exception of conventional inorganic supercapacitor electrode materials discussed so far, some kinds of organic materials and their carbon-based composites were considered for the evaluation of supercapacitor performances. Specific capacitance at a particular current density and retention with long cycles for various Pc electrode materials are listed in Table 2.9. Majority of the electrodes were examined in acidic electrolyte. Mu *et al.* reported the hydrothermal synthesis of tetranitro iron phthalocyanine (*TNFePc*) flowers and studied their symmetric supercapacitive property in coin cell configuration [122]. After that,

many research groups started to explore carbon supported MPcs to achieve enhanced performance as compared to its pristine counterparts.

Table 2.9: *Performances of MPc and MPc based composite supercapacitor electrodes*

Materials	Electrolyte	Specific Capacitance (*F/g @ A/g*)	Retention (%) @ # cycles	Ref.
TNFePc	Ethanol+TFA	63@0.3	71@700	[122]
GO/CoTPyzPz	1 M Na_2SO_4	500@2	50@1000	[123]
NiPc-rGO	1 M H_2SO_4	223.28 @ 1	88.24@1000	[124]
N-CuMe$_2$Pc nanorods/rGO	1 M H_2SO_4	291.6 @ 0.5	100.1 @ 5000	[125]

It is evident from published reports that majority of the literature is related to different functional group substituted MPc nano/microstructures and their carbon-based composites mainly in acidic electrolyte. To the best of my knowledge, there is no such report on unsubstituted MPcs. Finally, pristine form of MPcs will be analysed as supercapacitor electrode materials in alkaline electrolyte.

2.3.2.2 Conversion: Fuel cell

With the progress in energy storage systems, energy conversion systems also seek much attention due to the increasing demand of clean energy worldwide. Fuel cell is one type of energy conversion systems in which the chemical energy of externally supplied fuel i.e. hydrogen and oxygen is converted into electrical energy. Two reactions occur at electrodes of fuel cells: one is hydrogen oxidation reaction (HOR) at anode and another is ORR at cathode. The rate of ORR process is very sluggish in nature as compared to HOR. Thus, development of cathodic electrocatalyst design becomes important to accelerate the ORR process.

❖ **Mechanism of ORR:**

The mechanism of molecular oxygen (O_2) reduction occurs in two ways in which transfer of either two or four electrons take place. One mechanism involves two electron transfer where O_2 is partially reduced [as Eq. (2.6)] and hydrogen peroxide (H_2O_2) is produced as a by-product, which is undesirable as well as hazardous. In the other mechanism, complete reduction of O_2 follows four electron pathway as described in Eq. (2.7, 2.8). These equations are known as dissociative and associative reactions, respectively, depending on the dissociation (O-O bond break) of the chemisorbed O_2 onto the active sites (M*) of the electrocatalyst before/after protonation [126]. In principle, a four electron mechanism is recommended for complete reduction of O_2 into water (H_2O) in case of electrocatalytic ORR.

- **Two electron mechanism:**

$$O_2 + M^* \xrightarrow{e^- + H^+} HOO^* \xrightarrow{e^- + H^+} H_2O_2 + M^* \quad (2.6)$$

- **Four electron mechanism:**

$$\frac{1}{2}O_2 + M^* \rightarrow O^* \xrightarrow{e^- + H^+} HO^* \xrightarrow{e^- + H^+} H_2O + M^* \quad (2.7)$$

$$O_2 + M^* \xrightarrow{e^- + H^+} HOO^* \xrightarrow{e^- + H^+} H_2O + O^* \xrightarrow{e^- + H^+} HO^* \xrightarrow{e^- + H^+} H_2O + M^* \quad (2.8)$$

Adsorption of molecular O_2 onto the active sites of the catalyst is the most important step towards the ORR mechanism. There are 3 ways, shown in Figure 2.9, by which O_2 can be adsorbed onto the catalyst surface. For four electron pathway, the Griffiths mode and Bridge mode are desirable, while the Pauling mode is preferable for two electron mechanism [127, 128].

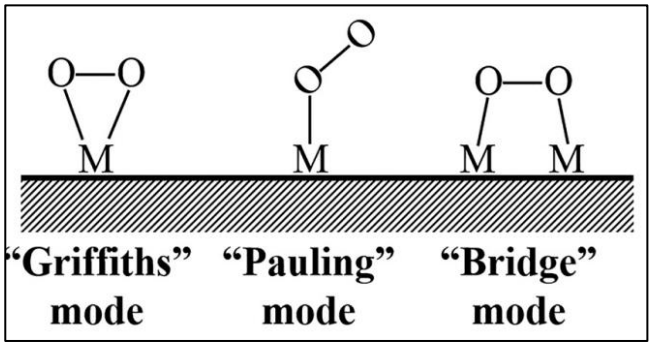

Figure 2.9: *Three adsorption modes for O on the surface of the catalyst [129]*

Electrocatalyst materials can be classified into four broad categories as shown schematically in Figure 2.10. These are briefly explained in the following section:

(a) Noble metal group:

Noble metal group elements include Platinum (*Pt*), Palladium (*Pd*) and their alloy with any transition metal (M). *Pt* and *Pd* based electrocatalysts still show the benchmark ORR performances in both acidic and alkaline electrolyte [126]. However, the natural resources unavailability, long term instability and high cost of *Pt* group metal led the scientists to search for alternative catalyst materials for large scale industrial application in fuel cell technology. Replacement of most efficient commercially available *Pt*- based electrocatalysts is highly challenging till date, from the point of view of practical ORR applications.

(b) Non Noble metal group:

Non noble metal group ORR electrocatalyst includes mainly transition metal based oxides, nitrides, carbides, phosphides, and chalcogenides. The main merits of these group materials are abundant resources, low cost, large scale production, etc. as compared to noble

metals. Another special class of organic materials, MPc comes under this category. ORR activities of these materials are awful as compared to *Pt* based catalysts; but they exhibit superior performance in alkaline media. These are therefore, very much suitable for alkaline fuel cells and metal air batteries. Still a long way to go for non-noble metal based catalysts to achieve the position in the family of ORR electrocatalysts.

(c) Carbon group:

A broad range of carbon materials *viz*. carbon nanotubes (*CNTs*), graphene, carbon quantum dots, carbon nanoribbons, carbon cages, etc. has been proclaimed as ORR electrocatalysts [130-132]. Superior ORR activity and resource abundance manifest these materials as potential candidates to replace the expensive noble metal based catalysts.

(d) Single atom group:

Single atom based electrocatalyst is a kind of emerging materials where the metal active sites are dispersed on a support matrix at the atomic level. These have gained enough research interest in the field of ORR electrocatalysts [133]. According to some recently published literature, these materials improve both ORR performance and stability under acidic conditions [134, 135]. High stability is the outcome of strong interaction between the single atoms and the host coupling sites. Although high ORR performance has been achieved by many research groups, the field of single atom based electrocatalyst should be explored further.

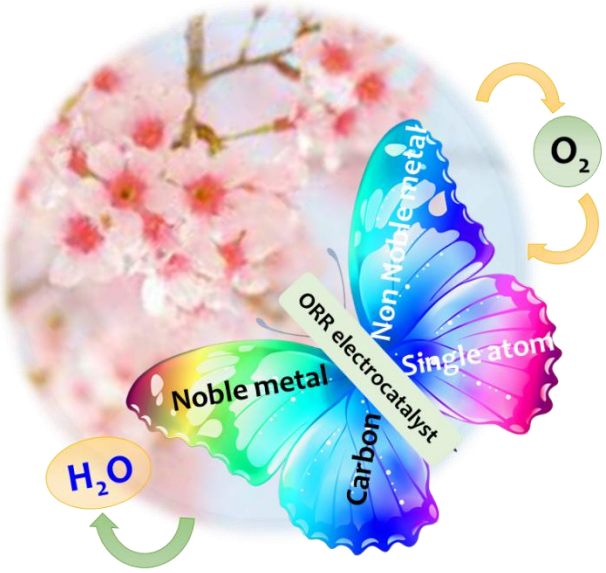

Figure 2.10: *Classifications of electrocatalyst materials*

To replace standard noble metal based catalysts, MPc were explored for oxygen reduction reaction (ORR). For performance comparison of various electrocatalysts, important parameters *viz*. onset potential (E_{onset}), half wave potential ($E_{1/2}$) and electron transfer number

(n) are considered here. In Table 2.10, ORR performances of pristine form of various MPcs are summarized. Iron phthalocyanine (*FePc*) is found as the best performing candidate over others as it followed the four electron transfer process of ORR. ORR activity was tested for all catalyst materials in the same alkaline medium i.e. 0.1 *M KOH*.

Table 2.10: *Performances of pristine MPc as ORR electrocatalyst*

Materials	E_{onset}(*V vs. RHE*)	$E_{1/2}$ (*V vs. RHE*)	n	Ref.
FePc+CoPc	0.952	0.879	4.0	[136]
K-FePc2Ph	0.946	0.882	3.7	[137]
cK-FePc2Ph	0.948	0.883	3.3	[137]
K-FePc5Ph	0.933	0.862	3.2	[137]
FePc	0.87	0.64	3.6-3.9	[138]
MnPc	0.83	0.54	3.6	[139]
PFe-Pc	1.046	0.94	3.47	[140]
ZnPc	0.72	0.52	1.9	[141]

As per the above table, it can be proclaimed that the ORR activity of *FePc* is closer to *Pt/C* as compared to manganese phthalocyanine (*MnPc*) and *ZnPc*. So, to achieve the improved performance of other MPcs *viz. CuPc*, *ZnPc*, etc., focusses were given on the heterostructure formation with carbon and TMDC based materials e.g. *rGO*, MoS_2, etc. The main features of carbon-based support materials like carbon black, carbon nanotube, and reduced graphene oxide, are their magnificent conductivity and π-π interaction between MPc and carbon support that, in turn, play the major role in the prevention of MPc molecule aggregation [142]. ORR performances of several forms of carbon based MPc composites are shown in Table 2.11. Almost all ORR activity is carried out in alkaline media, but Li *et al.* reported the ORR activity of bi-*FePc/GNS* in acidic media where the material followed four electron reaction pathway [143].

Table 2.11: *Performances of carbon supported MPc as ORR electrocatalyst*

Materials	Electrolyte	E_{onset} (*V vs. RHE*)	$E_{1/2}$ (*V vs. RHE*)	N	Ref.
CuPc/C	0.1 M KOH	0.81	0.72	4.0	[144]
ZnPc/rGO	0.1 M KOH	0.82	0.54	3.73	[141]
FeTAPc	0.1 M NaOH	0.86	---	2.99-3.64	[145]
FePc-Gr	0.1 M NaOH	0.97	---	3.99-4.44	[145]
bi-FePc/GNS	0.5 M H_2SO_4	0.76 [SHE]	---	3.7	[143]
FePc/GCB	0.1 M KOH	0.98	0.90	3.97	[146]
NiPc/GCB	0.1 M KOH	0.76	0.55	2.64	[146]
FePc/OMC	0.1 M KOH	0.725	0.623	3.95	[147]
FePc(CP)$_4$/Gr	0.1 M NaOH	0.921	---	3.8	[148]

There exists very few works based on the ORR activity of pristine and doped MoS_2 and the effect of presence of various dopants like vanadium, phosphorus, etc. Their performances are enlisted in Table 2.12. Pristine form of MoS_2 follows two electron pathway, whereas doped MoS_2 exhibits four electron pathway towards oxygen reduction. Only a single report is available on $FePc - MoS_2$ prepared by Kwon and his co-workers. They also investigated the ORR activity of $FePc - MoS_2$ in alkaline medium. These results are also included in Table 2.12.

Table 2.12: *Performances of MoS_2 and MPc - MoS_2 as ORR electrocatalyst*

Materials	E_{onset} (*V vs. RHE*)	$E_{1/2}$ (*V vs. RHE*)	N	Ref.
MoS_2 nanoflakes	0.80	0.64	1.9-2.1	[149]
Phosphorus doped MoS_2	0.96	0.80	3.4-3.6	[149]
Vanadium doped MoS_2	0.85	0.73	3.4-3.5	[150]
Oxygen incorporated MoS_2	0.94	0.80	4.0-4.1	[151]
FePc - MoS_2	0.90	0.89	4.0	[64]

Thorough survey of existing literature makes it clear that there is no report based on the ORR performance of *CuPc* and its heterostructure with *rGO* and MoS_2 nanosheets. Graphene has a very high surface-to-volume ratio that facilitates efficient electron transport, an essential criterion for electrocatalytic applications. The high surface-to-volume ratio of graphene makes it a promising candidate in the field of noble metal-free catalysis. In contrast to graphene, 2D MoS_2 may contain numerous unsaturated edges and dangling bonds. Such kinds of edge defects are responsible for enhanced electrocatalytic applications like ORRs [152]. In ORR applications, exposed Mo sites in 2D MoS_2 edges can be treated as active sites for O_2 adsorption, since negatively charged O atoms can easily be bound with positively charged Mo atoms [151]. Presence of vacancy defects in the basal plane also plays a role in improving ORR performances. In spite of the fact that cost of MoS_2 is reasonable and exhibits good chemical stability, its catalytic activity is still limited by poor carrier transport properties and the presence of highly inert basal planes.

However, some unique features those are very much beneficial to its application as ORR electrocatalysts. These are briefly introduced as follows:

(1) The unsaturated metallic edge centres furnish an intrinsic ORR activity upto a certain level and also provide possibility for functionalization with several materials.

(2) Active site accessibility by ORR reactants is dependent on the surface area; more active sites are provided by high surface area of catalyst materials. Surface area can be increased as a result of conversion of bulk MoS_2 to nanostructured MoS_2.

The above review indicates that electrocatalytic activity of *rGO* and MoS_2 based MPc hybrids towards ORR still needs further investigation.

2.3.2.3 Harvesting: Solar cell

Energy harvesting is the process of converting the ambient energy present in the atmosphere into electrical energy in order to power small electronic devices or circuits [153]. Solar cells are one of them in which solar radiation is converted into electrical energy. The basic four steps needed for such energy conversion are as follows:

1. Absorption process by which the absorber material is activated from a ground state to an excited state producing an electron-hole (e-h) pair.

2. The excited state (e-h pair) should be converted into free electron and hole as charge carriers, and

3. Transport mechanism by which photogenerated free negative and positive charge carriers are moved in two opposite directions, electrons towards the contact known as cathode and holes towards the contact, anode.

In some absorber materials, the excited state may be photogenerated free electron–free hole pair. In that case, step 1 and step 2 are intermingled. But, for some materials, the excited state may be an exciton, and steps 1 and 2 are then distinct.

❖ **Basic structures:**

There are several layers and two contacts present in solar cell structures. The core material is absorber which is capable of absorbing the light from the solar spectrum and producing an excited state. This state can be a pair of free electron and hole or bound electron and hole pair, called exciton that needs to be dissociated to form free electrons and holes. Absorber materials can be of different types *viz.* organic or inorganic semiconductors, dye molecules, quantum dots, perovskite materials, etc. In addition to the absorber materials, various transport layer materials need to be incorporated for improvement in the solar cell performances. Wide band gap materials that are capable to block electrons but allow the transport of holes with appropriate affinity level, are known as hole transport or electron blocking layer (HTL/EBL). Similarly, materials which are able to transport electrons but block holes are named as electron transport or hole blocking layer (ETL/HBL). Function of these layers is to prevent unwanted recombination of photogenerated electrons and holes at the electrodes. The contact materials can be metal or transparent conducting oxide (*TCO*). It provides low electrical resistance as well as a good amount of solar light transmission into the cell by virtue of its transparency towards the solar spectrum. indium tin oxide (*ITO*) or Fluorine doped tin oxide (*FTO*) are widely used *TCO*s.

On the basis of the positioning of transport layers, solar cell architectures can be of two types: conventional and inverted configurations illustrated schematically shown in Figure 2.11. In conventional architecture, HTL and ETL are deposited over *TCO* and absorber, respectively, whereas the position of HTL and ETL are interchanged in an inverted configuration.

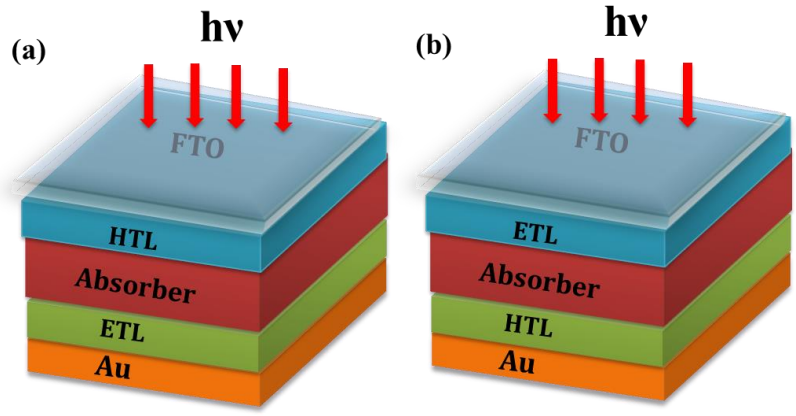

Figure 2.11: *(a) Conventional and (b) Inverted architecture of solar cell*

❖ **Basic Parameters:**

The performance of a solar cell is evaluated in terms of four basic parameters: Short circuit current density (J_{sc}), Open circuit voltage (V_{oc}), Fill factor (FF) and Power conversion efficiency (PCE). The optimum performance of a cell is judged by its FF and finally by the PCE.

Depending upon the type of absorber materials used, solar cells are classified into different categories like silicon solar cell, dye sensitized solar cell, organic solar cell, perovskite solar cell, etc. In this dissertation, performances of organic polymer and *Pb* free perovskite solar cells along with various transport layers will be investigated through their simulations using Silvaco ATLAS.

2.3.2.3.1 Organic polymer solar cell (OSC):

In this type of solar cells, small molecules and polymer kinds of organic semiconductors are used as solar light active layers. In OSCs, p-type (donor) and n-type (acceptor) semiconductors are used together. The p-type materials include small molecules like porphyrin, phthalocyanine and conjugated polymers *viz.* poly(p-phenylenevinylene (*PPV*), poly-3-hexylthiophene (*P3HT*), etc. Mainly, Fullerene derivatives *viz.* phenyl-C61-butyric acid methyl ester (*PCBM*) is primarily used as n-type material due to fast charge separation and high electron mobility in it.

There are two types of architectures - one is bilayer structure and the other is bulk heterojunction (BHJ) structure. In bilayer structure, donor (D) and acceptor (A) layers are successively deposited. In the latter, donor and acceptor with certain weight percentage are mixed homogeneously to form an interpenetrating network in nanoscale domains. The resulting absorber is deposited on a transparent electrode. The donor/acceptor interface facilitates exciton dissociation. Thus in BHJ, effectively large interface area and thereby, significantly increased exciton dissociation can be achieved, resulting in larger photocurrent. Thus, BHJ structure is found to be more efficient than bilayer structure [154, 155].

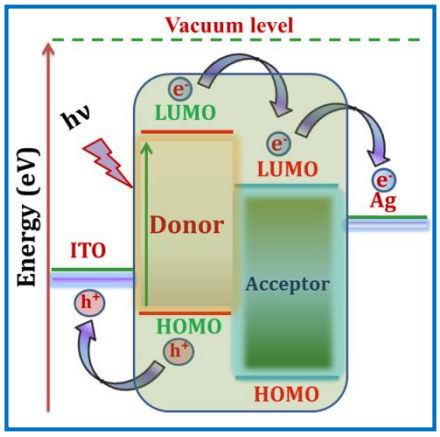

Figure 2.12: *Organic BHJ solar cell architecture*

❖ **Working principles:**

In OSCs, the conversion of solar energy into electrical energy involves few steps: generation, diffusion and dissociation of exciton, and subsequently transport of free charge carriers to the electrodes. Every step is important for the efficient operation of OSCs and is described below.

(a) Exciton generation:

When solar radiation is incident on OSCs, photons get absorbed by the absorber material. For each absorbed photon, an electron is excited from the highest occupied molecular orbital (HOMO) to the lowest unoccupied molecular orbital (LUMO) of the organic semiconductors. As organic materials possess very low (~3 - 5) dielectric constant [156, 157], such photon absorption leads to the generation of excitons, which are electrically neutral but Coulombically bound electron–hole pairs, rather than free charge carriers in inorganic semiconductors. Low permittivity makes the binding energy of the electron–hole pairs in organic absorber is significantly higher than that in inorganic materials [157]. As a consequence, only ~10 % of the generated excitons are converted to free charge carriers in

conjugated polymers [157]. For the purpose of dissociation of excitons, an electron donor and electron acceptor materials with appropriate energy band structures are required.

(b) Diffusion:

Diffusion of photogenerated excitons to reach at donor–acceptor interface is a crucial step. At the interface, dissociation of excitons takes place to yield free electron and hole pairs. So, exciton diffusion length is the determining factor for absorber layer thickness i.e. the donor–acceptor phase separation length or bilayer device length [158]. In case of organic semiconductors, exciton diffusion lengths are usually around 10–20 *nm* as per existing literature [159]. Diffusion of excitons over longer distances causes their decay through radiative or non-radiative recombination, to their ground state before reaching the interface. As a result, the efficiency of the solar cell falls.

(c) Dissociation:

The dissociation of excitons yields free charge carriers. Splitting of neutral excitons are accomplished either by externally applied electric field or by the local electric field appeared at donor–acceptor interface. A strong local electric field is generated due to the differences in the LUMO energy levels of the donors and acceptors at the interface. Such heterojunction interfaces are created by blending electron donors with electron acceptors. Now, the photoinduced charge transfer across the interface is an ultrafast (~ 45 *fs*) process compared to other competing relaxation processes [160]. Some controversies may exist in context with the mechanisms of exciton dissociation and complete process is still not clearly understood. Several pathways are proposed to create free carriers i.e. charge transfer (CT) complex or hot states. In the first case, CT complex is formed due to the transition of electron from LUMO of donor to LUMO of acceptor, therefore, hole is on the HOMO of a donor material and the electron is on the LUMO of acceptor molecule. As the hole and electron are quite close to each other, they are still Coulombically bound. In another approach, hot states are generated by gaining energy from energy level offset in LUMO and are used to generate free carriers directly.

(d) Collection:

After the dissociation step, transport and collection of free carriers at respective electrodes are also very important to achieve high efficiency solar cells. The carrier mobilities in the donor and acceptor materials are thus crucial for the charge carrier transportation. An external electric field may arise through use of asymmetrical contacts, where one low work-function (WF) metal is employed for collecting electrons and one high WF metal for collecting holes [161]. An ohmic contact between organic materials and electrodes is important to

efficiently collect the electrons at cathode and holes at anode. The nature of the electrode/organic material interfaces is really complex.

The whole mechanism for OSC is explained with the help of Figure 2.13. Initially, photons are absorbed with an efficiency η_{PA} that depends on absorption coefficients (α) of absorber molecules and excitons are produced. The photogenerated excitons diffuse with efficiency η_{ED} towards the donor-acceptor (D-A) interface. Next, charge is transferred to the acceptor with efficiency η_{CT}. An efficient charge transfer is commonly observed in presence of an energetic driving force towards a charge-transfer or a charge-separated state. After that, dissociation of the excitons into electron-hole pairs occurs with efficiency η_{CD}. This step, in an organic solar cell, is not yet completely understood and still an issue of controversial discussions. Separated charge carriers are transported with efficiency η_{CP}. Finally, charge is collected at the electrodes with efficiency η_{CC}. Loss of carriers may occur at electrodes if the electrode material is not chosen properly.

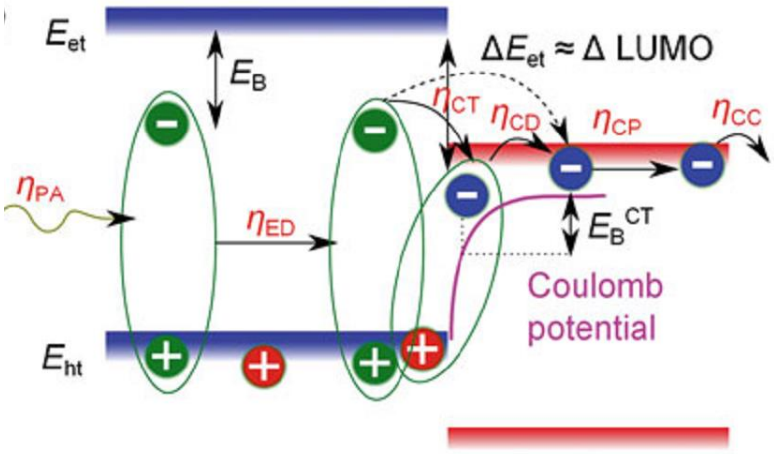

Figure 2.13: *Overall working principles of organic BHJ solar cell [162]*

❖ **Advantages:**

- Solution processability of organic semiconductor helps to produce low cost large area OSC fabrication.
- Low temperature processing techniques help to reduce the manufacturing energy consumption.
- Ability to print on large area plastic substrates ultimately leads to portable electronic applications.

Lot of theoretical as well as experimental works on polymer: fullerene based BHJ solar cells were reported. Poly[2-methoxy-5-(3´,7´-dimethyloctyloxy)-p-phenylene vinylene] [$OC_1C_{10}PPV$] and *P3HT* are two popular organic polymers employed as absorber materials with fullerene. Lenes *et al.* reported the experimental dependency of absorber material Poly[2-methoxy-5-(3′,7′-dimethyloctyloxy)-1,4-phenylenevinylene] [*MDMO-PPV*]*:PCBM* thickness on solar cell performances [163] and finally proclaimed that 100 *nm* thick absorber yields optimum performances. Riedel with his group conducted a comparative study of cells using $OC_1C_{10}PPV$ and *P3HT* based absorbers. The measurements indicated that *P3HT* based solar cells exhibit larger J_{sc} and FF due to significantly higher charge carrier mobility [164]. So, application of these two organic polymers in the field of solar cells will be explored further in this present dissertation. Performance comparison of both absorbers will be made on the basis of simulation using Silvaco ATLAS^{TM} tools. Some reports indicated the performance improvement in *P3HT:PCBM* inverted solar cell with additional carrier transport materials like vanadium dioxide (V_2O_5) [165], nickel oxide (*NiO*) [166], poly(3,4-Ethylenedioxythiophene) polystyrene sulfonate (*PEDOT:PSS*) [167], *ZnO* [168] etc. with silver (*Ag*) as top electrode. In addition, the influence of various metal electrode and transport layer materials will also be investigated for further enhancement in solar cell parameters.

2.3.2.3.2 Perovskite solar cell (PSC):

In recent years, halide perovskite (HP) based materials acquired immense importance as efficient solar light absorber for photovoltaic applications due to their outstanding optoelectronic properties like large carrier diffusion lengths, moderate carrier mobility, high visible light absorption coefficients and tunable optical bandgaps [169-171]. HPs are of two categories: one is organic-inorganic HP (OIHP) and the other all inorganic HP (IHP). General formulae for one type of HPs are ABX_3 [Figure 2.14], where A indicates the monovalent organic cation *viz.* methylammonium [MA^+ ($CH_3NH_3^+$)], formamidinium [FA^+ ($HC(CH_2)_2^+$)], etc. and inorganic cations like Cs^+; B represents divalent cations *viz.* Pb^{2+}, Sn^{2+}, etc. and X represents halide anions like Cl^-, Br^- and I^- [172].

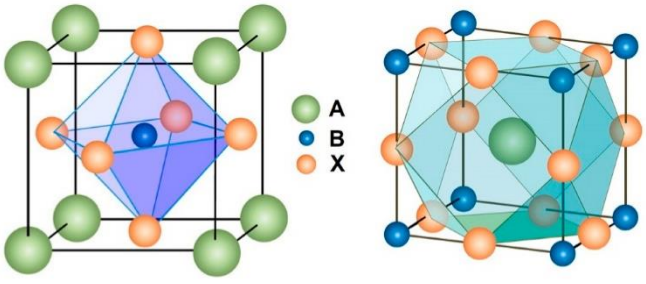

Figure 2.14: *Crystal structure of single perovskite (ABX_3)*

Although record PCE has been achieved from OHIP based solar cells, they suffer from chemical instability due to the presence of organic MA^+ or FA^+, which are volatile in nature and easily get decomposed to several components [Eqs. (2.9 and 2.10)] under the presence of external agitations e.g. heat, light, oxygen and moisture [173]. CH_3I / NH_3 products are formed by degradation of MA^+ cations and this reaction is irreversible in nature turning the reformation to MA^+ impossible.

$$MAPbI_3 \xrightarrow{h\nu \text{ or } \Delta} PbI_2 + Pb + I_2 + CH_3NH_2 + CH_3I + HI + NH_3 \quad (2.9)$$

$$MAPbBr_3 \xrightarrow{h\nu \text{ or } \Delta} CH_3NH_2 + PbBr_2 + HBr \quad (2.10)$$

This issue has urgently stimulated the investigation of IHP in which organic cations are replaced by inorganic cations. But there are also several degradation mechanisms like polymorphic transition, oxidation and hydration, those affect the stability of IHPs adversely. Now, all HP materials contain lead (*Pb*) whose toxicity severely causes environmental hazards. According to the 'lead free directives' [174], the maximum *Pb* concentration in every homogeneous material is restricted upto 0.1% by weight for any *Pb* based solar cells. Unfortunately, all HPs investigated so far as effective absorber materials contain more than 10% lead by weight [175]. Thus major attention is drawn towards the development of *Pb* free non-toxic perovskite materials to avoid the detrimental effect of *Pb*. Initially, Tin (*Sn*), Germanium (*Ge*), etc. are used in place of *Pb*, but rapid oxidation of *Sn* along with small amount of toxicity hinder the use of *Sn* in commercialization. In this regard, a new family of halide double perovskite based on non-toxic and ultra-stable titanium (+4) is unravelled with general chemical formula A_2TiX_6 (A = K^+, Rb^+, Cs^+, In^+, MA^+, or FA^+; X = *Cl*, *Br*, or *I*) [Figure 2.15]. Among them, Cs_2TiBr_6 will be focussed in this dissertation.

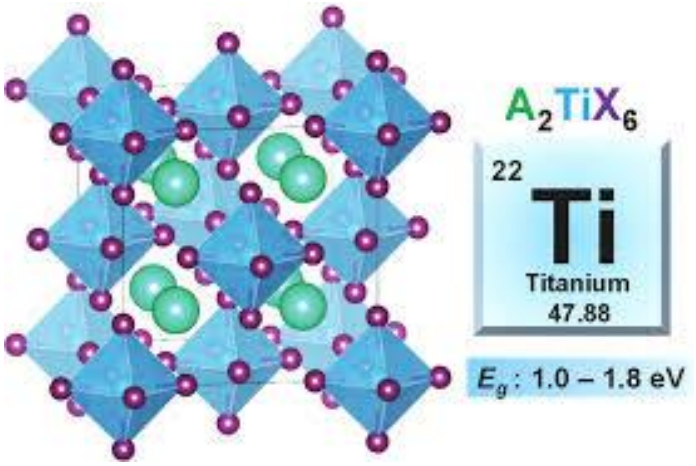

Figure 2.15: *Crystal structure of double perovskite (A_2BX_6)[176]*

Periodical evolution of *Pb* free double perovskite from *Pb* based single perovskite is schematically shown in Figure 2.16.

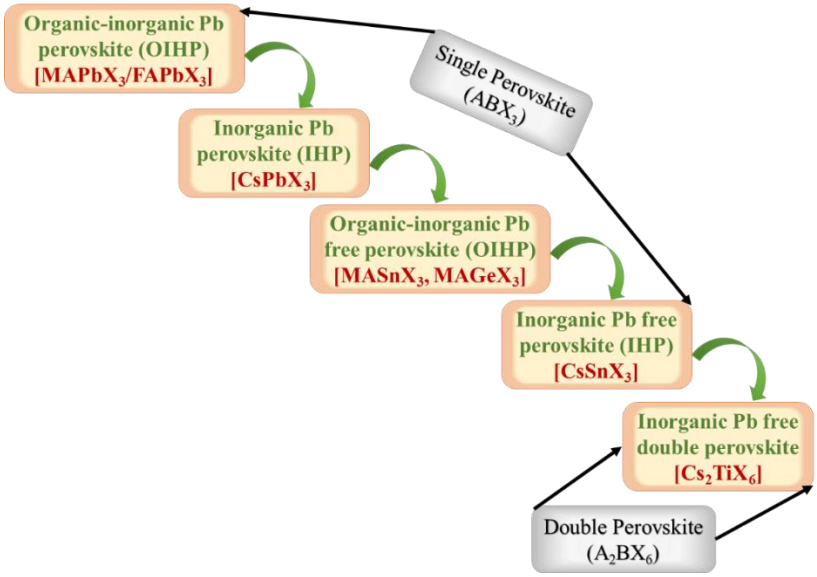

Figure 2.16: *Evolution of Pb free double perovskite (A_2BX_6)*

The technology for implementation of *Pb* based PSCs has been matured enough and OIHP solar cell offering record maximum PCE of around 24% has been reported. Here, performances of some recently reported *Pb* based PSCs are presented in Table 2.13.

Table 2.13: *Performances of Pb based OIHP and IHPs solar cell*

Absorber	J_{sc} (mA/cm^2)	V_{oc} (V)	FF (%)	PCE (%)	Ref.
$(FAI)_{0.81}(PbI_2)_{0.85}(MAPbBr_3)_{0.15}$	23.7	1.14	78	21.6	[177]
$(FAPbI_3)_{0.95}(MAPbBr_3)_{0.05}$	24.91	1.14	83.29	23.2	[178]
$CsPb_{1-x}Ca_xI_3$	17.9	0.945	80	13.5	[179]
$CsPbBr_3$	6.84	1.40	76.1	7.29	[180]
$CsPbBr_3$	5.08	1.21	66.7	4.1	[181]

Effect of *Pb* content as well as lack of stability of PSCs hinder their rapid industrialization. The major concern is the inherent toxicity of *Pb* content that causes severe health risk for peoples affecting central nervous system, renal, gastrointestinal, respiratory systems, and many more. The generation of *Pb* compounds during manufacturing and recycling processes of the perovskite based system demands some restrictions on large-scale implementation of PSCs. Initial strategy was to substitute *Pb* by other group IVA elements, such as tin (*Sn*) and germanium (*Ge*). Use of such *Pb* free perovskites yields high carrier mobilities and moderate conversion efficiencies, far away from those offered by cutting-edge *Pb* systems [182-185]. Table 2.14 summarizes the performances of some reported *Sn* and *Ge* based *Pb* free PSCs.

Table 2.14: *Performances of Pb free Sn and Ge based OIHP and IHPs solar cells*

Absorber	J_{sc} (mA/cm^2)	V_{oc} (V)	FF (%)	PCE (%)	Ref.
$MASnI_3$	11.82	0.45	40	2.14	[186]
$MASnIBr_{1.8}Cl_{0.2}$	14	0.38	57.3	3.1	[187]
$CsSnI_3$	25.71	0.38	49	4.81	[188]
$CsGeI_3$	18.78	0.51	51	4.94	[189]
$CsSnCl_3$	19.82	0.87	56	9.66	[190]
$CsSnBr_3$	21.23	0.85	58	10.46	[190]
$CsSn_{0.5}Ge_{0.5}I_3$	18.61	0.63	60.6	7.11	[191]

Sn and *Ge* based PSCs exhibit moderate PCE, but Babayigit *et al.* [192] reported high chances of rapid oxidation from Sn^{2+} to stable Sn^{4+} at ambient / aqueous environment due to their low redox potential. More importantly, use of Sn still causes toxicity, definitely much lower than that caused by the presence of *Pb*, and gives rise to some short-term effects on human systems. Ataxia, muscle weakness and irritation of gastrointestinal system are examples of such effects, which may in turn, lead to vomiting and diarrhoea. Plausible degradation pathways of *Ge* based PSCs and their tolerances to moisture, light, heat and oxygen are not investigated thoroughly and still under debate.

Apart from *Sn* and *Ge*, several metal cations i.e. Ag^{+}, Sb^{3+} and Bi^{3+} were used in synthesizing HPs. But these PSCs exhibit bandgaps higher than 2.0 *eV* (e.g. $Cs_3Bi_2I_9$-2.2 *eV*, $Cs_2AgBiBr_6$-2.2 *eV* and $Cs_3Sb_2I_9$-2.4 *eV*) making them unsuitable for photovoltaic applications [193-195]. The solar cell parameters for such kinds of *Pb* free PSCs are summarized in Table 2.15.

Table 2.15: *Performances of pb free (except Sn and Ge) OIHP and IHPs solar cells*

Absorber	J_{sc} (mA/cm^2)	V_{oc} (*V*)	FF (%)	PCE (%)	Ref.
$MA_3Bi_2I_9Cl_x$	0.18	0.04	38	0.003	[194]
$MA_3Bi_2I_9$	0.52	0.68	33	0.12	[194]
$Cs_3Bi_2I_9$	2.15	0.85	60	1.09	[194]
$MA_3Sb_2I_9$	5.41	0.62	60.82	2.04	[196]
$Cs_3Sb_2I_9$	2.91	0.60	48.11	0.84	[196]
$Cs_2AgBiBr_6$	4.08	1.01	70.92	2.92	[197]

In this scenario, Ju *et al.* [198] proposed a new family of *Pb* free inorganic HPs based on Titanium (Ti) with its very stable +4 oxidation state. Ti based HPs with general formula Cs_2TiX_6 (X=I/Br) offer a set of desirable properties like suitable bandgaps (1.38 - 1.78 *eV*) matched with solar radiation, efficient optical absorption, favourable defect properties and ultrahigh stability [176]. They reported the theoretical estimation as well as experimental validation of bandgaps tunable over in the range of (1.02 - 1.78 *eV*) arising from such PSCs. Several advantages of Ti, like earth abundance, biocompatibility and non-toxicity, make Cs_2TiX_6 very promising solar light absorber for future generation environment friendly *Pb* free PSCs. Such absorber materials exhibit excellent stability towards the environmental factors *viz*. light, moisture, heat, etc. These classes of materials are not yet explored much, and thus need further investigation. Experimental data determining the performances of Cs_2TiBr_6 solar cell are shown in Table 2.16, as reported by chen *et al.*[198]. Based on this work [198], Pb free Cs_2TiBr_6 will be simulated for the first time using TCAD from Silvaco ATLAS™. In addition, the role of various inorganic / organic HTLs in influencing solar cell performances deserves further investigation. The superhydrophobic property of organic MPcs used as HTL may characterize the solar cells with additional features of atmospheric moisture resistance and overall long term outdoor stability.

Table 2.16: *Performances of Pb free* Cs_2TiBr_6 based solar cell

Absorber	Type of investigation	J_{sc} (mA/cm^2)	V_{oc} (*V*)	FF (%)	PCE (%)	Ref.
FTO/TiO_2/C_{60}/Cs_2TiBr_6/ P3HT/Au	Experimental	5.69	1.02	56.4	3.28	[198]

2.4 Conclusions: This chapter has presented an overview of synthesis of organic semiconductors, 2D materials and their hybrid structures, along with their applications in the environment and energy sector. Various processes for the synthesis of each class of materials are summarized on the basis of available literature. Such summary helps us to introduce appropriate modifications in some existing methods and/or to adopt novel approaches for nanostructure preparation. For performance improvement of the pristine systems, formation of their hybrid structures has also reviewed. This chapter also presents an extensive literature survey in the field of applications of above materials that is required to identify gaps in existing literature and accordingly formulate the research problems dealt in this dissertation.

This chapter will present a brief description about the experimental techniques employed to carry out synthesis, characterizations and applications of MPcs and its hybrid nanostructures. Different synthesis routes may cause modulation in the morphology and dimension of materials. Various techniques followed to synthesize the nanostructured materials will be discussed here. Next, a brief description of several characterization tools employed to study the compositional, structural, morphological, and electrical properties of prepared nano / micro structures will be presented. Finally, methodologies adopted to explore the synthesized materials for various energy and environmental applications, will also be addressed here.

3.1 Synthesis Procedures:

Preparation of nanostructured materials involves either physical or chemical processes. Instead of using heavy and costly physical instruments, in this dissertation, chemical processes are considered for the growth of *ZnPc*, *CuPc* and their hybrid nanostructures.

3.1.1 Chemical process:

Apart from the cost effectiveness, the advantage of chemical method is primarily the good chemical homogeneity at the molecular level. A specific control over reaction kinetics leads to the formation of desired structural variation keeping the macroscopic properties unaltered. The general procedure of chemical synthesis involves reactions in aqueous/non-aqueous solution containing soluble or suspended salts. When the solution becomes supersaturated by the salt, the precipitation is formed either by homogeneous or by heterogeneous nucleation processes. One of the most promising solution processes for MPc nanostructure preparation is self-assembly, which offers some benefits: (i) several structures can be synthesized using basic building blocks of metal ions and organic ligands, (ii) different types of interactions i.e. π–π interactions, van der Waals interactions, etc. can be induced [199].

3.1.2 Hydrothermal / Solvothermal process:

Synthesis of pristine MPcs and their heterostructures through hydrothermal processes is carried out with an autoclave arrangement as shown in Figure 3.1. An autoclave is a device that is used to heat aqueous solution or organic solvents above their boiling point at a pressure higher than normal atmospheric pressure. It is basically a cylindrical stainless steel jacket [Figure 3.1(a)] fitted with screw cap. The cap should be fitted very tightly so that it can withstand very high-pressure created within the jacket during reaction. A cylindrical Teflon tube [Figure 3.1(b)] with a Teflon cap serves as the inert reaction chamber and is fitted within the iron chamber. The Teflon tube may be of different capacity like 100 *ml*, 50 *ml* etc. At most

80% volume is filled with solution. The autoclave is then inserted into the stainless-steel jacket and is kept in an oven at temperature below 250°C as per sample requirement.

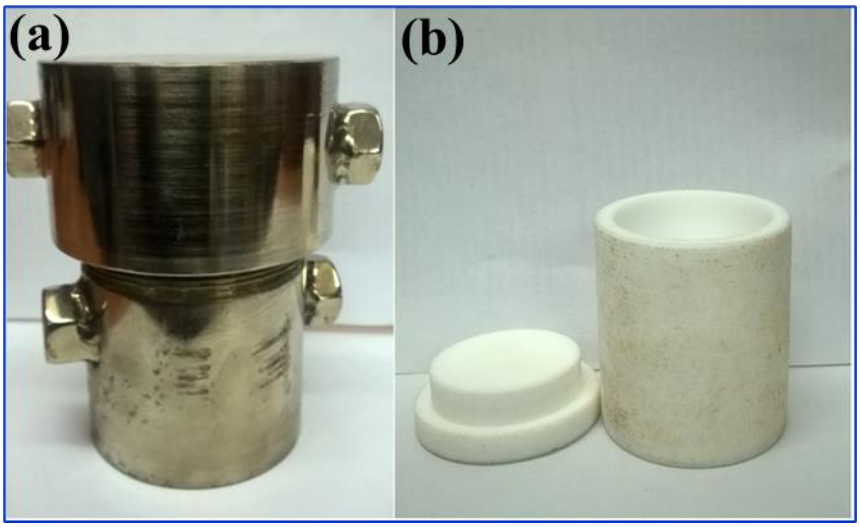

Figure 3.1: *Photographs of the (a) stainless-steel jacket and (b) Teflon tube*

As the reaction temperature for hydro (solvo) thermal is within 250°C, a simple low temperature oven is used in order to conduct the reaction. The photograph of the oven is shown in Figure 3.2 (a). The temperature of the oven is controlled with an accuracy of ± 0.5°C by an electronic temperature controller. After complete reaction, samples are filtered using vacuum filtration units as shown in Figure 3.2 (b).

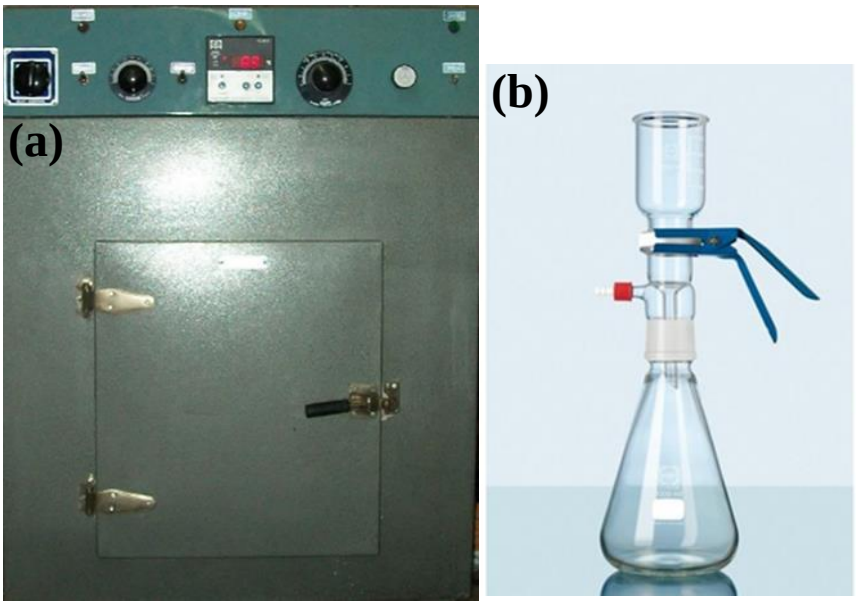

Figure 3.2: *(a) Photographs of oven and (b) Vacuum filtration set up*

Apart from the purpose of synthesis, the ovens can also be used for drying the sample. This process has lot of advantages *viz.* high product purity, homogeneity, single step process using simple equipment, lower energy requirement with faster reaction time, etc.

3.2 Characterization Tools:

There are several instruments available to confirm the proper formation of synthesized nanomaterials. Among them, XRD, FESEM, High Resolution Transmission Electron Microscopy (HRTEM), Energy Dispersive X-ray (EDX), XPS, UV-Vis analysis etc. are adopted in order to investigate structural, morphological and optical properties.

3.2.1 X-ray diffraction (XRD):

In 1895, the German physicist Roentgen discovered X-rays and so named due to its unknown nature at that time. In 1912, the exact nature of X-rays and its diffraction by atomic planes of crystals were properly discovered. This discovery offered a new direction to investigate the structure of matter.

Solid matter can be classified as follows:

1. Amorphous: The atoms are arranged in a random way. Glasses are amorphous materials.

2. Crystalline: The structure of a crystalline solid is described by considering its simplest repeating unit, termed as unit cell. The unit cell consists of lattice points that represent the locations of atoms. The dimensions of the unit cell are described by three axes *a*, *b*, *c* and the angles between them alpha (α), beta (β), gamma (γ). The entire crystal structure is formed by repeating this unit cell in three dimensions. About 95% of all solids can be described as crystalline.

Bragg's law governs the X-ray diffraction technique for structural analysis. When monochromatic X-rays incident on the crystal lattice [Figure 3.3], atomic planes cause reflection of incident X-rays. Thus, there exists a path difference in between the rays reflected from plane 1 and plane 2. Such rays will reinforce each other only when their path difference is an integral multiple of the incident X-ray wavelength.

The Bragg's law can be written as [200]: $2dsin\theta = n\lambda$ (3.1)

where, n is an integer and λ is the wavelength of the X-rays used, θ is Bragg angle and d is the interplanar spacing.

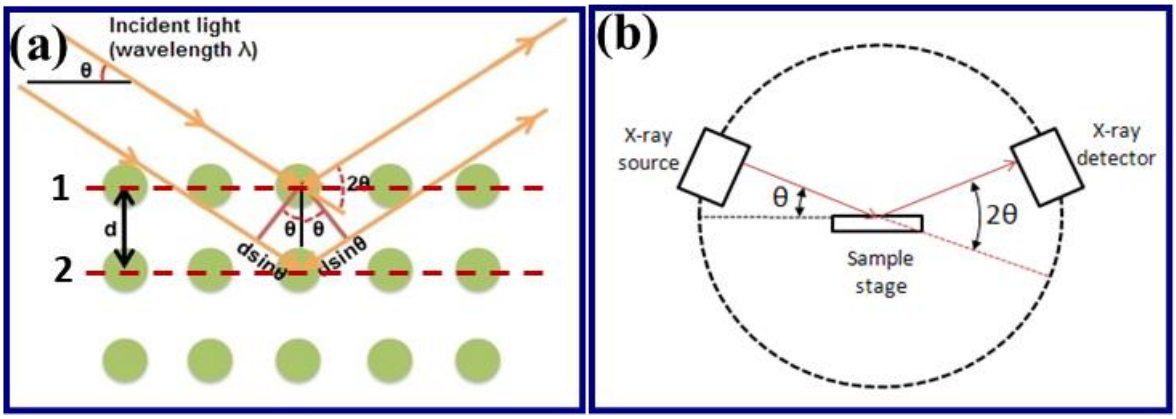

Figure 3.3: (a) Illustration of Bragg's law and (b) Schematic of X-ray diffractometer

A Rigaku Ultima III X-ray diffractometer is used for recording the diffraction pattern of the samples in θ-2θ configuration with *Cu* K_α radiation (λ =1.5404 *Å*) and operated at 40 *KV* voltage and 30 *mA* current. A photographic image of the X-ray diffractometer is shown in Figure 3.4.

Figure 3.4: *Experimental set up of X-Ray Diffractometer*

3.2.2 Fourier Transform Infrared Spectroscopy (FTIR):

Infrared spectroscopy provides the study of interactions between matter and electromagnetic (EM) fields in the IR region. In this spectral region, the EM waves mainly get coupled with the molecular vibrations. As a result of the introduction of Fourier-transform, the most significant advances in infrared spectroscopy have been achieved. This type of instrument employs an interferometer and exploits the well-established mathematical process of Fourier-transformation. FTIR spectroscopy has dramatically improved the quality of infrared spectra and minimized the time required to yield desired data.

Most of the commercially available FTIR spectrometers use the Michelson interferometer shown in Figure 3.5.

The basic Michelson Interferometer consists of following components:

(a) a broad-band light source which emits light covering the mid-IR range,

(b) a beam splitter made of KBr or CsI,

(c) two front surface coated mirrors: one is moving and the other is fixed, and

(d) a detector.

Working principles of Interferometer are as follows:

1) Light from the light source is directed to the beam splitter, which causes half of the light reflected and half transmitted.

2) The reflected light goes to the stationary mirror, where it gets reflected and reaches to the beam splitter. The transmitted light travels towards the moving mirror and is reflected back towards the beam splitter.

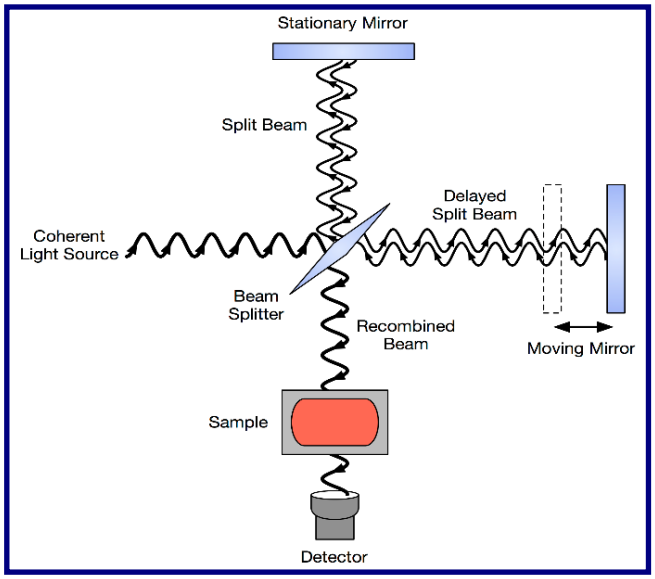

Figure 3.5: *Schematic of Michelson interferometer*

3) At the beam splitter, each of the two beams reflected from the stationary and moving mirrors splits into two: one goes back to the source (and "lost" since it does not reach the detector) and the other waves towards the detector. Thus, the detector sees two beams: one from the moving mirror and the other from the stationary mirror.

4) The two beams reached at the detector originate from the same source and possess have an optical path difference determined by the positions of the two mirrors. Thus the beams possess a fixed phase difference, and therefore, interfere.

5) The two beams may be made to interfere constructively or destructively for a particular frequency by positioning the moving mirror. If the moving mirror is scanned over a range, an interferogram is generated with its maximum intensity resulting from constructive interference, and the minimum intensity corresponding to destructive interference. Experimental set up for the FTIR spectrometer is shown in Figure 3.6.

Figure 3.6: *Experimental set up of FTIR spectrometer*

3.2.3 Ultraviolet-Visible spectroscopy (UV-Vis):

UV-Vis spectroscopy is a technique that measures the amount of discrete wavelengths of UV or visible light that are absorbed by or transmitted through a sample in comparison to a reference or blank sample. The energy of the ultraviolet radiation that are absorbed is equal to the energy difference i.e., bandgap ($\Delta E = h\nu$).

Two laws that govern the absorption of light by a medium are known as ***Lambert's law*** and ***Beer's law***. ***Lambert's law*** tells that the absorbance is directly proportional to the thickness/path length of the medium. ***Beer's law*** relates concentration of coloured components in solution to light transmission or absorption.

By combining these two laws, ***Beer - Lambert law*** [Figure 3.7] is as follows [201]:

$$\boldsymbol{\log (I_0/I_t) = A = \alpha cd} \quad (3.2)$$

where, $\boldsymbol{I_0}$ and $\boldsymbol{I_t}$ are the incident and transmitted light intensity respectively, $\boldsymbol{A}$ denotes absorbance, $\boldsymbol{\alpha}$ denotes molar absorptivity, $\boldsymbol{c}$ is concentration and $\boldsymbol{d}$ is path length. This is the basic principle of UV-Vis spectroscopy.

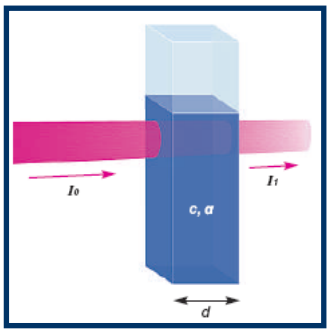

Figure 3.7: *Beer- Lambert law*

The incident photons with energies greater than the band gap energy are absorbed, while others are transmitted. This experiment thus provides an accurate measure of the band gap energy of any material. Figure 3.8 presents the experimental set up of the UV-Vis spectrophotometer. According to Bardeen [202], the relation between the absorption coefficient (α) and the band gap (E_g) of the material for the parabolic band structure is given by [202],

$$\alpha h\nu = A\,(h\nu - E_g)^n \quad (3.3)$$

where, A is a constant and ν is frequency of light, n is related to the electronic nature of the band gap, with values of 3, 2, 3/2, and 1/2 corresponding to indirect forbidden (IF), indirect allowed (IA), direct forbidden (DF), and direct allowed (DA) transitions, respectively.

Figure 3.8: *Experimental set up of UV-Vis spectrophotometer*

3.2.4 Field Emission Scanning Electron Microscope (FESEM):

A FESEM is a vacuum based electron microscope that instead of light uses an electron beam from a field emission source.

Figure 3.9 shows the internal construction of the FESEM instrument. It consists of an electron gun to generate an electron beam, electromagnetic lenses and apertures to focus the electron beam, detector and vacuum system.

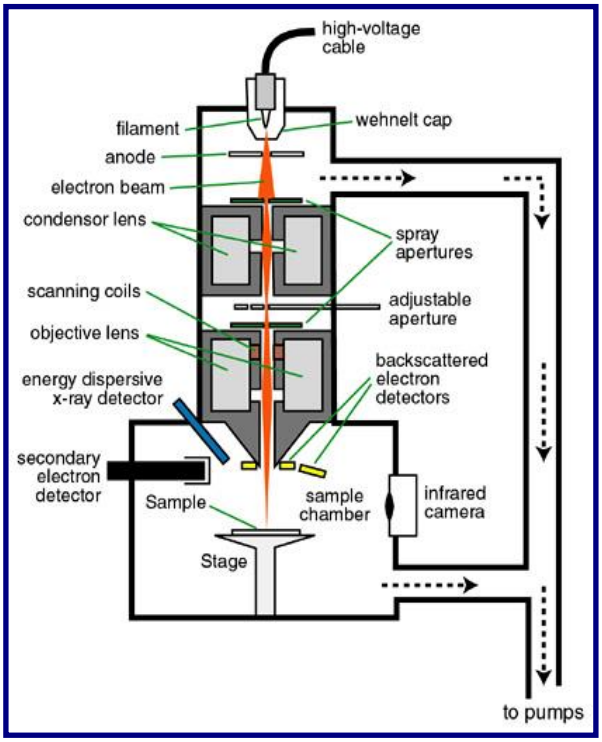

Figure 3.9: *Internal construction of FESEM*

The electron gun produces a stable electron beam with high current, small spot size, adjustable energy and small energy dispersion. In modern SEMs, field emission sources, which provide enhanced current and lower energy dispersion, are used instead of thermionic emission sources like tungsten "hairpin" (Φ=4.5 *eV*) or lanthanum hexaboride (LaB_6) (Φ=2.4 *eV*). Emitter lifetime is another important criterion for selection of electron sources. The most widely used electron gun is composed of three parts: a V-shaped hairpin tungsten filament (the cathode), a Wehnelt cylinder and an anode, as shown in Figure 3.9. In this system, a strong electric field forms on the finely oriented tip and the electrons are drawn toward the anode to form an intense electron beam. The combination of different lenses and apertures is used to focus the electron beam onto the sample and control the final size and position of beam.

EDX is one of the most versatile tools for analysing the compositions of the synthesized samples. It is sometimes also referred to as EDS or EDAX analysis. During EDX

analysis, the specimen is bombarded with an electron beam within an electron microscope. The bombarding electrons collide with the host atom and knock some of them off in the process. The electrons emitted from the inner shell are eventually filled with the outer shell electrons of higher energy, and thus gives rise to emission of X-ray in this method. Such X–rays emitted from atoms specify the characteristics of the elements. EDAX is a very important tool for identifying the chemical composition of a specimen. The image of FESEM set up is presented in Figure 3.10.

Figure 3.10: *FESEM (Hitachi S-4800) set up with EDS attachment*

In this dissertation, all the morphologies of nanostructured materials are studied with the assistance of the instrument FESEM, S-4800, Hitachi operated at less than 15 kV accelerating voltage. Small amount of powder sample is pasted on carbon tape. Sometimes, gold or silver coating is necessary for insulating material to eliminate the surface charge imbalance and to obtain a better resolution. The EDS part is attached with FESEM S-4800, Hitachi. This part is manufactured by Thermo Scientific, Model: Noran System - Thermo Scientific UltraDry EDS Detector.

3.2.5 High Resolution Transmission Electron Microscope (HRTEM):

It is a characterisation tool that is used to investigate the crystal structure and microstructure of the synthesized nanomaterials simultaneously by diffraction and imaging techniques. In 1931, Knoll and Ruska investigated the first prototype electron microscope.

In a conventional TEM, a thin sample is illuminated with an electron beam of uniform current density. Electron beam produced from the electron gun, generally made up of tungsten or LaB_6, is passed through several apertures and lenses as shown in Figure 3.11 and illuminates

the specimen. The electron beam is usually much more energetic than the beam used in SEM (150-250 *kV* in HRTEM compared to 5-30 *kV* in FESEM). The collimated beam is transmitted through the sample and the image is recorded digitally by a CCD camera or by direct exposure of a photographic emulsion.

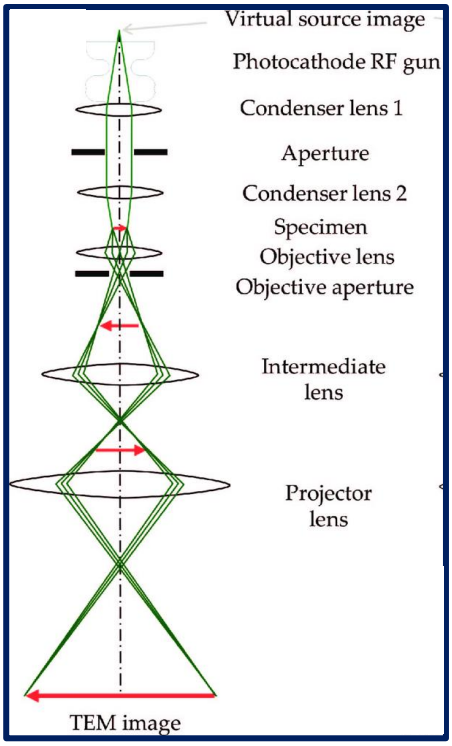

Figure 3.11: *Internal configuration of HRTEM*

The function of this microscope can be divided into two parts: high resolution TEM and selected area electron diffraction (SAED). The digital photograph of the HRTEM set up is provided in Figure 3.12

.

Figure 3.12: *Experimental set up of HRTEM (JEOL JEM-2100)*

To characterize the synthesized sample, a small amount of powder sample is dispersed in appropriate solvent by sonication, and the solution is drop-casted on carbon coated Cu grid. Next, the grid is dried for 2-3 *h* in a drying oven. Finally, sample is ready for measurement and the information such as particle size, shape, interparticle interaction, etc. are obtained.

3.2.6 X- Ray Photoelectron Spectroscopy (XPS):

XPS is one of the most powerful surface analytical techniques capable of providing accurate qualitative elemental analysis for all elements except hydrogen and helium, and quantitative composition, and also of determining the valence state of elements.

XPS is based on the photoelectric effect discovered by Hertz in 1887. In this case, electron is emitted from the surface due to the interaction of an X-ray photon of appropriate energy with the solid surface. The applied X-ray with 1-15 *KeV* energy, is capable of ejecting electrons not only from the outer shells but also from the core levels of all elements appearing in the periodic table; the scheme is presented in Figure 3.13(a).

The governing equation of this phenomenon is as follows [203]:

$$h\nu = E_b + E_{kin} + W_f \tag{3.4}$$

where, E_b is binding energy, E_{kin} is kinetic energy of photoelectron, W_f is the work function of the specimen under investigation. The experimental set up [Figure 3.13(b)] contains the

following parts: (*i*) an X-ray source, (*ii*) an electron energy analyser, combined with a detection system and (*iii*) a sample stage.

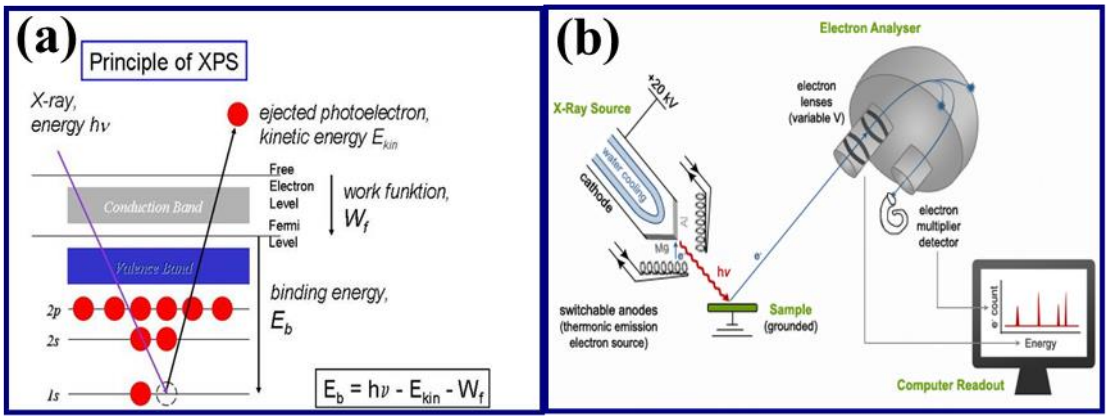

Figure 3.13: *(a) Basic principles and (b) constructions of XPS*

Sample analysis is performed on the SPECS with a hemispherical energy analyzer (HSA 3500). Photoelectrons are excited using the monochromatic *Mg* K_α X-ray (1253.6 *eV*) or *Al* K_α X-ray (1486.6 *eV*) as the excitation source operated at 10 *kV* and with an anode current 17 *mA*. 10^{-8}-10^{-9} *Torr* pressure range is required for XPS measurement. The photograph of the X-ray photoelectron spectroscopy is shown in Figure 3.14.

Figure 3.14: *Experimental set up of XPS (SPECS HSA 3500)*

3.2.7 Raman Spectroscopy:

Raman spectroscopy was named in the honour of its inventor, C.V. Raman, who, along with K.S. Krishnan, published the first paper on this technique [204]. Raman spectroscopy is based on the Raman effect that tells that the frequency of a small fraction of scattered radiation is different from the frequency of monochromatic incident radiation. A Raman spectrum is a plot of intensity of the scattered radiation as a function of its frequency

deviation from the incident radiation (usually in units of wavenumbers, cm^{-1}). This difference is called the Raman shift. In Raman spectroscopy, the sample is illuminated with a monochromatic laser beam that undergoes inelastic scattering through its interaction with vibrating molecules [205, 206] of the sample, produces the scattered light and thereby, forms a Raman spectrum. The deviation in frequency from that of the incident radiation provides information about the vibrational, rotational and other low frequency transitions in molecules [207].

In this work, Raman spectrum has been analysed by a confocal Raman spectrometer from alpha 300, Witec, Germany with Laser Source of wavelength 532 *nm*. The photograph of Raman set up shown in Figure 3.15.

Figure 3.15: *Photograph of Raman instrument*

3.2.8 Contact Angle Meter:

The property of wettability of any sample surface is measured using a characterization tool, known as contact angle meter. This property is important for catalysis, solar cell, coating applications, etc. Surface energy of a solid can also be determined from this measurement.

When any liquid droplet meets a solid surface, the angle between the solid surface and the liquid-vapor interface is defined as the contact angle. Wettability of solid surface by a liquid can be estimated using Young's equation. The degree of wetting depends upon the balance between the adhesive and cohesive forces acting at the solid-liquid interface. Adhesion is the tendency of clinging of two dissimilar particles/surfaces, while cohesion refers to the capability to cling two similar particles/surfaces. The rapidness with which the liquid be spread over the

solid surface can be explained by adhesion, while the cohesive force describes the ability of a liquid to maintain its droplet form avoiding contact with the solid surface.

Young's Equation: When a liquid droplet falls on a solid surface, different interfaces are created due to the simultaneous presence of solid, liquid and gas, as presented in Figure 3.16. If the interfacial free energy between the solid and vapor phases is γ_{SV}, liquid and vapor is γ_{LG}, solid and liquid is γ_{SL} and θ is the equilibrium contact angle at the solid liquid interface, they are related as [208]:

$$\gamma_{SV} - \gamma_{SL} - \gamma_{LV} \cos\theta = 0 \tag{3.5}$$

The zero value of θ implies the perfect wetting. If θ is within 0° to 90°, the solid surface is hydrophilic in nature. For 90°< θ <150°, the solid surface is hydrophobic in nature. θ>150° indicates the superhydrophobicity of the solid surface, which is also termed as "lotus effect".

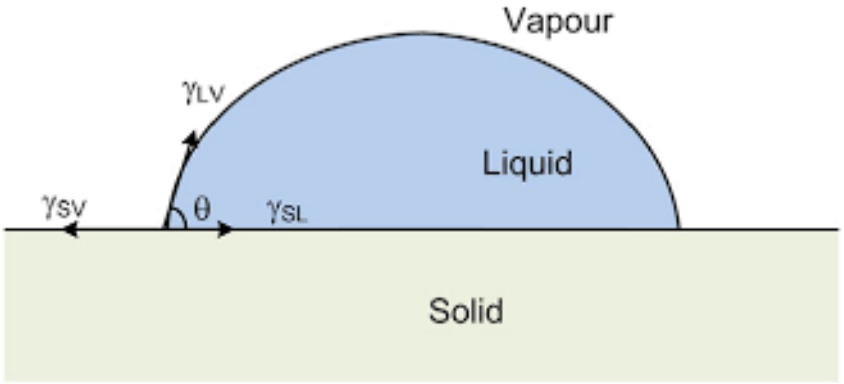

Figure 3.16: *Basic principle of Young's equation*

The instrument to study the wettability of the sample is OCA 15EC, which is manufactured by Dataphysics, Germany. The instrument comprises of five different parts: sample table, lens, camera, dosing system and external light. The data measurement is carried out through SCA software. The image of the instrument is displayed in Figure 3.17.

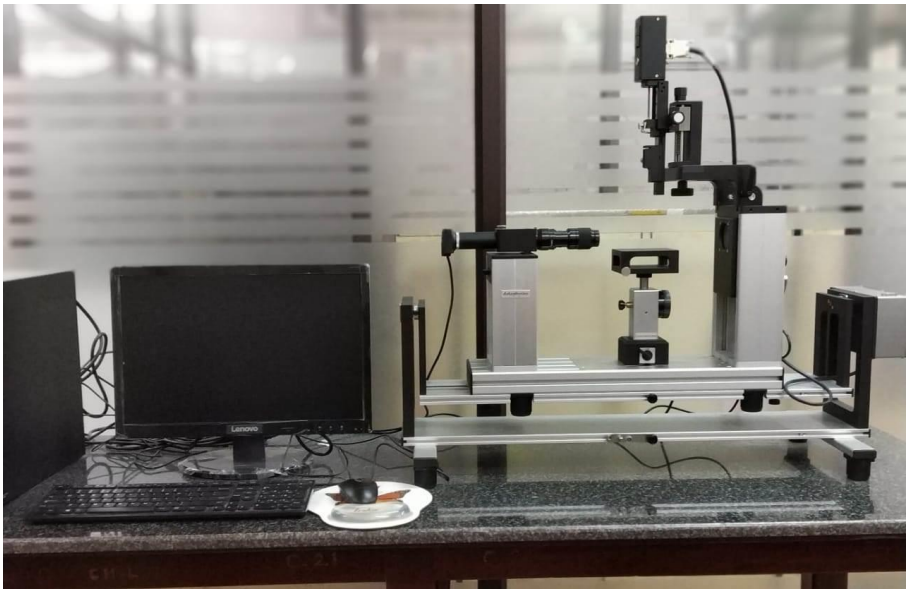

Figure 3.17: S*et up of contact angle meter*

3.3 Sono (Sonophoto) catalytic activity measurement:

The experimental set up and procedures for catalytic activity measurement are described below.

3.3.1 Experimental setup:

To perform sonocatalytic and sonophotocatalytic activity, two types of sonicators are used, one is bath sonicator [Figure 3.18(a)] and the other is probe sonicator [Figure 3.18(b)]. Here, Rectangular bath sonicator [Labman-LMUC 2A, 2.5 *L*] of 40 *KHz* frequency provides 50 *W* output power. A probe sonicator [PKS-750F] of 20 *KHz* frequency with 13 *mm* titanium probe is used which provides maximum 750 *W* output power. 15% of maximum output amplitude is utilized during the experiment. For the application of sonophotocatalysis, 400 *W* mercury lamp (λ> 400 *nm*) [Philips] is employed with bath sonicator.

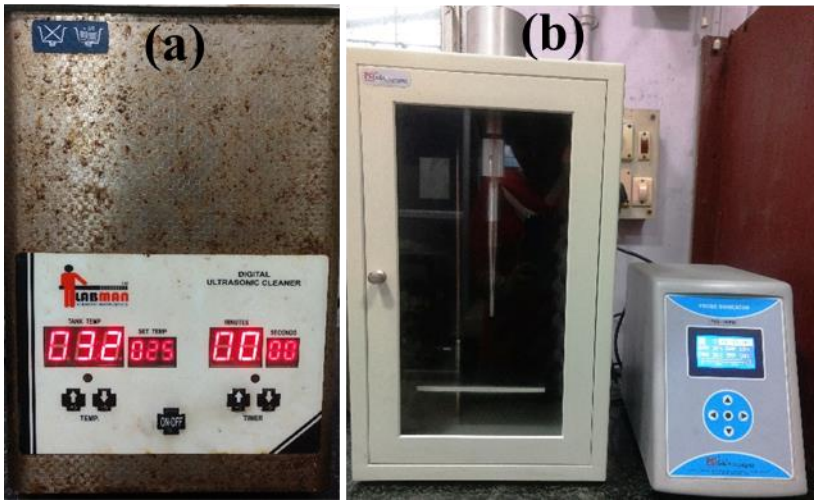

Figure 3.18: *Experimental set up of (a) Bath and (b) Probe sonicator*

3.3.2 Catalytic activity measurement:

Rhodamine B (*RB*) is chosen as a representative organic dye for sonocatalytic / sonophotocatalytic measurement using our synthesized materials. The as prepared catalyst is dispersed within a dye solution of $10^{-5}M$ initial concentration in a 60 *mL* quartz beaker. Prior to the excitation, solution is stirred in complete darkness for 60 *min* to acquire adsorption/desorption equilibrium. Then, the solution is subjected to ultrasonic irradiation. At a regular interval of 10 *min*, 5 *ml* solution is collected and centrifuged for 20 *min,* and then remnant *RB* concentration is detected by UV-Vis spectrophotometer. The catalytic efficiency is calculated from the intensity of the characteristic peak of *RB* observed at wavelength, λ = 554 *nm*.

In addition, the influence of different parameters *viz.* initial dye concentration, catalyst loading, scavenger, enhancer etc. on the sonodegradation of *RB* is also investigated.

3.4 Electrochemical measurements:

Electrochemical activity is measured on the basis of two modes: one is potentiostatic mode (controls the potential in between two electrodes) and the other is galvanostatic mode (controls the current in between two electrodes). Generally, electrochemical analysis is carried out in an electrochemical cell that may be a three / two electrode setup. All electrochemical measurements are performed in this dissertation using an electrochemical workstation (Autolab PGSTAT M204, Netherland) interfaced to a computer by Nova 1.1 software as shown in Figure 3.19.

Figure 3.19: *Set up of electrochemical workstation (Autolab PGSTAT M-204)*

3.4.1 Electrochemical cell:

An electrochemical cell is defined as a device capable of either generating electrical energy from chemical reactions or using electrical energy to cause chemical reactions. An electrolytic cell is a kind of electrochemical cell that drives a non-spontaneous redox reaction by the application of electrical energy. An electrolytic cell has two parts: electrolyte and electrodes. The electrolyte is usually a solution of water or other ionic solvents. When an external voltage is applied to the electrodes, the ions in the electrolyte are attracted to an electrode with opposite charge, where charge-transferring (also called faradaic or redox) reactions can take place. Now, a three electrode setup is described below.

(1) Working electrode: The reaction of interest takes place at this electrode. The synthesized materials are used as working electrode to investigate their performances.

(2) Reference electrode: It is one of the important parts of electrochemistry that serves as an experimental reference point. During the experiment, it maintains the constant potential. Very commonly used and commercially available reference electrodes are silver/silver chloride (*Ag/AgCl*), saturated calomel (Hg/Hg_2Cl_2), mercury/mercury oxide (*Hg/HgO*), etc.

(3) Counter electrode: This electrode is also named as an auxiliary electrode that completes the path of current in the system. It is basically used as a current source/sink, and thus mainly inert materials are preferred for this purpose. Graphite and platinum are two counter electrode materials widely used in recent days.

3.4.2 Cyclic Voltammetry (CV):

Cyclic Voltammetry (CV) is an electrochemical technique, which measures the current developed in an electrochemical cell during the cyclic voltage sweep. In CV curves, current is plotted with the potential of a working electrode. Each set of repetitive curves can be traced for different voltage sweep rates. CV data provides us the information about various

complex redox potentials and the electrochemical reaction involved between the reactions occurring at the electrode-electrolyte interface. In case of pseudocapacitive materials, oxidation and reduction peaks appear in CV data that help to understand the redox transformation of that material. CV technique is also employed to investigate the presence of many dissolved gases in the electrolyte. For example, in the presence of O_2, a large O_2 reduction peak appears in the CV curve suggesting the surface redox process responsible for the ORR catalytic activity.

3.4.3 Rotating Disk Electrode (RDE):

A rotating disk electrode (RDE) is a hydrodynamic working electrode used in electrocatalysis. One motor controller is used to control the rotational speed of the working electrode during experiments, where such rotation induces a flux of analyte to the electrode. The rotating disk (glassy carbon, GC) electrode is prepared by embedding a conductive disk in an inert non-conductive polymer or resin, attached to the electric motor having very precise control on the rotation rate. The rotation of the disk is usually described in terms of angular velocity. To study the ORR kinetics of catalyst coated electrodes in O_2 saturated electrolyte, the RDE current - potential values are normally recorded at various electrode rotation. If potential of RDE is varied linearly from low to high value, it is called linear sweep voltammetry (LSV). In order to obtain the steady-state curves, the potential scan rate is kept normally slow, typically less than 10 *mV/s*. The setup of RDE system is shown in Figure 3.20.

Figure 3.20: *RDE measurement set up*

3.4.4 Other measurements:

Apart from CV, RDE measurements, there are several techniques *viz*. galvanostatic charge discharge (GCD), electrochemical impedance spectroscopy (EIS), chronoamperometry, etc. To evaluate the electrochemical capacitance of materials under controlled current

conditions, GCD is a powerful method. This method is also known as chronopotentiometry that helps to measure various parameters such as:

- Capacitance
- Resistance
- Cyclability.

In this method, a current pulse is applied to the working electrode and the resulting potential is measured against a reference electrode as a function of time. For the investigation of durability of the electrode sample, GCD are performed for thousands of cycles and coulombic efficiency and capacitance retention are estimated with cycle number.

The fundamental approach of the EIS method is the application of a small amplitude sinusoidal excitation signal to the system under investigation and the response is measured in terms of current / voltage. EIS data dictates us the idea about the interaction between electrolyte and material under study (working electrode). This EIS data is graphically presented by Nyquist plot or Bode plot.

Chronoamperometry is a time-dependent measurement where a square-wave potential is applied to the working electrode. The current response of the electrode fluctuates according to the diffusion of an analyte from the bulk solution toward the electrode surface. Time dependent current for the diffusion controlled process occurring at working electrode is measured by this technique [209]. Chronoamperometry experiments are carried out to examine the long- term durability of the electrocatalysts.

3.4.5 Sample preparation:

For supercapacitor application, nickel foam is used as a current collector. Initially, foam is cut into pieces with 2 $cm \times 1\ cm$ dimension and sonicated in 4:1 mixture of water:HCl for 5 *min*. Then, they are washed with de-ionized (D.I) water and ethanol, dried at 60°C. The sample paste is made by taking synthesized material, carbon black and polyvinylidene fluoride (PVDF) in 8:1:1 ratio. Then a certain amount of N–Methyl Pyrrolidone (NMP) is added to it and stirred until the preparation of homogeneous slurry paste. Next, sample slurry is pasted on a cleaned nickel foam and dried at 60°C for 6 *h*. The mass loading of active material is estimated from the difference in weight of nickel foam before and after the sample coating. Alkaline (NaOH/LiOH) solution is used as electrolyte.

For the purpose of electrocatalytic measurement, catalyst ink is prepared as follows: 1 *mg* of synthesized catalyst materials are dispersed in 1 *ml* DMF solution, 5% 100 μL nafion solution is added and ultrasonicated for 30 *min* to form the homogeneous solution. Thus,

catalyst ink is prepared. $3\mu L$ ink is drop casted on the top of the working area [black portion] of GC electrode [Figure 3.21] and dried at 60°C in a vacuum oven. Electrocatalytic ORR is tested using 0.1 *M* KOH electrolyte. Prior to each measurement, high purity O_2 gas purging is done for 30 *min* to saturate the electrolyte. In this case, electrochemical cell consists of GC electrode with 3 *mm* diameter as working electrode, *Ag/AgCl* (saturated in 3 *M* KCl) as reference electrode and Pt wire as counter electrode, respectively for performing CV and LSV using RDE experiments. The measured potentials with respect to *Ag/AgCl* reference electrode are converted to the reversible hydrogen electrode (RHE) scale by the following Nernst equation [210]:

$$E_{RHE} = E_{Ag/AgCl} + 0.059pH + E^0_{Ag/AgCl} \tag{3.6}$$

where, E_{RHE} is the converted potential in reversible hydrogen electrode (RHE) scale, $E_{Ag/AgCl}$ is the experimental potential measured against the *Ag/AgCl* reference electrode, and $E^0_{Ag/AgCl}$ is the standard potential of *Ag/AgCl* at 25°C (0.1976 *V*). The electrochemical measurements are performed in 0.1 *M* KOH (pH=12) at room temperature; therefore,

$$E_{RHE} = E_{Ag/AgCl} + 0.9056 \tag{3.7}$$

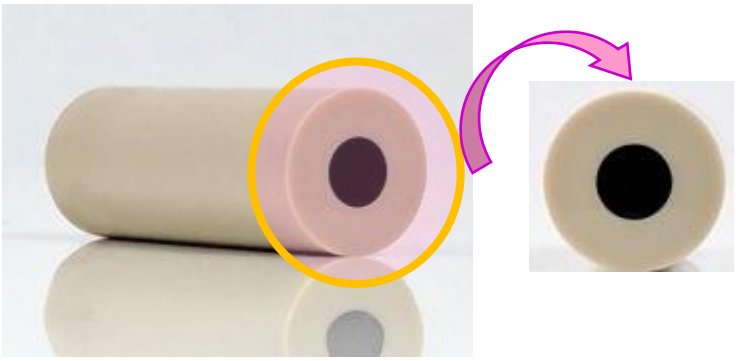

Figure 3.21: *Close view of working area of GC electrode*

3.5 Conclusions:

In this chapter, various useful techniques for the synthesis of MPc nanostructure and its hybrid are discussed. A detailed description of characterization techniques that will be used for the characterization of synthesized material is also described. The experimental methodologies involved in different applications of synthesized materials are next elaborately explained. Implementation of all these methodologies in the synthesis, characterization and potential applications of MPcs and their hybrids will be illustrated in the subsequent chapters of this dissertation.

This chapter will elaborate the synthesis routes of *CuPc*, *ZnPc*, their *rGO*, MoS_2 based heterostructures and characterization results.

4.1 Materials:

CuPc powder (*β* form) and phthalonitrile are purchased from Sigma Aldrich and all other chemicals *viz.* chloroform, TFA (CF_3COOH), copper (Cu) powder, zinc (Zn) powder, sodium dodecyl sulfate (*SDS*), ammonium heptamolybdate ($(NH_4)_6Mo_7O_{24}.4H_2O$), graphite powder, sodium nitrate ($NaNO_3$), potassium permanganate ($KMnO_4$), 30 *wt.%* hydrogen peroxide (H_2O_2), N, N-Dimethylformamide (*DMF*), sulfuric acid (H_2SO_4), hydrochloric acid (*HCl*), hydrazine hydrate, ammonia, sodium molybdate dihydrate ($Na_2MoO_4{\cdot}2H_2O$) and thiourea (NH_2CSNH_2) are bought from Merck, India. D.I water is used for reaction purposes. All chemicals are used without any additional purification.

4.2 Synthesis:

4.2.1 *ZnPc* nanoflake:

ZnPc nanoflakes are synthesized following a simple low temperature hydrothermal route. In this reaction, *Zn* powder (0.45 *mmol*), phthalonitrile (1.8 *mmol*), *SDS* (20 *mg*) and 10 *mg* of ammonium heptamolybdate are dispersed in 12 *ml* water. Then the solution is continuously stirred for 40 *min*. Next, the solution is sealed in a Teflon container (15 *ml* volume) and reaction temperature is maintained at 180°C for 24 *h*. Finally, the bluish purple precipitate is obtained after washing with 1*M* aqueous *HCl* solution, ethanol and water separately. The chemical reaction process is shown in Figure 4.1.

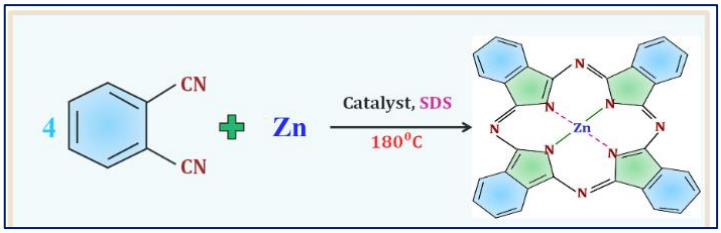

Figure 4.1: *Reaction process for synthesis* of *ZnPc nanoflake*

Different nanostructures of *CuPc* can be synthesized using various chemical routes e.g. solution (room temperature) and hydrothermal (low temperature) processes. The detailed descriptions of these synthesis techniques are explained in this chapter.

4.2.2 *CuPc* nanowire:

CuPc nanowires are synthesized from bulk *CuPc* powder using a simple self-assembly solution method [18, 211]. Initially, commercial *CuPc* powder (0.0001 *M*) is dispersed in 300 *ml* chloroform solution using ultrasonic bath sonicator. Then, *0.5 M* of *TFA* is added to the solution and stirred continuously for 8 *h*. After that, the bluish precipitate is vacuum filtered and dried at 60ºC for 6 *h*. In chloroform solution, Cu^{2+} ion of *CuPc* molecules interacts with CF_3COO^- ion that acts as bridging agent between two *CuPc* molecules and helps to the formation of *CuPc* nanowires [18]. The plausible nanowire formation mechanism is schematically presented in Figure 4.2.

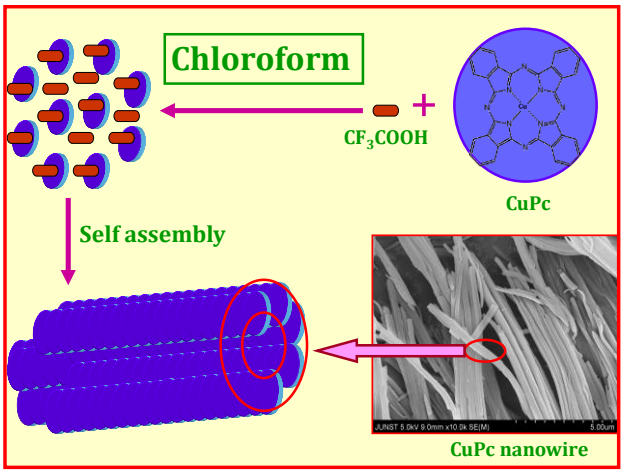

Figure 4.2: *Plausible formation mechanism of CuPc nanowire*

4.2.3 *CuPc* nanotube from nanowire:

For the growth of *CuPc* nanotubes, the as-prepared *CuPc* nanowires are dissolved in ethyl alcohol and the hydrothermal reaction temperature is maintained at 180°C for 24 *h*. The solution is then allowed to cool naturally for 12 *h* with subsequent annealing at 70°C resulting in the formation of *CuPc* nanotubes.

4.2.4 *CuPc* microrod:

Following the earlier literature [19], *CuPc* microrods are synthesized from its precursor materials through hydrothermal process. Phthalonitrile and *Cu* powder are taken in 4:1 ratio, whereas *SDS* and ammonium heptamolybdate are mixed in a 2:1 ratio in 80 *ml* D.I water. Then the solution is sealed in Teflon lined stainless steel autoclave and heated at 180°C for 24 *h*. The resulting bluish precipitate is washed by ethanol and water, and dried at 60° C for 6 *h*. The reaction is as follows:

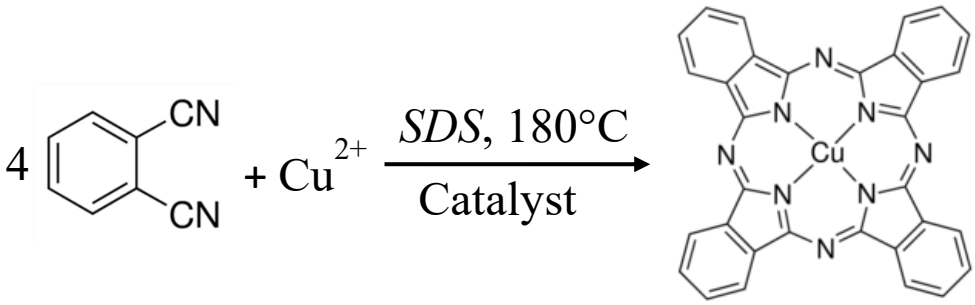

4.2.5 Graphene oxide (*GO*):

GO is synthesized by modified Hummer's method [212]. A small amount of fine graphite powder and $NaNO_3$ are mixed vigorously in concentrated H_2SO_4. Next, the beaker is kept in an ice bath and $KMnO_4$ is slowly added to this solution. Once the solution turns thicker, the ice bath is removed and water is added dropwise until the temperature reaches 90ºC. In the last step of preparing *GO*, 30 *wt.%* H_2O_2 is added, while the colour of the solution turns yellow. The precipitate is then repeatedly washed by centrifugation and the supernatant is collected. After drying in a vacuum oven for 12 *h* at 70ºC, the brown powder of *GO* is obtained. The complete reaction process is pictorially shown step by step in Figure 4.3.

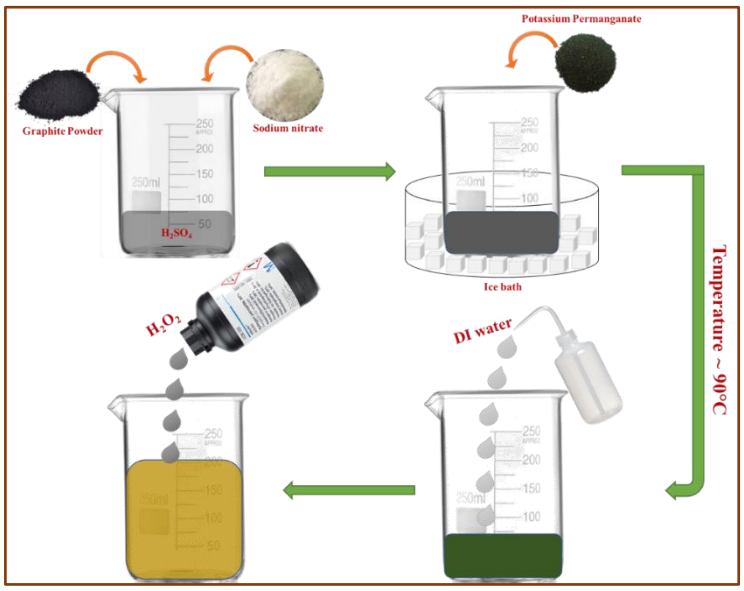

Figure 4.3: *Reaction steps of GO preparation*

4.2.6 Molybdenum disulfide (MoS_2):

MoS_2 nanostructure is prepared using green synthesis route as described in literature [63]. Initially, 0.5 *mM* sodium molybdate dihydrate and 2 *mM* thiourea are thoroughly mixed in 60 *ml* water. Then, the solution is transferred in the autoclave and reaction temperature and time are set at 200°C and 18 *h*, respectively. After cooling down, the black precipitate is washed with ethanol and water, and subsequent drying process is carried out at 60°C for 8 *h*. Thus, MoS_2 nanoflower is prepared.

4.2.7 *rGO-CuPc* hybrid:

Now certain amount of freshly prepared *GO* and *CuPc* nanotube are mixed thoroughly in *DMF* and the solution temperature is raised upto 90ºC. Hydrazine hydrate and ammonia solution are then added and after 1 *h*, the colour of solution turns black. The solution is then filtered and washed repeatedly with water. Finally, *rGO-CuPc* sample is collected after drying for 6 *h* at 70ºC. The synthesis process is schematically shown in Figure 4.4.

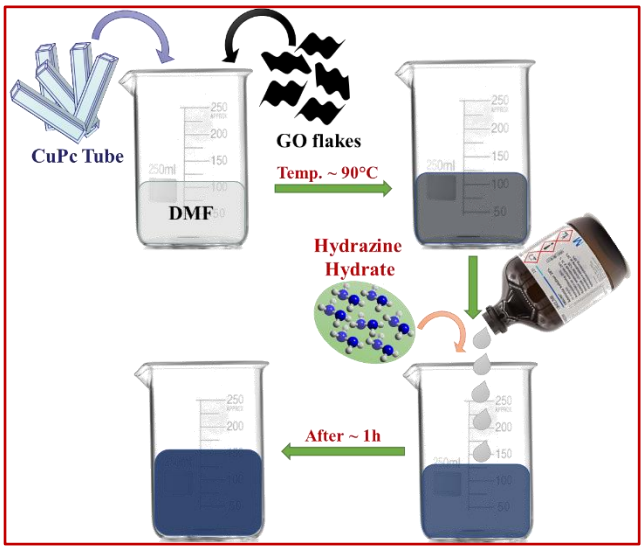

Figure 4.4: *Reaction steps of rGO - CuPc formation*

4.2.8 *MoS_2-CuPc* hybrid:

For the preparation of *MoS_2-CuPc*, 0.5 *mM* sodium molybdate dihydrate, 2 *mM* thiourea and 30 *mg CuPc* microrod are properly mixed in 60 *ml* D.I water and then the solution is kept in Teflon container at 200°C for 18 *h*. The bluish black precipitate is washed by ethanol and water, and dried at 60°C for 8 *h*. The complete process of heterostructure formation is pictorially presented in Figure 4.5.

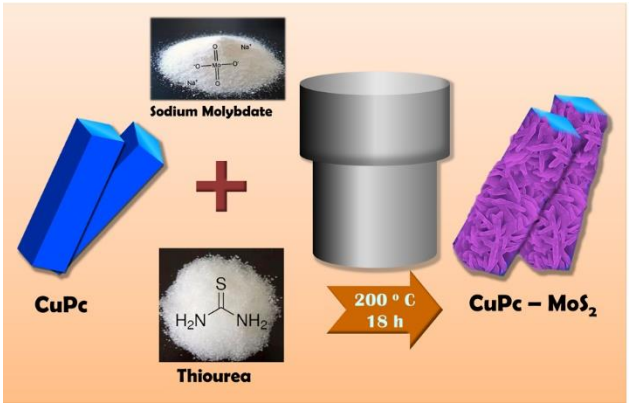

Figure 4.5: *Preparation scheme of MoS_2-CuPc heterostructure*

4.3 Characterizations:

4.3.1 *ZnPc* nanoflake:

❖ **Structural analysis:**

The crystallinity of the as-prepared *ZnPc* nanoflakes is analysed by XRD technique. As shown in Figure 4.6(a), the XRD peaks of *ZnPc* are obtained for the value of 2θ as 6.86º, 9.14º, 10.5º, 12.51º, 18.16º, 18.68º, 21.16º, 23.66º, 26.18º, 28.06º, which corresponds to reflection from $(\bar{1}01)$, (101), (002), (200), $(\bar{3}01)$, (202), $(\bar{1}12)$, (211), (212), (311) and $(\bar{3}13)$ planes of *ZnPc*, respectively which are. All the peaks more or less follow standard JCPDS data card (number: 39-1882) [213]. The chemical structure is studied by FTIR spectrum presented in Figure 4.6(b). The peaks at 726 and 777 cm^{-1} are assigned to the C-H out of plane deformation, while the peaks at 753, 1085, 1118, 1167 and 1286 cm^{-1} correspond to C-H in-plane bending. The peaks at 889 and 1411 cm^{-1} are assigned to isoindole stretching and peaks at 1060, 1332 and 1486 cm^{-1} corresponds to C-H bending, stretching vibrations of in-plane pyrrole and C=C benzene, respectively [6, 214].

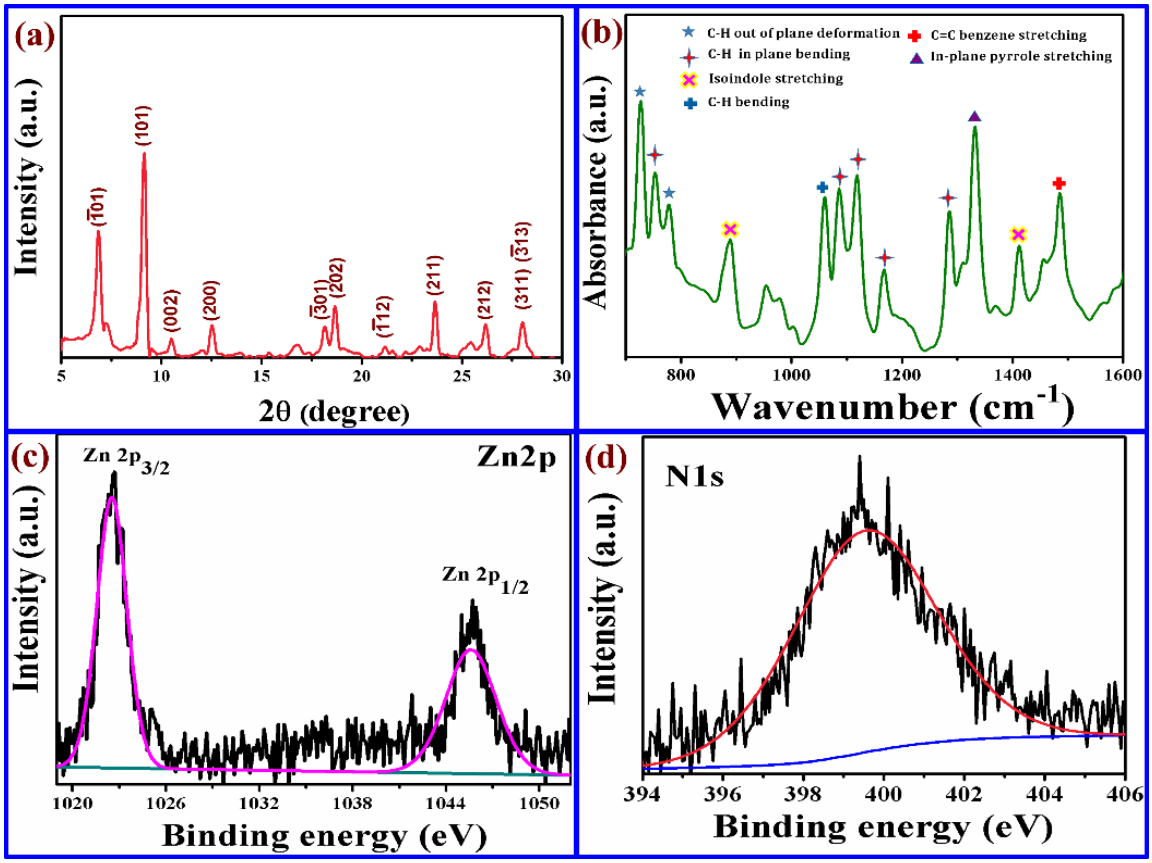

Figure 4.6: *(a) XRD pattern; (b) FTIR spectrum; high resolution spectra of (c) Zn 2p doublet and (d) N 1s of ZnPc nanoflakes.*

XPS technique is used for the confirmation of exact valence state of the constituent elements of *ZnPc*. The peaks positioned at 1022.5 *eV* and 1045.6 *eV* [Figure 4.6(c)] indicate the two spin-orbit split components i.e. *Zn* $2p_{3/2}$ and $2p_{1/2}$, respectively [215]. The Figure 4.6(d) presents the high resolution spectrum of N1s in the range of 394.5 to 403.0 *eV* [216].

❖ **Optical study:**

Figure 4.7 depicts the UV-Vis absorption spectrum of *ZnPc* nanoflakes. The absorption band from 300–450 *nm* corresponds to B band and the band 550 *nm* to 750 *nm* implies the Q-absorption band of *ZnPc*. In the Q band, the peaks observed at 604 *nm* and 667 *nm* are found mainly due to the monomeric π-π^* transition of the Pc^{-2} ring. The peak at 637 *nm* is appeared possibly for the vibronic band due to the dimers and multimers [23]. The extremely low intense absorption peaks in the lower and higher wavelength sides of 400 nm in UV-Vis spectra of ZnPc nanoflakes can be ascribed to n-π^* transition linking the nitrogen lone pair orbital with the LUMO [10.1155/2008/482373].

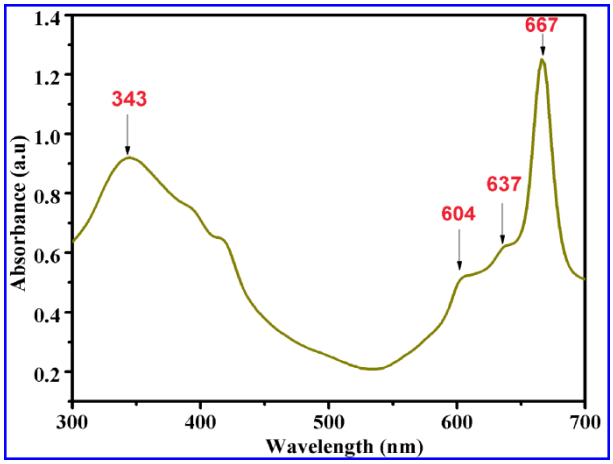

Figure 4.7: *UV-Vis spectrum of ZnPc nanoflakes*

❖ **Morphological analysis:**

Morphology of the synthesized *ZnPc* nanostructures is examined through FESEM technique and corresponding images are shown in Figure 4.8. From Figure 4.8(a) and (b), it is

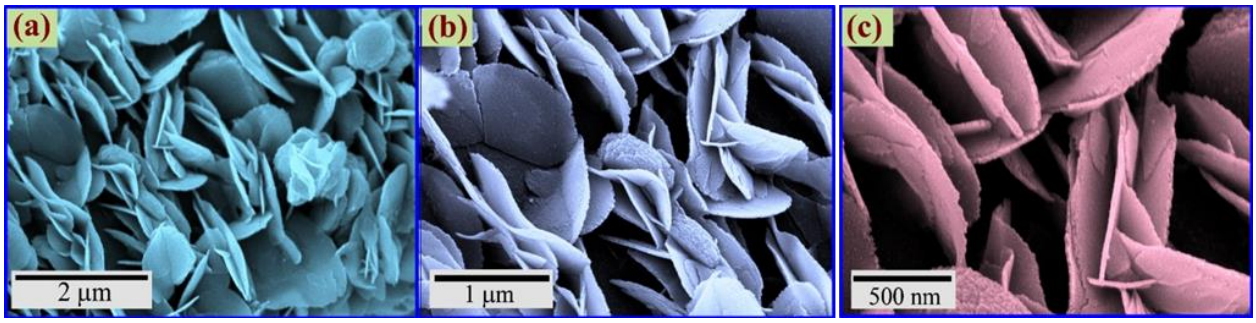

Figure 4.8: *FESEM images of ZnPc nanoflakes at (a) 2 µm, (b)1µm and (c) 500 nm length scale*

clearly seen that some nanoflakes are interconnected with each other. The diameter of the nanoflakes is ~ 700 *nm* and their thickness is ~ 20-40 *nm* as indicated in Figure 4.8(c).

A plausible growth mechanism of nanoflakes formation is depicted in Figure 4.9. In the reaction, ammonium molybdate acts as a catalyst to accelerate the hydrothermal reaction. At first small nuclei are formed, and they tend to grow the 2d sheet like morphology in the presence of surfactant at 180ºC. Here, *SDS* behaves as a structure-directing agent and decomposes into DS^- ($C_{12}H_{25}$-O-SO_3^-) and Na^+ ion in water medium. At the initial stage of reaction, small *ZnPc* nuclei are formed, where Zn powder acts as the nucleating agent and *SDS* provides the microenvironment for the synthesis of *ZnPc* [19].

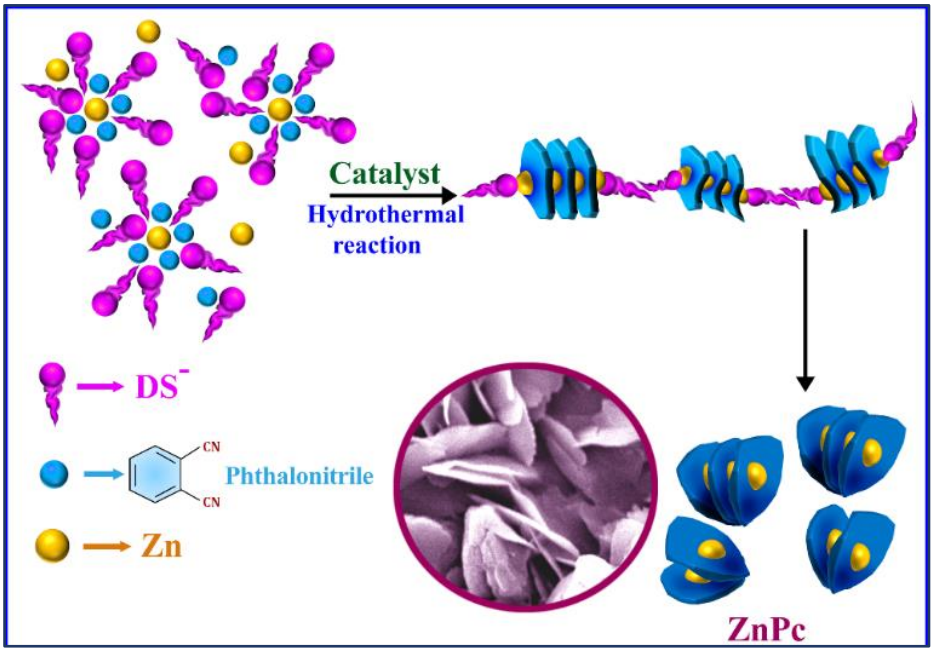

Figure 4.9: *Schematic formation process of ZnPc nanoflakes*

When temperature increases, *ZnPc* nuclei tend to form one dimensional nanostructure along the *c*-axis due to its monoclinic unit cell. But DS^- ions are anchored with the Zn^{2+} ions of *ZnPc* structure through the electrostatic attraction of anions and cations [19, 217]. Adsorption of DS^- ions blocks further nucleation and growth of the self-assembly process through π-π and van der Waals interaction for the formation of 1D phthalocyanine nanostructure. This soft templating behaviour of *SDS* in the solution phase profoundly modifies the final 2D nanoflake like structures [218]. Another important role of *SDS* is that it acts as an emulsifying agent in the solution phase to provide a hydrophobic environment, as a result hydrolysis of phthalonitrile precursor is prevented by this microenvironment [19]. When the temperature increases and reaches at 180ºC, surface tension of the system decreases. Such

reduced surface tension helps to lower the aggregation behaviours and to form a well resolved nanosheet like morphology. Similar kinds of observations are also found in literature [219].

4.3.2 *CuPc* nanowire:

❖ **Structural Analysis:**

The pure phase formation of synthesized *CuPc* nanowires is confirmed by XRD technique. The XRD diffraction pattern is shown in Figure 4.10(a). Two strong peaks positioned at 2θ = 6.92° and 7.46° confirm the formation of (001) and (110) planes of *CuPc* as per JCPDS card no: 06-0007. Rest of the peaks are well matched with the same card.

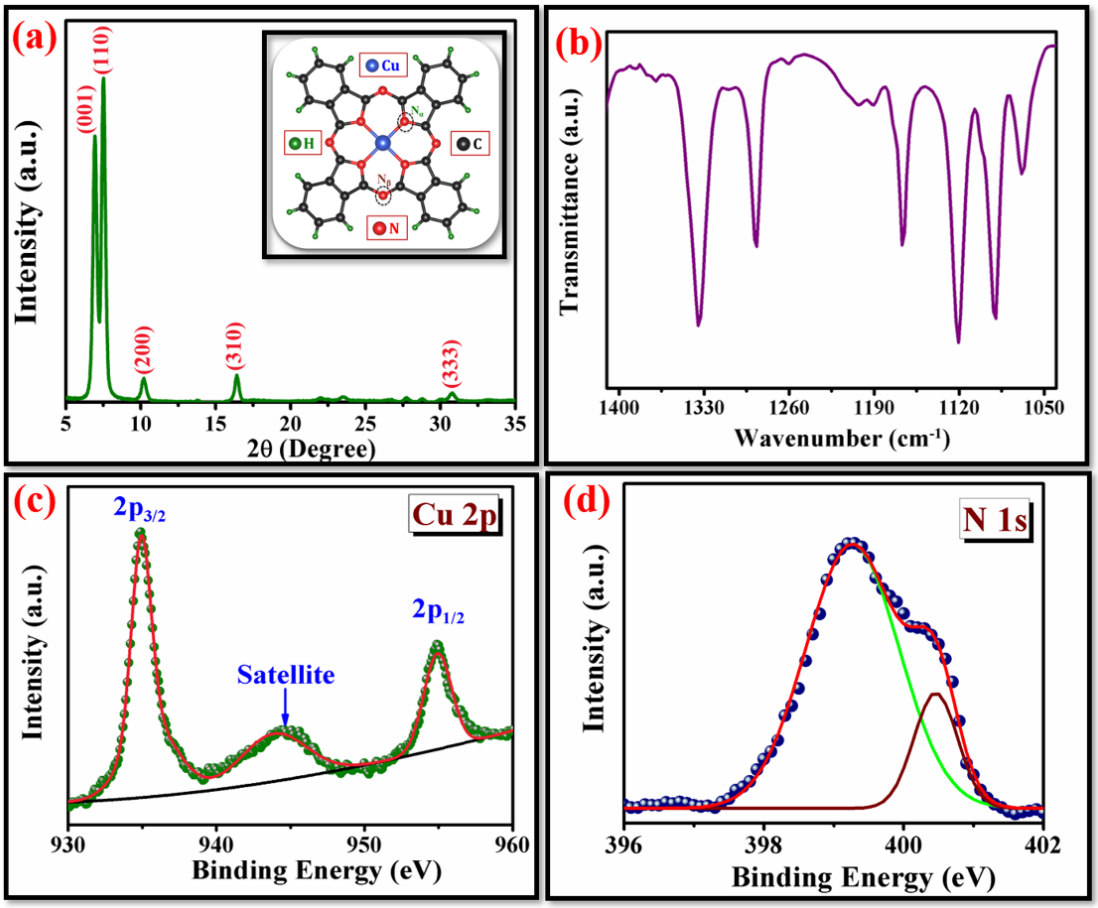

Figure 4.10: *(a) XRD pattern, Inset: molecular structure; (b) FTIR spectrum; high resolution spectra of (c) Cu 2p doublet and (d) N 1s of CuPc nanowire*

Our result also proclaims the high crystalline nature of *CuPc* nanowires. Inset of Figure 4.10(a) shows the molecular structure of *CuPc* ($C_{32}H_{16}N_8Cu$), where two different chemical environments of nitrogen atoms are presented. Four innermost nitrogen atoms are connected with the central *Cu* atom, while the rests interact with carbon atoms. This fact is also supported by FTIR data (transmittance mode) of our sample. Many prominent peaks are obtained in the FTIR spectrum shown in Figure 4.10(b). They indicate different types of chemical bonding, enlisted in table 4.1 [18].

Table 4.1: *Assignment of different chemical bonding in CuPc molecule*

Wavenumber (cm^{-1})	**Assignment**
1068, 1089	C-H in-plane deformation
1120	C-H in-plane deformation benzene in-plane deformation
1166	Cu-N
1286, 1334	C=N-C at bridge sites
1421, 1463	C-C ring stretching

To investigate the actual chemical composition and purity, high resolution XPS spectra for *Cu* and *N* are shown in Figure 4.10(c) and 4.10(d), respectively. Two distinct peaks are observed in *Cu 2p* region of which one is positioned at 935.1 *eV* and the other at 954.9 *eV*, corresponding to *Cu* $2p_{3/2}$ and *Cu* $2p_{1/2}$, respectively. This clearly reveals the existence of a normal Cu^{2+} state in *CuPc* nanostructure. From Figure 4.10(d), *N 1s* spectrum of *CuPc* consists of two peaks centred at 399.2 *eV* and 400.4 *eV* (separation ~1.2 *eV*) [220], which strongly indicate the presence of pyrrolic *N* (N_α) and meso *N* (N_β) atoms in the molecular *CuPc* structure [221, 222].

❖ **Morphology and composition analysis:**

To investigate the morphology of the as-prepared samples, FESEM technique is employed and results are presented in Figure 4.11(a)-(d) with the increasing order of magnification. Our prepared samples reveal uniform distribution of distinct wire like morphology. These *CuPc* nanowires are ~ 20-30 *μm* in length and ~ 150-250 *nm* in width.

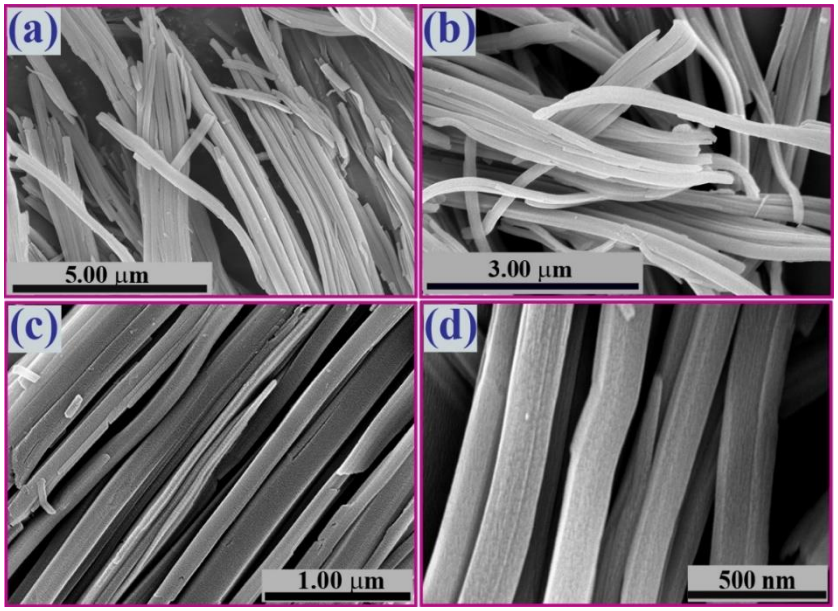

Figure 4.11: *(a), (b), (c) & (d) FESEM images of CuPc nanowires at different magnifications*

To investigate the elemental compositions of the grown nanowires, EDX is carried out and corresponding atomic percentage of elements (*C*, *Cu* and *N*) is shown in Figure 4.12. Further mapping of these elements on a small portion of the nanowire is displayed to confirm the proper elemental distribution over the nanowire.

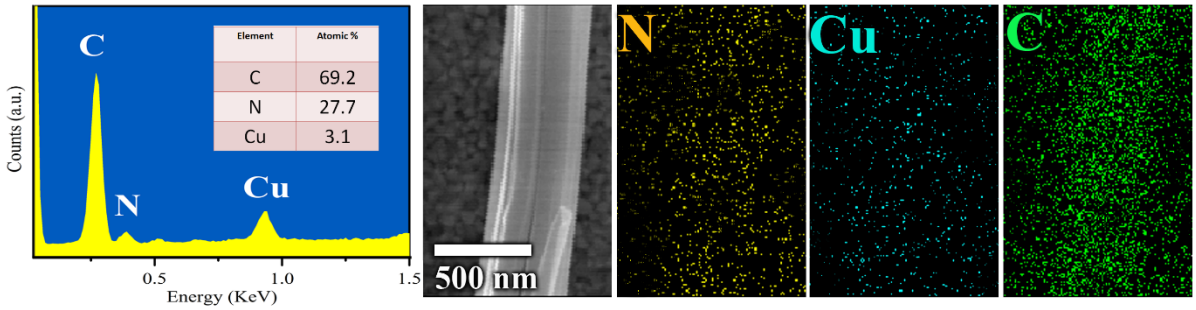

Figure 4.12: *EDX of CuPc nanowires*

The microstructure of as-prepared *CuPc* nanowires is shown in Figure 4.13(a). It is evident from the figure that *CuPc* nanowires are of ~ 20-30 *μm* length and ~ 100-200 *nm* width. To get more insight about the crystallinity, SAED pattern, as presented in Figure 4.13(b), is observed very carefully. For the main diffraction spot, the lattice spacing is found to be 1.19 *nm*, that corresponds to (110) planes of *α* phase *CuPc* nanowires. These results match with the XRD pattern and indicate the proper phase formation with very high crystalline nature.

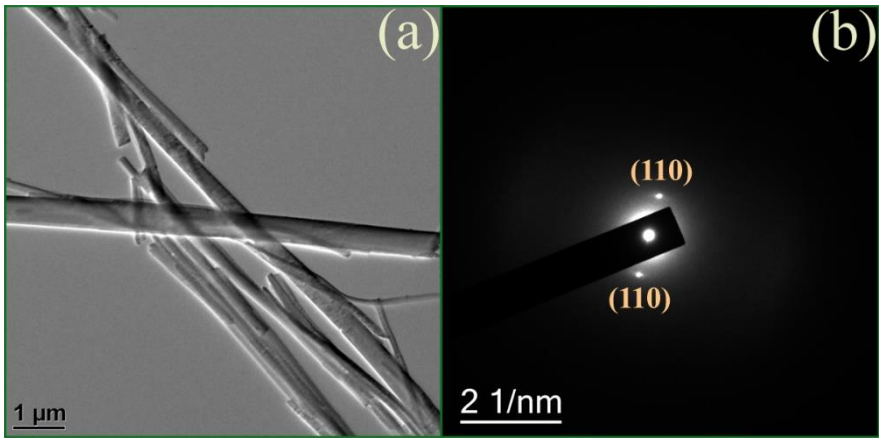

Figure 4.13: *(a) HRTEM image and (b) SAED pattern of CuPc nanowires*

❖ **Optical Study and band gap evaluation:**

The *CuPc* molecule has 4 pyrrole subunits with central Cu atom. These 4 pyrrole groups act as negatively charged ligands (Pc^{2-}) and central *Cu* atom as positive charge that forms the electric dipole [223]. A weak interaction exists between the delocalized *d* orbital of *Cu* atoms and the *π* orbitals of pyrrole groups. Thus, two molecular orbitals i.e. HOMO (*π*-orbitals) and LUMO (*π**-orbitals) are created and two characteristic absorption bands in the

UV-Vis spectrum, as shown in Figure 4.14(a) [224] are observed. The strong B band absorption lies in the region 300-500 *nm* and relative weak absorption Q band occupies 600-800 *nm* region. The main characteristic peaks found to appear at 377 *nm* and 628 *nm*, which correspond to B and Q bands, respectively. The characteristic Q band is further divided into two peaks at 628 *nm* and 750 *nm*, known as Davydov splitting.

The optical bandgap estimation of the *CuPc* nanowires is done using Eq. (3.3) in Chapter 3. For direct transition, *n* value is assumed as 1/2. Plot of $(\alpha h\nu)^2$ versus $h\nu$ is shown in Figure 4.14(b), and the value of E_g is calculated by finding the x- intercept of extrapolated Tauc plot.

In this case, the estimated band gap value for *CuPc* nanowires is found to be 2.49 *eV*.

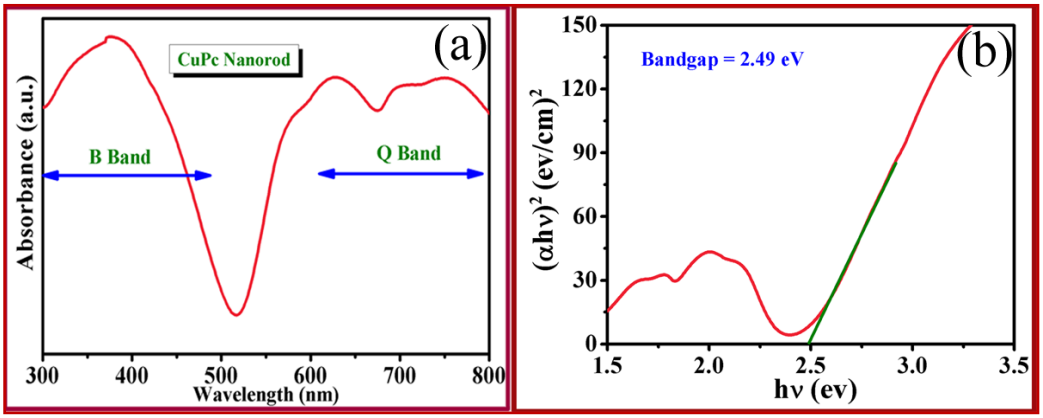

Figure 4.14: *(a) UV-Vis absorbance spectrum and (b) Band gap evaluation of CuPc*

4.3.3 *rGO-CuPc* hybrid:

❖ **Structural analysis:**

Figure 4.15(a) reveals the XRD pattern of *rGO-CuPc* hybrid in which two intense peaks at 2θ = 7.1° and 9.3° correspond to $(\bar{1}01)$ and (101) planes of pristine *CuPc* tube matched with JCPDS data card no: 39-1881. All other remaining small peaks are well matched with the same card. The presence of a broad hump around 2θ = 25° confirms the incorporation of *rGO* sheets within the pristine *CuPc* system.

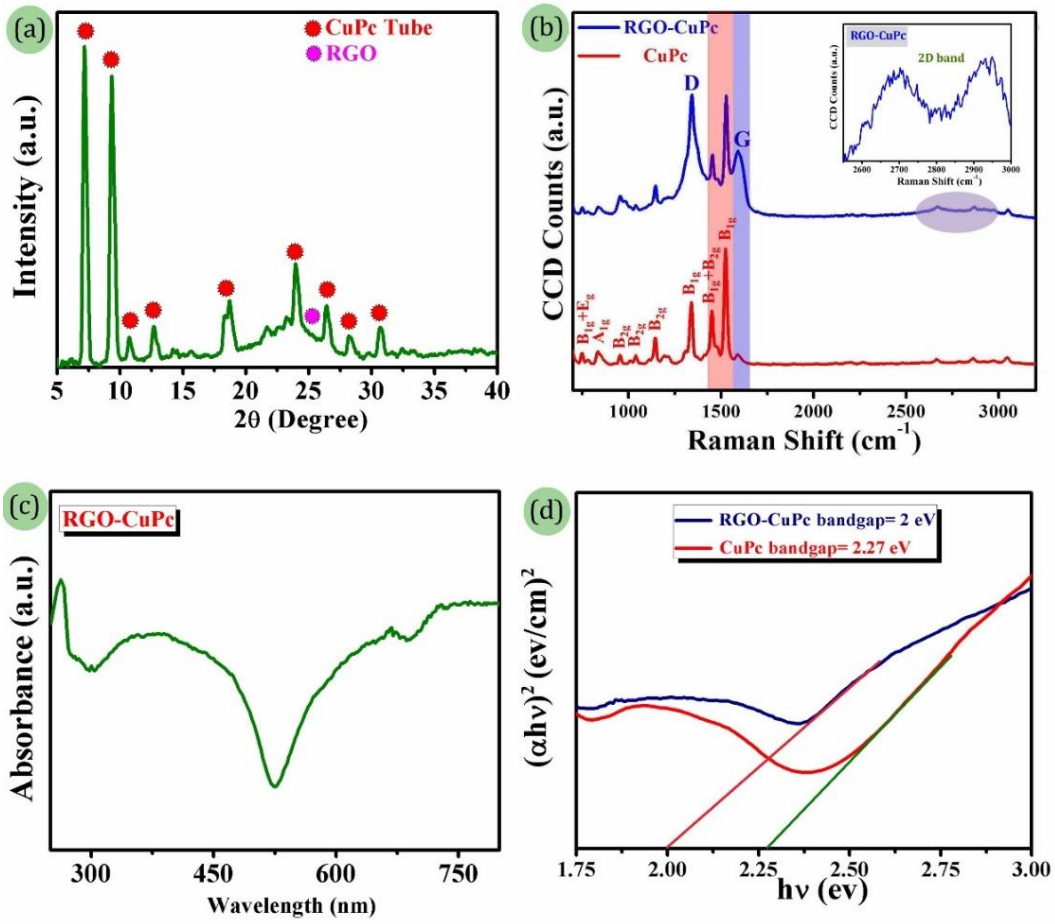

Figure 4.15: *(a) XRD pattern of rGO-CuPc hybrid; (b) Comparative Raman spectra of pure CuPc and rGO-CuPc hybrid; (c) UV-Vis absorbance and (d) band gap evaluation of rGO-CuPc hybrid*

Raman analysis:

For analysing the different vibrational modes, powder samples of *CuPc* and hybrid are considered. The full range of the Raman spectra has been shown (700-3200 cm^{-1}). For *CuPc*, the detected vibrational modes at 744, 830, 950, 1036, 1140, 1334, 1444 and 1520 cm^{-1} are assigned to the various in-plane and out-of-plane vibrations (depicted in Figure 4.15(b)). These results are in accordance with the work as reported by Ghorai et al. [225] and formation of *β*-phase of *CuPc* is ascertained. In *rGO-CuPc* hybrid, additional characteristic peaks corresponding to the well documented D (~1350 cm^{-1}) and G (~1595 cm^{-1}) bands of *rGO* are present. It is to be noted that since the B_{1g} peak of *CuPc* at 1334 cm^{-1} is in close vicinity of the D band of *rGO*, hence they do not appear separately in the hybrid. 2D peaks of *rGO* occur in the region of 2400-3200 cm^{-1}. Now the 2D region, in the form of a broad hump, can clearly be observed in the *rGO-CuPc* hybrid in the region of 2600-3000 cm^{-1}. Broad hump like nature is mainly an indication of multi-layered wrinkled graphene [226]. The magnified portion is shown in the inset of Figure 4.15(b), which clearly indicates the 2D band formation is clearly visible for the *rGO-CuPc* system. Strikingly, the same region is flat for the case of pure *CuPc*.

However, very small peaks are observed in both *CuPc* and the hybrid, and are related solely to low intense Raman peaks of *CuPc*.

❖ **UV-Vis analysis:**

To evaluate the optical bandgap, UV-Vis absorbance spectra of *rGO-CuPc* hybrid is carried out using DMF solution and displayed in Figure 4.15(c). The region between 300-500 *nm* corresponds to B band absorption and 600-800 *nm* to Q band. In case of hybrid, peak at 262 *nm* arises due to the presence of *rGO* [227]. Absorption edge of the pure *CuPc* tube [211] is slightly shifted to a higher wavelength region (red shift) in case of *rGO-CuPc* hybrid. Therefore, this can be ascribed to the electronic interactions between *rGO* and *CuPc*. Bandgap is determined using Eq. (4.2) and bandgap of *CuPc* nanotubes and *rGO-CuPc* hybrid are evaluated to be 2.27 *eV* and 2 *eV* as depicted in Figure 4.15(d). Depending on the degree of reduction, rGO exhibits optical bandgap of around 1.88 eV [DOI: 10.22068/ijmse.16.1.22]. So, for the rGO-CuPc composite, effective bandgap will be the average of bandgap for both materials i.e. 2.07 eV. Our obtained results are in close proximity with the average value. In another way, this bandgap reduction can also be ascribed due to the enhanced surface charge interaction between rGO and CuPc as there is almost 1*h* ultrasonication during the synthesis of rGO-CuPc. Thus, the incorporation of *rGO* sheets on *CuPc* results in the decrease in the bandgap [228, 229]. The *rGO* sheets bound to *CuPc* enhance the transfer of sonochemically generated electrons, and thus, suppresses the recombination by the separation of electron–hole pairs.

❖ **Raman imaging:**

For Raman imaging, a selected area (20 μm × 20 μm) of the hybrid powder spread on a substrate is chosen. As shown in Figure 4.16, Raman image mapping has been executed with wavenumbers corresponding to the most intense Raman peaks located around 1444 cm^{-1} and 1520 cm^{-1}, which correspond to the (B_{1g} + B_{2g}) and B_{1g} modes of vibrations of *CuPc*, whereas

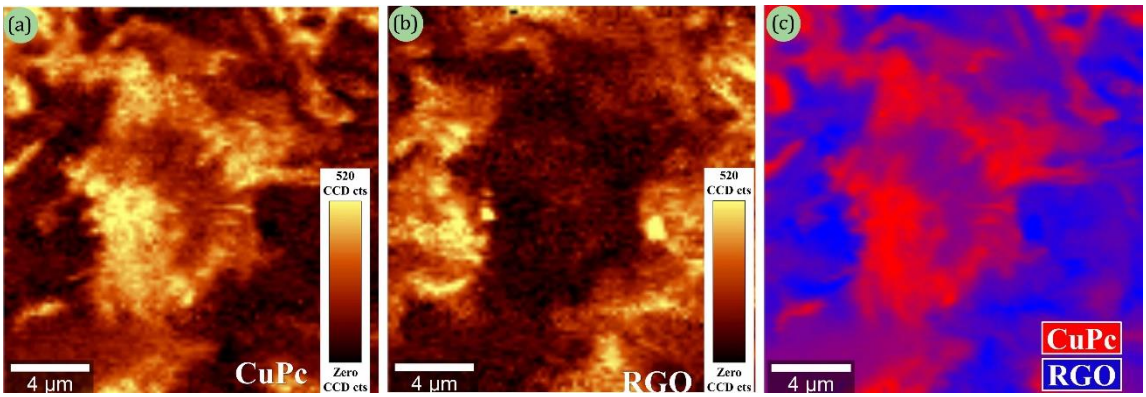

Figure 4.16: *Raman imaging of (a) CuPc, (b) rGO & (c) rGO-CuPc*

the characteristic G band (~1595 cm^{-1}) of *rGO* is considered. The peaks are detected and images corresponding to the spatial distribution of peak intensities have been mapped. (Regions of peak selection are marked by colour rectangles in red for *CuPc* and blue for *rGO*, as indicated in Figure 4.16(a) and (b)). The scale bars in the insets correspond to intensities (CCD counts), yellow being the maximum (~520 counts) and black being the minimum (~zero counts). Figure 4.16(c) shows the combined bitmap image of the two components in the hybrid. The combined bitmap clearly shows the distribution of the individual components in the hybrid in a small selected area.

❖ **Morphological analysis:**

Morphology of the as-prepared pristine *CuPc* tube and *rGO* enveloped *CuPc* tube are shown in Figure 4.17. Figure 4.17(a), (b) and (d) present the FESEM images in different magnifications. As shown in Figure 4.17(a), the wall thickness of pure *CuPc* tube is around ~ 70-100 *nm*. *CuPc* tube is properly enveloped by *rGO* sheets, as evident from Figure 4.17(b) and (d). Figure 4.17(c) depicts the magnified image of encircled portion of Figure 4.17(b). High resolution TEM images are displayed in Figure 4.17(e) and (f) from which the complete wrapping of *CuPc* tube by *rGO* sheets is also affirmed.

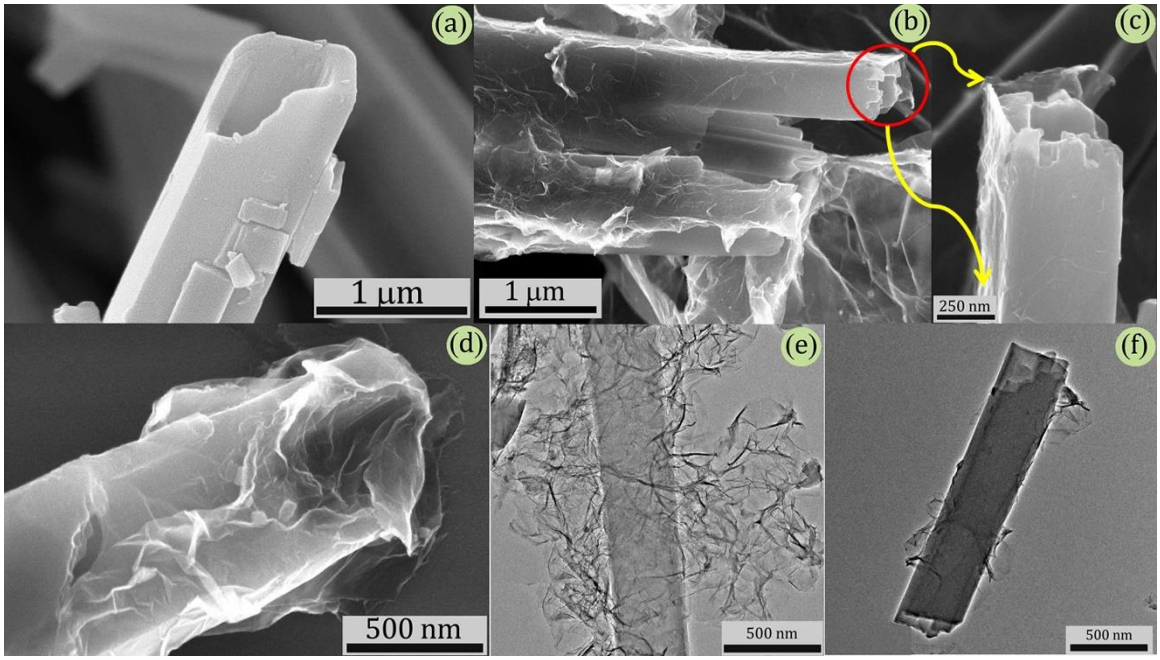

Figure 4.17: *(a) FESEM image of pristine CuPc tube; (b)-(d) FESEM of rGO enveloped CuPc tube; (e) and (f) HRTEM images of rGO-CuPc hybrid*

4.3.4 *MoS_2-CuPc* hybrid:

❖ **Structural analysis:**

Phase analysis of as-prepared samples is explored by the use of XRD measurement. XRD pattern of *MoS_2-CuPc* is presented in Figure 4.18(a), in which all crystallographic planes are identified. It is found that phases of both *MoS_2* and *CuPc* are coexisting in the diffraction pattern of *MoS_2-CuPc*. Intense peaks at 2θ = 7.3° and 9.4° proclaim the formation of $(\bar{1}01)$ and (101) planes of *CuPc*, respectively. All assigned peaks of *CuPc* are well conformed to JCPDS card no: 39-1881. For *MoS_2* sample, diffraction peaks observed at 2θ = 14.2°, 33.4°, 39.5° and 49° correspond to different planes like (002), (100), (103) and (105) respectively. The intense (002) plane indicates the formation of stacked layer of *MoS_2*. These peaks are indexed with the

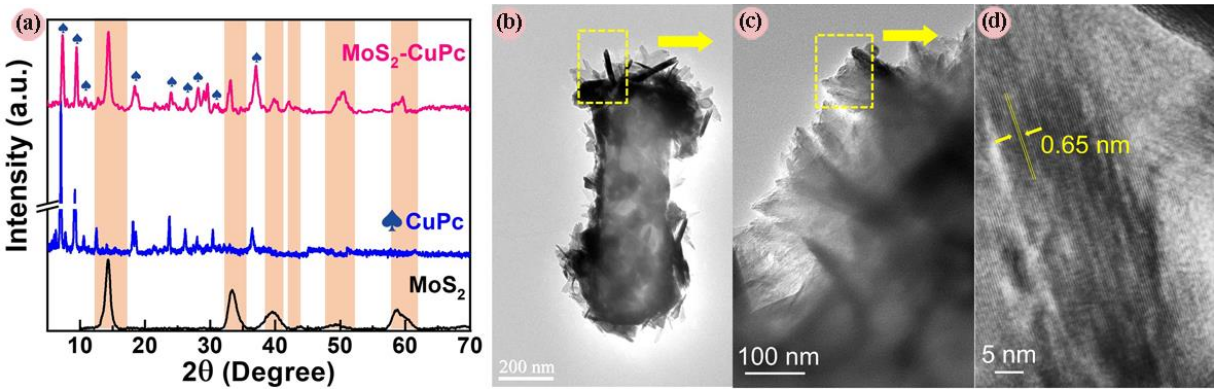

Figure 4.18: *(a) XRD pattern, (b) HRTEM microstructure, (c) magnified nanosheet on microrod and (d) high resolution lattice image of MoS_2-CuPc hybrid*

help of JCPDS 37-1492 card [230]. Crystal structure of hydrothermally prepared *MoS_2* at 200°C is hexagonal phase [2H form], and it is found in earlier works that with the increase in reaction temperature, higher crystallinity and lower defects can be achieved [231]. TEM microstructure of *MoS_2* decorated *CuPc* microrod is shown in Figure 4.18(b) and corresponding enlarged portion of nanosheet on the surface of microrod is presented in Figure 4.18(c). Figure 4.18(d) indicates the high resolution lattice image of heterostructure and exhibits the interlayer distance of 0.65 *nm* correspond to (002) plane of *MoS_2* nanosheet; it is in accordance with the XRD pattern of *MoS_2* [231]. The interlayer distance is increased for hydrothermally grown *MoS_2* as compared to bulk 2H *MoS_2* i.e. 0.62 *nm* [232]. From HRTEM microstructure, the thickness of the grown *MoS_2* nanosheet is observed to be ~12-14 *nm*. As the interlayer spacing is found as 0.65 *nm* for (002) plane, ~ 18-22 monolayers of *MoS_2* are stacked to form the nanosheet [233].

To obtain deeper insight for the oxidation states of constituent elements in the *MoS_2-CuPc* hybrid, high resolution XPS analysis is performed. The survey spectrum as presented in

Figure 4.19(a) proves the existence of *C, N, Cu, Mo* and *S* elements in the hybrid system. In *Cu 2p* XPS spectra as shown in Figure 4.19(b), deconvoluted peaks appear at 932 and 952 *eV*,

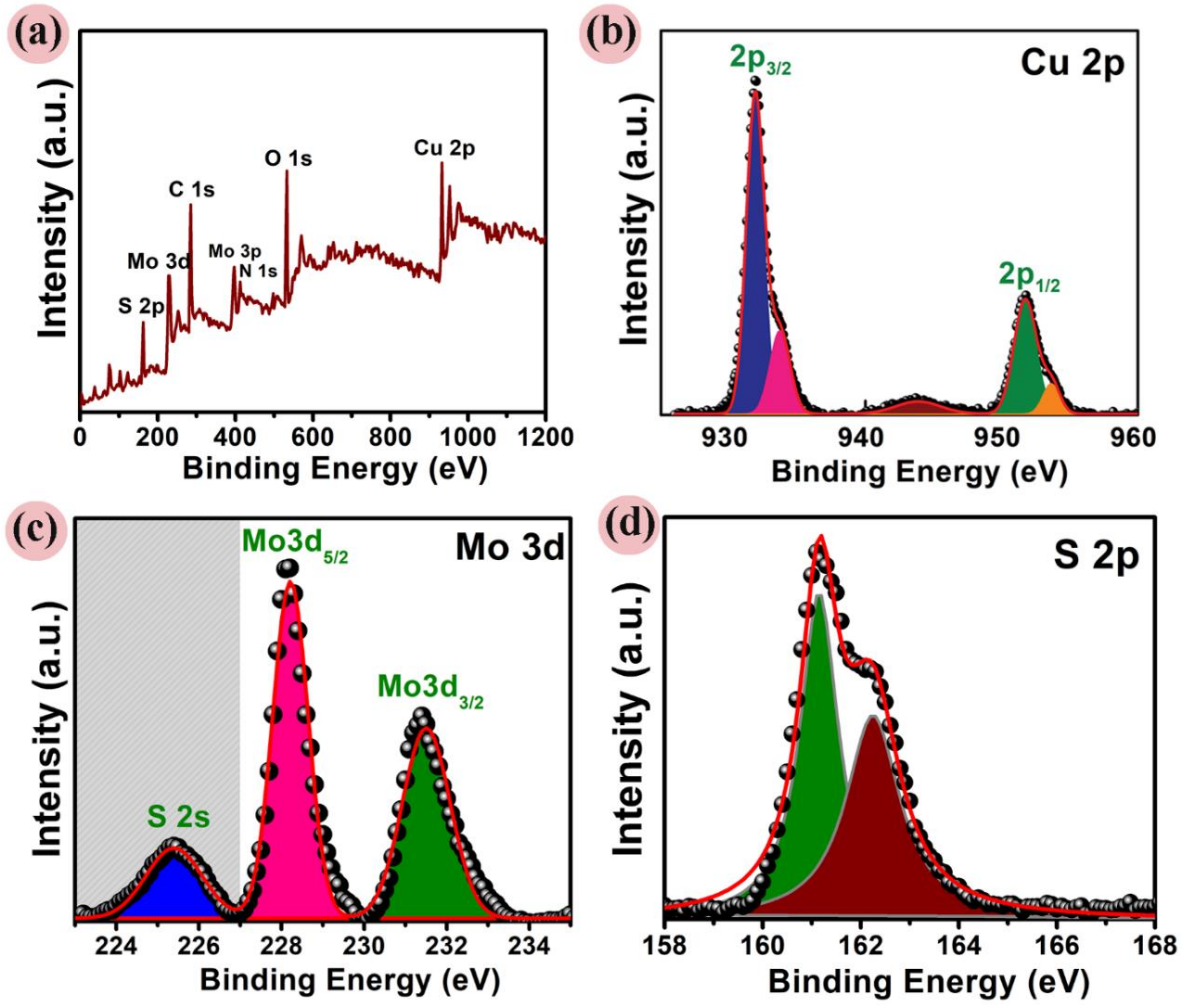

Figure 4.19: *(a) Survey spectrum, High resolution spectra of (b) Cu 2p, (c) Mo 3d and (d) S 2p*

and at 933.9 and 953.9 *eV* [separation 20 *eV*], and can be assigned to *Cu* $2p_{3/2}$ and *Cu* $2p_{1/2}$, respectively [234]. Weak satellite peak present at 943.9 *eV* clearly confirms the oxidation state of central *Cu* atom of *CuPc* in *Cu (II)* state [235, 236]. In Figure 4.19(c), the high resolution spectrum of *Mo 3d* exhibits two prominent peaks positioned at 228.2 *eV* and 231.4 *eV* (separation 3.2 *eV*), which are assigned to the doublet *Mo* $3d_{5/2}$ and $3d_{3/2}$, respectively [237]. Along with that, a small peak at 225.4 *eV* of *S 2s* is also found in the *Mo 3d* region. The fitting of these three peaks reveals the Mo^{4+} state formation. In Figure 4.19(d), two peaks at 162.2 *eV* and 161.1 *eV* are attributed to *S* $2p_{1/2}$ and *S* $2p_{3/2}$, respectively [238].

N 1s spectra of pristine *CuPc* and MoS_2-*CuPc* hybrid are presented in Figure 4.20(a) and (b) respectively. In *CuPc*, there are pyridinic N and pyrrolic N situated at 398.6 and 400.1 *eV*, respectively [239]. In *N 1s* of hybrid structure, pyridinic N and pyrrolic N are observed at 397.3 and 398.4 *eV* which are shifted to lower binding energy compared to pristine system that

manifests the co-ordination to both nitrogen with *Mo* ions at hybrid interface [240]. In addition to that, *Mo 3p* peak also appears in *N 1s* of hybrid system, and is absent in pristine *CuPc* system.

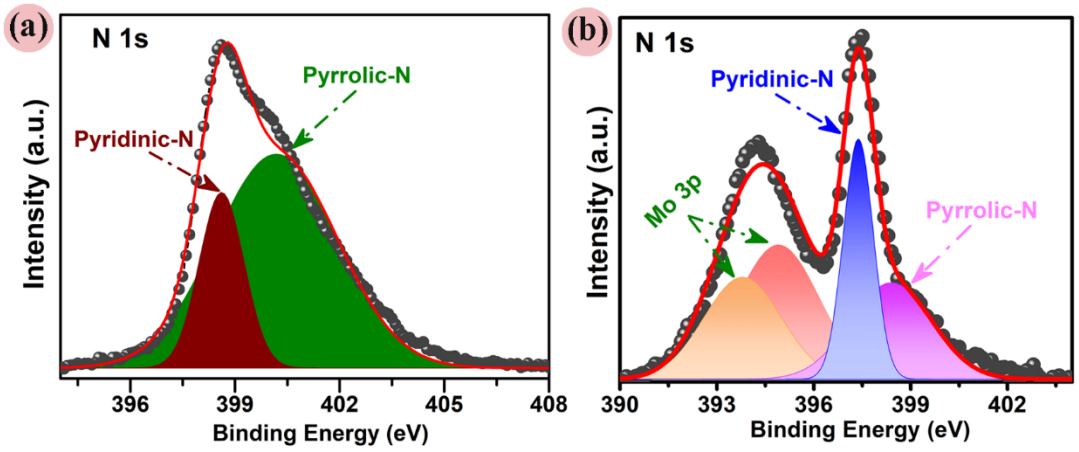

Figure 4.20: *N 1s spectra of (a) CuPc and (b) MoS_2-CuPc*

❖ **Morphological analysis:**

FESEM images of hydrothermally synthesized *CuPc* rectangular rod, prior to the growth of *MoS_2* nanoflakes, are shown in Figure 4.21(a) and (b). The rods are in random orientation and have an almost smooth surface with approx. 15-20 *μm* length and 350-450 *nm* width. After the hydrothermal step of *MoS_2* preparation, enormous amount of crosslinked *MoS_2* nanoflakes are homogenously grown on the surface of rectangular *CuPc* microrod as shown in Figure 4.21(c). From the highly magnified image in Figure 4.21(d), the thickness of the

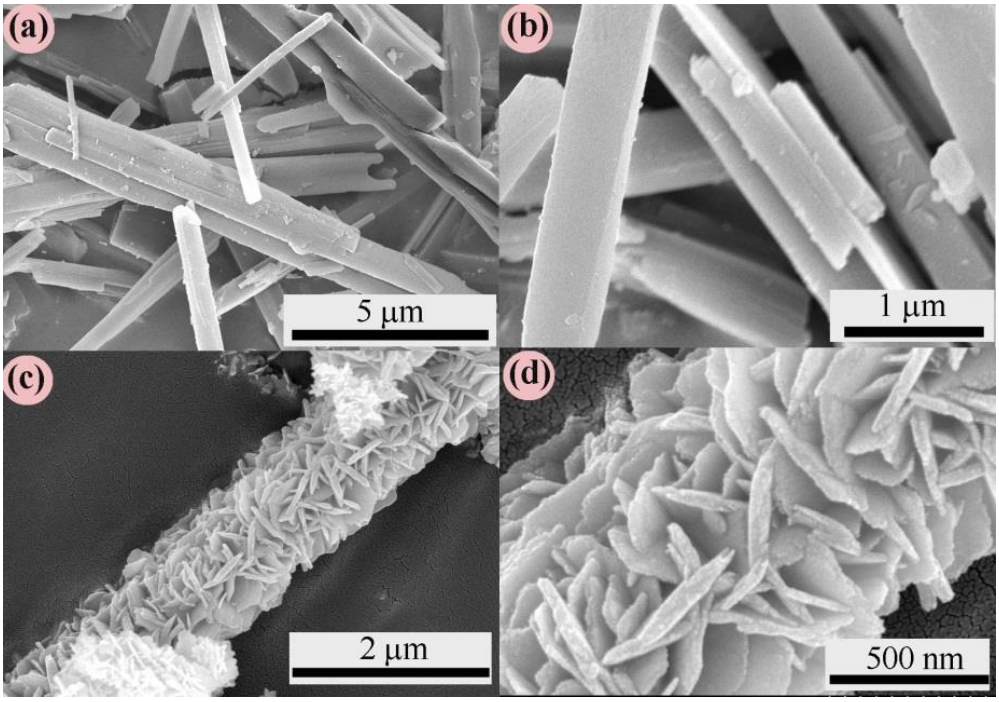

Figure 4.21: *(a) Low, (b) High magnification FESEM images of CuPc rod, (c) Low and (d) High magnification images of MoS_2-CuPc hybrid*

deposited MoS_2 nanoflakes is found to be of the order of 10-15 *nm*. For comparison, pristine MoS_2 flowers, composed of a huge number of nanoflakes are displayed in Figure 4.22.

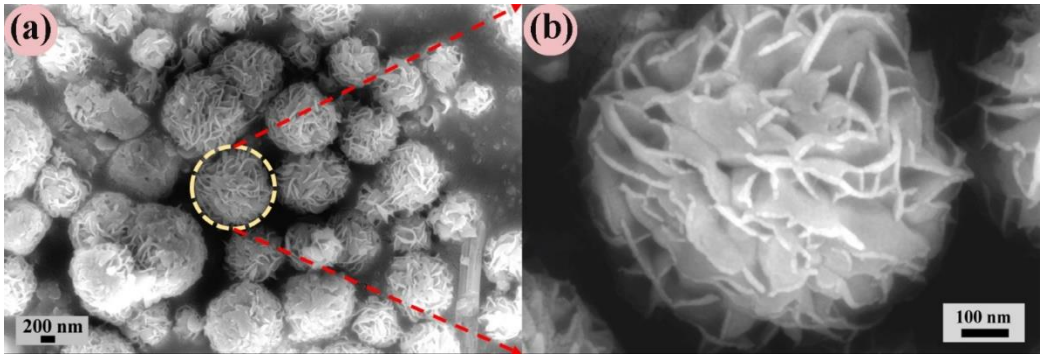

Figure 4.22: *FESEM images of MoS_2 microflower in different magnifications*

Plausible growth mechanism of *MoS_2-CuPc* hybrid system is also explored in this dissertation. In this case, *CuPc* microrods act as backbone to guide the deposition of 2D *MoS_2* sheet along the length. The drawback of agglomeration of *MoS_2* flowers can be overcome by combining 2D *MoS_2* sheet and 1D *CuPc* rod [241]. Initially, surface energy of the nucleating substrate plays an important role during the growth process [242]. Therefore, the vertical growth of *MoS_2* is kinetically favourable along the *CuPc* rod. In general, heterogeneous nucleation requires less energy than homogeneous nucleation [242, 243]. As a result, low energy is needed for *MoS_2* to be grown on *CuPc* microrod in hydrothermal synthesis.

In the first step, *CuPc* is sonicated in D.I water rigorously to achieve well dispersion due to its hydrophobic nature. Henceforth, sodium molybdate and thiourea are added and stirred for one hour. Next, *MoO_4^{2-}* and *$(NH_2)_2CS$* are synchronized along the *CuPc* rod as shown in Figure 4.23. Hydrothermal temperature is also crucial factor to obtain proper deposition of stable 2H-*MoS_2* [244]. High temperature is always beneficial for the formation of uniform *MoS_2* with high crystallinity due to its uniform nucleation procedure. So the temperature is maintained at 200°C.

$$Na_2MoO_4 \rightarrow 2Na^+ + MoO_4^{2-} \tag{4.2}$$

$$NH_2CSNH_2 + 2H_2O \rightarrow 2NH_3 + H_2S + CO_2 \tag{4.3}$$

$$MoO_4^{2-} + 3H_2S \rightarrow MoS_2 + 3H_2 + SO_4^{2-} \tag{4.4}$$

$$2Na^+ + SO_4^{2-} \rightarrow Na_2SO_4 \tag{4.5}$$

In the hydrothermal process, the reaction proceeds by the above-mentioned equations. During the reaction, released H_2S from the thiourea [Eq. (4.3)], reacts with *MoO_4^{2-}* and

produces MoS_2, as described by Eq. (4.4). In the autoclave, as the temperature and pressure start to rise, MoS_2 is nanoparticulated at a specific time. It is termed as nucleation occurring at the third step of the synthesis scheme. It helps to reduce the thermodynamic barrier between the *CuPc* and MoS_2 [242]. Due to the presence of facile thermal convection and concentration gradient, fluent transportation of molecules as well as ions towards the surface occurs at this stage[38]. Besides, thiourea efficiently synchronizes with molybdenum as the reductive functional group NH_2 participates in the reaction with the oxygen of MoO_4^{2-}. Therefore, MoS_2 nuclei are developed on the surface of *CuPc* rod. The whole process is schematically shown in Figure 4.23. As the reaction time continues, immature layer of MoS_2 flakes is generated from the nucleus on *CuPc*. With time, petal like structure as shown in Figure 4.23 is finally emerged. The {001} crystal plane of MoS_2 has the lowest surface energy for which the highest rate of crystal growth is achieved [245]. As time increases, surface energy at the MoS_2 edge increases steadily with respect to the surface site. Thus, a fresh crystal plane avails the chance to be nucleated along the [001] direction imposed by van der Waals force. Thus, the regrowth takes place on the same crystal plane. Such stepwise nucleation and growth are attributed to interlayer stacking and bonding of MoS_2 on *CuPc*.

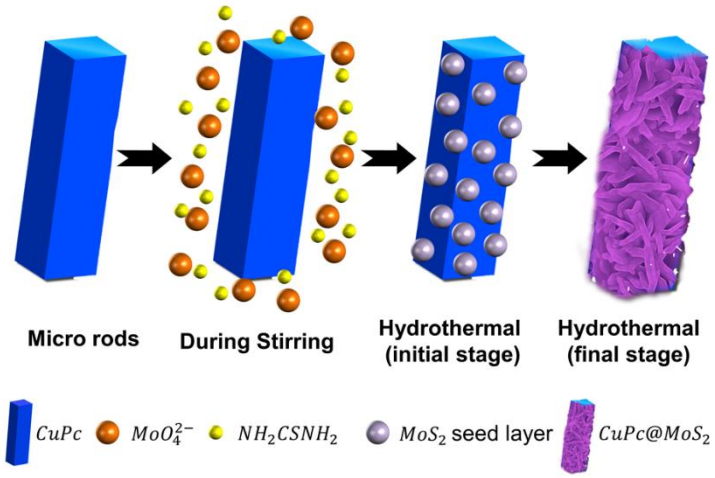

Figure 4.23: *Plausible growth mechanism of MoS_2-CuPc preparation*

❖ **Composition analysis:**

EDX elemental mapping of MoS_2-*CuPc* hybrid, as shown in Figure 4.24, is carried out. It confirms the presence of *C*, *N*, *Cu*, *Mo* and *S* along with the focused portion of MoS_2-*CuPc* hybrid.

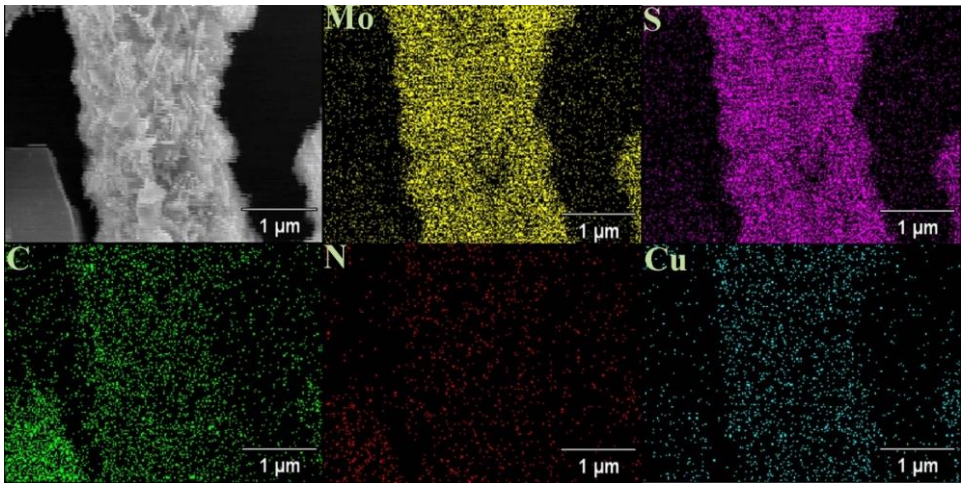

Figure 4.24: *EDX elemental mapping of MoS_2-CuPc*

EDX spectrum and the corresponding atomic percentages are presented in Figure 4.25, and the *Mo* to *S* atomic ratio is estimated to be 1 : 2.1, which is in good agreement with the actual stoichiometric ratio of MoS_2.

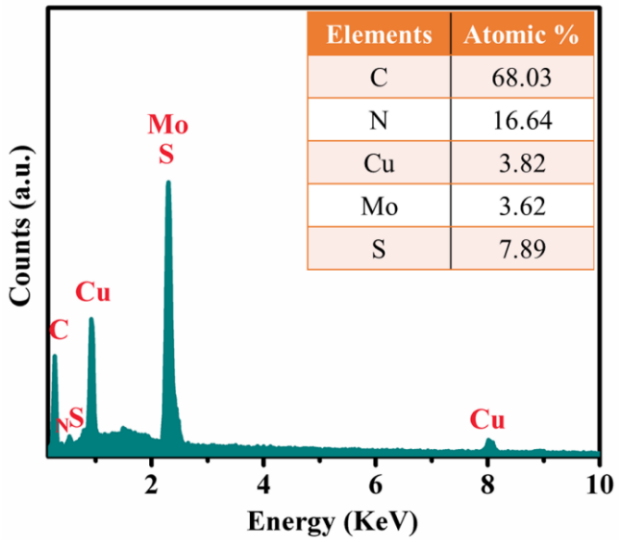

Figure 4.25: *EDX spectrum of MoS_2-CuPc heterostructure with atomic percentage*

4.4 Conclusions:

Among various MPcs, *ZnPc* and *CuPc* nanostructures have been successfully synthesized through low temperature processes. All pristine phthalocyanine and their heterostructures with *rGO* and MoS_2 have been prepared through hydro / solvothermal methods. After that, several characterization techniques have been employed to study the proper formation of nanostructured materials. Some modifications on existing synthesis route and novel approaches adopted for the preparation of several MPc nanostructures and their hybrids have revealed new synthesis prospects of different nanostructure of MPcs, other than *CuPc*, *ZnPc* and their heterostructures.

5.1 Introduction:

In the last few decades, due to the rapid industrial development in India, different sectors are facing major environmental issues related to waste water management. Different types of organic dyes used in textile industry, cause different hazardous effects on human health as well as aquatic life [246]. So, catalytic destruction of *RB* is necessary as it has some adverse effects on skin, respiratory and gastrointestinal systems [247]. For dye degradation, *ZnO* and TiO_2 are so far considered as well-known photocatalysts under UV light illumination due to their wide band gaps (3.1-3.3 *eV*) [248-252]. As the solar spectrum contains maximum percentage of visible light, visible light activated catalysts can efficiently utilize the solar radiation; *CuPc* and *rGO-CuPc* hybrids possessing appropriate forbidden bandgaps are employed in this dissertation. Using these catalysts, moderate photocatalytic performances have been reported [62] in 3.5 *h*. To achieve better performance in a short period, ultrasonic irradiation is introduced.

In this chapter, sonophotocatalytic degradation of *RB* using *CuPc* nanowires is initially investigated employing a bath sonicator. Sonocatalytic activity of *rGO-CuPc* heterostructures is also carried out by using a probe sonicator towards *RB* dye removal.

5.2 Sonophotocatalysis by *CuPc* nanowires:

Efficient sonophotocatalytic degradation of *RB* with the chemically synthesized *CuPc* nanowires at room temperature is performed. Ultrasound irradiation combined with visible light in sonophotocatalysis produces synergistic effects that play an important role in superior dye degradation performance. The plausible reaction mechanism is also thoroughly discussed. The influences of several parameters *viz*. initial dye concentration, catalyst dosage, etc. on decolorization efficiency are also investigated.

❖ **Decolorization efficiency and kinetic study:**

In this experiment, sonocatalysis, photocatalysis and sonophotocatalysis are investigated under the presence of *CuPc* nanowires along with visible light illumination. Figure 5.1(a) presents the sonophotocatalytic degradation profile of *RB* dye under visible illumination with the presence of catalyst. The figure shows that the maximum absorption peak intensity around $\lambda \sim 554$ *nm* decreases with increasing irradiation time. The initial concentration (C_0), final concentration (C) and decolorization efficiency (D) follow a mathematical relationship given as [62]:

$$D = \frac{C_0 - C}{C_0} \times 100\% \qquad (5.1)$$

Figure 5.1(b) presents the plot of decolorization efficiency (%) for sono, photo and sonophotocatalysis measurements with irradiation time. From this, it can be concluded that maximum efficiency of ~81% is achieved by sonophotocatalysis within 60 *min*, whereas only 22.8% and 56.8% degradation can be achieved respectively by photocatalysis and sonocatalysis under with similar operating conditions.

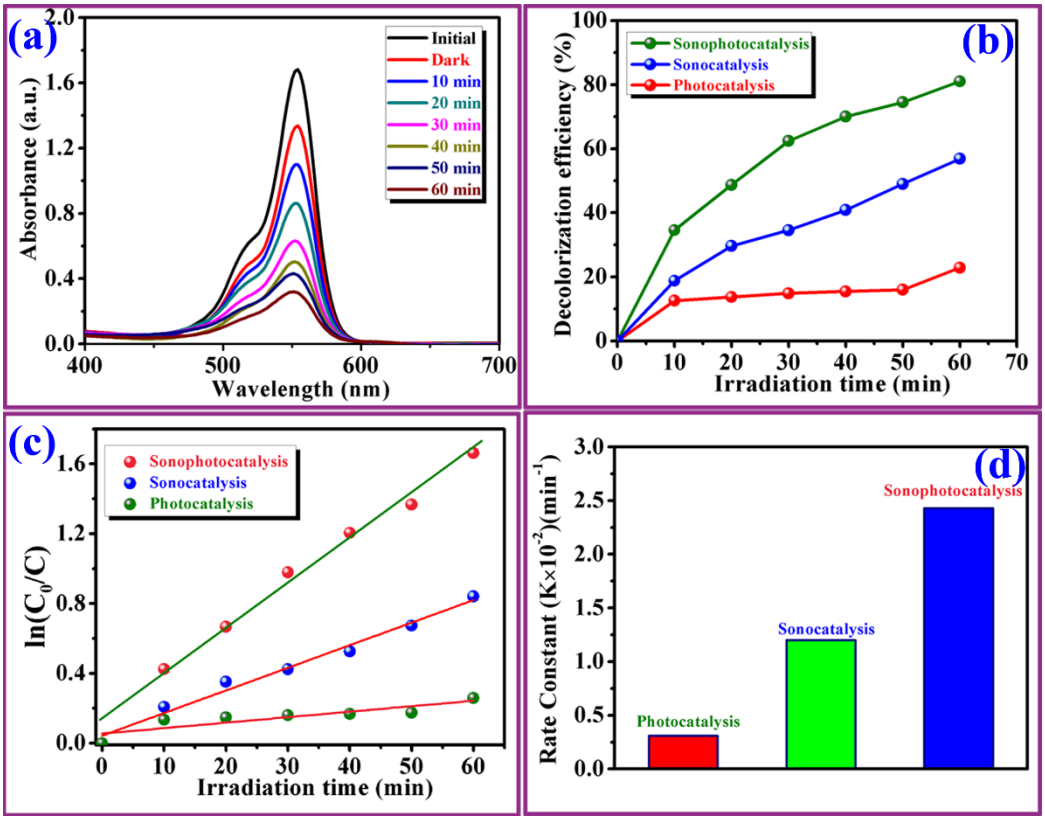

Figure 5.1: *(a) Degradation profile of RB during sonophotocatalytic process, comparative (b) Decolorization efficiency, (c) Kinetic study and (d) Rate constant for sono, photo and sonophotocatalysis processes*

The kinetic study is carried out by following Langmuir Hinshelwood apparent first-order kinetics model [253], according to which we can write,

$$ln(\frac{C_0}{C}) = Kt \tag{5.2}$$

Here, *K* denotes the pseudo first-order rate constant (min^{-1}) to be estimated from the reaction kinetics. The fitted curves for sono, photo and sonophotocatalysis are shown in Figure 5.1(c). Synergy index (*SyI*) is an important parameter that is used to describe the correlation between individual processes and sonophotocatalytic process. *SyI* can be determined by using the following formula [254]:

$$SyI = \frac{K_{sonophoto}}{K_{photo}+K_{sono}} \tag{5.3}$$

where, $K_{sonophoto}$, K_{sono} and K_{photo} are the rate constants for sonophoto, sono and photocatalysis, respectively. From the comparative kinetic study, it is found that $K_{sonophoto}>K_{sono}>K_{photo}$ and the values of these rate constants for three different catalytic processes are summarized in the bar graph as shown in Figure 5.1(d). For *SyI* <1, sonophotocatalysis is the combined effect of both sonocatalysis and photocatalysis, while for *SyI* >1, synergistic degradation effect is predominant. *SyI* is evaluated from Eq. (5.3) and found to be 1.609, which implies that the rate constant value for sonophotocatalysis is higher than the sum of the rate constants for sonocatalysis and photocatalysis. Thus, sonophotocatalytic degradation of *RB* dye occurs at a rate faster than the respective individual processes under same experimental conditions due to an interesting synergistic effect in between ultrasonic and visible light irradiation [255].

❖ **Effect of initial dye concentration:**

From the application point of view, it is important to investigate the influence of initial *RB* concentration on sonophotocatalytic degradation efficiency. The catalytic decolorization efficiency (%) and reaction kinetics are studied by varying the initial *RB* concentration from $1.0 \times 10^{-5}\,M$ to $2 \times 10^{-5}\,M$ and the results are presented in Figure 5.2(a) and 5.2(b), respectively. The catalyst dosage and reaction time are 83.33 *mg/L* and 60 *min*, respectively. Our experimental results indicate that decolorization efficiency (%) is inversely proportional to the initial dye concentration. Increasing concentration of dye leads to reduction in the degradation efficiency as well as the rate constant value. Results are summarized in Table 5.1. There are different reasons behind such efficiency degradation. First, a certain amount of catalyst dosage is able to produce only certain amount of light induced electron-hole pair [256]. Secondly, with increasing dye concentration, more *RB* molecules are adsorbed onto the surface of *CuPc* nanowires, occupying more no. of active sites, and thus maximum amount of visible light is absorbed by *RB* molecules rather than catalyst, thereby efficiency falls [89]. Lastly, the production of $OH^{\bullet}$ radicals decreases due to the inaccessible active sites on the catalyst surface, that in turn, lowers the catalytic performance. Thus, it can be stated that sonophotocatalysis process is favorable at low concentration of organic pollutant.

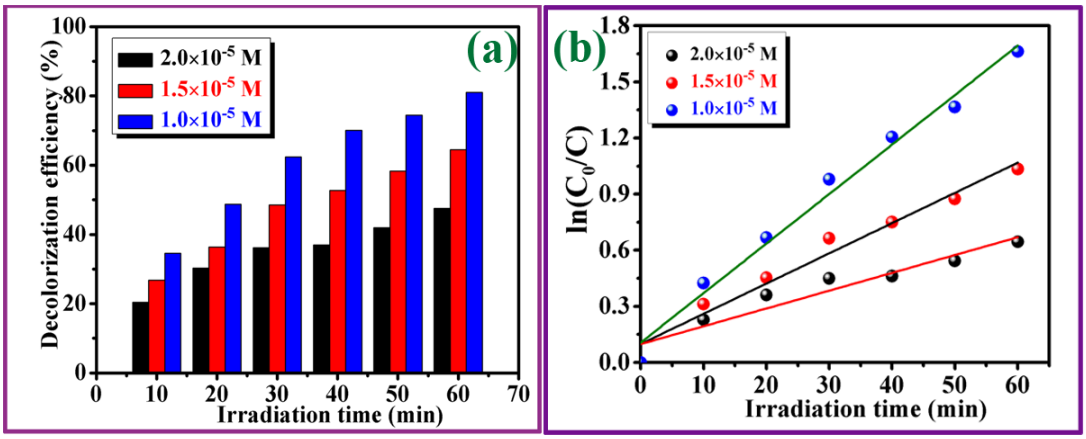

Figure 5.2: *(a) Influence of initial dye concentration and (b) corresponding kinetic study*

Table 5.1: *Effect of initial dye concentration on degradation parameters*

Initial dye concentration ($\times 10^{-5}$ *M*)	Rate constant (min^{-1})	Efficiency (%)
1	0.0243	81
1.5	0.0161	64.4
2	0.0095	47.5

❖ **Effect of catalyst dosage:**

The influence of the catalyst dosage on the decolorization efficiency of *RB* dye is also investigated in this experiment. Figure 5.3(a) and 5.3(b) present the change in degradation efficiency (%) with time for the increase in catalyst dosage in the range from 16.67 *mg/L* to 116.67 *mg/L* keeping other experimental conditions fixed and corresponding linearly fitted kinetic curves, respectively. The efficiency and rate constant values for different catalyst dosage are summarized in Table 5.2. It is observed that as the dosage increases, efficiency and rate constant initially increase due to the availability of larger number of active sites [96, 257]; but beyond 83.33 *mg/L*, a decline in efficiency is observed that may occur due to two reasons:

1. Due to high catalyst dosage, catalyst particles tend to agglomerate with each other reducing active sites for *RB* adsorption,

2. Excessive catalyst concentration inhibits the propagation of ultrasound and light waves to the catalyst surface [258, 259].

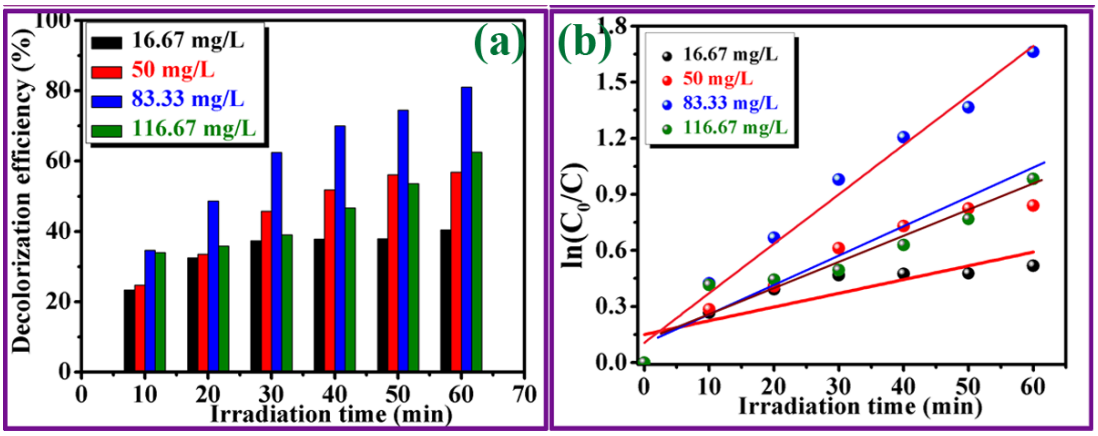

Figure 5.3: *(a) Effect of catalyst dosage and (b) corresponding kinetic modeling*

Table 5.2: *Effect of catalyst dosage on degradation parameter*

Catalyst dosage (*mg/L*)	Rate constant (min^{-1})	Efficiency (%)
16.67	0.0073	40.4
50	0.0140	56.8
83.33	0.0243	81
116.67	0.0137	62.5

❖ **Effects of radical scavenger and enhancer:**

In industrial wastewater, several ions may be present that either help to enhance or to diminish the catalytic degradation of dyes. To investigate their effect, 0.1 *M KCl* and 3.6 *mM* ammonium persulfate (*APS*) are used as scavenger and enhancer, respectively. Sonophotocatalytic *RB* degradation profile under the presence of scavenger and catalyst is presented in Figure 5.4(a). Use of scavenger degrades efficiency from 81% to 75% as chloride ions are strong $OH^{\bullet}$ radical scavenger; possible reactions are as follows [89, 260]:

$$OH^{\bullet} + Cl^{-} \rightarrow Cl^{\bullet} + OH^{-} \quad (5.4)$$

$$OH^{\bullet} + Cl^{-} \rightarrow HOCl^{\bullet -} \quad (5.5)$$

$$Cl^{\bullet} + Cl^{-} \rightarrow Cl_2^{\bullet -} \quad (5.6)$$

$$Cl^{-} + h^{+} \rightarrow Cl_2/Cl^{\bullet} \quad (5.7)$$

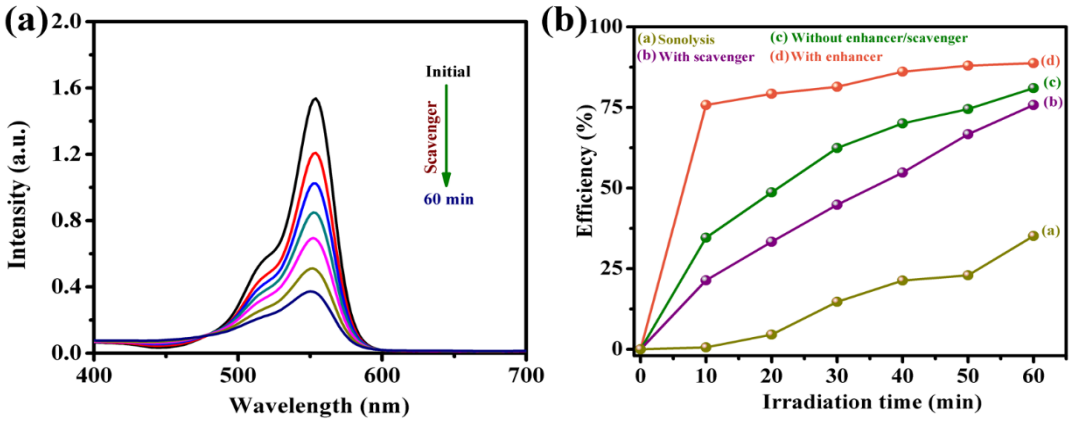

Figure 5.4: *(a) Effect of scavenger on RB degradation and (b) Comparative study with enhancer, scavenger and sonolysis*

Scavenger test also affirms the dominant role of radicals in dye decolorization. Efficiency is also enhanced from 81% to 89% with the use of *APS*, as sulfate radicals finally help to generate more $OH^{\bullet}$ radicals. The plausible reactions are presented below [89]:

$$S_2O_8{}^{2-} + ultrasound \rightarrow 2SO_4{}^{\bullet-} \quad (5.8)$$

$$SO_4{}^{\bullet-} + H_2O \rightarrow SO_4{}^{2-} + H^+ + OH^{\bullet} \quad (5.9)$$

$$SO_4{}^{\bullet-} + dye \rightarrow By - products \quad (5.10)$$

In addition to that, one control experiment is carried out without catalyst just to determine the effect of ultrasonic irradiation and only 35% of *RB* decolorization is obtained. Comparative results with enhancer, scavenger and control experiment are shown in Figure 5.4(b).

Earlier in Chapter 2 [section 2.3.1.1], it have been already stated that during the cavitation process of sonocatalysis, a localized high temperature and pressure are created within the center of the bubble, but it does not cause any serious effect on *CuPc* nanostructures; they are not cracked during the catalytic treatment. To ensure that, morphological study is carried out after sonophotocatalytic degradation process, and more or less similar kind of wire-like structure is observed as evident from Figure 5.5.

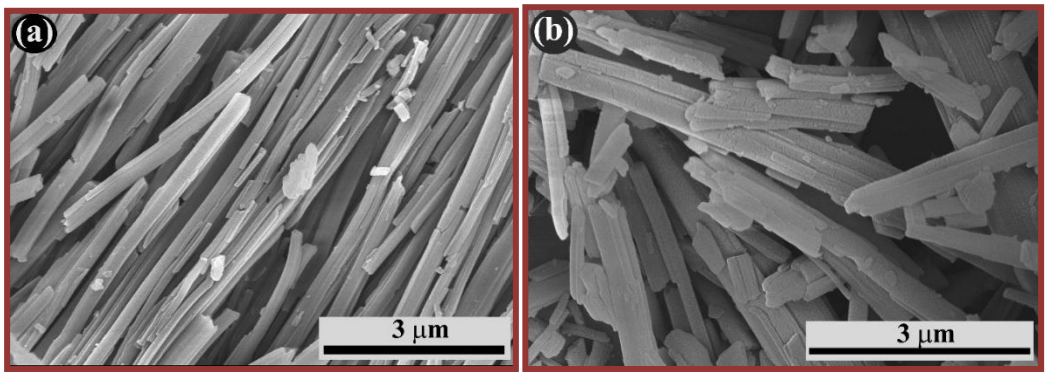

Figure 5.5: *CuPc nanowire (a) before and (b) after sonophotocatalytic degradation*

❖ **Synergistic effect and mechanism of sonophotocatalytic degradation:**

Photocatalysis in combination with the sonocatalysis process provides a synergy effect that can help to degrade organic pollutants from industrial wastewater. Prominent synergistic effects are observed because of the basic mechanism of chemical effects to degrade pollutants and physical effects to provide the effective contact between the generated radicals and organic pollutants [261]. As a consequence of using ultrasonic irradiation, some chemical effects like generation of radicals and physical effects *viz.* shock waves, cause generation of cavity bubbles and micro-turbulence.

When aqueous solution is irradiated by ultrasound, cavitation bubbles are formed. The ultrasound assisted catalysis of organic compounds occurs in three different regions in the aqueous solution: (1) within the cavity, (2) in the bulk solution and (3) at the interface region between the cavitation bubbles and the bulk solution, and. In regions (1) and (3), the pyrolysis and radical reactions mainly occur while in region (2), the reactions with $OH^{\bullet}$ radicals are predominant. On account of ultrasound irradiation in the aqueous medium, two phenomena play the important role for decomposition of *RB* dye; one is generation of "hotspot" and the other is "sonoluminescence". Mechanisms of these two processes are already described in Chapter 2. Significant amount of $OH^{\bullet}$ radicals can be generated by ultrasonication of pure water following the reactions mentioned in Eqs. [2.1-2.5]:

As *RB* dye is hydrophilic in nature, decolorization of *RB* dye is achieved through the hydroxylation reaction in the bulk liquid medium. The generated $OH^{\bullet}$radicals possess high reactivity and short life time. Under normal conditions, they always try to recombine with another $OH^{\bullet}$ to form water molecules (H_2O) or hydrogen peroxide (H_2O_2) before arriving at the surface of the *RB* molecule. Thus, there are some uncertainties about the amount of $OH^{\bullet}$ radicals that effectively come in contact with the dye surface [262]. Such uncertainties can be eradicated if the visible light driven photocatalysis and sonocatalysis are applied together and the effect of sonophotocatalysis is greater than the combined effect of two individual processes, which is also in good correlation with our experimental findings. Apart from these, this process has certain advantages:

(i) Ultrasonic vibration can cause the cleaning of the catalyst surface by removing the unwanted pollutants, thus providing more active sites on the surface, and thereby enhancing the catalytic action towards the decomposition of *RB* dye.

(ii) Both oxidation and reduction processes of the *RB* dye are favorably influenced by the ultrasonication process [263, 264].

(iii) Sonication process intensifies micro-turbulence in the liquid, which helps in proper mixing of catalysts in the aqueous solution by inhibiting the agglomeration of catalyst particles. It therefore, reduces the mass transfer limitations, and enhances the degradation efficiency.

(iv) The synergistic effect of visible light and ultrasonic irradiation facilitates much higher concentration of $OH^{\bullet}$ radical that is mainly responsible for degradation. As a whole, this synergy helps to decompose and mineralize the generated intermediate by products.

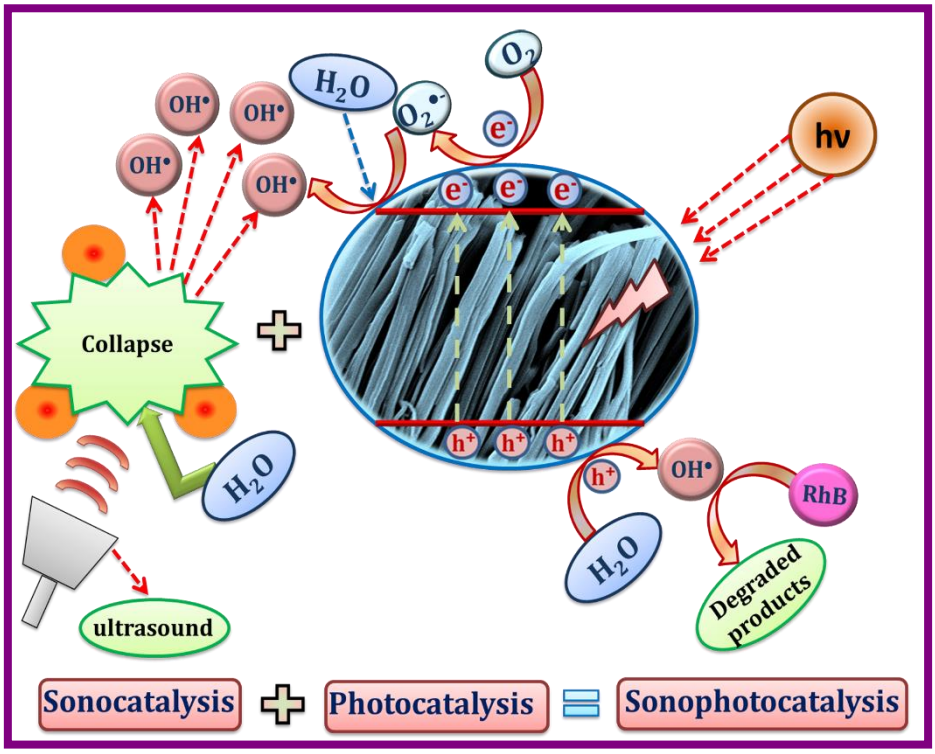

Figure 5.6: *Schematic representation of reaction mechanism for RB degradation*

The plausible reaction mechanisms can be represented in a pictorial form as shown in Figure 5.6. On visible light illumination, *CuPc* molecules got excited through the process of intersystem crossing (ISC). Thus, electrons from HOMO are elevated to LUMO level by creating holes in HOMO. These electrons react with molecular oxygen and produce ${O_2}^{\bullet -}$radicals, which further create $OH^{\bullet}$ radicals. These radicals act as strong oxidizing agents and help to mineralize the pollutants completely. The reactions that govern sonophotocatalytic process are as follows [23]:

$$CuPc \xrightarrow{h\nu} {}^{1}CuPc^{*}(e^{-} + h^{+}) \xrightarrow{ISC} {}^{3}CuPc^{*} \quad (5.11)$$

$${}^{3}CuPc^{*} + O_2 \rightarrow CuPc^{\bullet +} + {O_2}^{\bullet -} \quad (5.12)$$

$${O_2}^{\bullet -} + H_2O \rightarrow HO_2^{\bullet} + OH^{-} \quad (5.13)$$

$$HO_2^{\bullet} + H_2O \rightarrow H_2O_2 + OH^{\bullet} \quad (5.14)$$

$$H_2O_2 \rightarrow 2OH^{\bullet} \quad (5.15)$$

$$OH^{\bullet} + RB \rightarrow Endspecies \quad (5.16)$$

$$CuPc^{\bullet+} + RB \rightarrow Endspecies \quad (5.17)$$

Our synthesized *CuPc* nanostructures can efficiently degrade ~ 81% towards *RB* dye degradation within 60 *min*. This performance is much better than those in more-or-less all cases reported so far. To compare the performances of various organic and inorganic materials along with their composites, results based on different degradation processes are compiled in Table 5.3.

Table 5.3: *Results for different catalysts based on degradation process*

Sample	Dye	Efficiency (%)	Time (*h*)	Mechanism	Ref.
TNCuPc/TiO₂	*RB*	87	4	Photocatalysis	[221]
FeTNPc/BiOCl	*MO*	~35	1	Photocatalysis	[265]
ZnTCPc/UIO-66 (Zr)	*MB*	~65	1	Photocatalysis	[266]
CuPc/rGO	*RB*	~40	1	Photocatalysis	[62]
PDIC12/CuTcPc	*RB*	~50	1	Photocatalysis	[267]
TNFePc	*RB*	~68	1	Photocatalysis	[268]
CuPcTs/TiO₂	*MO*	~52	1	Photocatalysis	[269]
ZnPc	*RB*	88.5	11	Photocatalysis	[23]
CuO- TiO₂/ rGO	*MO*	~62	1	Sonophotocatalysis	[270]
TiO₂/NiO	*MO*	~69	1	Sonophotocatalysis	[271]
CNTs/TiO₂	*MO*	66.2	1	Sonophotocatalysis	[272]
CuPc nanowire	***RB***	**81**	**1**	**Sonophotocatalysis**	**Our work**

5.3 Sonocatalytic degradation by *rGO-CuPc* heterostructure:

rGO enveloped *CuPc* nanotube (*rGO-CuPc*) is chemically synthesized and well characterized. Next, its applicability in the field of sonocatalytic *RB* dye removal using probe sonicator is examined. Influence of various process parameters on dye degradation is also probed in this chapter. A plausible reaction pathway towards dye removal is described in detail.

❖ **Decolorization efficiency and kinetic study:**

Comparative study of sonocatalytic removal of *RB* dye in presence of *rGO-CuPc* hybrid and pristine *CuPc* tube is carried out, respectively. In these set of experiments, different

parameters such as initial dye concentration, catalyst dosage, ultrasonic power and irradiation time, all are kept constant for both samples. Figure 5.7(a) presents the UV-Vis absorbance spectrum of *RB* aqueous solution catalyzed by *rGO-CuPc* hybrid system for regular time interval. Above spectrum shows that intensity of the peak positioned at 554 *nm* decreases with increase in irradiation time and almost completely disappears after a time interval of 100 *min*. This finding asserts the effectiveness of the hybrid system for successful decolorization of such textile dye. Figure 5.7(b) and 5.7(c) show the relative absorbance plot and the corresponding logarithmic plot of *RB* degradation due to the pristine and hybrid system. The relative concentration is found to decrease with irradiation time, and beyond 100 *min* approaches near zero value in hybrid system. Kinetic study of *RB* degradation is usually performed by following Langmuir-Hinshelwood model for pseudo first order reaction kinetics as mentioned in Eq. (5.2).

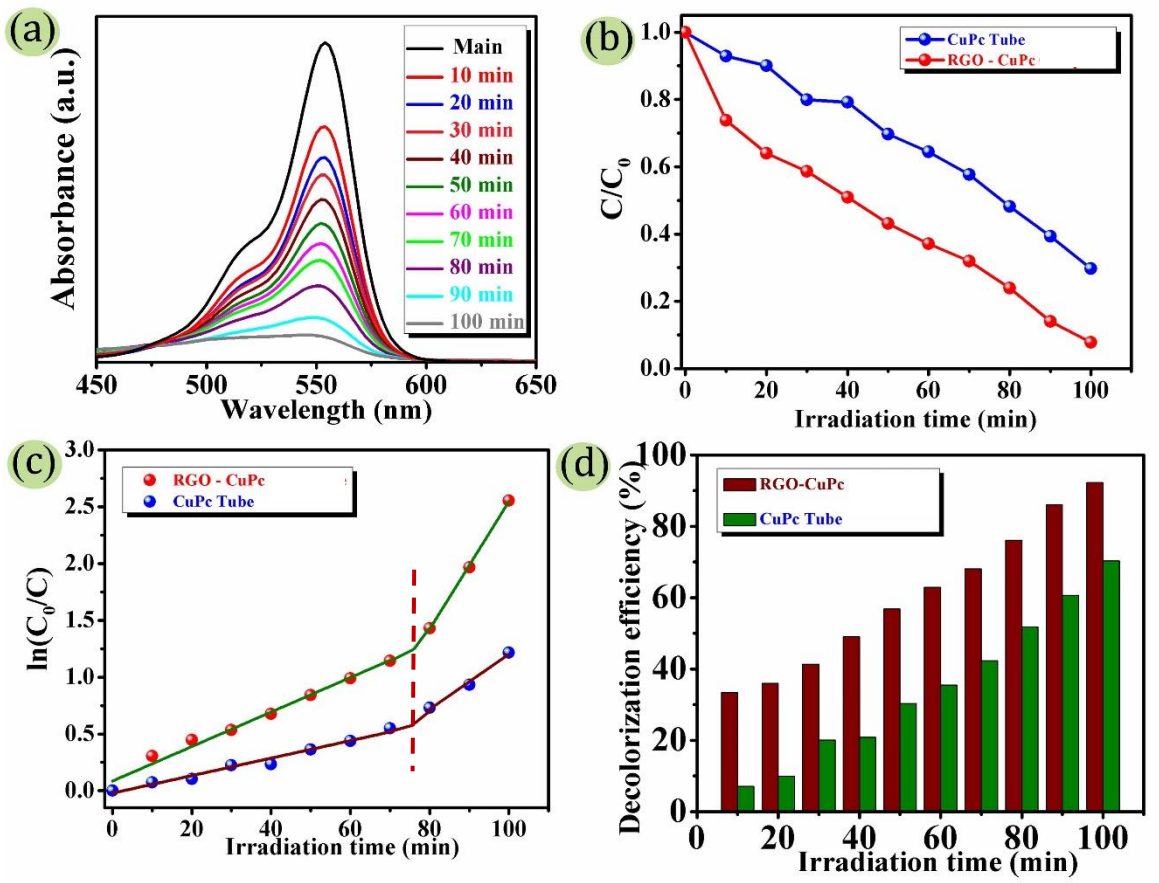

Figure 5.7: *(a) Degradation profile of RB during sonocatalytic process using rGO-CuPc, Comparison of (b) Relative concentration variation, (c) Logarithmic plot with respect to time and (d) Decolorization efficiency for both samples*

For both the samples, the logarithmic decay graph is divided into two decay zones with two distinct *K* values: 1st zone for first 70 *min* and 2nd zone for last 30 *min* [273, 274]. It

is clear from Figure 5.7(c) that the degradation rate is much higher in the 2nd zone compared to that in the 1st zone for both the cases [249]. Different rate constant values for two different samples are given in Table 5.4. From these data, it can be proclaimed that *rGO-CuPc* hybrid exhibits nearly double and even higher rate constants in 1st and 2nd zone compared to those for pristine *CuPc* tube, respectively. In both cases, 2nd zone rate constants are around 3.5 times larger than 1st zone. Variation of decolorization efficiency [calculated from Eq. (5.1)] of *rGO-CuPc* and pure *CuPc* are shown in Figure 5.7(d) with irradiation time. With increase in time, efficiency increases and finally reaches values of 92.22% and 70%, respectively. Here, surrounding *rGO* layers restrict the recombination of electron hole pairs within *CuPc*, thus enhancing its catalytic performance with respect to pristine *CuPc*.

Table 5.4: *Rate constant values for CuPc and rGO-CuPc hybrid*

Sample	Rate Constant ($\times 10^{-2}$) (min^{-1})	
	1st zone (K_1)	2nd zone (K_2)
Pristine *CuPc* Tube	0.7	2.42
rGO-CuPc	1.5	5.62

❖ **Effects of radical Enhancer and Scavenger:**

To explore the role of radical enhancers or scavengers during sonocatalytic removal, *APS* and sodium carbonate (Na_2CO_3) are used respectively. Figure 5.8(a) and 5.8(b) presents the variation of relative concentration and decolorization efficiency, respectively in the presence of enhancer and scavenger along with those of *rGO-CuPc* hybrid. *APS* with 2 *mM* concentration enhances the reaction rate as well as the decolorization efficiency from around 92% to 96% (approx.) of *RB* under similar operating conditions like catalyst dosage, reaction time and ultrasonic power. Due to ultrasound, the addition of peroxydisulfate ($S_2O_8{}^{2-}$) can cause the generation of sulfate radicals ($SO_4{}^{\bullet-}$) which then react with water and form hydroxyl ($OH^{\bullet}$) radicals indicated by Eqs. (5.8 to 5.10) [89].

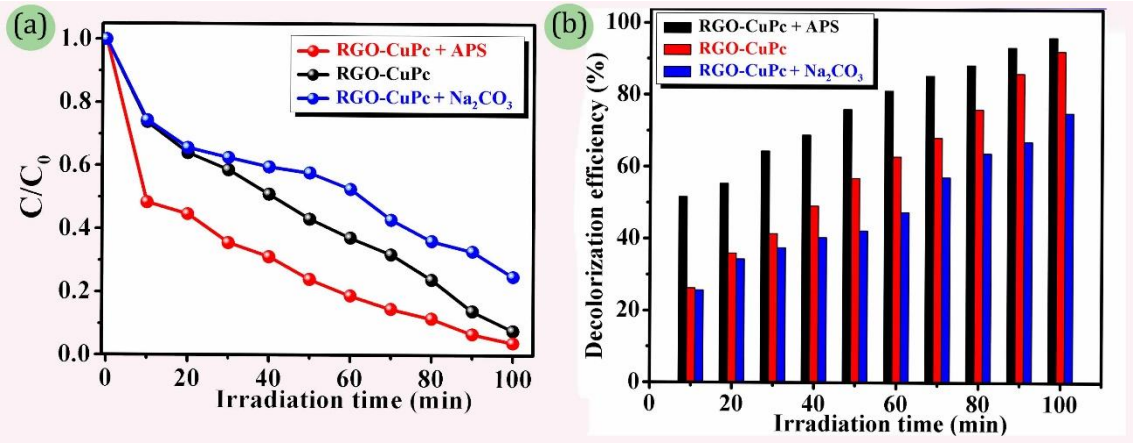

Figure 5.8: *(a) Relative concentration variation and (b) decolorization efficiency with enhancer and scavenger for RB removal*

The contribution of radical scavenger is not only just reduction of the decolorization efficiency, but also proclaiming the free radical ($OH^{\bullet}$) attack as the dominant controlling mechanism of sonocatalytic degradation of organic dye in comparison with pyrolysis alone. The addition of Na_2CO_3 causes the decrease in decolorization efficiency approximately from 92.22% to 75% within 100 *min* reaction time. $OH^{\bullet}$ radicals produced from cavitation bubbles are scavenged by ${CO_3}^{2-}$anion and CO_2 is released in the system. Scavenger can also hamper the cavitation effects leading to decrease in the decolorization efficiency of the pollutant [86]. The plausible reactions [Eqs. (5.18-5.20)] under the presence of radical scavenger are as follows [86]:

$${CO_3}^{2-} + OH^{\bullet} \rightarrow {CO_3}^{\bullet-} + OH^{-} \quad (5.18)$$

$$2{CO_3}^{\bullet-} + H_2O \rightarrow 2CO_2 + {HO_2}^{-} + OH^{-} \quad (5.19)$$

$${HO_2}^{-} + OH^{\bullet} \rightarrow OH^{-} + HO_2 \quad (5.20)$$

❖ **Effects of others parameters:**

There are several other parameters such as dissolved gas, pH etc. that influence the sonocatalytic degradation. The effect of dissolved gases on the degradation efficiency is also investigated using N_2 gas at ultrasonic frequency 20 *kHz*. The highest absorption peak falls under the N_2 atmosphere as shown in Figure 5.9(a). From Figure 5.9(b), it is evident that degradation efficiency is reduced to 66.43 % from 92.22 % in N_2 saturated aqueous solution. During ultrasonic degradation, dissolved oxygen plays the important role to produce $OH^{\bullet}$ radicals which are primarily responsible for dye degradation. Thus, this result also describes the reaction mechanism accurately [5]. Solution pH is also an important parameter that influences the *RB* degradation under ultrasonic vibration. Sonocatalysis has been performed under three different pH values and the resulting decolorization efficiencies are

presented in Table 5.5. Figure 5.9(c) also presents the above results with irradiation time for *rGO-CuPc* sample. In acidic pH, efficiency decreases due to corrosion of the catalyst surface and powerful radical scavenging property of Cl^- ion [89]. In alkaline pH, efficiency reduces to a greater extent due to decrease of oxidation potential of $OH^\bullet$ radical at high pH value. Thus *RB* degradation ability of $OH^\bullet$ radical is lower in alkaline solution than in acidic solution [97].

Table 5.5: *Performance of rGO-CuPc heterostructure under pH variation*

Sample name	pH~1	pH~6	pH~10
rGO-CuPc	77.6%	92.22%	51.00%

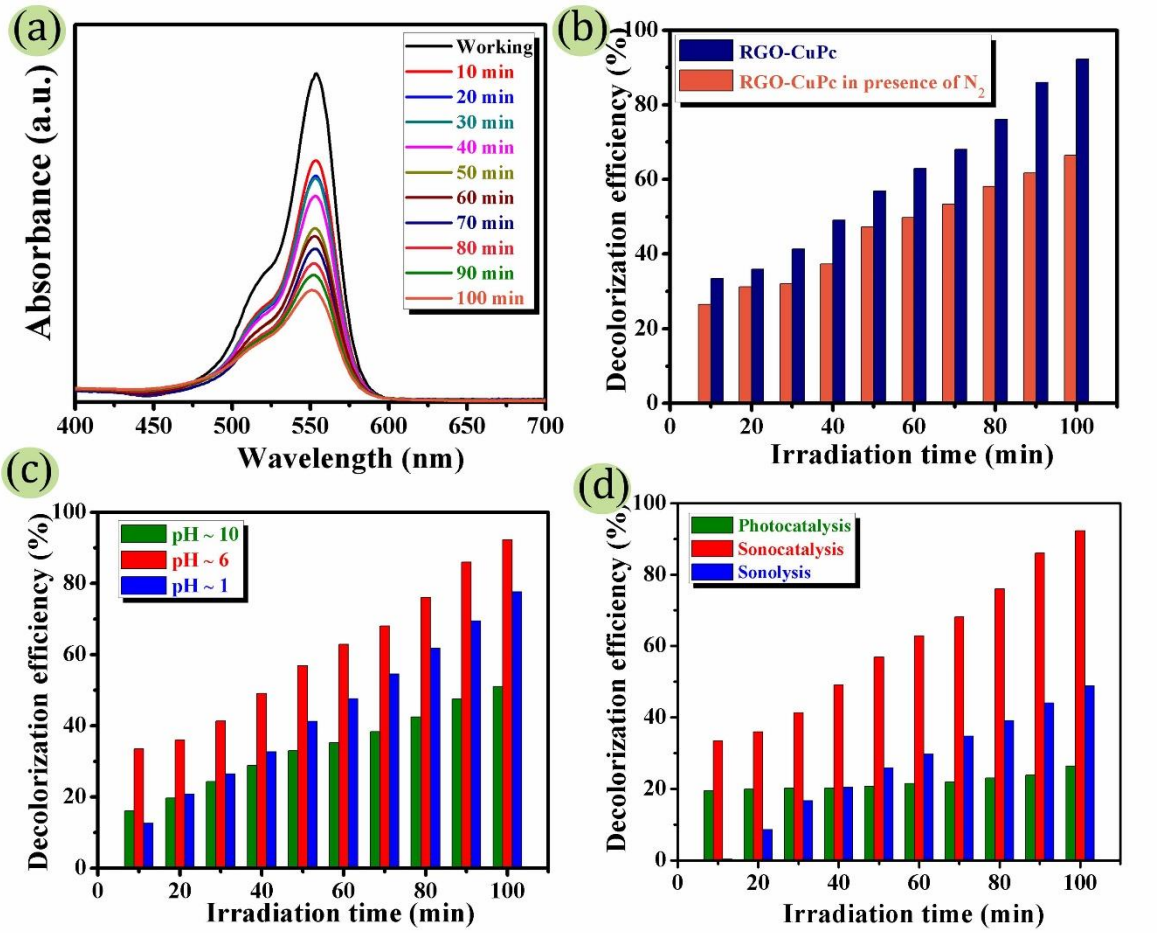

Figure 5.9: *(a) Absorbance spectra of RB under N_2 atmosphere; Effect of (b) dissolved N_2 gas; (c) pH variation on sonocatalytic degradation and (d) Comparison between photocatalysis, sonocatalysis and sonolysis*

To reveal the effectiveness of this process in comparison with conventional photocatalysis and sonolysis (absence of catalyst), we have performed the experiment using visible light and only ultrasonic irradiation keeping all other experimental conditions unaltered. For comparison, degradation efficiencies for these processes are depicted in Figure 5.9(d). By photocatalysis, ~26.35% decolorization efficiency is obtained within 100 *min*, while using

ultrasonication ~92.22% efficiency is achieved. Another difference from conventional photocatalysis is that ultrasound driven catalysis is a quite time efficient removal method, implying within a shorter duration, higher efficiency can be achieved. From point of view of degradation efficiency, sonocatalysis that does not involve any external light source comes out as the most powerful technique. The sonolysis process, without catalyst, is also carried out and found to degrade ~ 48% *RB* due to generation of $OH^{\bullet}$ radicals through cavitation process.

❖ Proposed Pathway for sonocatalytic degradation:

Due to the effect of sonoluminescence, a broad spectrum of visible light is emitted. *CuPc* is excited by visible light and creates sonogenerated electron-hole pairs [Eq. (5.11)]. The excited electrons in the LUMO level of *CuPc* are transferred to the *rGO* sheets [Eq. (5.21)]. The electron transfer rate is guided by thermal radiation generated from the collapse of cavitation bubbles. The trapped electrons get readily transferred into oxygen molecules to produce superoxide ($O_2{}^{\bullet-}$) radical ions [Eq. (5.22)]. The electron-hole pairs may recombine or react with water molecules. But introduction of *rGO* sheets reduces the chances of recombination of electron-hole pairs [275]. The $OH^{\bullet}$ radicals formed by both sonolysis and catalysis, directly decompose the dye molecules into the end products following Eq. [(5.13-5.17)]. The complete reaction pathway of sonocatalytic degradation is depicted in Figure 5.10.

$$^{3}CuPc^{*} + RGO \rightarrow CuPc^{\bullet+} + RGO(e^{-}) \quad (5.21)$$

$$RGO(e^{-}) + O_2 \rightarrow RGO + O_2{}^{\bullet-} \quad (5.22)$$

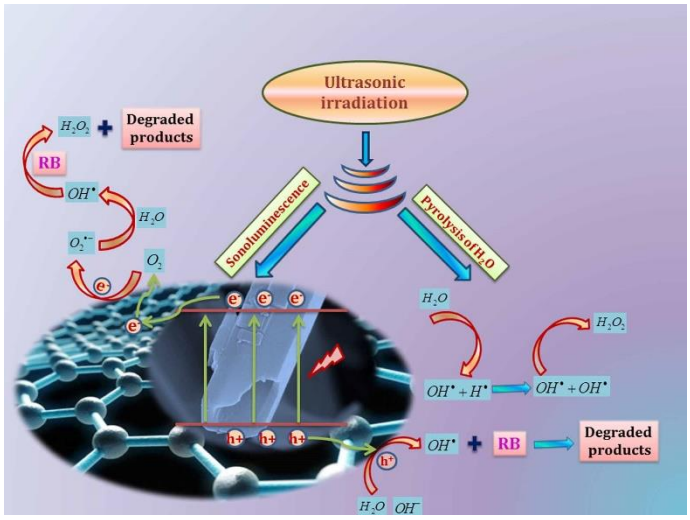

Figure 5.10: *Schematic representation of proposed reaction mechanism*

In the sonocatalysis reaction, electron transfer resistance and separation efficiency of sonogenerated charge carriers (electrons and holes) are the most crucial factors to yield the

improved charge separation, EIS measurement of pristine *CuPc* tube and *rGO-CuPc* hybrid is performed. Their experimental and fitted Nyquist plots are shown in Figure 5.11(a). Electron transfer resistance can be determined from the semicircular arc radius of EIS spectra in high frequency region. In general, the small radius of the arc indicates low electron transfer resistance [276]. In this case, *rGO-CuPc* catalyst shows prominent depressed semicircle in high frequency region as compared to pristine *CuPc* tube. To determine the exact value of charge transfer resistance (R_{ct}), both EIS spectra are fitted by Randles circuit which is shown in Figure 5.11(b). The value of R_{ct} is found as 177 *Ω* and 47.7 *Ω* for *CuPc* tube and *rGO-CuPc*, respectively. The lowest electron transfer resistance can be ascribed to introduction of *rGO* nanosheets with *CuPc* tubes to form intimate interfacial contact with each other that can enhance the interfacial charge transfer process leading to further improvement of the catalytic activity [277].

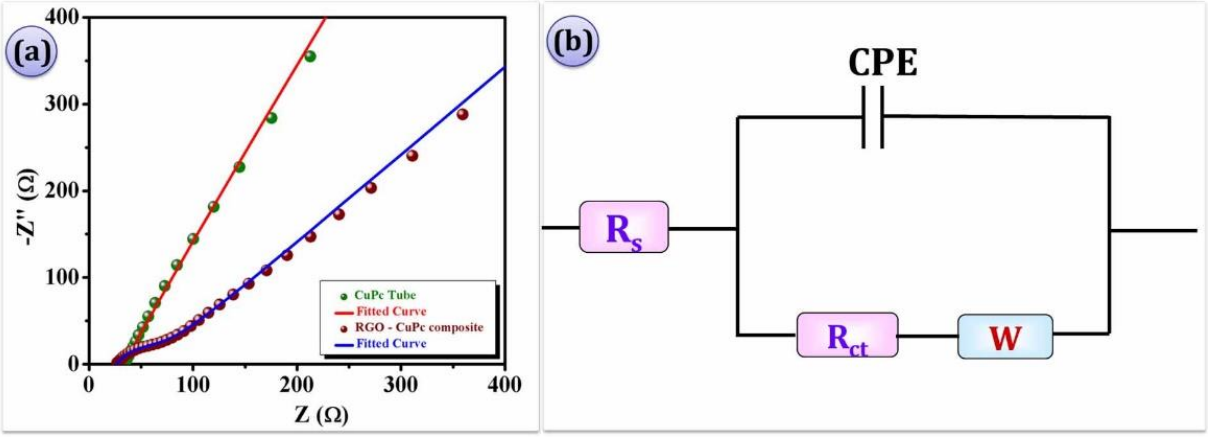

Figure 5.11: *(a) EIS measurement of CuPc tube and rGO-CuPc; (b) Equivalent circuit*

The improved catalytic performance has a good agreement with wettability. From the contact angle measurement, enhanced wettability of *CuPc* is observed caused by the wrapping with *rGO* sheet. Surface of *CuPc* nanotube is hydrophobic in nature and exhibits water contact angle of 140° with significant stability upto 500*s* [Figure 5.12(a)]. After *rGO* modifications, the sample exhibits an initial contact angle of 90°, followed by rapid fall of water droplet is observed within 140 s [Figure 5.12(b)]. Thus, hydrophilic nature is incorporated in *CuPc* tube by wrapping with *rGO* sheets, which enhance the charge transfer mechanism and thereby, sonocatalytic dye degradation.

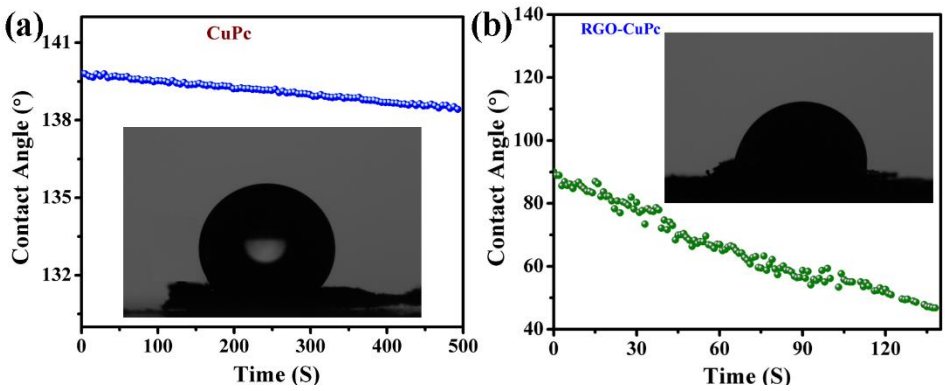

Figure 5.12: *Contact angle of (a) CuPc and (b) rGO-CuPc with stability*

Morphology retention after sonocatalysis with advanced probe sonicator is an important issue. To perform this, samples are collected after catalysis through vacuum filtration and repeatedly washed by ethanol and D.I water. Next, the samples are dried at 60°C for 2 *h*. After that, morphology of the *rGO-CuPc* is observed by FESEM; the corresponding images are shown in Figure 5.13. The figure reveals the presence of more or less similar kind of *rGO* enveloped *CuPc* tube-like structures. Such degradation in morphology is absent after sonocatalytic treatment of 100 *min*.

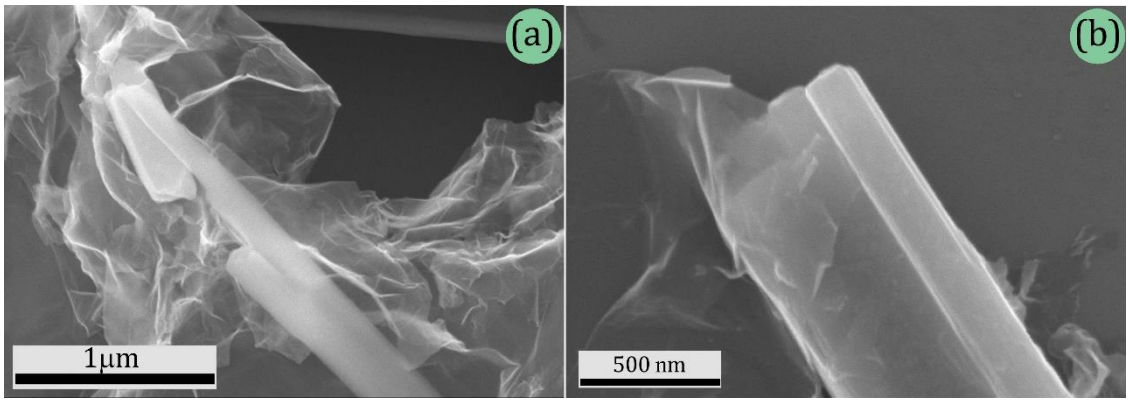

Figure 5.13: *Morphology of rGO-CuPc with (a) low and (b) high magnifications after 100 min sonocatalysis*

5.4 Conclusions:

In brief, sonophotocatalytic *RB* dye degradation has been explored under the presence of *CuPc* nanowires. To investigate the synergistic effect of sonophotocatalytic process, a comparative study of individual processes has been made and *RB* decolorization efficiency as high as ~81% within 60 *min* of irradiation time has been reported. The effects of initial dye concentration, catalyst dosage and other factors on degradation efficiency have also been probed to establish the optimum operating conditions. The plausible synergy mechanism of sonophotocatalysis has been explained. In order to improve the *RB* removal efficiency, *rGO-*

CuPc heterostructure has been employed as sonocatalyst. Comparative study has also been carried out to find out the role of *rGO* in the hybrid system with respect to the pristine material, and maximum ~ 92.22 % *RB* decolorization has been achieved within 100 *min* of irradiation time. Influences of the enhancer, radical scavenger, pH and dissolved gas on the degradation efficiency have been investigated. Studies reported in the present chapter have led the final choice of *rGO-CuPc* hybrid as an efficient sonocatalyst and *CuPc* nanowire as sonophotocatalyst for wastewater treatment.

6.1 Introduction:

In response to changing environmental conditions, energy has become a primary focus of the scientific community. Thus, development of some emerging materials as well as technology is of prime focus for energy storage and conversion. The rapidly growing field of flexible and wearable electronic devices causes a crying need for high-performance lightweight energy storage devices. SC is one of such attractive energy storage devices. In this chapter, supercapacitive properties of unsubstituted *ZnPc* and *CuPc* will be examined in alkaline media. To meet the increasing energy demands, renewable energy conversion systems like fuel cells play a major role. To overcome the shortcomings of noble metal based electrocatalysts as stated in Chapter 2 [section 2.3.2.2], it is very urgent to invent some noble metal free efficient ORR electrocatalysts as alternatives to *Pt*. Here, the applicability of *CuPc* hybrids with *rGO* and MoS_2 will be explored in ORR applications due to their various exciting inherent properties, low cost and abundant supply.

6.2 Storage: Electrochemical Supercapacitor

6.2.1 *CuPc* nanowires:

Electrochemical measurements are carried out in 1*M NaOH* solution in three electrode configurations. CV graph is recorded in the potential window 0 to 0.6 *V* vs. *Ag/AgCl*. The influence of varying scan rates (5 – 100 mVs^{-1}) on voltammetric current responses is shown in Figure 6.1(a). The CV nature of *CuPc* nanowires predominantly comprises faradaic redox peaks positioned at 0.4 *V* and 0.2 *V* in *NaOH* electrolyte at a low scan rate of 5 *mV/s*. *CuPc* molecules contain pyrrolic nitrogen atoms having strong electron donating properties [278]. Such pyrrolic groups help to improve both the pseudocapacitive behavior and specific capacitance. The specific capacitance can be evaluated by using the following formula [279]:

$$C = \frac{\int_{V_1}^{V_2} JdV}{\nu(V_2 - V_1)} \quad (F/g) \tag{6.1}$$

where, J is current density (A/g), ν is scan rate (Vs^{-1}) and $(V_2 - V_1)$ is the potential window (V). The estimated capacitance value from the CV graph with respect to varying scan rates is presented in Figure 6.1(b). The values of specific capacitance are 406, 286, 196, 109 and 66 *F/g* at the scan rate of 5, 10, 20, 50 and 100 mVs^{-1} respectively. It is found that the value of specific capacitance reduces at higher scan rates [280]. This can be ascribed to the diffusion limit of ions present in the electrolyte solution. In case of low scan rates, the electrolyte ions

are allowed to access maximum surface area of electrode material over longer diffusion times. This indicates improvement in ion storage capability of material as well as specific capacitance values. Similarly, high scan rates provide shorter diffusion times reducing the chance of interaction of the ions with the electrode material surface.

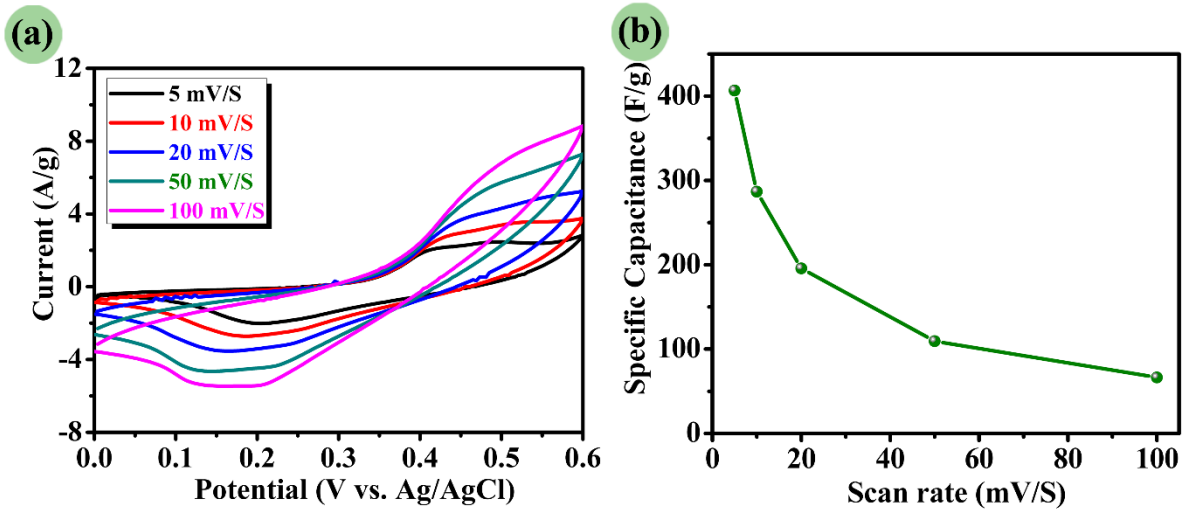

Figure 6.1: *Electrochemical properties of CuPc nanowires: (a) CV graph and (b) Specific capacitance at various scan rates*

To obtain deeper insight, GCD profile is recorded at different values of current density in the potential window 0 – 0.5 *V* vs. *Ag/AgCl*, and is shown in Figure 6.2(a). The specific capacitance can be estimated using the following formula [281] as:

$$C = \frac{I\Delta t}{m\Delta V} \quad \text{(F/g)} \tag{6.2}$$

where, I is discharging current (A), Δt is discharging time (Sec), m is mass (g) and ΔV the potential window (V). The capacitance value obtained for 0.3 *A/g* is 260 *F/g* and the specific capacitance gradually decreases with increase in current density, as evident in Figure 6.2(b).

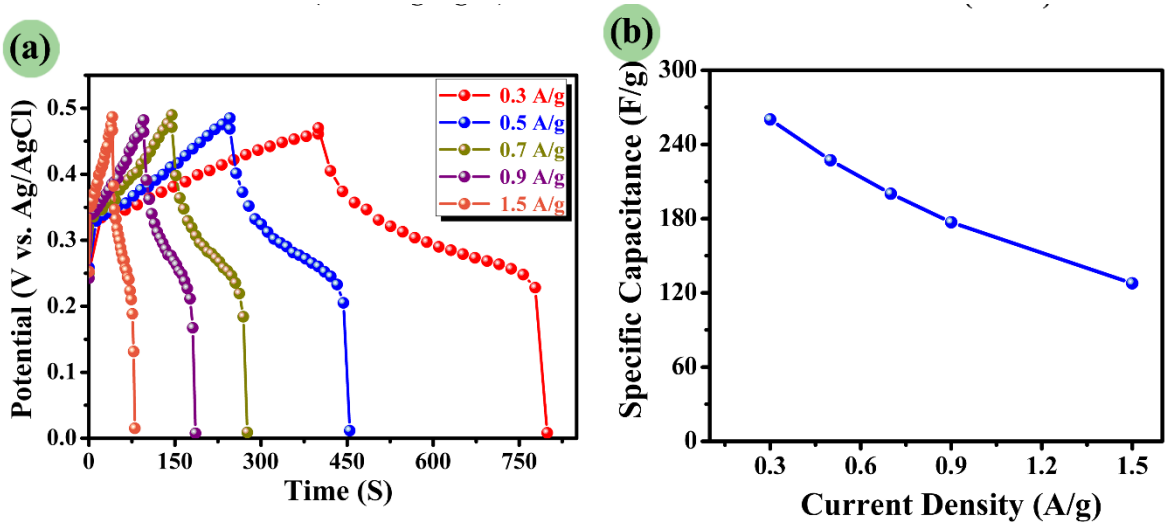

Figure 6.2: *Electrochemical properties of CuPc nanowires:(a) Charge Discharge profile and (b) Specific capacitance at different current densities*

Similar to low scan rate, low current density also provides longer time to the electrolyte ions to acquire more active sites on the surface of the electrode material. As a result, specific capacitance is enhanced. Similarly, electrolyte ions get less time to access the surface-active sites on the electrode at high current density that results in low specific capacitance.

EIS measurement is performed to gain deeper insights into the charge transfer mechanism that takes place at the electrode/electrolyte interface. Nyquist plot consists of the real component (X- axis) and the imaginary component (Y-axis). The real part provides the information associated with the ohmic property, whereas the imaginary part shows capacitive behavior of the electrode material. In our case, electrolyte is water with ionic salts e.g. *NaOH* that behaves as ionic liquid. The migration of ions determines the current in the aqueous bulk solution, where the resistance to ionic migration is denoted by the term "solution resistance" (R_S). In three electrode system, R_s is the uncompensated solution resistance between the working and reference electrodes. There is a transition between electronic and ionic conduction at the electrode-electrolyte interface. Across the solution/electrode interface of each electrode, the electric charge transfer process is guided by an electrochemical reaction (electrolysis) [282]. Electrochemical discharge of the species is determined by their electrochemical polarizability, i.e. their ability to liberate or acquire an electron at electrochemical potential. Immediately adjacent to the electrode, the impedance generated by the discharge processes occurring in "Helmholtz" interfacial layer of the sample are represented by "charge transfer" resistance R_{ct}. In this study, conventional double-layer capacitor, C_{dl} do not behave ideally due to the distribution of currents and electroactive species. Instead, these capacitors behave as a constant phase element (CPE) offering a reactance defined as follows [283]:

$$Z_{CPE} = \frac{1}{Y_0 (\mathrm{j}\omega)^n} \tag{6.3}$$

where, Y_0 is assumed to be pure capacitor (C) and the value of the exponent *n* is equal to 1 in ideal case. For CPE, the value of *n* should be less than 1.

In the Nyquist plot shown in Figure 6.2(a), a depressed semicircle is observed at high frequency region that corresponds to a parallel combination of resistance and capacitance. The intercept of that semicircle on the X-axis denotes the series resistance (R_S). An electrical equivalent circuit is used to fit the experimentally observed Nyquist plot as shown in the inset of Figure 6.3(a).

For *CuPc* nanowires, R_S is obtained as 1.67 Ω from fitted data and 1.78 Ω from experimental data. It indicates that the circuit fitting is appropriate here. The diameter of the

semicircle denotes the charge transfer resistance (R_{ct}). The value of R_{ct} is found as 14 Ω. Both the *n* values associated with CPEs are fractional and approach to 1.

According to the enlarged illustration of the semicircle shown in the inset of Figure 6.3(a), it is found that the semicircle is not proper, rather depressed to some extent. Cole - Cole distribution function is expressed as follows [284],

$$F(\tau) = \frac{1}{2\pi}[sin(\alpha\pi)/(cosh(1-\alpha)s - cos(\alpha\pi))] \quad (6.4)$$

where, $s = ln(\tau/\tau_0)$, τ is the relaxation time and τ_0 is the relaxation time where $F(\tau)$ attains its peak value. The value of α (radian) can be determined from the angle between the real axis and the radius of the semicircular arc. When α=0, this relation denotes Debye relaxation (proper semicircle), and for 0 < α <1, non - Debye type relaxation (depressed semicircle) [285]. In this case, the estimated value of α is 0.317 suggesting that the fitted values of R_s and R_{ct} are based on Cole-Cole distribution.

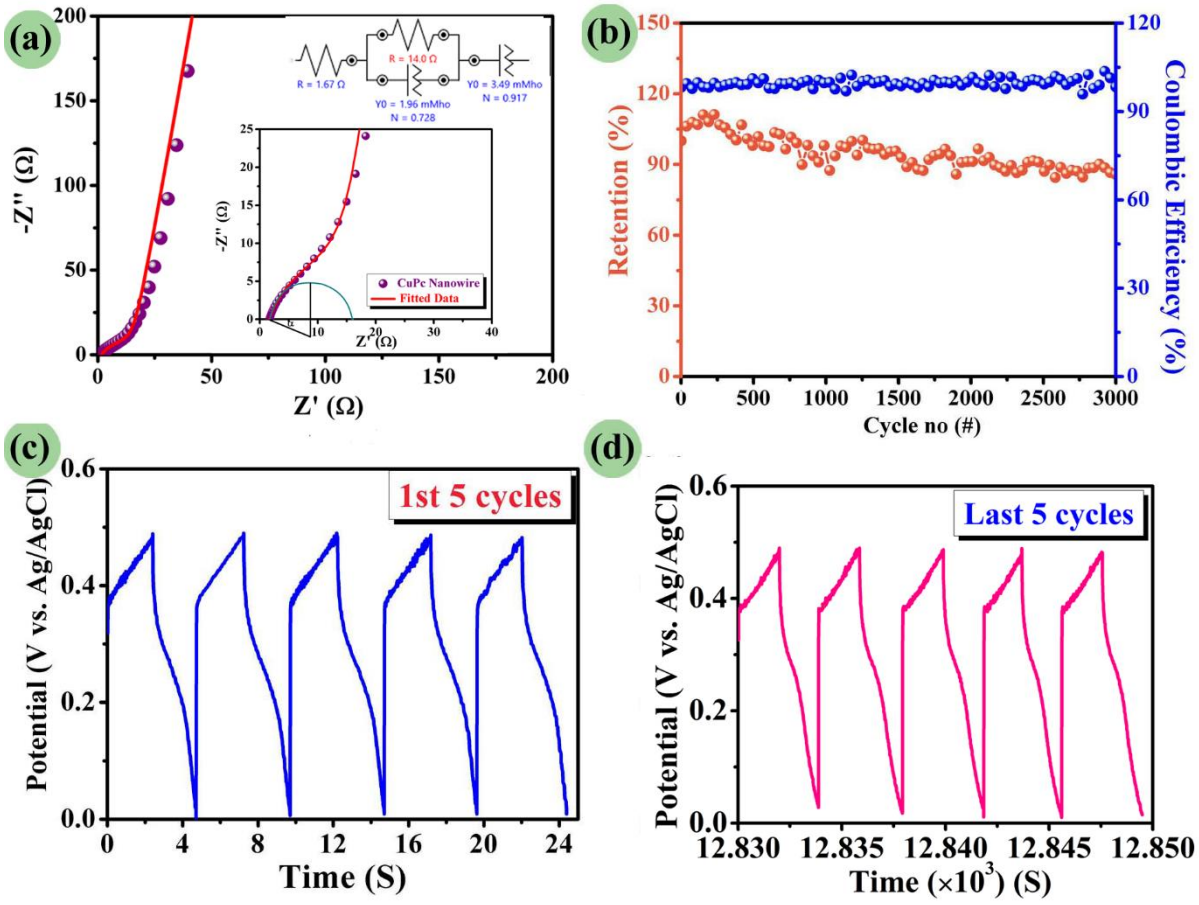

Figure 6.3: *CuPc nanowires: (a) Nyquist plot and fitted circuit (Inset); (b) Capacitance retention and Coulombic efficiency; (c) first and (d) last 5 cycles among 3000 cycles*

There are two important parameters namely stability and coulombic efficiency that describe the long time stability of the material. Coulombic efficiency (η) is defined as [283]:

$$\eta = \frac{t_d}{t_c} \times 100\% \tag{6.5}$$

where, t_d and t_c are the discharging and charging time, respectively. Here, stability of our electrode is measured at 6 *A/g* by running 3000 charge - discharge cycles continuously, which is reflected from Figure 6.3(b). Almost 99% efficiency and only 15% capacitance loss with respect to the initial value are observed. The slight increasing trend in the specific capacitance is noted in the first 250 cycles. It can be attributed to the activation process and wettability of the surface of electrode material in the electrolyte [286, 287]. Beyond that, the depreciation of capacitance retention is observed due to slight detachment of active material into the electrolyte after long cycle of charge - discharge operation [288]. Among 3000 cycles, the first and the last 5 cycles are presented in Figure 6.3(c) and 6.3(d), respectively, indicating that the pseudocapacitive nature of the charge-discharge curve is preserved. Finally, reusability of any material demands the retention of nanostructure after such long cycling operation. Therefore, morphological study is repeated for electrode sample after 3000 cycles. FESEM images of *CuPc* nanowires are shown in Figure 6.4, proclaiming that almost wire-like morphology is preserved.

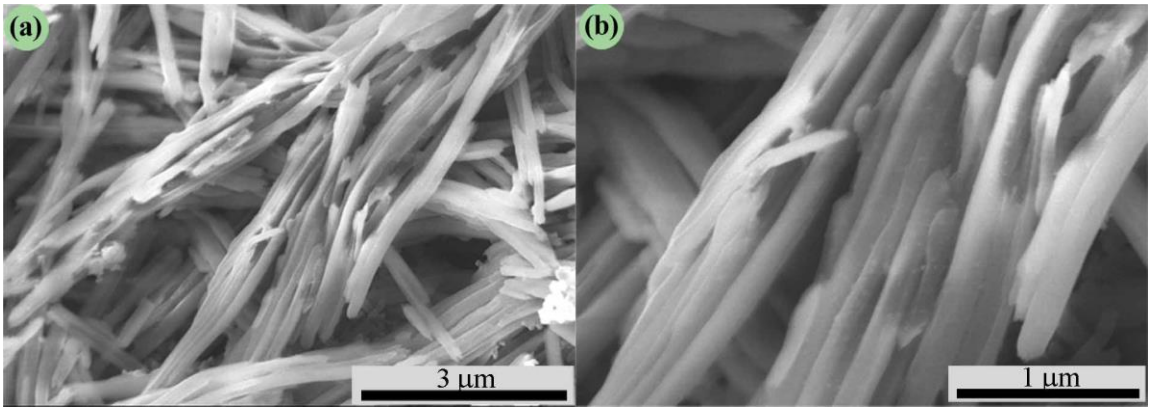

Figure 6.4: *CuPc nanowires in two different magnifications: scale bar of (a) 3 µm and (b) 1 µm after 3000 charge discharge cycles*

6.2.2 ZnPc nanoflakes:

To evaluate the electrochemical properties of *ZnPc* nanoflakes, CV and GCD measurements are carried out in a three-electrode cell. Figure 6.5(a) shows the typical CV curves of *ZnPc* electrode at different scan rates in 1*M* aqueous *LiOH* electrolyte. The values of

areal capacitance are calculated using Eq. (6.1) where J is taken as mA/cm^2. A decreasing trend in capacitance with increasing scan rates are observed in Figure 6.5(b).

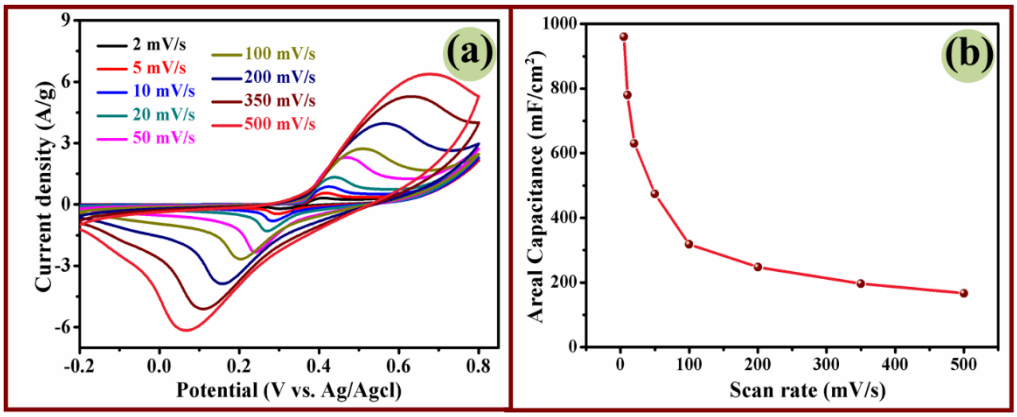

Figure 6.5: *Electrochemical performances of ZnPc flakes:(a) CV graph and (b) Specific capacitance at various scan rates*

To further determine the electrochemical performances, GCD measurements are also done at constant current density and are shown in Figure 6.6(a). The electrode exhibits areal capacitance of 486.4 mF/cm^2 at current density 2.4 mA/cm^2 [Figure 6.6(b)].

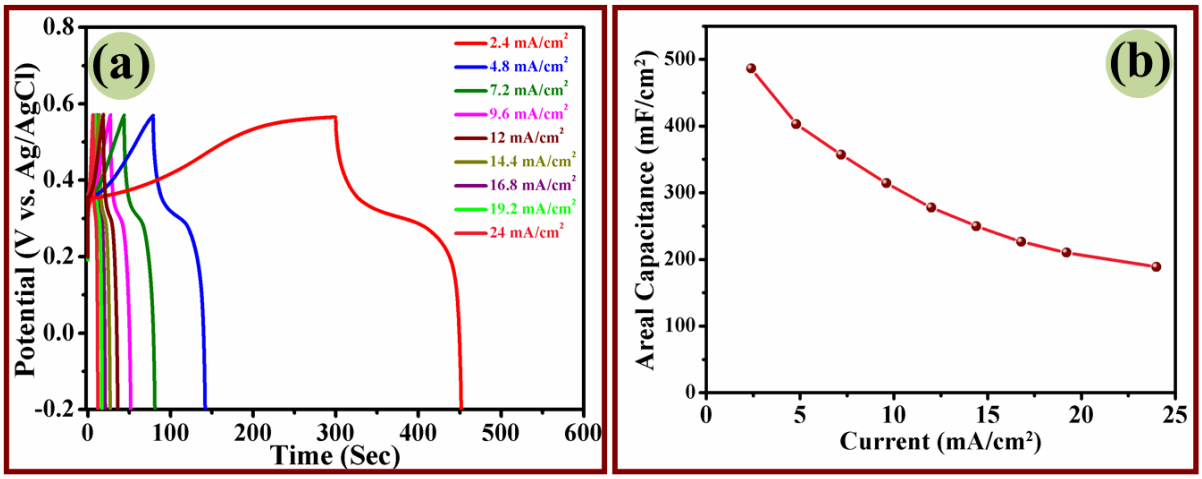

Figure 6.6: *Electrochemical performances of ZnPc flakes: (a) Charge Discharge profile and (b) Specific capacitance at different current densities*

Some important parameters need to be investigated for practical applications of supercapacitor. The long-term cycling stability is one of them. Cycling stability of *ZnPc* electrodes are investigated by continuous measurements of GCD over 2000 cycles at a current density of 72 mA/cm^2 within the same potential range. The first and last five cycles are shown in Figure 6.7(a). It can be seen that, charge discharge curve of the last five cycles retains their original form that represents the long-term cycle stability. After 2000 cycles, electrode shows a slight decrease in capacitance that clearly indicates good capacitance retention. The variation

of specific capacitance retention and coulombic efficiency as a function of cycle number are presented in Figure 6.7(b). Initially, the specific capacitance increases due to slow penetration of liquid electrolyte into the active material of *ZnPc* electrode. After that, slightly decreasing nature is observed with the increase in the cycle number and finally 95.13% retention is achieved. Coulombic efficiency is calculated by using Eq. (6.5) and 98.99% efficiency is achieved after 2000 cycles.

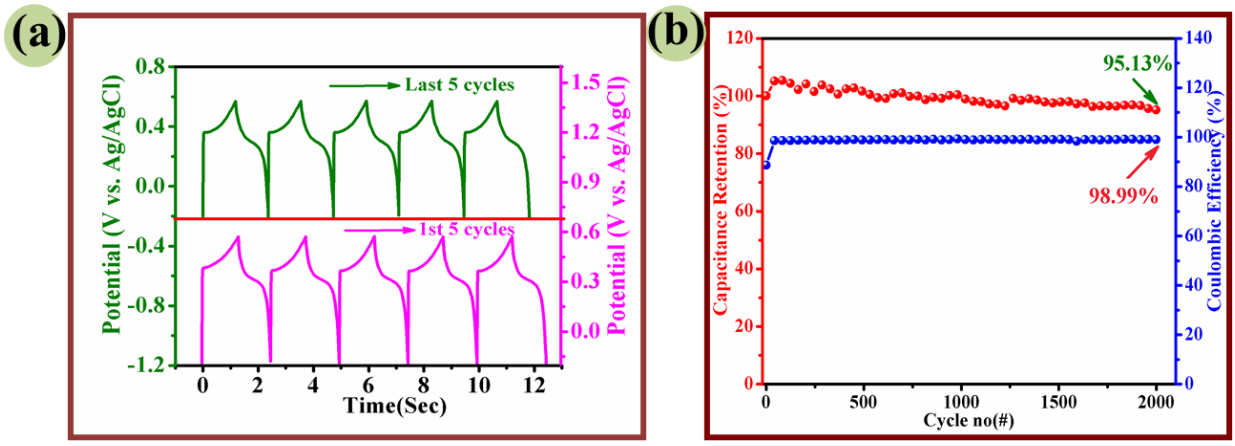

Figure 6.7: *(a) First 5 and last 5 charge discharge cycles and (b) Coulombic efficiency and retention after 2000 cycles*

6.3 Conversion: Electrochemical oxygen reduction reaction

6.3.1 *rGO-CuPc* hybrid:

In order to investigate the ORR activity, CV and LSV measurements of pristine *CuPc* nanotube and *rGO-CuPc* hybrid are carried out in O_2 saturated 0.1 M *KOH* solution. As evident from LSVs presented in Figure 6.8(a), 6.8(b) and 6.8(c), the magnitude of current density (j_{ORR}) increases with increasing rotation speed ranging from 225 *rpm* to 1600 *rpm*. Associated parameters of ORR process for all samples are presented in Table 6.1. Notably, ~1.5 fold and ~1.3 fold enhancement in j_{ORR} at 1600 *rpm* is observed for *rGO-CuPc* hybrid material compared to pristine *CuPc* and *rGO*, respectively. The onset potential value remains unaffected for all rotation speeds in every catalyst.

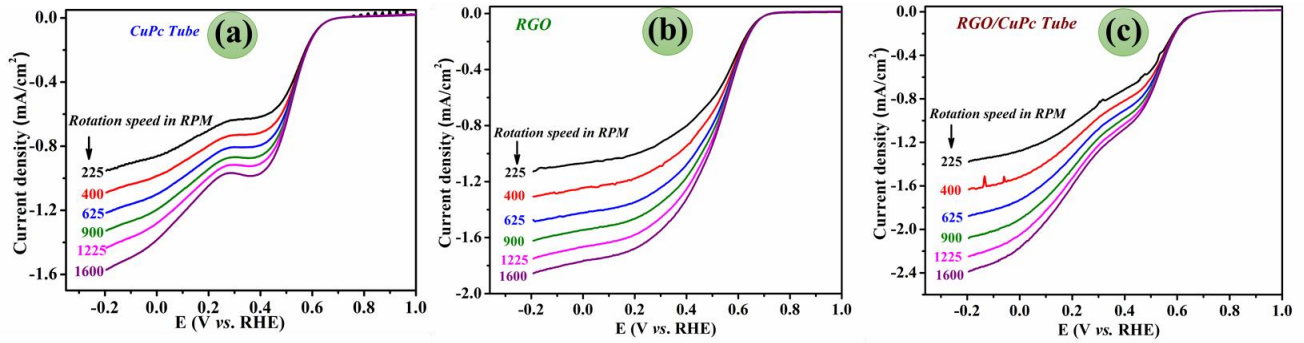

Figure 6.8: *RDE current responses for (a) CuPc, (b) rGO and (c) rGO-CuPc*

Table 6.1: *Kinetic parameters for ORR process. All potentials are measured in RHE.*

Electrocatalyst	E_{ORR} (*V*)	E_{Onset} (*V*)	j_{ORR} (*mA/cm²*)	n	Tafel Slopes (*mV/dec*)
CuPc tube	0.50	0.69	-1.57	2.7	82
rGO	0.56	0.71	-1.85	2.93	81
rGO-CuPc	0.58	0.72	-2.39	3.5	78

Moreover, as shown in Figure 6.9(a), 6.9(b) and 6.9(c), the *Koutecky–Levich (K-L)* plots are linear and almost parallel in nature for various electrode potentials, suggesting a first order reaction kinetics. The typical *K-L* equation [Eq.(6.7)] is given as [152]:

$$\frac{1}{J} = \frac{1}{J_K} + \frac{1}{J_L} \tag{6.6}$$

$$\frac{1}{J} = \frac{1}{J_K} + \frac{1}{B\omega^{1/2}} \tag{6.7}$$

with $B = 0.21\, nFD^{2/3}\nu^{-1/6}C_{O_2}$ and $J_K = nFKC_{O_2}$.

In Eqs.[6.6, 6.7], J, J_K *and* J_L represent the measured, kinetic and diffusion - limiting current densities, respectively; *n* represents the number of electrons transferred per oxygen molecule, F is the Faraday constant (F = 96485 $C\ mol^{-1}$), D is the diffusion coefficient of O_2 in 0.1 *M KOH* ($1.9 \times 10^{-5}\ cm^2/s$), ν is the kinematic viscosity of the electrolyte (0.01 cm^2/s), and C_{O_2} is the bulk concentration of O_2 ($1.2 \times 10^{-6}\ mol/cm^3$). In this case, as the rotation speed is in *rpm*, the constant factor 0.21 is used.

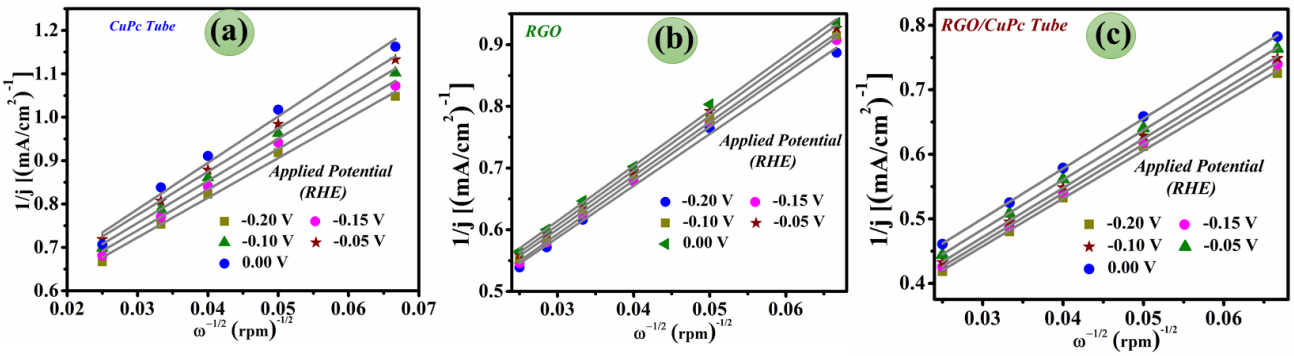

Figure 6.9: *K-L plots of (a) CuPc, (b) rGO and (c) rGO-CuPc at various potentials*

The number of electron transfer, calculated from the slope of the curves, is found to be ~2.7, 3.0 and 3.5 for pristine *CuPc* tube, *rGO* and *rGO-CuPc* hybrid, respectively, as presented in Figure 6.10(a). The CV graph of all samples in O_2 saturated electrolyte is shown in Figure 6.10(b). As evident from the figure, *rGO-CuPc* hybrid exhibits a positive shift (~80

mV) in cathodic ORR peak (E_{ORR}) compared to pure *CuPc* in O_2 saturated solution. CV of hybrid system is also carried out in N_2 saturated solution and shown in Figure 6.10(b) that clearly confirms the absence of oxygen reduction peak. Tafel plots in Figure 6.10(c) of the as-synthesized catalysts exhibit smaller slope for *rGO-CuPc* than their individual counterparts (*CuPc* and *rGO*), that indicates the improved activity of the hybrid. The superiority in catalytic activity for *rGO-CuPc* hybrid is ascribed to the synergistic effect between them as well as high conductivity of graphene. Being a supplementary electron provider, *rGO* helps to enhance the sluggish kinetics of ORR. In addition, *rGO* acts as a peroxide cleaner to remove the intermediate peroxide accumulated on the surface of the cathode catalyst, leading to the improved ORR activity of hybrid material.

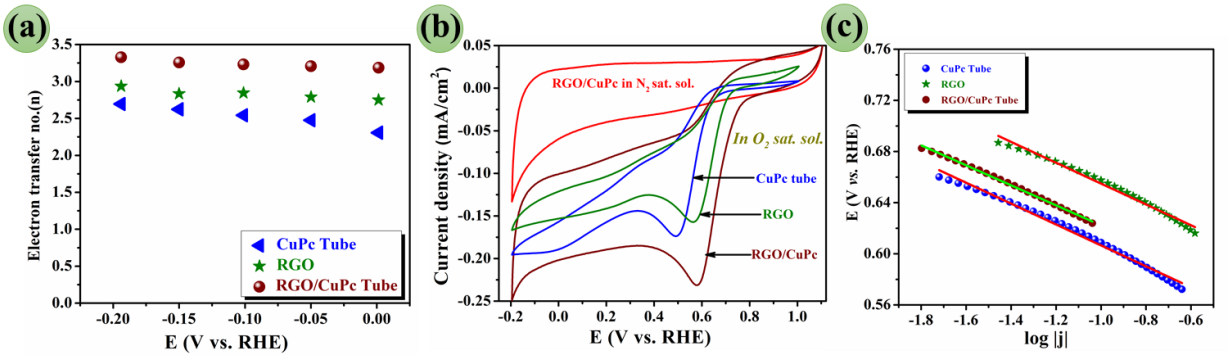

Figure 6.10: *(a) Electron transfer number at different potentials, comparison of (b) CV graph and (c)Tafel plots of three samples*

6.3.2 *MoS_2-CuPc* hybrid:

In order to evaluate the ORR activity of *MoS_2-CuPc* as electrocatalyst, LSV measurement is performed in O_2 saturated 0.1*M KOH* solution in the potential window -0.1 *V* to 0.9 *V* vs. RHE at 10 mVs^{-1} scan rate. Rotational speed is varied from 400 to 2500 *rpm* for each case. Figure 6.11(a), 6.11(b) and 6.11(c) depict the polarization curves for *CuPc*, *MoS_2* and *MoS_2-CuPc* samples, respectively with varying rotational speed. For each samples, magnitude of limiting current density increases with the increasing rotation speed due to the reduction of diffusion length. The K-L plots ($1/j$ *vs* $\omega^{-1/2}$) at different potentials are shown in Figure 6.11(c), 6.11(d) and 6.11(e) for *CuPc*, *MoS_2* and *MoS_2-CuPc* samples, respectively. Slopes of linearly fitted K-L plots at various potentials are used to calculate the number of electron transfer (n) [Eq.(6.7)] as shown in Figure 6.12(a). Pristine *CuPc* and *MoS_2* can reduce the O_2 partially via two electron transfer pathway, whereas *MoS_2-CuPc* can efficiently reduce O_2 by following four electron pathway. Similar observation is found in previous reports for pristine *MoS_2* [64].

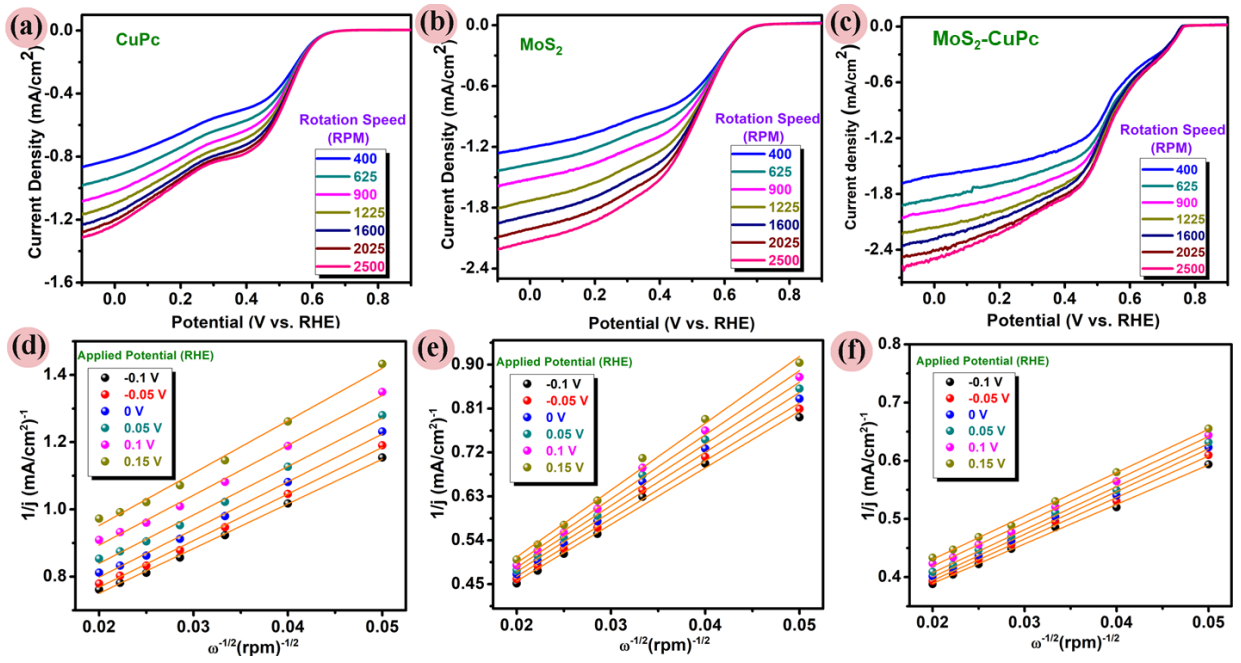

Figure 6.11: *RDE current responses for (a) CuPc, (b) MoS_2 and (c) MoS_2-CuPc at different rpm; corresponding K-L plots of (d) CuPc, (e) MoS_2 and (f) MoS_2-CuPc at varying potential*

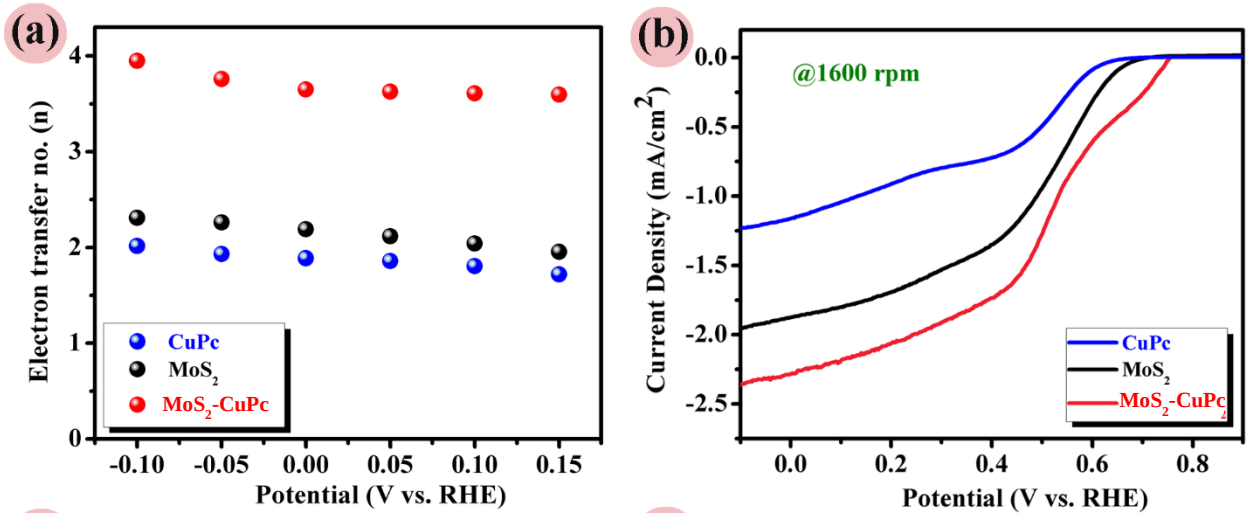

Figure 6.12: *(a) Electron transfer no. at different potential and (b) comparison of LSV at 1600 rpm.*

Comparative LSV at 1600 *rpm* for all samples are shown in Figure 6.12(b). Several important parameters, as listed in Table 6.2, are extracted from LSV that, in turn, help to investigate the electrocatalytic activity of catalysts towards ORR. Among them, E_{onset} remains constant for every rotational speed in each case. It is evident from Table 6.2 that for *MoS_2-CuPc*, E_{onset} is higher than those for pristine *MoS_2* and *CuPc*, respectively by 40 *mV* and 90 *mV*. Again, $E_{1/2}$ determines the electroactivity of material, and for *MoS_2-CuPc*, the value of $E_{1/2}$ is larger by 50 *mV* and 20 *mV* compared to those for *CuPc* and *MoS_2* respectively. Large $E_{1/2}$ indicates the superior ORR kinetics of *MoS_2-CuPc*.

Table 6.2: *Kinetic parameters for ORR process. All potentials are in RHE scale*

Catalyst	E_{onset} (*V*)	E_{orr} (*V*)	$E_{1/2}$ (*V*)	j_{orr} (mA/cm^2)	n (@ -0.1*V*)
CuPc	0.66	0.52	0.46	-1.23	2.0
MoS_2	0.71	0.57	0.49	-1.96	2.3
MoS_2-CuPc	0.75	0.59	0.51	-2.36	3.9

CV measurements are recorded at 10 mVs^{-1} in O_2 saturated 0.1 *M KOH* solution and shown in Figure 6.13(a). A pronounced cathodic peak corresponds to E_{orr} is observed in the CV graph for all cases; such values of E_{orr} are listed in Table 6.2. Prominent positive shifts in all potentials demonstrate remarkably enhanced ORR performance of hybrid nanostructures. The limiting current density (j_{orr}) at 1600 *rpm* for *MoS_2-CuPc* is found to be -2.36 mA/cm^2, which is higher than those in respective counterparts. The long-term stable operation is an important issue for catalytic application. Here, durability test is performed through chronoamperometric response of *MoS_2-CuPc* catalyst for 8000 *s* at 0.6 *V* vs. RHE. For comparison, standard *Pt/C* is also examined under similar operating conditions as presented in Figure 6.13(b). This *MoS_2-CuPc* reveals very slight reduction in current by around 2.4 % after 8000 s, whereas 12.6 % decay is observed for *Pt/C* with respect to initial current. Such stable operation is ascribed to highly crystalline nature [as observed in XRD pattern] that may be beneficial for the structural stability.

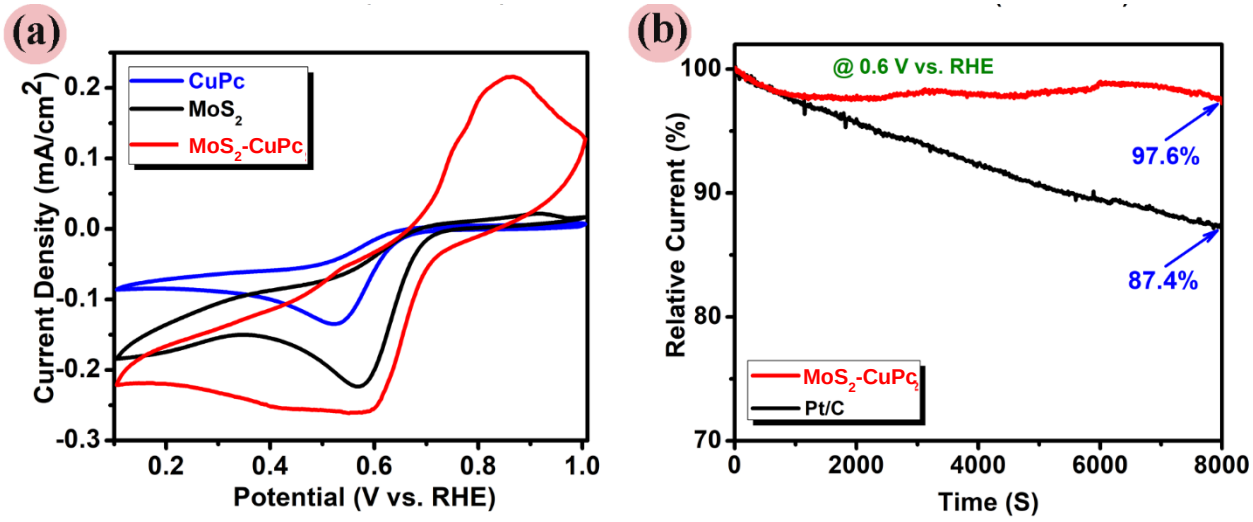

Figure 6.13: *(a) CV graph of three samples and (b) chronoamperometric stability of MoS_2-CuPc and Pt/C.*

The structure - activity relationship is an important perspective for better understanding of the electrocatalyst towards ORR. Engineering the morphological structures is an approach for enhancing the electrochemical performance of catalysts efficiently. It

involves several factors such as mass transfer, active site exposure, ionic/electronic conductivity, local electronic configurations, etc. 1D microrod possesses high length to diameter ratio that in turn, facilitates large electrode/electrolyte interface [289]. In the absence of *CuPc* 1D microstructure, there is always a tendency for MoS_2 nanoflakes to stack together through π-π interaction and forms 3D flower like structure that in turn results the blockage of electroactive edge sites [290]. Thus, limited ORR activity of MoS_2 is observed. In the presence of *CuPc* microrod in hydrothermal process, ultrathin MoS_2 nanoflakes are uniformly deposited in a vertical orientation over the entire wall surface of *CuPc* microrod with numerous exposed edge active sites that support an efficient ORR process [291]. It is also worth noting that the whole hybrid composed of *CuPc* and MoS_2 reveals enhanced ORR activity than that of pure MoS_2 sheets as well as pristine *CuPc*. Therefore, the role of *CuPc* can be assumed to be a support to grip the MoS_2 nanoflakes rather than a co-catalyst. Due to such supportive effects of the 1D microstructures, the fully exposed active sites and efficient mass/electron transfer can be achieved [291]. Comparative overall performances of phthalocyanine based catalysts are summarized in Table 6.3. However, compared with the Fe/Co-based phthalocyanine (*FePc/CoPc*) materials, *CuPc* normally exhibits poor ORR activity [as shown in Table 6.3], that needs to be enhanced. Therefore, MoS_2 2D nanosheet is grown over 1D structure to synergistically improve the activity by engineering the structure. Pristine 1D *CuPc* and flower-like MoS_2 show moderate ORR activity, but their heterostructure manifests improved activity.

Table 6.3: *Performnaces of various catalysts in alkaline electrolyte*

Materials	$\mathbf{E_{onset}}$ **(*V vs. RHE*)**	$\mathbf{E_{1/2}}$ **(*V vs. RHE*)**	**n**	**Ref.**
FePc	0.87	0.64	3.6-3.9	[138]
MoS_2	0.65	---	2.7	[292]
NiPc/GCB	0.76	0.55	2.64	[146]
FePc/OMC	0.725	0.623	3.95	[147]
MoS_2/graphene	0.73	---	3.75-3.90	[292]
FePc-MoS_2	0.90	0.89	4.0	[64]
MoS_2-CuPc	0.75	0.51	3.9	This work

The formation of edge active sites for electrocatalyst samples is investigated through determination of electrochemically active surface area (ECSA). ECSA is estimated by calculating the value of C_{dl} for all samples and is found to be directly proportional to C_{dl}. For that purpose, CV responses for *CuPc*, MoS_2 and MoS_2-*CuPc* are recorded in the non-Faradic region as shown in Figure 6.14(a), 6.14(b) and 6.14(c), respectively. From the slope of the linearly fitted graphs, C_{dl} is evaluated. The C_{dl} value is highest for MoS_2-*CuPc* as compared to

those for their individual counterparts, as depicted in Figure 6.14(d) The trend of edge active sites follows the following order: *MoS_2- CuPc >MoS_2>CuPc*. This result clearly indicates the formation of more edge active sites in the hybrid.

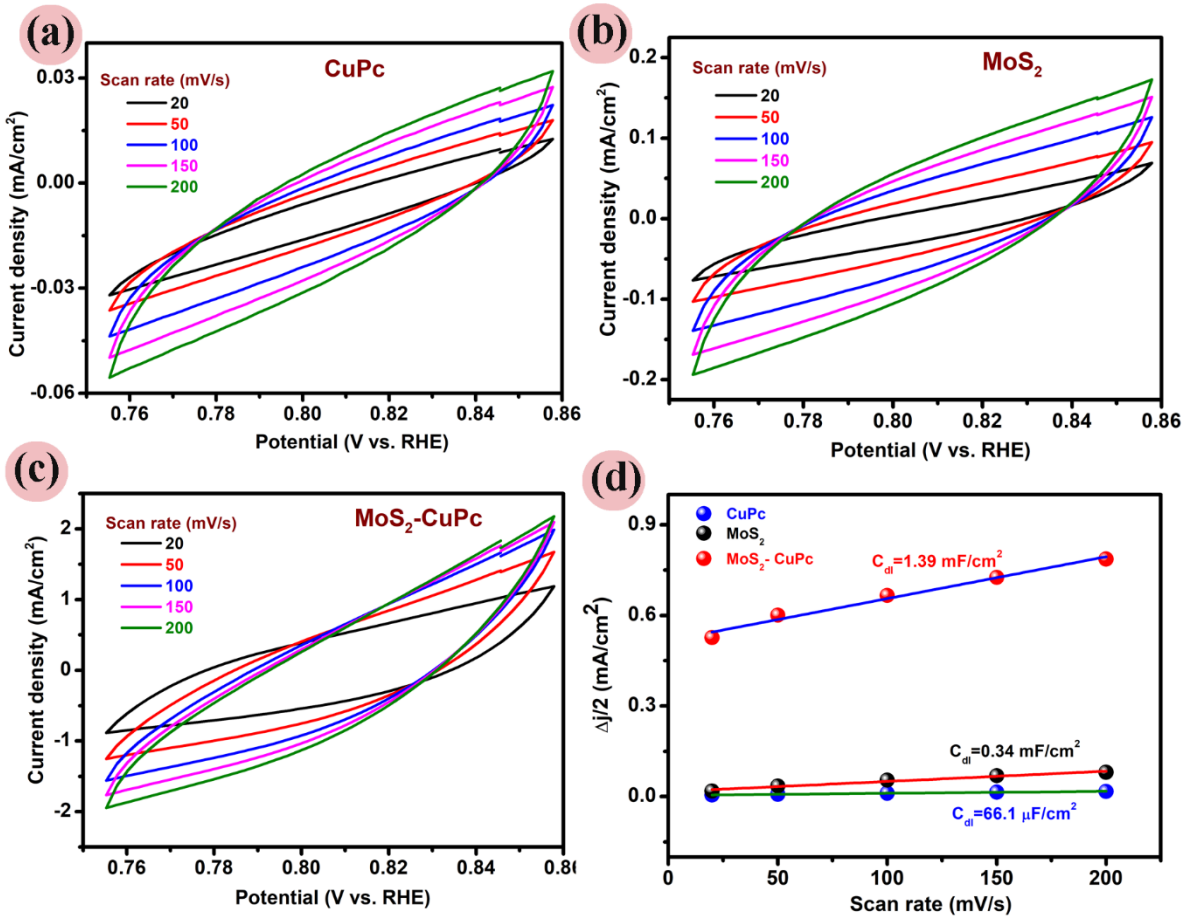

Figure 6.14: *CV graph of (a) CuPc, (b) MoS_2, (c) MoS_2-CuPc and (d) estimation of C_{dl}*

Further detail characterization is performed to determine the role of edge active centers. For this purpose, the ORR performances of *MoS_2-CuPc* and pure *CuPc* are investigated in 0.1 *M KOH* with addition of 5 *mM KSCN*. As seen from Figure 6.15, in presence of *KSCN*, both $E_{1/2}$ and current density get reduced that reveals the poisoning effect of M−N (M= Mo/Cu) sites by the coordination of SCN^- ions to the M sites which implies the deterioration in performances of both samples. Due to the effect of *KSCN*, $E_{1/2}$ is shifted by -30 *mV* and -80 *mV* for *CuPc* and *MoS_2-CuPc*, respectively. Therefore, Mo-N sites are the predominant active edge sites for ORR than Cu-N sites due to the strong $E_{1/2}$ shift in hybrid system than pristine *CuPc* [293-295]. Based on the above results, highly crystalline, uniform and dense nanosheet decorated *CuPc* microrod may act as promising ORR electrocatalyst due to its pronounced catalytic activity in alkaline media, excellent durability and facile preparation method.

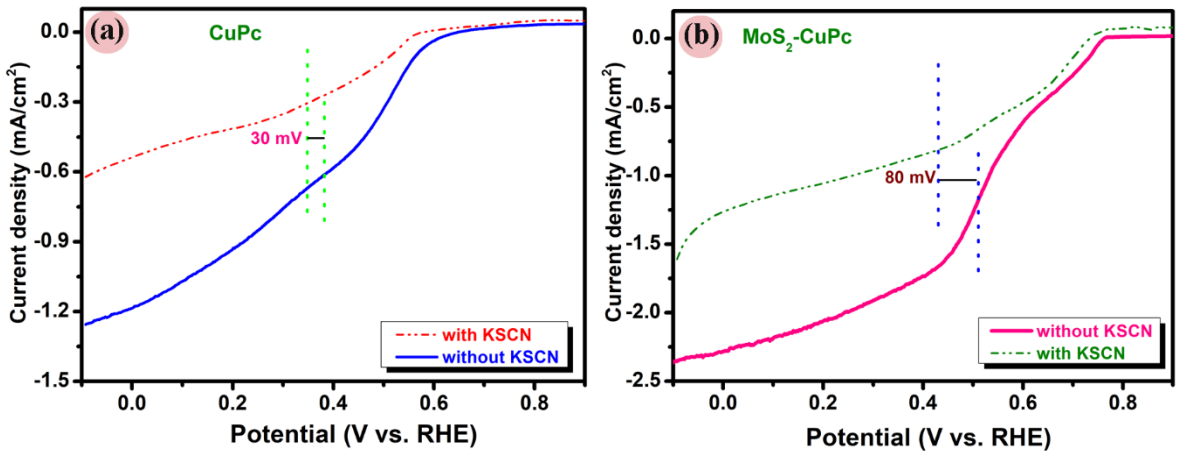

Figure 6.15: *Effect of KSCN in (a) CuPc and (b) MoS_2-CuPc hybrid*

LSV and corresponding plot of electron transfer number (*n*) at various potentials for commercially available 20 *wt% Pt/C* are shown in Figure 6.16.

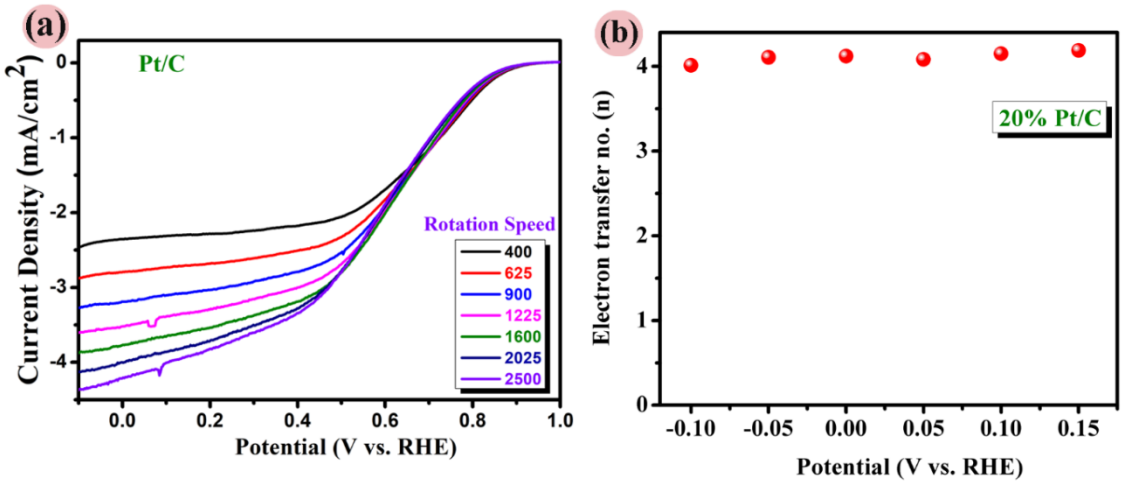

Figure 6.16: *(a) RDE plots and (b) corresponding electron transfer number (n) of Pt/C*

6.4 Conclusions:

In the present chapter, two types of electrochemical activities for the energy storage and conversion have been discussed using MPc nanostructured electrode and their hybrid with *rGO* and MoS_2. Initially, performance of pristine forms of *CuPc* and *ZnPc* nanostructures has been examined for supercapacitive activity in alkaline media. Both the materials have shown moderate activity and the approach may be extended for the symmetric/asymmetric supercapacitor device fabrication. For the hybrid systems, synergistic effect in between *rGO* and *CuPc*, is mainly responsible for the improvement of the performances as compared to individual counterparts. *MoS_2-CuPc* has emerged as the best performing electrocatalyst for cathodic ORR process.

7.1 Introduction:

Organic photovoltaic devices have attracted research interest over conventional silicon based inorganic photovoltaic devices having inherent limitations of high reflection and low absorption of the solar spectrum. While adequate absorption of solar radiation needs quite a thick silicon layer (in the order of μm) [296], a very thin (100-300 *nm*) layer of active material used in OSC is found to absorb enough solar radiation. This keeps the production cost of OSC low. Other advantages of organic polymer based solar cells are their low weight, mechanical flexibility, semi-transparency, and easy manufacturing process. But their prime limitation is low PCE. Organic materials inherently possess low permittivity and thus make dissociation of photo-generated excitons difficult. Researchers are trying hard to improve the efficiency by adopting different pathways such as incorporation of different transport layers, exploring new absorber materials, etc. [297, 298]. In contrast, quite large values of PCE have been reported for *Pb*-based solar cells [299-301]. The environmental issues associated with the hazardous effects raised from *Pb* content materials suggest use of new *Pb*-free perovskite material as absorber. Theoretical and experimental results have established superior intrinsic stability of IHPs over OIHPs [302-305].

In this dissertation, various transport layer materials for both electrons and holes are explored for further performance improvement in OSCs as well as *Pb* free PSCs. The entire solar cell study is based on simulation. Solar cell performances of two types of organic BHJ absorbers, $OC_1C_{10}PPV$*:PCBM* and *P3HT:PCBM*, and cesium based *Pb* free double-perovskite (Cs_2TiBr_6) are investigated. Suitability of different materials including *CuPc*, one of our synthesized and characterized materials is also examined as transport layers in OSCs as well as PSCs.

7.2 ATLAS simulation of solar cells:

In this dissertation, design and simulation of solar cells are carried out through a commercial semiconductor device simulator ATLAS, from SILVACO, Inc. Due to the reduction in overall semiconductor device dimensions, ATLAS become an important tool to characterize as well as optimize electronic devices for a wide range of applications. This type of device simulation guides us to gain the knowledge about the physical processes within a device and eventually helps to predict the behaviour of the device. Reliability as well as scalability of electronic devices can be furnished by the simulation upto certain extent, which in turn, enhances the production speed with minimized risk and uncertainties. Atlas is a

versatile 2D as well as 3D device simulator to carry out DC, AC, and transient analysis for wide varieties of semiconductor material-based devices. There are some major tools incorporated in this software such as ATHENA, ATLAS, DECKBUILD, TONYPLOT, etc. Here, the device configurations are constructed using DECKBUILD, and ATLAS platform is used to simulate it. The simulated results are displayed with the help of TONYPLOT. The generalized simulation code is provided in Appendix.

7.3 Simulation of organic solar cells:

In this chapter, performances of BHJ solar cells [Figure 2.12 in Chapter 2] using two different polymer blends as the active materials are compared. Investigations are further extended for two different cathode materials. At first, the BHJ of *OC_1C_{10}PPV:PCBM* is simulated by Silvaco ATLAS. The solar cell parameters are investigated with variation in the above active layer thickness to find out the appropriate thickness that yields the highest conversion efficiency. As *P3HT:PCBM* matrix is very popular due to its long-time outdoor stability [306], BHJ solar cell with *P3HT:PCBM* blend of the above thickness is also simulated, and a comparison of the above two OSCs is made. Finally, different transport layer materials are incorporated with best performing organic polymer blend to further improve the solar cell performance.

7.3.1 *OC_1C_{10}PPV:PCBM* based Organic solar cell:

For simulation of organic polymer based BHJ solar cells, the simplest device configuration as Cathode/Absorber/Anode is considered [Figure 7.1]. Parameters used for simulation of solar cell with *OC_1C_{10}PPV:PCBM* blend are summarized in Table 7.1 [307].

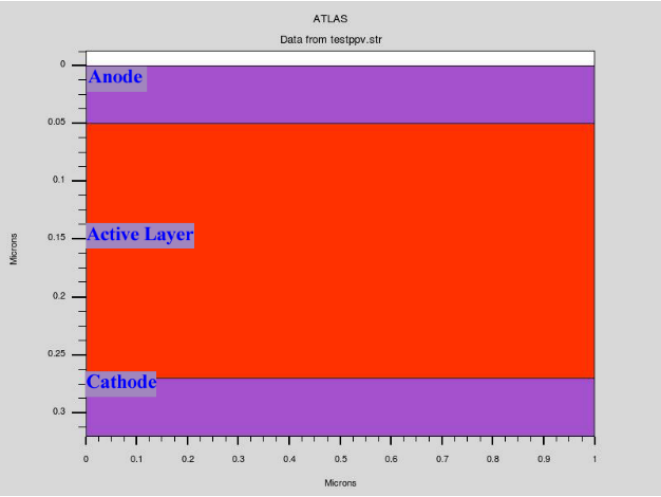

Figure 7.1: *Simulated device configuration of basic solar cell*

Table 7.1: *Parameters for OC_1C_{10}PPV:PCBM based solar cell simulation*

Parameters	Value
d (nm)	Variable
ε_r	3.4
χ *(eV)*	2.9
E_g*(eV)*	1.34
N_c, N_v *(cm^{-3})*	2.5×10^{19}
k_f *(s^{-1})*	1.5×10^{6}
μ_n *(cm^2/Vs)*	2.5×10^{-3}
μ_p *(cm^2/Vs)*	3×10^{-4}
a.singlet (nm)	1.3

Thickness of the absorber material is denoted by *'d'*. ε_r, χ *and* E_g denote relative permittivity, electron affinity and bandgap energy of the BHJ polymer blend, respectively. μ_n (μ_p) is the mobility of electrons (holes), N_c, N_v is the density of states at conduction and valence band edges and k_f specifies the decay rate of excitons.

Initially, solar cell with *ITO/OC_1C_{10}PPV:PCBM/Al* configuration is simulated by Silvaco ATLAS software. The thickness dependent solar cell performance is studied by varying the thickness of absorber material from 80 *nm* to 350 *nm* keeping all other parameters intact. The resulting *J-V* characteristics is presented in Figure 7.2.

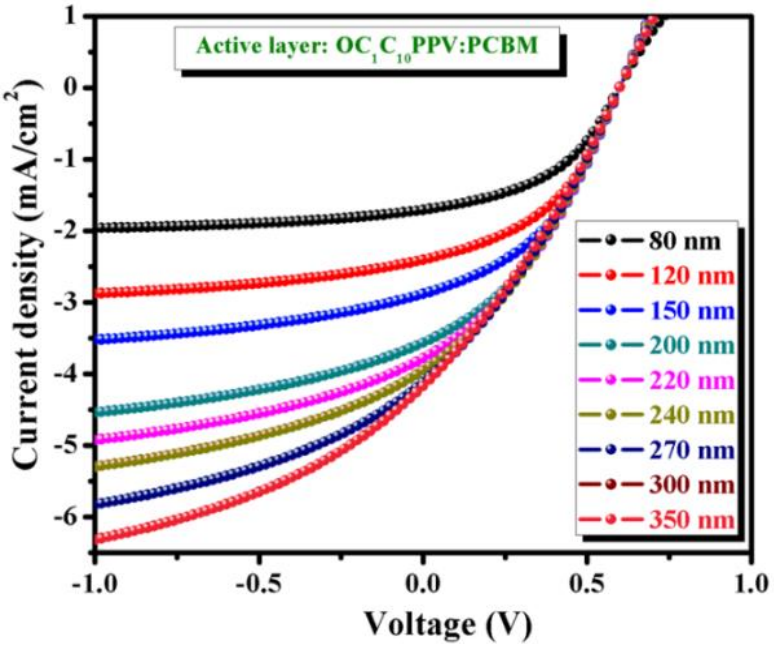

Figure 7.2: *J-V characteristics for different thickness of OC_1C_{10}PPV: PCBM blend*

As seen from Figure 7.2, the value of J_{sc} is increased with the increase in absorber layer thickness up to 300 *nm*. The thickness dependency of J_{sc} and FF is presented in Figure 7.3(a). Initially, J_{sc} value increases from 1.707 *mA/cm^2* @ 80 *nm* to 4.17 *mA/cm^2* @ 300 *nm* and then slightly decreases beyond 300 *nm*. Significant enhancement in J_{sc} is attributed to the fact

that a thicker absorber can absorb greater amount of solar radiation that causes generation of appreciable amount of photogenerated excitons. Dissociation of such excitons finally yield large free carrier density. Beyond 300 *nm*, a slight declining tendancy in J_{sc} is observed. Despite of higher photo absorption, chances of carrier recombination are also increased in thick active layer. The value of FF gradually falls with the increase in layer thickness. Although proper understanding of FF is still under debate, many factors *viz.* interfacial recombination, carrier mobility, series (R_s) and shunt (R_{sh}) resistances, morphology and miscibility of donor-acceptor polymer influence it [308]. The variations in series and shunt resistances also affect the shape of the *J-V* characteristics with increasing absorber thickness [309]. Thus, FF varies.

The influences of active layer thickness on V_{oc} and PCE are presented in Figure 7.3(b). The V_{oc} remains almost invariant to layer thickness beyond 150 *nm*. The value of V_{oc} is directly related to the effective energy gap between the LUMO level of the acceptor and the HOMO level of the donor, thereby providing the primary driving force towards charge separation. The value of V_{oc} for OSC can be determined by the following empirical relation [308]:

$$V_{oc}(in\ eV) = \left(\left|E_{HOMO}^{donor}\right| - \left|E_{LUMO}^{acceptor}\right|\right) - 0.3 \tag{7.1}$$

where, 0.3 *eV* is an empirical value for efficient charge separation [310]. In the present case, the value of V_{oc} should be around 1*V*. Losses due to both radiative (V_r) and non radiative recombination voltage (V_{nr}), V_{nr} being the dominant one, make V_{oc} much smaller than the estimated value (here of 1*V*). Such loss in V_{oc} in turn, limits the PCE in OSC. With the increase in active material thickness, the overall efficiency of the device increases, attains initially a maximum value, and then starts to fall. The reason for such fall in PCE is that the carriers have to cover a longer path to reach the electrodes and result in enhanced recombination in too thick

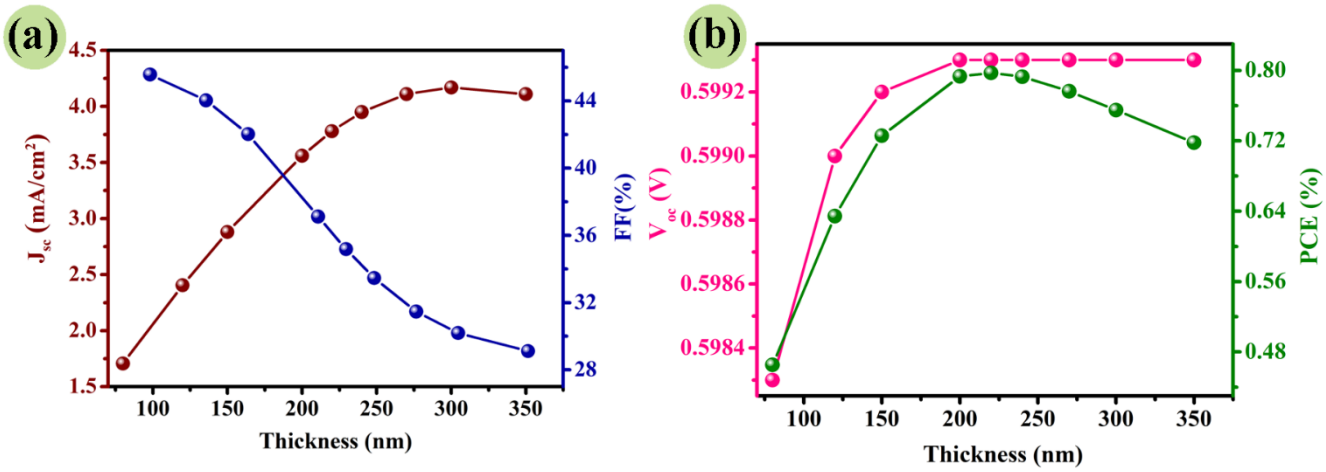

Figure 7.3: *Impact of $OC_1C_{10}PPV$:PCBM blend thickness variation on (a) J_{sc} and FF and (b) PCE and V_{oc}*

active layer. Thus, 220 *nm* thick *OC_1C_{10}PPV:PCBM* polymer blend is found to yield the highest PCE and V_{oc}, and moderate J_{sc} and FF.

Next, the role of electrode WF is investigated using aluminium (*Al*) (WF ~ 4.1 *eV*) and *Ag* (WF ~ 4.26 *eV*) with 220 *nm* *OC_1C_{10}PPV:PCBM* blend thickness. Corresponding *J-V* characteristics are shown in Figure 7.4. When *Al* is replaced by *Ag*, higher value of cathode work function causes reduction in built-in potential. It reduces the electric field across the active material and causes inefficient collection of photo-generated carriers [311]. Therefore, the value of V_{oc} decreases.

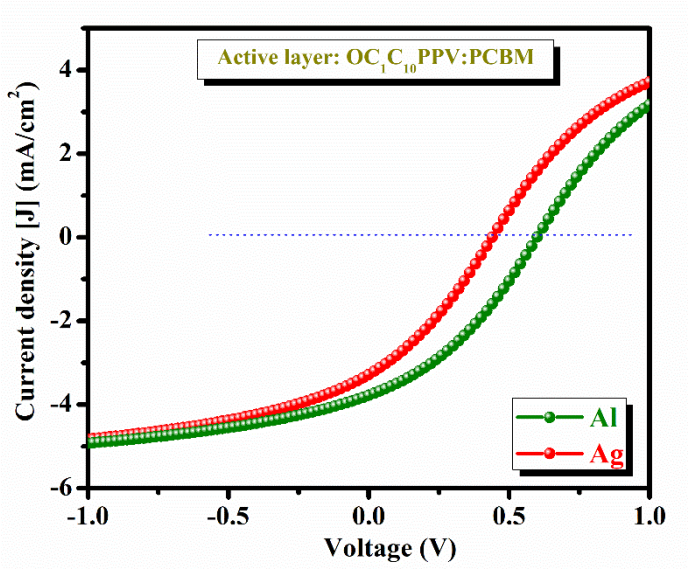

Figure 7.4: *J-V graph of OC_1C_{10}PPV:PCBM solar cell with Al and Ag cathodes*

7.3.2 *P3HT:PCBM* based Organic solar cell:

Next, a *P3HT:PCBM* based solar cell will be investigated here. The cell of similar configuration as *PPV* based one is simulated here just by replacing the donor polymer with *P3HT*. Parameters used for *P3HT:PCBM* based simulation are summarized in Table 7.2.

Table 7.2: *Parameters used for P3HT:PCBM solar cell simulation*

Parameters	Value	Ref
d (nm)	220	Our work
ε_r	3.4	[312]
χ *(eV)*	3.7	[155]
E_g *(eV)*	1.5	Our work
N_c, N_v (cm^{-3})	5.0×10^{20}	[155]
k_f (s^{-1})	1.4×10^{4}	[312]
μ_n (cm^2/Vs)	0.1	[312]
μ_p (cm^2/Vs)	0.01	[312]
a.singlet (nm)	1.8	[312]

The simulated *J-V* characteristics of *P3HT:PCBM* based solar cell with two different electrode materials, *Al* and *Ag* are presented in Figure 7.5. When *Al* is used instead of *Ag*, all the solar cell parameters improve, especially, V_{oc}, which is strongly affected in a similar manner as described in earlier section.

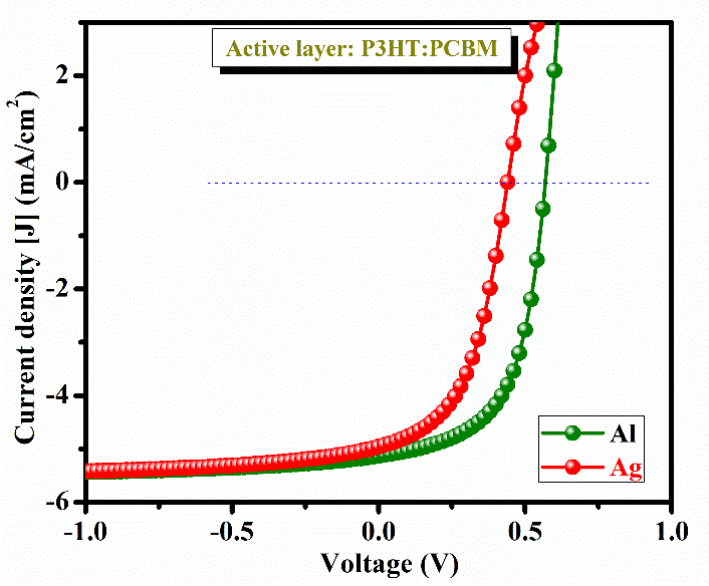

Figure 7.5: *J-V graph of P3HT:PCBM solar cell with Al and Ag cathodes*

7.3.3 Comparison of *OC_1C_{10}PPV and P3HT* based solar cells:

Finally, performances of two photoactive materials (220 *nm* thick) are compared considering *Al* as the cathode material. *J-V* characteristics for both absorber materials are shown in Figure 7.6. The entire Air mass 1.5G (AM 1.5G) spectrum of solar radiation lies in the wavelength range of 300-1000 *nm* [313]. *PPV* based donor material exhibits narrow absorption coverage; absorption edge observed around 550 *nm*. In contrast, broader absorption coverage [300 -700 *nm*] of *P3HT* causes significant absorption of solar radiation, and therefore, generation of larger number of excitons than in *PPV*. As a result, remarkable enhancement in J_{sc} is observed for *P3HT:PCBM* solar cell as compared to *PPV* based solar cell.

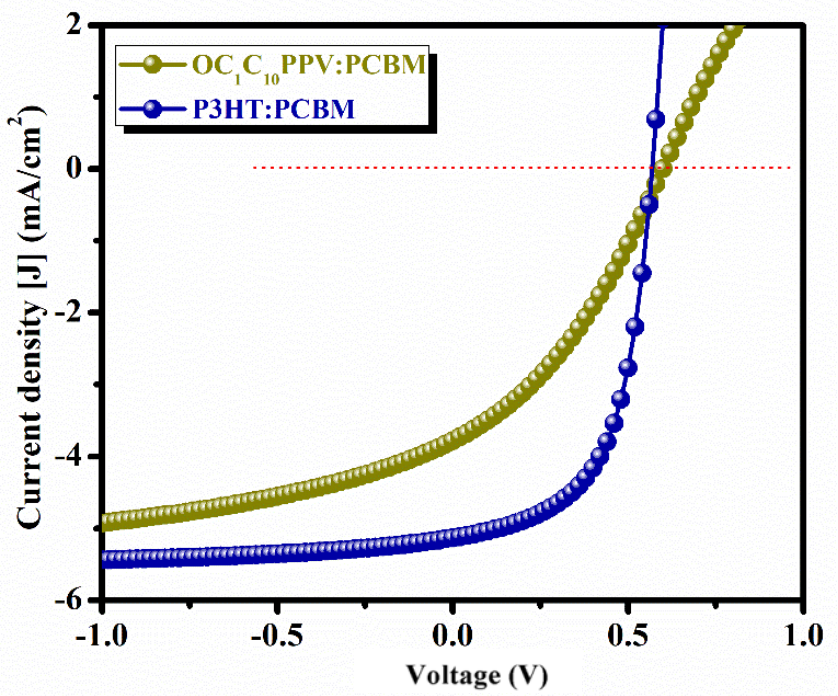

Figure 7.6: *Comparative J-V characteristics of two polymer blends with Al cathode*

Key solar cell parameters are extracted from the *J-V* characteristics and presented in Table 7.3, which establish the superiority of *Al* as cathode material over *Ag* for both types of polymer blend. It is evident from Table 7.3 that the *P3HT:PCBM* system exhibits superior performance than *OC_1C_{10}PPV:PCBM* for both cathode materials. As compared to *OC_1C_{10}PPV:PCBM* solar cell, *P3HT:PCBM* solar cell exhibits J_{sc} and FF improved by more than 44% and 63%, respectively with Al as cathode material. The value of FF determines the quality of a solar cell. When *OC_1C_{10}PPV* is replaced by *P3HT*, R_{sh} increases from 0.34 $K\Omega cm^2$ to 0.84 $K\Omega cm^2$, while R_s decreases from 97 Ωcm^2 to 18.6 Ωcm^2; All these result in the *J-V* characteristics closer to the ideal one. In addition, the PCE value approximately gets doubled for *P3HT:PCBM* system with around 5% reduction in V_{oc}. Such depreciation has also been experimentally reported in literature [164]. Higher hole mobility in *P3HT* may be responsible for such improved performance than *PPV* based solar cell [314]. Thus, the investigations presented in last few sections, establishes the *P3HT:PCBM* solar cell with *Al* cathode as the best performing one. Therefore, in the following section, approaches will be made to further improve its performance.

Table 7.3: *Simulated parameters for both solar cells with various cathode materials*

Active Material (220 nm)	J_{sc} (mA/cm^2)		V_{oc} (V)		FF (%)		PCE (%)	
	Ag	Al	Ag	Al	Ag	Al	Ag	Al
OC_1C_{10}PPV: PCBM	3.28	3.78	0.4397	0.5993	31.86	35.18	0.4597	0.7973
P3HT: PCBM	4.95	5.13	0.4397	0.5683	49.33	57.55	1.075	1.679

7.3.4 Performance improvement of *P3HT:PCBM* solar cell:

In some polymer blend, variations in photoactive layer thickness impose complex influence on solar cell parameters. In order to find the optimum absorber layer thickness, the trade-off between light absorption and charge carrier collection should be made. A thick active layer is capable of absorbing significant amount of radiation, and yields large no of photogenerated carriers, but it also hampers efficient charge collection due to nongeminate bulk recombination. In recent time, Li *et al.* reported the range of optimum active layer thickness obtained from experimental as well as simulation based study for three different polymer blends [315]. The range of optimum thickness was found as 145-155 *nm* for *P3HT:PCBM* blend. Another experimental study done by Islam and his group revealed that highest solar light absorbance was observed for 150 *nm* (approx.) thick *P3HT:PCBM*. In addition, there is other design criterion related to choice of the top metal electrode in the above OSCs. The top metal must possess high stability in air, as it is exposed to atmosphere. Gold (*Au*) (WF ~ 5.1 *eV*) offers significant intrinsic stability in air compared to *Al* and *Ag*, as they both exhibit the rapid oxidation tendency [316]. Comparative solar cell parameters obtained from simulation of 150 *nm* thick *P3HT:PCBM* active layer with *Al* and *Au* top electrodes are listed in Table 7.4.

Table 7.4: *Key parameters for P3HT:PCBM solar cells with various top electrodes*

P3HT:PCBM (150 *nm*)	J_{sc} *(mA/cm^2)*	V_{oc} *(V)*	FF (%)	PCE (%)
Al	3.82	0.20	50.66	0.39
Au	4.35	0.36	69.28	1.08

The results obtained so far proclaim quite low PCE. Therefore, to boost the conversion efficiency further, investigation is carried out for the above structure incorporating additional transport layers in it in order to prevent the interfacial carrier recombination.

A generalized device structure with interfacial layers has been presented in Figure 2.11 in Chapter 2. Transport layers offer multiple functionalties. First, they lower the energy barrier between the photoactive layer and the electrode: and thus favor efficient charge extraction through ohmic contacts. Second, appropriate transport materials can serve as selective contacts for single charge carriers i.e. electrons or holes. Finally, transport layers provide protection of underlying absorber layer. Inverted OSC configuration is adopted here. Traditionally, a layer of the TCO namely FTO (WF ~ 4.4 *eV*) is used as the bottom layer of solar cell. In between FTO and the absorber, ETLs are added, specifically, *n*-type materials *viz.* TiO_2, *ZnO* and *CdS* are tried here. On the other side, *p*-type interface layer is inserted in between absorber and the top electrode. Generally, *p*-type layer like *PEDOT:PSS* is used as standard HTL in conventional design, but its acidic nature poses serious limitations in long-term stability of the device [317]. To overcome the problem, several *p*-type inorganic transition metal oxides — V_2O_5 [318], MoO_3 [319], WO_3 [320], *NiO* [321], etc. are used. In this chapter, inorganic *NiO* and organic *CuPc* are now investigated as the replacement of *PEDOT:PSS*. Excellent hydrophobicity of *CuPc* is one prime advantage that is beneficial for protection of the cell from atmospheric moisture.

Initially, *ZnO* and *CuPc* are chosen respectively as ETL and HTL, in *P3HT:PCBM* solar cell. The effect of variation in thickness of *ZnO* and *CuPc* on the cell performances is studied. The thickness of the *ZnO* layer is first varied, keeping absorber and *CuPc* thickness as 150 *nm* and 10 *nm*, respectively. A 60 *nm* thick *ZnO* layer yields the highest efficiency and fill factor as evident from Figure 7.7(a). Next, thickness optimization of *CuPc* is carried out taking

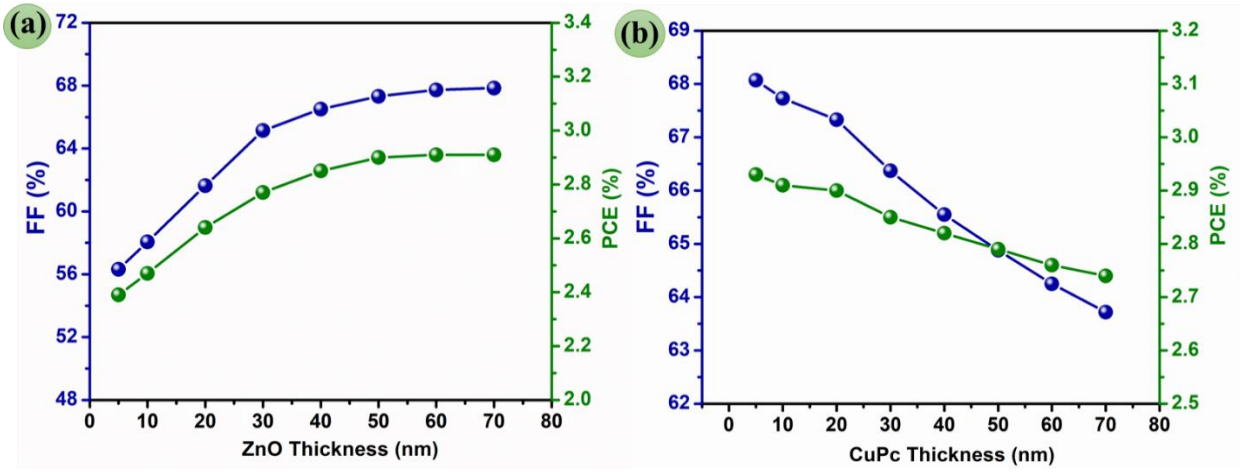

Figure 7.7: *Effect of thickness variation of (a) ZnO and (b) CuPc on P3HT: PCBM solar cell*

150 *nm* thick absorber and 60 *nm* thick *ZnO* layer, from which a 10 *nm CuPc* layer is found to perform the best [Figure 7.7(b)].

Next, the solar cell configured with all the above optimised layers are simulated, where electron mobility (μ_n) in the absorber polymer blend is varied over the range of 10^{-5} to 10^3 cm^2/Vs. Variation of hole mobility (μ_p) is also considered using the common useful approximation: $\mu_n = 10\mu_p$ [312]. Dependence of J_{sc} and V_{oc} on electron mobility in the active material is presented in Figure 7.8(a) and 7.8(b), respectively. After an initial increase, J_{sc} attains a more-or-less saturated value for μ_n varying over a range of (10^{-3}-1) cm^2/Vs. The value of V_{oc} falls due to the increase of the Langevin recombination at higher mobilities ($\mu_n > 0.1$ cm^2/Vs) [322]. Langevin recombination (R) increases with increase in carrier mobility through the radiative recombination constant k, expressed as follows:

$$k = \frac{q}{\epsilon_0 \epsilon_r}(\mu_n + \mu_p) \tag{7.2}$$

Where the Langevin recombination (R) itself is given as:

$$R = k(np - n_i^2) \tag{7.3}$$

Here, n_i is the intrinsic carrier density, n and p are electron and hole concentration, ϵ_0 is the permittivity of vacuum and ϵ_r is the relative permittivity of semiconductor.

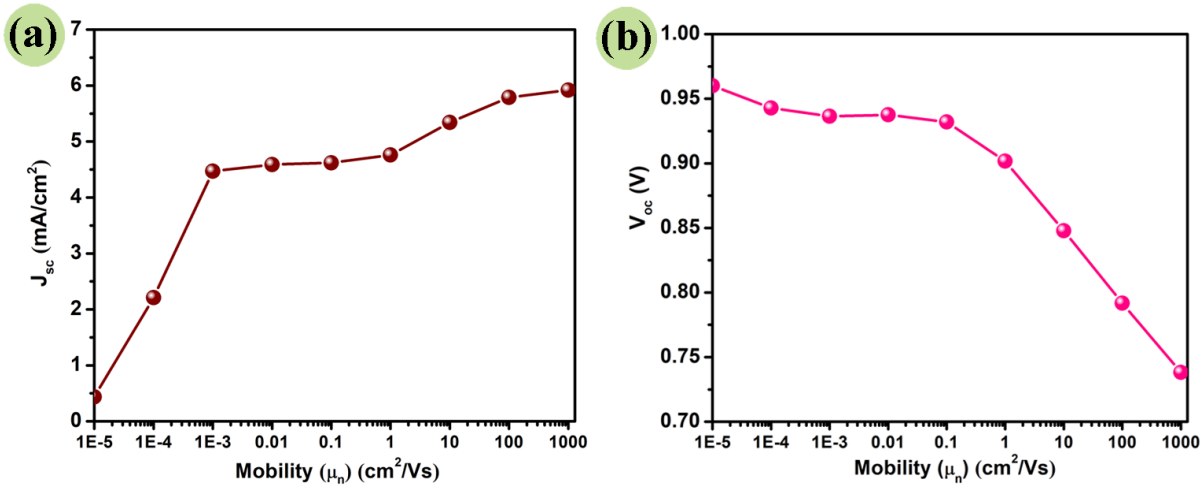

Figure 7.8: *Effect of active layer carrier mobility variation on (a)J_{sc} and (b) V_{oc} for P3HT:PCBM solar cell*

The variation of FF and PCE is depicted in Figure 7.9(a) and 7.9(b), respectively. This trend in variation of FF with carrier mobility results from the opposite kind of mobility dependence of J_{sc} and V_{oc}. The highest PCE is observed around $\mu_n = 0.1$ to 1 cm^2/Vs. Beyond this range of μ_n, i.e. for both high and low values of electron mobility, deterioration in PCE appears as evident from Figure 7.9(b). For low mobility, PCE decreases due to increased carrier recombination and reduced dissociation probability of excitons [312]. The optimum solar cell

performance in terms of FF and PCE is obtained at electron mobility of 1 cm^2/Vs. Thus, further investigations will be carried out with μ_n= 1 cm^2/Vs and μ_p=0.1 cm^2/Vs.

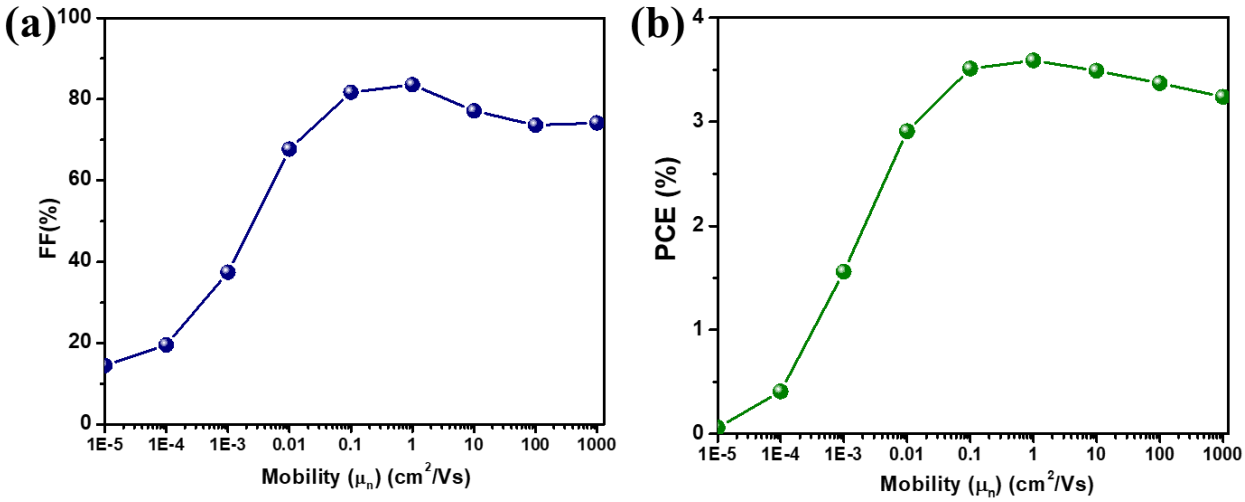

Figure 7.9: *Effect of active layer carrier mobility variation on (a) FF and (b) PCE for P3HT:PCBM solar cell*

Using the optimum carrier mobilities, HTLs of various materials (*PEDOT:PSS*, *CuPc* and *NiO*) are tried with *ZnO* as ETL. The simulated *J-V* characteristics of cell with different HTLs are shown in Figure 7.10(a). The energy band diagram of *P3HT:PCBM* device structure with additional transport layers are presented in Figure 7.10(b). As clear from Figure 7.10(b), the ETL not only aids electrons to reach the cathode, but also puts a barrier to flow of generated holes. Similarly, introduction of HTL allows holes to flow to anode but blocks electrons. *PEDOT:PSS* is widely used HTL material and very much suitable for conventional architecture where it gets deposited on FTO. But in inverted cell configuration, when deposited over organic

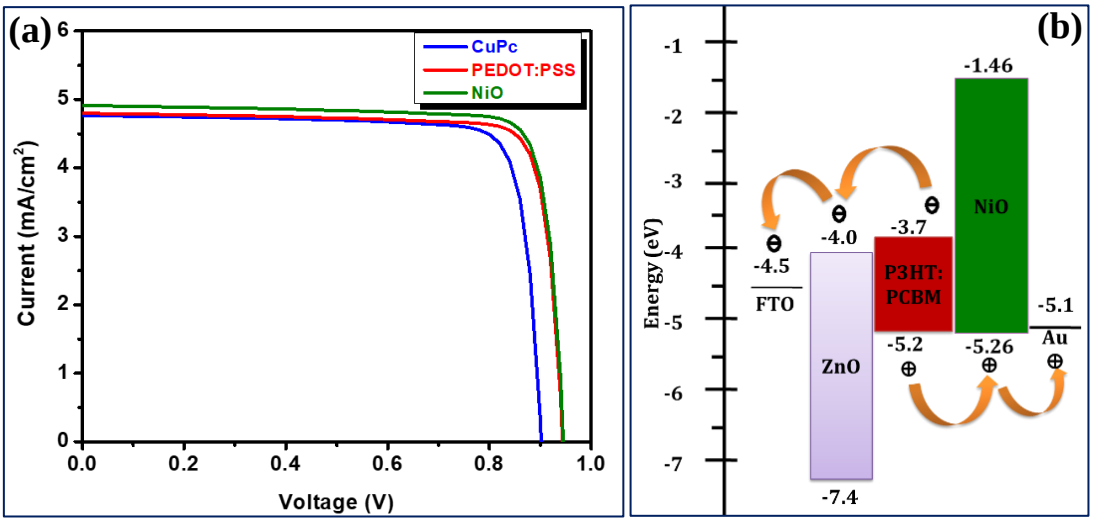

Figure 7.10: *P3HT:PCBM solar cell (a) J-V characteristics with various HTLs and (b) Energy band diagram*

(hydrophobic) polymers, film morphology and electrical properties of *PEDOT:PSS* get severely affected due to its hydrophilic nature. As evident from the results summarized in Table 7.5, employing CuPc as HTL along with ZnO as ETL, yields a PCE 3.3 times higher than that of the cell having no transport layer [Table 7.4]. However, *NiO* emerges as the best candidate for HTL.

Table 7.5: *Solar cell parameters for different HTL materials*

HTL	J_{sc} *(mA/cm^2)*	V_{oc} *(V)*	FF (%)	PCE (%)
CuPc	4.76	0.902	83.57	3.59
PEDOT: PSS	4.79	0.944	84.39	3.82
NiO	4.91	0.945	84.52	3.92

In the next step towards optimisation of the solar cell configuration, *NiO* is used as the HTL material, and the other three materials (*CdS*, *TiO_2*, *ZnO*) are tried as ETLs. Results summarized in Table 7.6 proclaim *ZnO* as the best ETL material. Slightly larger values of V_{oc}, FF and PCE are observed in *ZnO* as compared to *TiO_2* based solar cell. The reason for slight increament in V_{oc} in *ZnO* based cell is ascribed to the slower rate of recombination of charge carriers. Experimental evidence of smaller time constant for charge recombination in *ZnO* than *TiO_2* has been presented by Son et al. [323]. In addition, higher transparency of *ZnO* than other ETL materials in UV to visible region allows more photons to reach the photoactive layer, resulting the high PCE in *ZnO* based OSC [324]. So, the proposed configuration of the best performing solar cell is finalised as *FTO/ZnO/P3HT:PCBM/NiO/Au*, which yields ~4% PCE and ~ 84% FF on the basis of optimised carrier mobilities. Incorporation of transport layers on either side of absorber layer creates many heterojunction interface (ETL/absorber and absorber/HTL). Transport of generated electrons/holes from active layers to respective electrodes is aided by these junctions. Thus, efficient charge seperation is accomplished, which in turn, led to significant enhancement in solar cell parameters.

Table 7.6: *Solar cell parameters for different ETL materials*

ETL	J_{sc} *(mA/cm^2)*	V_{oc} *(V)*	FF (%)	PCE (%)
CdS	4.83	0.946	82.07	3.75
TiO_2	4.91	0.944	82.51	3.82
ZnO	4.91	0.945	84.52	3.92

A maximum PCE of only ~ 4% is achieved from organic polymer based solar cell with incorporated tranport layers. To get reasonably larger PCE, PSC will be next explored. However, high performing PSCs are in general *Pb* based materials that cause environmental hazards. Thus, a PSC based on an environment friendly absorber material will be investigated in next section.

7.4 Simulation of Lead free perovskite solar cell:

Among various *Pb*-free perovskites, Cs_2TiBr_6 is chosen here due to few advantages of *Ti* as mentioned earlier in Chapter 2. In designing Cs_2TiBr_6 based PSC, cell architecture is comprised of a light-absorbing layer of perovskite, ETL and HTL. Proper choice of material and thickness of above layers is very crucial in determining the overall performance of designed cell. The schematic structure of such PSC is shown in Figure 7.11. *FTO* is used as the cathode, while the anode material is chosen as *Au*, *Ag* or *Cu*. For ETL, inorganic metal oxide such as TiO_2 [325], *ZnO* [326], SnO_2 [327] are commonly used. Organic materials *viz.* polytriarlyamine (PTAA) [325], *spiro-OMeTAD* [194] and *PEDOT:PSS* are the initial choice for HTL [328]. But their chemical and thermal instability and high cost are important deterrent towards proper development of such PSCs. However, *P3HT* and *CuPc*, a small molecule organic material are expected to be the potential candidates for HTL. *P3HT* possesses good optical and electrical properties, supports easy fabrication processes [329] and of low cost, while *CuPc* exhibits good thermal and chemical stability and moisture resistance property, which make it appropriate for encapsulation layer of PSCs [330, 331]. Along with organic HTLs, inorganic HTLs such as, *NiO*, *CuI* may be the potential alternatives for transport layers in PSCs. However, the properties like large bandgap, suitable work function, deep VB level around 5.3 *eV* [332] have made *NiO* more popular. In this section, three hole transporting materials – two organic (*CuPc* and *P3HT*) and the third one inorganic (*NiO*), are explored along with TiO_2 as the electron acceptor.

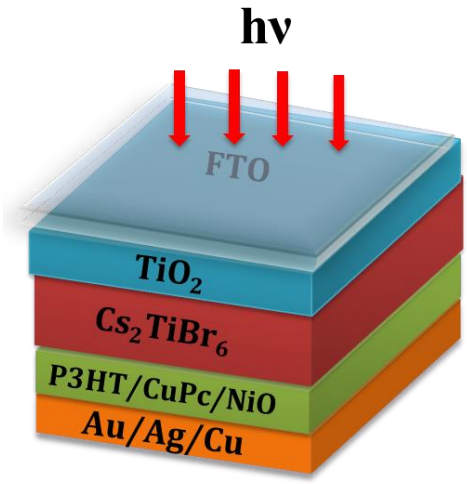

Figure 7.11: *Schematic structure of proposed Cs_2TiBr_6 solar cell*

For simulation of the *Pb* free PSC, the thickness of Cs_2TiBr_6 absorber material is taken as 200 *nm* as per the existing literature [198]. In addition to efficient electron collection, as TiO_2 behaves also as a window layer to allow incident solar radiation to reach the absorber material, thickness of TiO_2 must be chosen properly. In order to investigate the influence of one transport layer, its thickness is varied in presence of the other layer, following the scheme reported in [333]. The thickness of TiO_2 is first varied between (10-100) *nm* with a 10 *nm* thick *NiO* film. Simulation results presented in Figure 7.12(a) show that the FF falls monotonically with thickness of TiO_2, whereas slight improvement appears in PCE. It was experimentally observed that around 10 *nm* thin TiO_2 film yields 75% (approx.) transmittance of incident solar radiation, while thicker films cause enhanced light scattering and reduce effective utilization of incident illumination [334]. Thus, the thickness of ETL is chosen here as 10 *nm*. Similarly, *NiO* layer thickness is varied over the range of (5 – 100) *nm* taking thickness of TiO_2 and Cs_2TiBr_6 layers, respectively as 10 *nm* and 200 *nm*. Result in Figure 7.12(b) demonstrates the gradual deterioration in FF for the variation in *NiO* thickness over the entire range. Thick transport layers, however, show a tendency for development of cracks over large areas [334]. On the other hand, as too thin *NiO* and TiO_2 layers lack reproducibility and may get affected by the presence of pinholes, at least 10 or 20 *nm* thickness is recommended for their pinhole free deposition [333]. Thus, we choose a 10 *nm* thick *NiO* layer, which also yields the highest FF, as is evident from Figure 7.12 (b).

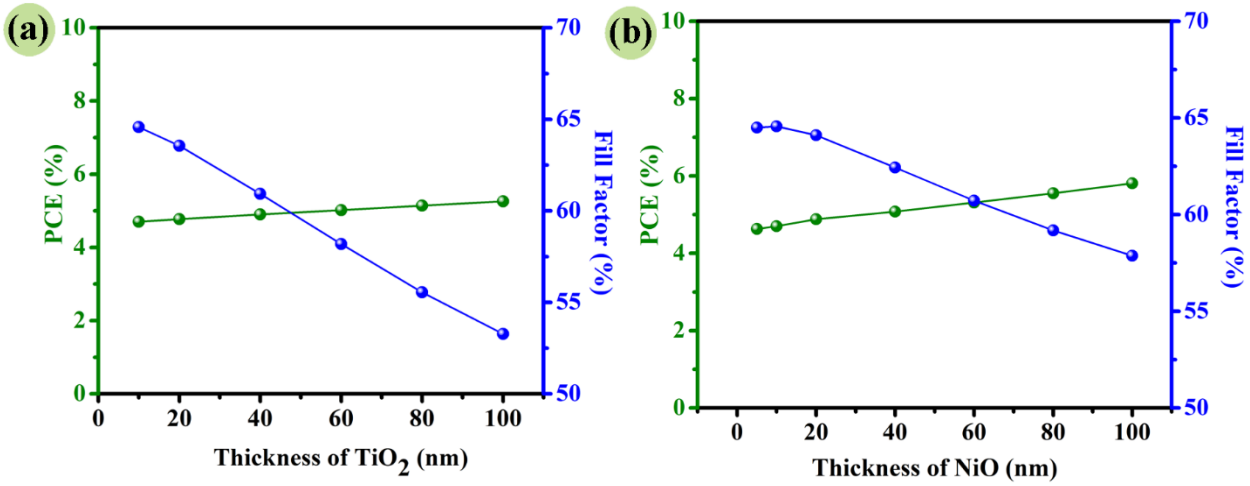

Figure 7.12: *Impact of thickness variation of (a) TiO_2 and (b) NiO layers on FF and PCE for Cs_2TiBr_6 based PSC*

In this study, influences of different HTLs on the cell performance are also investigated. For simulation of a cell with *TiO_2* and *CuPc*, *P3HT (S1)* [*S stands for simulation*] or *NiO*, the time - resolved photoluminescence (PL) decay times of individual materials are taken from the existing literature. The simulated *J-V* characteristics and the various solar cell parameters extracted from them are presented respectively in Figure 7.13 and Table 7.7.

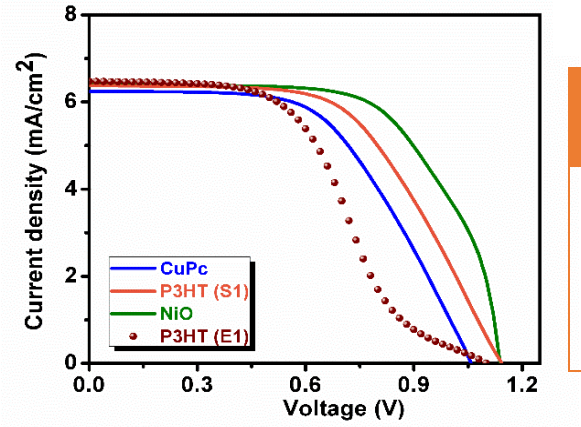

Figure 7.13: *J-V characteristics of Cs_2TiBr_6 solar cell with different HTLs*

Table 7.7: *Solar cell parameters for different HTLs*

HTL material	J_{sc} *(mA/cm^2)*	V_{oc} *(V)*	FF (%)	PCE (%)
CuPc	6.24	1.05	55.30	3.65
P3HT (S1)	6.37	1.14	56.62	4.12
NiO	6.40	1.14	64.57	4.70
P3HT (E1)	6.47	1.10	45.46	3.24

Results indicate *NiO* outperforms the other two hole transporting materials - *CuPc* and *P3HT*. In order to validate our simulated results, *Cs_2TiBr_6* cell with *TiO_2* and *P3HT (E1)* [*E stands for Experimental*] is further simulated taking the PL lifetime of *TiO_2/Cs_2TiBr_6* and *Cs_2TiBr_6/P3HT* interfaces from the work reported by Chen et al. [198].

The simulated results [row 4, Table 7.7] match reasonably with the experimental results reported in Ref. [198]. However, presence of glass substrate and defect densities in the

materials in real solar cell structure may be responsible for the above mismatch appeared between the experimental and simulated results.

Next, different cell configurations with undoped and doped transport layers are simulated further. Existing literature reported that presence of some of the dopants may improve the overall performance, but degrade cell stability in case of *P3HT* [335]; while in the case of *CuPc*, dopants impose a negative impact on film morphology [336]. As apparent from Figure 7.13, *NiO* has emerged as the most efficient of all the three HTL materials considered here. Therefore, different device configurations marked as (A - E) with undoped and doped TiO_2 and *NiO* layers are further simulated here.

The *J-V* characteristics of various cell configurations are presented in Figure 7.14 and the solar cell parameters, determined from the above characteristics are shown in Table 7.8.

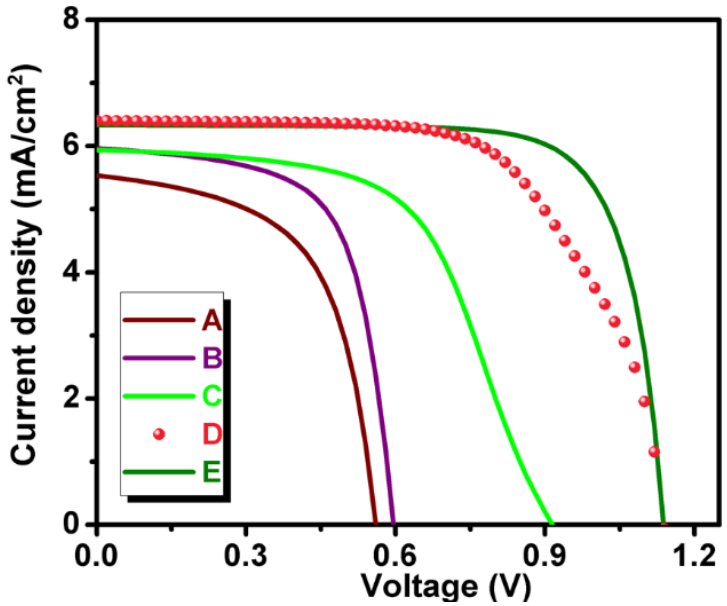

Figure 7.14: *J-V characteristics of Cs_2TiBr_6 solar cell with different configurations*

Table 7.8: *Solar cell parameters for different cell configurations*

Device Configuration	J_{sc} (mA/cm^2)	V_{oc} (V)	FF (%)	PCE (%)
(A) FTO/Cs_2TiBr_6/Au	5.53	0.56	58.20	1.81
(B) FTO/n+ TiO_2/Cs_2TiBr_6/Au	5.96	0.59	64.69	2.29
(C) FTO/Cs_2TiBr_6/p+ NiO/Au	5.94	0.91	57.50	3.12
(D) FTO/TiO_2/Cs_2TiBr_6/NiO/Au	6.40	1.14	64.57	4.70
(E) FTO/n+ TiO_2/Cs_2TiBr_6/p+ NiO/Au	6.33	1.14	76.34	5.50

Simulated results reveal the prominent roles of the two terminal layers n^+ *TiO₂* [Conf. B] and p^+ *NiO* [Conf. C] in improving performance of the basic cell [Conf. A]. Here, *TiO₂* and *NiO* layers are doped with dopant concentration 10^{16} cm^{-3} and 10^{19} $cm^{-,3}$ respectively. *NiO* with exact stoichiometric form is a wide bandgap semiconductor and possesses very high intrinsic resistivity [337], which results in poor FF of the corresponding cell. Thus, heavier doping is chosen for *NiO*. Doping in both *TiO₂* and *NiO* layers reduces the interfacial charge transport resistances and facilitates efficient carrier extraction. This leads to modification in the *J-V* characteristics through tremendous improvement in FF. Similar influence of doping in transport materials has also been reported experimentally [333]. Performance of the final cell structure [Conf. E] with both doped layers is improved synergistically in terms of FF and PCE. It yields respectively 17% and 18% increment in PCE and FF with respect to the cell with undoped layers [Conf. D].

The maximum achievable FF is estimated using the expression given below [338]:

$$FF = \frac{v_{oc} - \ln(v_{oc} + 0.72)}{v_{oc} + 1} \tag{7.4}$$

with $v_{oc} = \frac{qV_{oc}}{\eta KT}$. Here, v_{oc} is defined as normalized open circuit voltage and η is the ideality factor for diodes. For perovskite based absorber, V_{oc} exceeds 1, and thus FF may be as large as 0.9, calculated using Eq. (7.4) with η=1. It sets the theoretical limit to FF that can never be realized in practice. Since the SRH recombination model is employed in simulation, η=2 [339], instead of its ideal value 1 is considered in estimating the FF, and the maximum attainable limit of FF comes out to be 82%. The simulated FF appears as around 76%, well below the theoretical limit, as it should be. Thus, to enhance the cell performance, doping of transport layers can be treated as an effective way to modulate their electrical and optical properties.

The role of different electrode materials is further examined in the present study. All the above results are obtained with *Au* as the anode material. After otherwise finalizing the structure of the proposed solar cell, its performance is investigated for other two anode materials, such as *Ag* and *Cu* (WF ~ 4.7 *eV*). Simulated results are presented in Figure 7.15 and Table 7.9. Results indicate that the cell performance improves with metal of higher work function. Both the table and figure also reveal that *Au* outperforms the other two anode materials. Thus, the structure of the proposed inorganic *Pb*-free PSC finally emerges as *FTO/n^+ TiO_2 (10 nm)/Cs_2TiBr_6 (200 nm)/p^+ NiO (10 nm)/Au*.

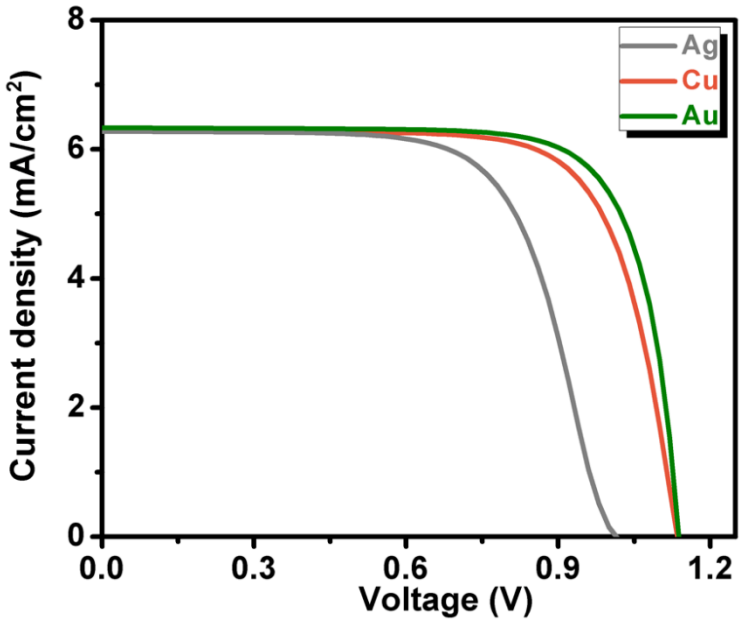

Figure 7.15: *J-V characteristics of Cs_2TiBr_6 solar cell with various anode materials*

Table 7.9: *Solar cell parameters for different anode materials*

Electrode	J_{sc} *(mA/cm²)*	V_{oc} *(V)*	FF (%)	PCE (%)
Silver (*Ag*)	6.27	1.01	66.91	4.26
Copper (*Cu*)	6.28	1.13	73.48	5.24
Gold (*Au*)	6.33	1.14	76.34	5.50

Experiments based on *Pb* PSC reported 330 *nm* as the optimum thickness for absorber materials [340-343]. Therefore, the proposed cell is further simulated with 330 *nm* thick absorber material (Cs_2TiBr_6) along with both 10 *nm* thick n^+ TiO_2 and p^+ *NiO* layers. The *J-V* characteristics are shown in Figure 7.16 and the resulting cell parameters are listed in Table 7.10. The table also includes results of the earlier Conf. E (with 200 *nm* thick Cs_2TiBr_6) for easy comparison. Respective enhancements in PCE and J_{sc} by almost 54% and 61% are clearly evident, along with nominal deteriorations in FF and V_{oc}.

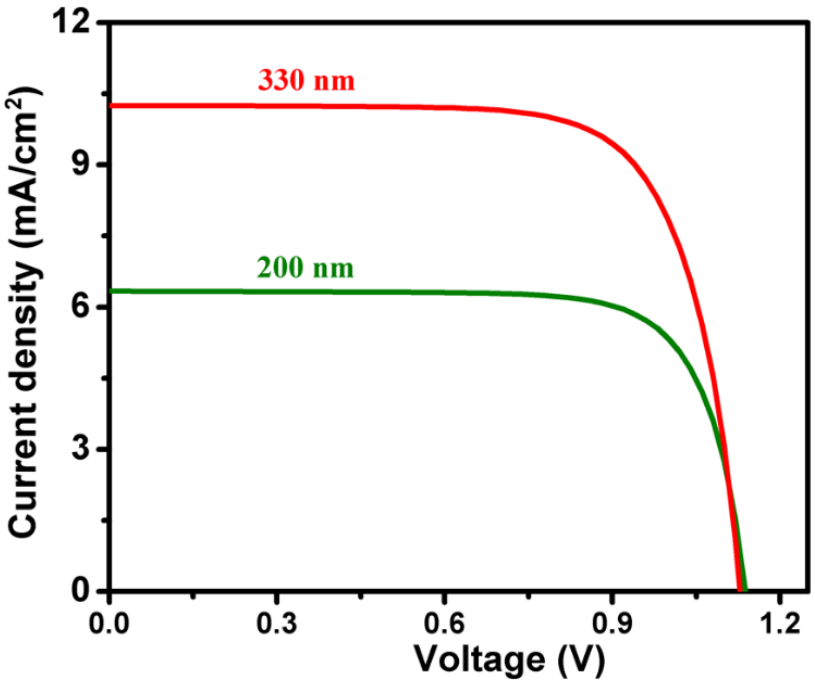

Figure 7.16: *J-V characteristics of two different absorber thicknesses in Cs_2TiBr_6 solar cell*

Table 7.10: *Solar cell parameters for different absorber thickness*

Thickness *(nm)*	**J_{sc} *(mA/cm²)***	**V_{oc} *(V)***	**FF (%)**	**PCE (%)**
200	6.33	1.14	76.34	5.50
330	10.25	1.12	73.59	8.51

The final simulated structure and corresponding energy band diagram are presented in Figure 7.17(a) and 7.17(b), respectively.

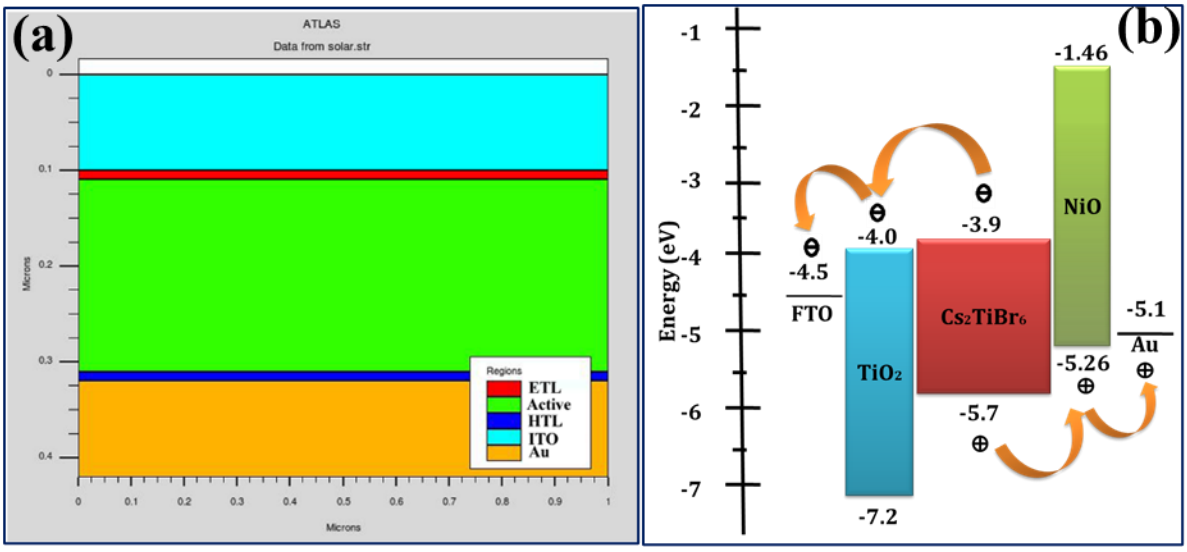

Figure 7.17: *Cs_2TiBr_6 solar cell: (a) final simulated structure and (b) Energy band diagram*

7.5 Conclusions:

In this chapter, two different kinds of solar cells have been studied through their simulation using Silvaco ATLAS Device simulator.

In the first part, performances of organic polymer based BHJ solar cells with *OC_1C_{10}PPV:PCBM* and *P3HT:PCBM* as absorber materials have been optimized and compared. From simulations of cells with cathode of *Al* and Ag, *Al* has been found to outperform *Ag*. The BHJ solar cell with *P3HT:PCBM* blend has yielded PCE more than double of that offered by the other one, for both cathode materials, although the highest efficiency thus achieved lies only around 1.7%. Next, performance of *P3HT:PCBM* blend has been further improved by incorporating transport layers for efficient collection of both types of photogenerated carriers in inverted cell configuration. *Au* has been used as the top electrode due to its inherent high atmospheric stability. After optimization of transport layer materials and their thicknesses, more than 3 times improvement in PCE, with respect to the basic cell, has been achieved using *CuPc* as HTL and *ZnO* as ETL. However, the final structure, evolved as *FTO/ZnO/P3HT:PCBM/NiO/Au,* yields PCE, FF and V_{oc} respectively of around 4%, 84% and 0.945, a truly remarkable improvement.

Lead free inorganic *Cs_2TiBr_6* perovskite solar cell has been studied in the second part of the chapter. The sole available report [198] on *Cs_2TiBr_6* established superior thermal, optical and moisture stability of the material with respect to OIHP material. In addition, *Cs_2TiBr_6* based solar cell was also reported to provide around 330 *h* of stable operation [198]. Thus, long duration stable operation and most importantly, the environment friendly nature are expected to develop *Cs_2TiBr_6* PSC as one of the front runners in the field of next generation solar cell. Therefore, in order to improve the performance of *Cs_2TiBr_6* PSC, it has been further designed and simulated with various transport layers - *TiO_2* as the material for ETL, and *CuPc*, *P3HT* and *NiO* for HTL. To derive even higher PCE, three anode materials – *Au*, *Ag* and *Cu* have also been explored. The proposed *Cs_2TiBr_6* (200 *nm*) PSC employing doped *TiO_2* (10 *nm*) and *NiO* (10 *nm*) layers has resulted in PCE of 5.5% against that of only 3.3% reported in the-then sole available work on *Cs_2TiBr_6* based PSC [198], an experimental investigation made by Chen *et. al.* In presence of *CuPc* as HTL, the PCE gets doubled in comparison with basic device configuration [conf. A] with an ETL of *TiO_2*. The best performing structure has emerged finally as *FTO/TiO_2 (10 nm)/Cs_2TiBr_6 (330 nm)/NiO (10 nm)/Au*, yielding PCE as high as 8.5%, much higher than that offered by the above organic solar cells, but still quite low compared to the *Pb*-based PSCs.

Though *NiO* has been found to be the best performing HTL material for both OSCs and PSCs, strong moisture resistance property of *CuPc* [Figure 5.12 in Chapter 5] makes it very attractive material for HTL in above cases. Thus, *CuPc* will be the appropriate choice for HTL material in designing highly stable solar cells, although their efficiencies will be compromised to some extent.

The final chapter summarizes the remarkable findings and contributions of this dissertation to some energy and environment related fields, and also points out the future scopes of further research. The first section of this chapter summarises the significant results obtained from research works carried out and presented in this dissertation. The next section focusses on the possible scopes of works that can be pursued as further extension of the above work.

8.1 Summary of results:

A comprehensive survey of existing literature in all the fields like synthesis, characterization, catalysis, solar cell, etc. are performed thoroughly in order to formulate the research problems based on *CuPc* and *ZnPc*, two prominent members of the family of organic semiconductor namely MPc, and their hybrid structures with 2D layered materials *rGO* and MoS_2. In this dissertation, synthesis of above materials and their appropriate applications in the field of next generation electronic devices including supercapacitors, fuel cells and solar cells are explored.

ZnPc nanoflakes, *CuPc* nanowires, nanotubes, microrods, *rGO* wrapped *CuPc* nanotube and MoS_2 decorated *CuPc* microrods are successfully synthesized following proper synthesis routes. All such synthesized samples are subsequently subjected to extensive characterization processes to confirm their proper formation.

To resolve environmental issue related to wastewater released from textile industry, *CuPc* nanowires and *rGO-CuPc* hybrid are employed as catalysts in the processes for waste water treatment. Ultrasound based AOPs are also employed in the presence of catalyst for degradation of textile dyes (*viz. RB*) present in wastewater. By the process of sonophotocatalysis with *CuPc* nanowires as catalyst, around 81% *RB* degradation efficiency is achieved in 60 *min,* using bath sonicator as the source of ultrasound. *rGO-CuPc* hybrid efficiently removes around 92% *RB* in 100 *min* in presence of ultrasonic irradiation from probe sonicator. The influences of several parameters *viz.* dissolved gas, pH, scavenger, enhancer, etc. on catalytic activity are also investigated. The significant contribution of *rGO* to the hybrid system is also probed to justify the enhancement of catalytic activity as compared to pristine *CuPc* nanotube. The *CuPc* nanowires and *rGO-CuPc* hybrid emerge as efficient sonophotocatalyst and sonocatalyst respectively, for the waste water treatment. As per the Examiner's comment, it is true that efficiency of RB dye degradation is low as compared to other standard inorganic materials. Metal Phthalocyanine (MPc) class of organic materials are not well studied in the field of photocatalysis, so our objective is to investigate about the

activity of such materials to have new insights. I have performed the catalysis of RB taking very small amount of catalyst (CuPc) dosage as compared to reported inorganic materials. CuPc is expected to act as promising semiconductor material in modern electronics involving organic materials, e.g. in organic solar cell, OFET, etc. and also to be used as self-cleaning material in future electronic devices.

In the context of energy storage and conversion, electrochemical properties *viz.* supercapacitance and ORR are examined using MPcs and their hybrids. Pristine forms of *CuPc* and *ZnPc* are employed as supercapacitor anode materials in alkaline media, and both are found to exhibit moderate activity with good cycling stability. Next, electrocatalytic ORR activity of *rGO-CuPc* and MoS_2*-CuPc* hybrids are investigated using 0.1 *M KOH* electrolyte. Both follow the efficient four electron reaction pathway for the reduction of O_2 as compared to their individual counterparts. Excellent stability is observed in MoS_2*-CuPc* hybrid as compared to *Pt/C*. Thus, MoS_2*-CuPc* hybrid emerges as the potential electrocatalyst material for future generation metal-air battery and fuel cell applications.

Finally, for the purpose of solar energy harvesting, simulation based studies are carried out for two different kinds of solar cells using Silvaco ATLAS Device simulator. Organic polymer based BHJ solar cells are studied first with OC_1C_{10}*PPV:PCBM* and *P3HT:PCBM* as absorber materials. *P3HT:PCBM* is found to be the more efficient photon absorber, yielding PCE of 1.7% for the BHJ solar cell. In attempt to improve the cell performance, various transport layers are introduced on either side of the absorber, where the materials and their thicknesses are optimized properly. *P3HT:PCBM* solar cell designed with HTL of *CuPc* improves the cell efficiency by 3.3 times compared to its basic structure. However, the most efficient cell configuration emerges as *FTO/ZnO/P3HT:PCBM/NiO/Au*, offering PCE and FF of around 4% and 84%, respectively. Next, new kind of *Pb*-free double perovskite absorber material, Cs_2TiBr_6 is chosen as a replacement of traditional *Pb*-based materials due to the environmental issues raised from the presence of *Pb*. A variety of HTL materials are tried to improve the performance of the cell with ETL of TiO_2. Among them, HTL of *CuPc* makes the PCE almost double of that of the basic device structure. Following a sequence of optimizing steps, the final structure results as *FTO/*TiO_2*(10 nm)/*Cs_2TiBr_6*(330 nm)/NiO(10 nm)/Au*, yielding PCE as much as 8.5%. Although this PCE is much higher than that obtained from the above organic polymer based solar cell, it is still quite low with respect to the PCE offered by *Pb*-based PSCs. But most importantly, high moisture stability of *CuPc* and long duration stable performance *of* Cs_2TiBr_6 are expected to make such material combination popular in designing environment friendly solar cells in near future.

8.2 Future scopes of work:

The work presented in this dissertation carry quite importance in the present scenario, reflected from recent literature, and, may be further extended in the following directions. Among various MPcs, *CuPc* and *ZnPc* nanostructures and *CuPc* based heterostructures have been synthesized and characterized here. Recently, Verma et al. has synthesized *CuPc* nanotube, described in this thesis, for the preparation of *rGO-CuPc* hybrid, and carried out measurements to find their tribological properties [344]. In addition, wastewater remediation by the photo assisted dye removal as well as aqueous *Cr(VI)* reduction process using *GO*/*N-CuMe*$_2$*Pc* nanorod hybrid and *TAZnPc-PANI@Fe*$_2$*O*$_3$, respectively has been reported in recent years [345, 346]. As an extension of the work in the fields of energy storage, one may fabricate symmetric/asymmetric SC devices using *CuPc* as electrode material, and study their suitability for driving portable electronic components. There are lots of possibilities to synthesize *ZnPc* based heterostructures as well as *CuPc* heterostructures with different materials other than *rGO* and MoS_2. Hybrids of *ZnPc* and *CuPc* with carbon and *MXenes* have also been examined as electrode materials for SC and ORR applications [235, 347, 348].

In the field of photocatalytic applications, efficiency of dye removal process by any single material is limited by fast recombination of photogenerated electron hole pairs, that in turn, hamper the generation of $OH^{\cdot}$ radicals. These $OH^{\cdot}$ radicals help to degrade organic contaminants present in wastewater. Type II heterojunction was well studied for efficient photocatalytic activity due to the increase in charge carrier separation, and thereby, reducing the recombination of electrons and holes [349-351]. The effect of type I heterojunction on photocatalytic degradation of pollutants is still unexplored. In recent years, investigation of photocatalytic hydrogen production using type I heterojunction have been initiated [352]. A recent study [353] demands that photocatalytic H_2 production by water splitting can also be accomplished by *CuPc* and *ZnPc* based type I heterojunction. In addition, ultrasound along with light assisted catalytic activity of such hetero-interface needs further investigation.

In the field of solar energy harvesting, the work on environment friendly PSC [354] presented in this dissertation, has already arrested intense interest of researchers and as a result, a number of works have been already reported [355-357]. In some works, a variety of HTL and ETL materials are used in simulation of Cs_2TiBr_6 solar cells to achieve higher PCE. In addition, life cycle assessment of Cs_2TiX_6 and $Cs_2TiI_{6-x}Br_x$ based solar cells has been investigated by Chakraborty *et al.* in recent times [358]. Such studies proclaim the emerging prospects of these

classes of *Pb* free perovskite based solar cells to preserve the environmental sustainability. There are other numerous *Pb* free double perovskite materials *viz.* $Cs_2AgBiBr_6$ [359-361], $Cs_2AgSbBr_6$ [360, 362, 363] etc. Investigation of such *Pb* free solar cell based on simulation and experiment will open up a new era of environment friendly solar cells.

Appendix

In Silvaco ATLAS simulation platform, DECKBUILD is the central runtime environment in which entire device structures can be specified by the users. Before starting to write the program code for any device simulation, ATLAS is called by users to perform the device simulation in the following way:

go atlas

// Structure specification

***** Definition of Mesh***

X.MESH LOCATION=<VALUE> SPACING=<VALUE>

Y.MESH LOCATION=<VALUE> SPACING=<VALUE>

***** Assignment of different materials in several regions***

REGION number=<integer> <material type> <position parameters>

***** Definition of electrode***

ELECTRODE NAME=<electrode name> <position parameters>

***** Specification of doping***

DOPING <distribution type> <dopant type> <position parameters>

// Description of material models

***** Definition of material parameters***

MATERIAL <identification> <material parameters>

[*material parameters include Electron affinity (AFFINITY), room temperature band gap (EG300), electron (MUN) and hole (MUP) mobility, electron (TAUN0) and hole (TAUP0) recombination lifetimes, valence (NV300), conduction (NC300) band density of states etc.*]

***** Specification of doping***

MODELS <physical model> <model-dependent parameters> <general parameters>

[*The physical models are classified into five categories: mobility, recombination, carrier statistics, impact ionization, and tunnelling. SINGLET, Langevin and Singlet dissociation models are used in OSC simulation and Shockley-Read-Hall (SRH) is used in PSC simulation.*]

***** Assignment of contact materials***

CONTACT NAME=<name> <property specification>

// Selection of numerical solution methods

***** Specification of method***

METHOD <methods>

[*Three numerical techniques i.e. GUMMEL, NEWTON and BLOCK are commonly used. NEWTON is set as the default method*.]

// Specification of optical source

Beam num=<VALUE>, f. radiate=<library name>

[*To incorporate uniform photogeneration rate, C-interpreter function stored in library is used.*]

// Solution specification

LOG OUTFILE=<filename>

SOLVE V(initial) =<VALUE> V(step) =<VALUE> V(final)=<VALUE> name=electrode

LOAD INFILE=<filename>

SAVE OUTFILE=<filename>

// Analysis of results

EXTRACT INITIAL INFILE=”<filename>”

[*Indication of file name before extraction of parameters*]

EXTRACT NAME="V_{oc}" X.VAL from CURVE(v."anode,” i."cathode") where Y.VAL=0.0

[*Extraction of V_{oc} from simulated I-V data*]

TONYPLOT IVcurve.dat [*graphical presentation of simulated data*]

end

Bibliography

(1) https://www.emersonautomationexperts.com/2014/technologies/process-engineering-of nanotechnology/

(2) Ramsden, J. Essentials of nanotechnology, BookBoon: 2008.

(3) Zhang, T.; Okitsu, K.; Tursun, Y.; Talifur, D.; Abulizi, A. Enhanced sono-photocatalytic activity of $AgCl_{0.75}Br_{0.25}$ with different dimensional graphene. Ceramics International 2020, 46, 23877-23887, DOI: 10.1016/j.ceramint.2020.06.164.

(4) Zhang, H.; Qiao, J.; Li, G.; Zhang, M.; Li, S.; Wang, J.; Song, Y. Construction of coated Z-scheme Pd-$BaZrO_3$@WO_3 composite with enhanced sonocatalytic activity for diazinon degradation in aqueous solution. Sci Total Environ 2019, 663, 97-109, DOI: 10.1016/j.scitotenv.2019.01.196.

(5) Saharan, P.; Chaudhary, G. R.; Lata, S.; Mehta, S. K.; Mor, S. Ultra-fast and effective treatment of dyes from water with the synergistic effect of Ni doped ZnO nanoparticles and ultrasonication. Ultrason Sonochem 2015, 22, 317-325, DOI: 10.1016/j.ultsonch.2014.07.004.

(6) Wang, Y.; Gai, L.; Ma, W.; Jiang, H.; Peng, X.; Zhao, L. Ultrasound-Assisted Catalytic Degradation of Methyl Orange with Fe_3O_4/Polyaniline in Near Neutral Solution. Industrial & Engineering Chemistry Research 2015, 54, 2279-2289, DOI: 10.1021/ie504242k.

(7) Gholami, P.; Dinpazhoh, L.; Khataee, A.; Orooji, Y. Sonocatalytic activity of biochar-supported ZnO nanorods in degradation of gemifloxacin: Synergy study, effect of parameters and phytotoxicity evaluation. Ultrason Sonochem 2019, 55, 44-56, DOI: 10.1016/j.ultsonch.2019.03.001.

(8) He, Y.; Ma, Z.; Junior, L. B. Distinctive binary g-C_3N_4/MoS_2 heterojunctions with highly efficient ultrasonic catalytic degradation for levofloxacin and methylene blue. Ceramics International 2020, 46, 12364-12372, DOI: 10.1016/j.ceramint.2020.01.287.

(9) Brütting, W. Introduction to the physics of organic semiconductors. Physics of organic semiconductors 2005, 1-14.

(10) Menke, T. Molecular Doping of Organic Semiconductors: A Conductivity and Seebeck Study. 2013.

(11) Braun, A. v.; Tcherniac, J. Über die produkte der einwirkung von acetanhydrid auf phthalamid. Berichte der deutschen chemischen Gesellschaft 1907, 40, 2709-2714, DOI: https://doi.org/10.1002/cber.190704002202

(12) Sun, Q.; Zhu, Y.; Han, D.; Wang, C.; Zhang, Y.; Liu, C.; Wang, L.; Wang, L. Blended polymer as composite insulating layers for organic field effect transistor. Solid-State Electronics 2022, 189, 108194, DOI: 10.1016/j.sse.2021.108194.

(13) Derrien, T. L.; Lauritzen, A. E.; Kaienburg, P.; Hancox, E.; Nicklin, C.; Riede, M. Interfacial rearrangements and strain evolution in the thin film growth of ZnPc on glass. Physical Review Materials 2022, 6, 033401, DOI: 10.1103/PhysRevMaterials.6.033401.

(14) Trefon-Radziejewska, D.; Juszczyk, J.; Krzywiecki, M.; Hamaoui, G.; Horny, N.; Antoniow, J. S.; Chirtoc, M. Thermal characterization of morphologically diverse copper phthalocyanine thin layers by scanning thermal microscopy. Ultramicroscopy 2021, 233, 113435, DOI: 10.1016/j.ultramic.2021.113435.

(15) Feng, G.; Zhu, M.; Lin, X.; Xu, L.; Gao, X. Preparation of a CuPc Organic Phototransistor and Research on its Dynamic Photoelectric Properties. Journal of Electronic Materials 2021, 51, 133-140, DOI: 10.1007/s11664-021-09294-9.

(16) Heutz, S.; Salvan, G.; Jones, T. S.; Zahn, D. R. T. Effects of annealing on the properties of molecular thin film heterostructures. Advanced Materials 2003, 15, 1109-1112, DOI: 10.1002/adma.200304742

(17) Brown, C. J. Crystal structure of β-copper phthalocyanine. Journal of the Chemical Society A: Inorganic, Physical, Theoretical 1968, 2488-2493, DOI: 10.1039/J19680002488

(18) Jung, J. S.; Lee, J. W.; Kim, K.; Cho, M. Y.; Jo, S. G.; Joo, J. Rectangular Nanotubes of Copper Phthalocyanine: Application to a Single Nanotube Transistor. Chemistry of Materials 2010, 22, 2219-2225, DOI: 10.1021/cm903492k.

(19) Li, J.; Wang, S.; Li, S.; Wang, Q.; Qian, Y.; Li, X.; Liu, M.; Li, Y.; Yang, G. One-pot synthesis and self-assembly of copper phthalocyanine nanobelts through a water-chemical route. Inorganic chemistry 2008, 47, 1255-1257, DOI: 10.1021/ic7018583

(20) Xia, D.-c.; Li, W.-c.; Xu, W.; Yu, S.-k.; Fan, C.-x.; Cheng, C.-h.; Fan, Z.-q.; Du, G.-t.; Cong, F.-d.; Du, X.-g. Preparation of copper phthalocyanine crystals using solvothermal

synthesis. Chemical Research in Chinese Universities 2008, 24, 407-410, DOI: 10.1016/S1005-9040(08)60086-0

(21) Xia, D.; Yu, S.; Shen, R.; Ma, C.; Cheng, C.; Ji, D.; Fan, Z.; Wang, X.; Du, G. A novel method for the direct synthesis of crystals of copper phthalocyanine. Dyes and Pigments 2008, 78, 84-88, DOI: 10.1016/j.dyepig.2007.10.013.

(22) Ge, S.; Zhang, Y.; Huang, B.; Huang, S.; Tie, W.; Lei, Y.; He, Q.; Tu, G.; Qin, Q.; Niu, S.; Li, M.; Li, D.; Zheng, Z. Synthesis of highly crystalline copper phthalocyanine needles by solvothermal method. Materials Letters 2016, 163, 61-64, DOI: 10.1016/j.matlet.2015.10.020.

(23) Guo, Z.; Chen, B.; Zhang, M.; Mu, J.; Shao, C.; Liu, Y. Zinc phthalocyanine hierarchical nanostructure with hollow interior space: solvent–thermal synthesis and high visible photocatalytic property. Journal of colloid and interface science 2010, 348, 37-42, DOI: 10.1016/j.jcis.2010.04.035

(24) Geim, A. K.; Novoselov, K. S. The rise of graphene. In Nanoscience and technology: a collection of reviews from nature journals; World Scientific: 2010; 11-19, DOI: 10.1142/9789814287005_0002

(25) Das, B.; Sarkar, D.; Maity, S.; Chattopadhyay, K. K. Ag decorated topological surface state protected hierarchical Bi_2Se_3nanoflakes for enhanced field emission properties. Journal of Materials Chemistry C 2015, 3, 1766-1775, DOI: 10.1039/c4tc02035a.

(26) Wang, F.; Li, L.; Huang, W.; Li, L.; Jin, B.; Li, H.; Zhai, T. Submillimeter 2D Bi_2Se_3 Flakes toward High-Performance Infrared Photodetection at Optical Communication Wavelength. Advanced Functional Materials 2018, 28, 1802707, DOI: 10.1002/adfm.201802707.

(27) Sha, R.; Maity, P. C.; Rajaji, U.; Liu, T.-Y.; Bhattacharyya, T. K. Review—$MoSe_2$ Nanostructures and Related Electrodes for Advanced Supercapacitor Developments. Journal of The Electrochemical Society 2022, 169, 013503, DOI: 10.1149/1945-7111/ac4aad.

(28) Ashfaq, M.; Talreja, N.; Chauhan, D.; Viswanathan, M. R. Synthesis of Cu-doped 2D-WS_2 nanosheet-based nano-antibiotic materials for inhibiting E. Coli and S. aureus bacterial strains. New Journal of Chemistry 2022, 46, 5581-5587, DOI: 10.1039/d1nj05931a.

(29) Zhang, C.; Fei, B.; Yang, D.; Zhan, H.; Wang, J.; Diao, J.; Li, J.; Henkelman, G.; Cai, D.; Biendicho, J. J.; Morante, J. R.; Cabot, A. Robust Lithium–Sulfur Batteries Enabled by Highly

Conductive WSe_2-Based Superlattices with Tunable Interlayer Space. Advanced Functional Materials 2022, 2201322, DOI: 10.1002/adfm.202201322.

(30) Du, Z.; Feng, L.; Guo, Z.; Yan, T.; Hu, Q.; Lin, J.; Huang, Y.; Tang, C.; Fang, Y. Ultrathin h-BN/Bi_2MoO_6 heterojunction with synergetic effect for visible-light photocatalytic tetracycline degradation. Journal of Colloid and Interface Science 2021, 589, 545-555, DOI: 10.1016/j.jcis.2021.01.027

(31) Zdanowicz, E.; Herman, A. P.; Opolczynska, K.; Gorantla, S.; Olszewski, W.; Serafinczuk, J.; Hommel, D.; Kudrawiec, R. Toward h-BN/GaN Schottky Diodes: Spectroscopic Study on the Electronic Phenomena at the Interface. ACS Appl Mater Interfaces 2022, 14, 6131-6137, DOI: 10.1021/acsami.1c20352.

(32) Li, W.; Wang, F.; Chu, X.-s.; Liu, X.-y.; Dang, Y.-y. Regulation of bandgap and interfacial conductivity: Construction of carbon-doped three-dimensional porous h-BN/rGO hybrid for hydrogen evolution. Applied Surface Science 2021, 560, 150053, DOI: 10.1016/j.apsusc.2021.150053.

(33) Zhong, Q.; Li, Y.; Zhang, G. Two-dimensional MXene-based and MXene-derived photocatalysts: Recent developments and perspectives. Chemical Engineering Journal 2021, 409, 128099, DOI: 10.1016/j.cej.2020.128099.

(34) Ma, C.; Ma, M. G.; Si, C.; Ji, X. X.; Wan, P. Flexible MXene-Based Composites for Wearable Devices. Advanced Functional Materials 2021, 31, 2009524, DOI: 10.1002/adfm.202009524.

(35) Liang, Z.; Xue, Y.; Wang, X.; Zhou, Y.; Zhang, X.; Cui, H.; Cheng, G.; Tian, J. Co doped MoS_2 as cocatalyst considerably improved photocatalytic hydrogen evolution of g-C_3N_4 in an alkalescent environment. Chemical Engineering Journal 2021, 421, 130016, DOI: 10.1016/j.cej.2021.130016.

(36) Yu, H.; Ma, H.; Wu, X.; Wang, X.; Fan, J.; Yu, J. One-Step Realization of Crystallization and Cyano-Group Generation for g-C_3N_4 Photocatalysts with Improved H_2 Production. Solar RRL 2020, 5, 2000372, DOI: 10.1002/solr.202000372.

(37) Zhu, Q.; Xu, Z.; Qiu, B.; Xing, M.; Zhang, J. Emerging Cocatalysts on g-C_3N_4 for Photocatalytic Hydrogen Evolution. Small 2021, 17, e2101070, DOI: 10.1002/smll.202101070.

(38) Wang, Y.; Lv, H.; Grape, E. S.; Gaggioli, C. A.; Tayal, A.; Dharanipragada, A.; Willhammar, T.; Inge, A. K.; Zou, X.; Liu, B.; Huang, Z. A Tunable Multivariate Metal-Organic Framework as a Platform for Designing Photocatalysts. J Am Chem Soc 2021, 143, 6333-6338, DOI: 10.1021/jacs.1c01764.

(39) Li, H.; Eddaoudi, M.; O'Keeffe, M.; Yaghi, O. M. Design and synthesis of an exceptionally stable and highly porous metal-organic framework. nature 1999, 402, 276-279, DOI: 10.1038/46248

(40) Yan, J.; Liu, T.; Liu, X.; Yan, Y.; Huang, Y. Metal-organic framework-based materials for flexible supercapacitor application. Coordination Chemistry Reviews 2022, 452, 214300, DOI: 10.1016/j.ccr.2021.214300.

(41) Guo, B.; Xiao, Q. l.; Wang, S. h.; Zhang, H. 2D Layered Materials: Synthesis, Nonlinear Optical Properties, and Device Applications. Laser & Photonics Reviews 2019, 13, 1800327, DOI: 10.1002/lpor.201800327.

(42) Sang, M.; Shin, J.; Kim, K.; Yu, K. Electronic and Thermal Properties of Graphene and Recent Advances in Graphene Based Electronics Applications. Nanomaterials 2019, 9, 374, DOI: 10.3390/nano9030374.

(43) Avouris, P.; Xia, F. Graphene applications in electronics and photonics. Mrs Bulletin 2012, 37, 1225-1234, DOI: 10.1557/mrs.2012.206.

(44) Perreault, F.; Fonseca de Faria, A.; Elimelech, M. Environmental applications of graphene-based nanomaterials. Chem Soc Rev 2015, 44, 5861-5896, DOI: 10.1039/c5cs00021a.

(45) Huang, Y.; Liang, J.; Chen, Y. An overview of the applications of graphene-based materials in supercapacitors. Small 2012, 8, 1805-1834, DOI: 10.1002/smll.201102635.

(46) Kannan, M. V.; Gnana Kumar, G. Current status, key challenges and its solutions in the design and development of graphene based ORR catalysts for the microbial fuel cell applications. Biosens Bioelectron 2016, 77, 1208-20, DOI: 10.1016/j.bios.2015.10.018.

(47) Zhang, C.; Mahmood, N.; Yin, H.; Liu, F.; Hou, Y. Synthesis of phosphorus-doped graphene and its multifunctional applications for oxygen reduction reaction and lithium ion batteries. Adv Mater 2013, 25, 4932-4937, DOI: 10.1002/adma.201301870.

(48) Wilson, J. A.; Yoffe, A. D. The transition metal dichalcogenides discussion and interpretation of the observed optical, electrical and structural properties. Advances in Physics 1969, 18, 193-335, DOI: 10.1080/00018736900101307.

(49) Rahmanian, E.; Malekfar, R.; Pumera, M. Nanohybrids of Two-Dimensional Transition-Metal Dichalcogenides and Titanium Dioxide for Photocatalytic Applications. Chemistry 2018, 24, 18-31, DOI: 10.1002/chem.201703434.

(50) Kadam, S. R.; Enyashin, A. N.; Houben, L.; Bar-Ziv, R.; Bar-Sadan, M. Ni–WSe_2 nanostructures as efficient catalysts for electrochemical hydrogen evolution reaction (HER) in acidic and alkaline media. Journal of Materials Chemistry A 2020, 8, 1403-1416, DOI: 10.1039/c9ta10990k.

(51) Chen, X.; Liu, C.; Mao, S. Environmental Analysis with 2D Transition-Metal Dichalcogenide-Based Field-Effect Transistors. Nano-micro Lett. 2020, 12, 95, DOI: 10.1007/s40820-020-00438-w.

(52) Paul, T.; Ghatak, S.; Ghosh, A. Percolative switching in transition metal dichalcogenide field-effect transistors at room temperature. Nanotechnology 2016, 27, 125706, DOI: 10.1088/0957-4484/27/12/125706.

(53) Li, H.; Shi, Y.; Chiu, M.-H.; Li, L.-J. Emerging energy applications of two-dimensional layered transition metal dichalcogenides. Nano Energy 2015, 18, 293-305, DOI: 10.1016/j.nanoen.2015.10.023.

(54) Memon, F. H.; Rehman, F.; Lee, J.; Soomro, F.; Iqbal, M.; Khan, S. M.; Ali, A.; Thebo, K. H.; Choi, K. H. Transition Metal Dichalcogenide-based Membranes for Water Desalination, Gas Separation, and Energy Storage. Separation & Purification Reviews 2022, 1-15, DOI: 10.1080/15422119.2022.2037000.

(55) Ashokkumar, M.; Lee, J.; Iida, Y.; Yasui, K.; Kozuka, T.; Tuziuti, T.; Towata, A. The detection and control of stable and transient acoustic cavitation bubbles. Physical chemistry chemical physics 2009, 11, 10118-10121.

(56) Odacı, C.; Aydemir, U. The surface plasmon resonance-based fiber optic sensors: A theoretical comparative study with 2D TMDC materials. Results in Optics 2021, 3, 100063, DOI: 10.1016/j.rio.2021.100063.

(57) Coleman, J. N.; Lotya, M.; O'Neill, A.; Bergin, S. D.; King, P. J.; Khan, U.; Young, K.; Gaucher, A.; De, S.; Smith, R. J. Two-dimensional nanosheets produced by liquid exfoliation of layered materials. Science 2011, 331, 568-571, DOI: 10.1126/science.1194975

(58) Jayabal, S.; Saranya, G.; Wu, J.; Liu, Y.; Geng, D.; Meng, X. Understanding the high-electrocatalytic performance of two-dimensional MoS_2 nanosheets and their composite materials. Journal of Materials Chemistry A 2017, 5, 24540-24563.

(59) Tan, C.; Chen, J.; Wu, X.-J.; Zhang, H. Epitaxial growth of hybrid nanostructures. Nature Reviews Materials 2018, 3, DOI: 10.1038/natrevmats.2017.89.

(60) Huang, X.; Tan, C.; Yin, Z.; Zhang, H. 25th anniversary article: Hybrid nanostructures based on two-dimensional nanomaterials. Advanced Materials 2014, 26, 2185-2204.

(61) Tan, C.; Zhang, H. Two-dimensional transition metal dichalcogenide nanosheet-based composites. Chemical Society Reviews 2015, 44, 2713-2731.

(62) Jha, A.; Ghorai, U. K.; Banerjee, D.; Mukherjee, S.; Chattopadhyay, K. K. Surface modification of amorphous carbon nanotubes with copper phthalocyanine leading to enhanced field emission. RSC Adv. 2013, 3, 1227-1234, DOI: 10.1039/c2ra21776g.

(63) Mukherjee, M.; Ghorai, U. K.; Samanta, M.; Santra, A.; Das, G. P.; Chattopadhyay, K. K. Graphene wrapped Copper Phthalocyanine nanotube: Enhanced photocatalytic activity for industrial waste water treatment. Applied Surface Science 2017, 418, 156-162, DOI: 10.1016/j.apsusc.2017.01.222.

(64) Wang, Y.; Sunarso, J.; Wang, F.; Zhao, B.; Liu, X.; Chen, G. Electrospinning and hydrothermal synthesis of recyclable MoS_2/CNFs hybrid with enhanced visible-light photocatalytic performance. Ceramics International 2017, 43, 11028-11033, DOI: 10.1016/j.ceramint.2017.05.145.

(65) Kwon, I. S.; Kwak, I. H.; Kim, J. Y.; Abbas, H. G.; Debela, T. T.; Seo, J.; Cho, M. K.; Ahn, J. P.; Park, J.; Kang, H. S. Two-dimensional MoS_2/Fe-phthalocyanine hybrid nanostructures as excellent electrocatalysts for hydrogen evolution and oxygen reduction reactions. Nanoscale 2019, 11, 14266-14275, DOI: 10.1039/c9nr04156g.

(66) Ding, L.; Jiang, D.; Wen, Z.; Xu, Y.; Guo, Y.; Ding, C.; Wang, K. Ultrasensitive and visible light-responsive photoelectrochemical aptasensor for edifenphos based on Zinc

phthalocyanine sensitized MoS_2 nanosheets. Biosens Bioelectron 2020, 150, 111867, DOI: 10.1016/j.bios.2019.111867.

(67) Ibrahim, S.; Pal, T.; Ghosh, S. The sonochemical functionalization of MoS_2 by zinc phthalocyanine and its visible light-induced photocatalytic activity. New Journal of Chemistry 2019, 43, 10118-10125, DOI: 10.1039/c8nj05976d.

(68) Perevalov, V. P.; Vinokurov, E. G.; Zuev, K. V.; Vasilenko, E. A.; Tsivadze, A. Y. Modification and application of metal phthalocyanines in heterogeneous systems. Protection of Metals and Physical Chemistry of Surfaces 2017, 53, 199-214, DOI: 10.1134/s2070205117020186.

(69) Kozbial, A.; Gong, X.; Liu, H.; Li, L. Understanding the intrinsic water wettability of molybdenum disulfide (MoS_2). Langmuir 2015, 31, 8429-8435.

(70) Choi, S.; Shaolin, Z.; Yang, W. Layer-number-dependent work function of MoS_2 nanoflakes. Journal of the Korean Physical Society 2014, 64, 1550-1555, DOI: 10.3938/jkps.64.1550.

(71) Rees, N. V.; Compton, R. G. Electrochemical Applications of Power Ultrasound. Ultrasound in Chemistry: Analytical Applications 2008, 81-105.

(72) Pirsaheb, M.; Moradi, N. Sonochemical degradation of pesticides in aqueous solution: investigation on the influence of operating parameters and degradation pathway – a systematic review. RSC Advances 2020, 10, 7396-7423, DOI: 10.1039/c9ra11025a.

(73) Cheng, X.; Zhang, M.; Xu, B.; Adhikari, B.; Sun, J. The principles of ultrasound and its application in freezing related processes of food materials: A review. Ultrasonics sonochemistry 2015, 27, 576-585.

(74) Gielen, B.; Jordens, J.; Janssen, J.; Pfeiffer, H.; Wevers, M.; Thomassen, L. C. J.; Braeken, L.; Van Gerven, T. Characterization of stable and transient cavitation bubbles in a milliflow reactor using a multibubble sonoluminescence quenching technique. Ultrasonics Sonochemistry 2015, 25, 31-39.

(75) Khataee, A.; Vahid, B.; Saadi, S.; Joo, S. W. Development of an empirical kinetic model for sonocatalytic process using neodymium doped zinc oxide nanoparticles. Ultrason Sonochem 2016, 29, 146-55, DOI: 10.1016/j.ultsonch.2015.09.004.

(76) Ashokkumar, M. The characterization of acoustic cavitation bubbles–an overview. Ultrasonics sonochemistry 2011, 18, 864-872.

(77) Ghodbane, H.; Hamdaoui, O. Degradation of Acid Blue 25 in aqueous media using 1700 kHz ultrasonic irradiation: ultrasound/Fe (II) and ultrasound/H2O2 combinations. Ultrasonics Sonochemistry 2009, 16, 593-598.

(78) Weavers, L. K.; Malmstadt, N.; Hoffmann, M. R. Kinetics and mechanism of pentachlorophenol degradation by sonication, ozonation, and sonolytic ozonation. Environmental science & technology 2000, 34, 1280-1285.

(79) Yasui, K. Multibubble Sonoluminescence from a Theoretical Perspective. Molecules 2021, 26 (15), DOI: 10.3390/molecules26154624.

(80) Hammer, D.; Frommhold, L. Spectra of sonoluminescent rare-gas bubbles. Physical Review Letters 2000, 85, 1326.

(81) Putterman, S. J.; Weninger, K. R. Sonoluminescence: How bubbles turn sound into light. Annual Review of Fluid Mechanics 2000, 32, 445-476.

(82) Barber, B. P.; Hiller, R. A.; Löfstedt, R.; Putterman, S. J.; Weninger, K. R. Defining the unknowns of sonoluminescence. Physics Reports 1997, 281, 65-143.

(83) Vazquez, G.; Camara, C.; Putterman, S.; Weninger, K. Sonoluminescence: nature's smallest blackbody. Optics letters 2001, 26, 575-577.

(84) Bagal, M. V.; Gogate, P. R. Sonochemical degradation of alachlor in the presence of process intensifying additives. Separation and purification technology 2012, 90, 92-100.

(85) Raut-Jadhav, S.; Saharan, V. K.; Pinjari, D. V.; Saini, D. R.; Sonawane, S. H.; Pandit, A. B. Intensification of degradation of imidacloprid in aqueous solutions by combination of hydrodynamic cavitation with various advanced oxidation processes (AOPs). Journal of Environmental Chemical Engineering 2013, 1, 850-857.

(86) Raut-Jadhav, S.; Pinjari, D. V.; Saini, D. R.; Sonawane, S. H.; Pandit, A. B. Intensification of degradation of methomyl (carbamate group pesticide) by using the combination of ultrasonic cavitation and process intensifying additives. Ultrasonics Sonochemistry 2016, 31, 135-142.

(87) Golash, N.; Gogate, P. R. Degradation of dichlorvos containing wastewaters using sonochemical reactors. Ultrasonics sonochemistry 2012, 19, 1051-1060.

(88) Khataee, A.; Saadi, S.; Vahid, B.; Joo, S. W.; Min, B. K. Sonocatalytic degradation of Acid Blue 92 using sonochemically prepared samarium doped zinc oxide nanostructures. Ultrason Sonochem 2016, 29, 27-38, DOI: 10.1016/j.ultsonch.2015.07.026.

(89) Khataee, A.; Saadi, S.; Vahid, B. Kinetic modeling of sonocatalytic degradation of reactive orange 29 in the presence of lanthanide-doped ZnO nanoparticles. Ultrason Sonochem 2017, 34, 98-106, DOI: 10.1016/j.ultsonch.2016.05.026.

(90) Khataee, A.; Soltani, R. D.; Karimi, A.; Joo, S. W. Sonocatalytic degradation of a textile dye over Gd-doped ZnO nanoparticles synthesized through sonochemical process. Ultrason Sonochem 2015, 23, 219-30, DOI: 10.1016/j.ultsonch.2014.08.023.

(91) Khataee, A.; Saadi, S.; Vahid, B.; Joo, S. W. Sonochemical synthesis of holmium doped zinc oxide nanoparticles: Characterization, sonocatalysis of reactive orange 29 and kinetic study. Journal of Industrial and Engineering Chemistry 2016, 35, 167-176, DOI: 10.1016/j.jiec.2015.12.028.

(92) Song, L.; Zhang, S.; Wu, X.; Wei, Q. Synthesis of porous and trigonal TiO_2 nanoflake, its high activity for sonocatalytic degradation of rhodamine B and kinetic analysis. Ultrason Sonochem 2012, 19, 1169-73, DOI: 10.1016/j.ultsonch.2012.03.011.

(93) Chen, X.; Dai, J.; Shi, G.; Li, L.; Wang, G.; Yang, H. Sonocatalytic degradation of Rhodamine B catalyzed by beta-Bi_2O_3 particles under ultrasonic irradiation. Ultrason Sonochem 2016, 29, 172-7, DOI: 10.1016/j.ultsonch.2015.08.010.

(94) Sancheti, S. V.; Saini, C.; Ambati, R.; Gogate, P. R. Synthesis of ultrasound assisted nanostuctured photocatalyst (NiO supported over CeO_2) and its application for photocatalytic as well as sonocatalytic dye degradation. Catalysis Today 2018, 300, 50-57, DOI: 10.1016/j.cattod.2017.02.047.

(95) He, L. L.; Liu, X. P.; Wang, Y. X.; Wang, Z. X.; Yang, Y. J.; Gao, Y. P.; Liu, B.; Wang, X. Sonochemical degradation of methyl orange in the presence of Bi_2WO_6: Effect of operating parameters and the generated reactive oxygen species. Ultrason Sonochem 2016, 33, 90-98, DOI: 10.1016/j.ultsonch.2016.04.028.

(96) Zhou, M.; Yang, H.; Xian, T.; Li, R. S.; Zhang, H. M.; Wang, X. X. Sonocatalytic degradation of RhB over $LuFeO_3$ particles under ultrasonic irradiation. J Hazard Mater 2015, 289, 149-157, DOI: 10.1016/j.jhazmat.2015.02.054.

(97) Khataee, A.; Kayan, B.; Gholami, P.; Kalderis, D.; Akay, S. Sonocatalytic degradation of an anthraquinone dye using TiO_2-biochar nanocomposite. Ultrason Sonochem 2017, 39, 120-128, DOI: 10.1016/j.ultsonch.2017.04.018.

(98) Zhu, L.; Chung, J. D.; Oh, W. C. Rapid sonochemical synthesis of novel PbSe-graphene-TiO_2 composite sonocatalysts with enhanced on decolorization performance and generation of ROS. Ultrason Sonochem 2015, 27, 252-261, DOI: 10.1016/j.ultsonch.2015.05.037.

(99) Nuengmatcha, P.; Chanthai, S.; Mahachai, R.; Oh, W.-C. Sonocatalytic performance of ZnO/graphene/TiO_2 nanocomposite for degradation of dye pollutants (methylene blue, texbrite BAC-L, texbrite BBU-L and texbrite NFW-L) under ultrasonic irradiation. Dyes and Pigments 2016, 134, 487-497, DOI: 10.1016/j.dyepig.2016.08.006.

(100) Meng, Z. D.; Zhu, L.; Choi, J. G.; Park, C. Y.; Oh, W. C. Sonocatalytic degradation of Rhodamine B in the presence of C_{60} and CdS coupled TiO_2 particles. Ultrason Sonochem 2012, 19, 143-50, DOI: 10.1016/j.ultsonch.2011.05.006.

(101) Khataee, A.; Kayan, B.; Kalderis, D.; Karimi, A.; Akay, S.; Konsolakis, M. Ultrasound-assisted removal of Acid Red 17 using nanosized Fe_3O_4-loaded coffee waste hydrochar. Ultrason Sonochem 2017, 35, 72-80, DOI: 10.1016/j.ultsonch.2016.09.004.

(102) Panahian, Y.; Arsalani, N.; Nasiri, R. Enhanced photo and sono-photo degradation of crystal violet dye in aqueous solution by 3D flower like F-TiO_2(B)/fullerene under visible light. Journal of Photochemistry and Photobiology A: Chemistry 2018, 365, 45-51, DOI: 10.1016/j.jphotochem.2018.07.035.

(103) Panahian, Y.; Arsalani, N. Synthesis of Hedgehoglike F-TiO_2(B)/CNT Nanocomposites for Sonophotocatalytic and Photocatalytic Degradation of Malachite Green (MG) under Visible Light: Kinetic Study. J Phys Chem A 2017, 121, 5614-5624, DOI: 10.1021/acs.jpca.7b02580.

(104) Kumar, R.; Kumar, G.; Akhtar, M. S.; Umar, A. Sonophotocatalytic degradation of methyl orange using ZnO nano-aggregates. Journal of Alloys and Compounds 2015, 629, 167-172, DOI: 10.1016/j.jallcom.2014.12.232.

(105) Dinesh, G. K.; Anandan, S.; Sivasankar, T. Synthesis of Fe/ZnO composite nanocatalyst and its sonophotocatalytic activity on acid yellow 23 dye and real textile effluent. Clean Technologies and Environmental Policy 2016, 18, 1889-1903, DOI: 10.1007/s10098-016-1117-z.

(106) Reddy, D. R.; Dinesh, G. K.; Anandan, S.; Sivasankar, T. Sonophotocatalytic treatment of Naphthol Blue Black dye and real textile wastewater using synthesized Fe doped TiO_2. Chemical Engineering and Processing: Process Intensification 2016, 99, 10-18, DOI: 10.1016/j.cep.2015.10.019.

(107) Zhang, M.; Shao, C.; Guo, Z.; Zhang, Z.; Mu, J.; Zhang, P.; Cao, T.; Liu, Y. Highly efficient decomposition of organic dye by aqueous-solid phase transfer and in situ photocatalysis using hierarchical copper phthalocyanine hollow spheres. ACS Appl Mater Interfaces 2011, 3, 2573-8, DOI: 10.1021/am200412t.

(108) Guo, X.; Zhou, X.; Li, X.; Shao, C.; Han, C.; Li, X.; Liu, Y. Bismuth oxychloride (BiOCl)/copper phthalocyanine (CuTNPc) heterostructures immobilized on electrospun polyacrylonitrile nanofibers with enhanced activity for floating photocatalysis. J Colloid Interface Sci 2018, 525, 187-195, DOI: 10.1016/j.jcis.2018.04.028.

(109) Priyanka, K. P.; Sankararaman, S.; Balakrishna, K. M.; Varghese, T. Enhanced visible light photocatalysis using TiO_2 /phthalocyanine nanocomposites for the degradation of selected industrial dyes. Journal of Alloys and Compounds 2017, 720, 541-549, DOI: 10.1016/j.jallcom.2017.05.308.

(110) Han, X.; Han, Z.; Li, J.; Zhao, J.; Zhao, X. Coordinative integration of copper (II) and iron (II) phthalocyanine into amidoximated PAN fiber for enhanced photocatalytic activity under visible light irradiation. J Colloid Interface Sci 2019, 533, 333-343, DOI: 10.1016/j.jcis.2018.08.076.

(111) Soloveichik, G. L. Battery technologies for large-scale stationary energy storage. Annual review of chemical and biomolecular engineering 2011, 2, 503-527.

(112) San Martin, I.; San Martin, J. J.; Aperribay, V.; Eguia, P. European Association for the Development of Renewable Energies. Environment and Power Quality, Energy Storage Technologies for Electric Applications, Spain 2011.

(113) Saleem, A. M.; Desmaris, V.; Enoksson, P. Performance Enhancement of Carbon Nanomaterials for Supercapacitors. Journal of Nanomaterials 2016, 2016, 1-17, DOI: 10.1155/2016/1537269.

(114) Akinwolemiwa, B.; Peng, C.; Chen, G. Z. Redox Electrolytes in Supercapacitors. Journal of The Electrochemical Society 2015, 162, A5054-A5059, DOI: 10.1149/2.0111505jes.

(115) Al Ashraf, A. Nitrogen and sulfur-doped carbon nanofiber mixed oxides composites for supercapacitor applications. 2016.

(116) Zheng, J.; Hu, T.; Zhang, Y.; Lv, T.; Tian, F.; Meng, C. Template-free synthesis of porous V_2O_5 flakes as a battery-type electrode material with high capacity for supercapacitors. Colloids and Surfaces A: Physicochemical and Engineering Aspects 2018, 553, 317-326, DOI: 10.1016/j.colsurfa.2018.05.090.

(117) Xu, X.; Wu, J.; Yang, N.; Na, H.; Li, L.; Gao, J. Cr_2O_3: a novel supercapacitor electrode material with high capacitive performance. Materials Letters 2015, 142, 172-175, DOI: 10.1016/j.matlet.2014.12.022.

(118) Wu, F.; Wang, X.; Hu, S.; Hao, C.; Gao, H.; Zhou, S. Solid-state preparation of CuO/ZnO nanocomposites for functional supercapacitor electrodes and photocatalysts with enhanced photocatalytic properties. International Journal of Hydrogen Energy 2017, 42, 30098-30108, DOI: 10.1016/j.ijhydene.2017.10.064.

(119) Liu, P.; Zhu, Y.; Gao, X.; Huang, Y.; Wang, Y.; Qin, S.; Zhang, Y. Rational construction of bowl-like MnO_2 nanosheets with excellent electrochemical performance for supercapacitor electrodes. Chemical Engineering Journal 2018, 350, 79-88, DOI: 10.1016/j.cej.2018.05.169.

(120) Kennaz, H.; Harat, A.; Guellati, O.; Momodu, D. Y.; Barzegar, F.; Dangbegnon, J. K.; Manyala, N.; Guerioune, M. Synthesis and electrochemical investigation of spinel cobalt ferrite magnetic nanoparticles for supercapacitor application. Journal of Solid State Electrochemistry 2017, 22, 835-847, DOI: 10.1007/s10008-017-3813-y.

(121) Jadhav, V. V.; Zate, M. K.; Liu, S.; Naushad, M.; Mane, R. S.; Hui, K. N.; Han, S.-H. Mixed-phase bismuth ferrite nanoflake electrodes for supercapacitor application. Applied Nanoscience 2015, 6, 511-519, DOI: 10.1007/s13204-015-0469-8.

(122) Mu, J.; Shao, C.; Guo, Z.; Zhang, M.; Zhang, Z.; Zhang, P.; Chen, B.; Liu, Y. Solvothermal synthesis and electrochemical properties of 3D flower-like iron phthalocyanine hierarchical nanostructure. Nanoscale 2011, 3, 5126, DOI: 10.1039/c1nr10627a.

(123) Lekitima, J. N.; Ozoemena, K. I.; Jafta, C. J.; Kobayashi, N.; Song, Y.; Tong, D.; Chen, S.; Oyama, M. High-performance aqueous asymmetric electrochemical capacitors based on graphene oxide/cobalt(ii)-tetrapyrazinoporphyrazine hybrids. Journal of Materials Chemistry A 2013,1, 2821, DOI: 10.1039/c2ta01325h.

(124) Madhuri, K. P.; John, N. S. Supercapacitor application of nickel phthalocyanine nanofibres and its composite with reduced graphene oxide. Applied Surface Science 2018, 449, 528-536, DOI: 10.1016/j.apsusc.2017.12.021.

(125) Ramachandran, R.; Hu, Q.; Wang, F.; Xu, Z.-X. Synthesis of N-$CuMe_2Pc$ nanorods/graphene oxide nanocomposite for symmetric supercapacitor electrode with excellent cyclic stability. Electrochimica Acta 2019, 298, 770-777, DOI: 10.1016/j.electacta.2018.12.163.

(126) Tian, X.; Lu, X. F.; Xia, B. Y.; Lou, X. W. Advanced Electrocatalysts for the Oxygen Reduction Reaction in Energy Conversion Technologies. Joule 2020, 4, 45-68, DOI: 10.1016/j.joule.2019.12.014.

(127) Dadyburjor, D. B.; Jewur, S. S.; Ruckenstein, E. Selective oxidation of hydrocarbons on composite oxides. Catalysis Reviews—Science and Engineering 1979, 19 (2), 293-350.

(128) Marković, N. M.; Ross Jr, P. N. Surface science studies of model fuel cell electrocatalysts. Surface Science Reports 2002, 45 (4-6), 117-229.

(129) Li, C.; Tan, H.; Lin, J.; Luo, X.; Wang, S.; You, J.; Kang, Y.-M.; Bando, Y.; Yamauchi, Y.; Kim, J. Emerging Pt-based electrocatalysts with highly open nanoarchitectures for boosting oxygen reduction reaction. Nano Today 2018, 21, 91-105, DOI: 10.1016/j.nantod.2018.06.005.

(130) Ortiz-Medina, J.; Wang, Z.; Cruz-Silva, R.; Morelos-Gomez, A.; Wang, F.; Yao, X.; Terrones, M.; Endo, M. Defect engineering and surface functionalization of nanocarbons for metal-free catalysis. Advanced Materials 2019, 31, 1805717.

(131) Wu, K. H.; Wang, D. W.; Su, D. S.; Gentle, I. R. A discussion on the activity origin in metal-free nitrogen-doped carbons for oxygen reduction reaction and their mechanisms. ChemSusChem 2015, 8, 2772-2788.

(132) Niu, W.; Pakhira, S.; Marcus, K.; Li, Z.; Mendoza-Cortes, J. L.; Yang, Y. Apically Dominant Mechanism for Improving Catalytic Activities of N-Doped Carbon Nanotube Arrays in Rechargeable Zinc–Air Battery. Advanced Energy Materials 2018, 8, 1800480.

(133) Chen, Y.; Ji, S.; Chen, C.; Peng, Q.; Wang, D.; Li, Y. Single-atom catalysts: synthetic strategies and electrochemical applications. Joule 2018, 1242-1264.

(134) Yi, J.-D.; Xu, R.; Wu, Q.; Zhang, T.; Zang, K.-T.; Luo, J.; Liang, Y.-L.; Huang, Y.-B.; Cao, R. Atomically dispersed iron–nitrogen active sites within porphyrinic triazine-based

frameworks for oxygen reduction reaction in both alkaline and acidic media. ACS Energy Letters 2018, 3, 883-889.

(135) Wang, J.; Huang, Z.; Liu, W.; Chang, C.; Tang, H.; Li, Z.; Chen, W.; Jia, C.; Yao, T.; Wei, S. Design of N-coordinated dual-metal sites: a stable and active Pt-free catalyst for acidic oxygen reduction reaction. Journal of the American Chemical Society 2017, 139, 17281-17284.

(136) Ma, Y.; Li, J.; Liao, X.; Luo, W.; Huang, W.; Meng, J.; Chen, Q.; Xi, S.; Yu, R.; Zhao, Y.; Zhou, L.; Mai, L. Heterostructure Design in Bimetallic Phthalocyanine Boosts Oxygen Reduction Reaction Activity and Durability. Advanced Functional Materials 2020, 30, 2005000, DOI: 10.1002/adfm.202005000.

(137) Valverde-Gonzalez, A.; Guan, L. Z.; Ferrer, M. L.; Iglesias, M.; Maya, E. M. Iron Phthalocyanine-Knitted Polymers as Electrocatalysts for the Oxygen Reduction Reaction. ACS Appl Mater Interfaces 2020, 12, 32681-32688, DOI: 10.1021/acsami.0c07412.

(138) Mukherjee, B. Solvothermally Synthesized Iron Phthalocyanine Nanostructure for High ORR Response: A Joint Experimental Investigation and DFT Analysis. Journal of The Electrochemical Society 2020, 167, 116501, DOI: 10.1149/1945-7111/ab9e3a.

(139) Mukherjee, M.; Samanta, M.; Banerjee, P.; Chattopadhyay, K. K.; Das, G. P. Endorsement of Manganese Phthalocyanine microstructures as electrocatalyst in ORR: Experimental and computational study. Electrochimica Acta 2019, 296, 528-534, DOI: 10.1016/j.electacta.2018.11.043.

(140) Anandhababu, G.; Abbas, S. C.; Lv, J.; Ding, K.; Liu, Q.; Babu, D. D.; Huang, Y.; Xie, J.; Wu, M.; Wang, Y. Highly exposed Fe-N_4 active sites in porous poly-iron-phthalocyanine based oxygen reduction electrocatalyst with ultrahigh performance for air cathode. Dalton Trans 2017, 46 (6), 1803-1810, DOI: 10.1039/c6dt04705j.

(141) Mukherjee, M.; Samanta, M.; Ghorai, U. K.; Murmu, S.; Das, G. P.; Chattopadhyay, K. K. One pot solvothermal synthesis of ZnPc nanotube and its composite with RGO: A high performance ORR catalyst in alkaline medium. Applied Surface Science 2018, 449, 144-151, DOI: 10.1016/j.apsusc.2018.01.155.

(142) Jiang, Y.; Lu, Y.; Lv, X.; Han, D.; Zhang, Q.; Niu, L.; Chen, W. Enhanced catalytic performance of Pt-free iron phthalocyanine by graphene support for efficient oxygen reduction reaction. Acs Catalysis 2013, 3, 1263-1271.

(143) Li, T.; Peng, Y.; Li, K.; Zhang, R.; Zheng, L.; Xia, D.; Zuo, X. Enhanced activity and stability of binuclear iron (III) phthalocyanine on graphene nanosheets for electrocatalytic oxygen reduction in acid. Journal of Power Sources 2015, 293, 511-518, DOI: 10.1016/j.jpowsour.2015.05.099.

(144) Ding, L.; Qiao, J.; Dai, X.; Zhang, J.; Zhang, J.; Tian, B. Highly active electrocatalysts for oxygen reduction from carbon-supported copper-phthalocyanine synthesized by high temperature treatment. International Journal of Hydrogen Energy 2012, 37 (19), 14103-14113, DOI: 10.1016/j.ijhydene.2012.07.046.

(145) Liu, Y.; Wu, Y.-Y.; Lv, G.-J.; Pu, T.; He, X.-Q.; Cui, L.-L. Iron(II) phthalocyanine covalently functionalized graphene as a highly efficient non-precious-metal catalyst for the oxygen reduction reaction in alkaline media. Electrochimica Acta 2013, 112, 269-278, DOI: 10.1016/j.electacta.2013.08.174.

(146) Zhang, Z.; Yang, S.; Dou, M.; Liu, H.; Gu, L.; Wang, F. Systematic study of transition-metal (Fe, Co, Ni, Cu) phthalocyanines as electrocatalysts for oxygen reduction and their evaluation by DFT. RSC Advances 2016, 6, 67049-67056, DOI: 10.1039/c6ra12426g.

(147) Li, M.; Bo, X.; Zhang, Y.; Han, C.; Guo, L. Comparative study on the oxygen reduction reaction electrocatalytic activities of iron phthalocyanines supported on reduced graphene oxide, mesoporous carbon vesicle, and ordered mesoporous carbon. Journal of Power Sources 2014, 264, 114-122, DOI: 10.1016/j.jpowsour.2014.04.101.

(148) Cui, L.; Lv, G.; Dou, Z.; He, X. Fabrication of iron phthalocyanine/graphene micro/nanocomposite by solvothermally assisted π–π assembling method and its application for oxygen reduction reaction. Electrochimica Acta 2013, 106, 272-278, DOI: 10.1016/j.electacta.2013.05.077.

(149) Huang, H.; Feng, X.; Du, C.; Song, W. High-quality phosphorus-doped MoS2 ultrathin nanosheets with amenable ORR catalytic activity. Chem Commun (Camb) 2015, 51 (37), 7903-6, DOI: 10.1039/c5cc01841b.

(150) He, T.; Xu, L.; Zhang, Y.; Huang, H.; Jiao, H. High-quality vanadium-doped MoS_2 ultrathin nanosheets as an efficient ORR catalyst. New Journal of Chemistry 2019, 43 (3), 1611-1616, DOI: 10.1039/c8nj05365k.

(151) Huang, H.; Feng, X.; Du, C.; Wu, S.; Song, W. Incorporated oxygen in MoS_2 ultrathin nanosheets for efficient ORR catalysis. Journal of Materials Chemistry A 2015, 3 (31), 16050-16056, DOI: 10.1039/c5ta01600b.

(152) Zhou, J.; Xiao, H.; Zhou, B.; Huang, F.; Zhou, S.; Xiao, W.; Wang, D. Hierarchical MoS_2–rGO nanosheets with high MoS_2 loading with enhanced electro-catalytic performance. Applied Surface Science 2015, 358, 152-158, DOI: 10.1016/j.apsusc.2015.07.187.

(153) Beeby, S. P.; Cao, Z.; Almussallam, A. Kinetic, thermoelectric and solar energy harvesting technologies for smart textiles. In Multidisciplinary Know-How for Smart-Textiles Developers; Elsevier: 2013; pp 306-328.

(154) Swapna, P.; Rao, Y. S. Simulation Studies on Semiconducting Single Walled Carbon Nanotube Based Bilayer and Bulk Hetero Junction Organic Solar Cells. Materials Today: Proceedings 2015, 2 (4-5), 1634-1641, DOI: 10.1016/j.matpr.2015.07.090.

(155) Wiedenmann, O.; Abdellah, A.; Scarpa, G.; Lugli, P. Design and fabrication of organic solar cells structured via nanoimprint lithography. Journal of Physics: Conference Series 2009, 193, 012115, DOI: 10.1088/1742-6596/193/1/012115.

(156) Miranda, P. B.; Moses, D.; Heeger, A. J. Ultrafast photogeneration of charged polarons in conjugated polymers. Physical Review B 2001, 64 (8), 081201.

(157) Mayer, A. C.; Scully, S. R.; Hardin, B. E.; Rowell, M. W.; McGehee, M. D. Polymer-based solar cells. Materials today 2007, 10 (11), 28-33.

(158) Nunzi, J.-M. Organic photovoltaic materials and devices. Comptes Rendus Physique 2002, 3 (4), 523-542.

(159) Mozer, A. J.; Sariciftci, N. S. Conjugated polymer photovoltaic devices and materials. Comptes Rendus Chimie 2006, 9 (5-6), 568-577.

(160) Sariciftci, N. S.; Braun, D.; Zhang, C.; Srdanov, V. I.; Heeger, A. J.; Stucky, G.; Wudl, F. Semiconducting polymer-buckminsterfullerene heterojunctions: Diodes, photodiodes, and photovoltaic cells. Applied physics letters 1993, 62 (6), 585-587.

(161) Parker, I. D. Carrier tunneling and device characteristics in polymer light-emitting diodes. Journal of Applied Physics 1994, 75 (3), 1656-1666.

(162) Tress, W. Organic solar cells. In Organic Solar Cells; Springer: 2014; pp 67-214.

(163) Lenes, M.; Koster, L. J. A.; Mihailetchi, V. D.; Blom, P. W. M. Thickness dependence of the efficiency of polymer:fullerene bulk heterojunction solar cells. Applied Physics Letters 2006, 88 (24), 243502, DOI: 10.1063/1.2211189.

(164) Riedel, I.; Dyakonov, V. Influence of electronic transport properties of polymer-fullerene blends on the performance of bulk heterojunction photovoltaic devices. physica status solidi (a) 2004, 201 (6), 1332-1341, DOI: 10.1002/pssa.200404333.

(165) Wu, J.; Zhang, Y.; Xu, P.; Guo, W.; Shen, L.; Ruan, S. Role of solution-processed V_2O_5 in P3HT:PCBM based inverted polymer solar cells. Synthetic Metals 2013, 170, 7-10, DOI: 10.1016/j.synthmet.2013.02.012.

(166) Yu, W.; Shen, L.; Ruan, S.; Meng, F.; Wang, J.; Zhang, E.; Chen, W. Performance improvement of inverted polymer solar cells thermally evaporating nickel oxide as an anode buffer layer. Solar Energy Materials and Solar Cells 2012, 98, 212-215, DOI: 10.1016/j.solmat.2011.11.011.

(167) Lim, F. J.; Ananthanarayanan, K.; Luther, J.; Ho, G. W. Influence of a novel fluorosurfactant modified PEDOT:PSS hole transport layer on the performance of inverted organic solar cells. Journal of Materials Chemistry 2012, 22 (48), 25057, DOI: 10.1039/c2jm35646e.

(168) Aprilia, A.; Wulandari, P.; Suendo, V.; Herman; Hidayat, R.; Fujii, A.; Ozaki, M. Influences of dopant concentration in sol–gel derived AZO layer on the performance of P3HT:PCBM based inverted solar cell. Solar Energy Materials and Solar Cells 2013, 111, 181-188, DOI: 10.1016/j.solmat.2012.12.033.

(169) Zhou, Y.; Zhao, Y. Chemical stability and instability of inorganic halide perovskites. Energy & environmental science 2019, 12 (5), 1495-1511.

(170) Fu, H. Review of lead-free halide perovskites as light-absorbers for photovoltaic applications: from materials to solar cells. Solar Energy Materials and Solar Cells 2019, 193, 107-132.

(171) Stranks, S. D.; Eperon, G. E.; Grancini, G.; Menelaou, C.; Alcocer, M. J. P.; Leijtens, T.; Herz, L. M.; Petrozza, A.; Snaith, H. J. Electron-hole diffusion lengths exceeding 1 micrometer in an organometal trihalide perovskite absorber. Science 2013, 342 (6156), 341-344.

(172) Li, S.; Liu, P.; Pan, L.; Li, W.; Yang, S.-E.; Shi, Z.; Guo, H.; Xia, T.; Zhang, S.; Chen, Y. The investigation of inverted pin planar perovskite solar cells based on $FASnI_3$ films. Solar Energy Materials and Solar Cells 2019, 199, 75-82.

(173) Juarez-Perez, E. J.; Ono, L. K.; Maeda, M.; Jiang, Y.; Hawash, Z.; Qi, Y. Photodecomposition and thermal decomposition in methylammonium halide lead perovskites and inferred design principles to increase photovoltaic device stability. Journal of Materials Chemistry A 2018, 6 (20), 9604-9612, DOI: 10.1039/c8ta03501f.

(174) Directive, E. U. Restriction of the use of certain hazardous substances in electrical and electronic equipment (RoHS). Off. J. Eur. Communities 2013, 46, 19-23.

(175) Abate, A. Perovskite Solar Cells Go Lead Free. Joule 2017, 1 (4), 659-664, DOI: 10.1016/j.joule.2017.09.007.

(176) Ju, M.-G.; Chen, M.; Zhou, Y.; Garces, H. F.; Dai, J.; Ma, L.; Padture, N. P.; Zeng, X. C. Earth-abundant nontoxic titanium (IV)-based vacancy-ordered double perovskite halides with tunable 1.0 to 1.8 eV bandgaps for photovoltaic applications. ACS Energy Letters 2018, 3 (2), 297-304.

(177) Bi, D.; Yi, C.; Luo, J.; Décoppet, J.-D.; Zhang, F.; Zakeeruddin, Shaik M.; Li, X.; Hagfeldt, A.; Grätzel, M. Polymer-templated nucleation and crystal growth of perovskite films for solar cells with efficiency greater than 21%. Nature Energy 2016, 1 (10), DOI: 10.1038/nenergy.2016.142.

(178) Jeon, N. J.; Na, H.; Jung, E. H.; Yang, T.-Y.; Lee, Y. G.; Kim, G.; Shin, H.-W.; Il Seok, S.; Lee, J.; Seo, J. A fluorene-terminated hole-transporting material for highly efficient and stable perovskite solar cells. Nature Energy 2018, 3 (8), 682-689, DOI: 10.1038/s41560-018-0200-6.

(179) Lau, C. F. J.; Deng, X.; Zheng, J.; Kim, J.; Zhang, Z.; Zhang, M.; Bing, J.; Wilkinson, B.; Hu, L.; Patterson, R.; Huang, S.; Ho-Baillie, A. Enhanced performance via partial lead replacement with calcium for a $CsPbI_3$ perovskite solar cell exceeding 13% power conversion

efficiency. Journal of Materials Chemistry A 2018, 6 (14), 5580-5586, DOI: 10.1039/c7ta11154a.

(180) Yuan, H.; Zhao, Y.; Duan, J.; Wang, Y.; Yang, X.; Tang, Q. All-inorganic $CsPbBr_3$ perovskite solar cell with 10.26% efficiency by spectra engineering. Journal of Materials Chemistry A 2018, 6 (47), 24324-24329, DOI: 10.1039/c8ta08900k.

(181) Duan, J.; Zhao, Y.; He, B.; Tang, Q. Simplified Perovskite Solar Cell with 4.1% Efficiency Employing Inorganic $CsPbBr_3$ as Light Absorber. Small 2018, 14 (20), e1704443, DOI: 10.1002/smll.201704443.

(182) Zhou, D.; Zhou, T.; Tian, Y.; Zhu, X.; Tu, Y. Perovskite-Based Solar Cells: Materials, Methods, and Future Perspectives. Journal of Nanomaterials 2018, 2018, 1-15, DOI: 10.1155/2018/8148072.

(183) Gratzel, M. The Rise of Highly Efficient and Stable Perovskite Solar Cells. Acc Chem Res 2017, 50 (3), 487-491, DOI: 10.1021/acs.accounts.6b00492.

(184) Green, M. A.; Ho-Baillie, A. Perovskite Solar Cells: The Birth of a New Era in Photovoltaics. ACS Energy Letters 2017, 2 (4), 822-830, DOI: 10.1021/acsenergylett.7b00137.

(185) Correa-Baena, J.-P.; Saliba, M.; Buonassisi, T.; Grätzel, M.; Abate, A.; Tress, W.; Hagfeldt, A. Promises and challenges of perovskite solar cells. Science 2017, 358 (6364), 739-744.

(186) Fujihara, T.; Terakawa, S.; Matsushima, T.; Qin, C.; Yahiro, M.; Adachi, C. Fabrication of high coverage $MASnI_3$ perovskite films for stable, planar heterojunction solar cells. Journal of Materials Chemistry C 2017, 5 (5), 1121-1127, DOI: 10.1039/c6tc05069g.

(187) Tsai, C. M.; Mohanta, N.; Wang, C. Y.; Lin, Y. P.; Yang, Y. W.; Wang, C. L.; Hung, C. H.; Diau, E. W. Formation of Stable Tin Perovskites Co-crystallized with Three Halides for Carbon-Based Mesoscopic Lead-Free Perovskite Solar Cells. Angew Chem Int Ed Engl 2017, 56 (44), 13819-13823, DOI: 10.1002/anie.201707037.

(188) Song, T.-B.; Yokoyama, T.; Aramaki, S.; Kanatzidis, M. G. Performance Enhancement of Lead-Free Tin-Based Perovskite Solar Cells with Reducing Atmosphere-Assisted Dispersible Additive. ACS Energy Letters 2017, 2 (4), 897-903, DOI: 10.1021/acsenergylett.7b00171.

(189) Chen, L.-J. Synthesis and optical properties of lead-free cesium germanium halide perovskite quantum rods. RSC Advances 2018, 8 (33), 18396-18399, DOI: 10.1039/c8ra01150h.

(190) Chen, L. J.; Lee, C. R.; Chuang, Y. J.; Wu, Z. H.; Chen, C. Synthesis and Optical Properties of Lead-Free Cesium Tin Halide Perovskite Quantum Rods with High-Performance Solar Cell Application. J Phys Chem Lett 2016, 7 (24), 5028-5035, DOI: 10.1021/acs.jpclett.6b02344.

(191) Chen, M.; Ju, M. G.; Garces, H. F.; Carl, A. D.; Ono, L. K.; Hawash, Z.; Zhang, Y.; Shen, T.; Qi, Y.; Grimm, R. L.; Pacifici, D.; Zeng, X. C.; Zhou, Y.; Padture, N. P. Highly stable and efficient all-inorganic lead-free perovskite solar cells with native-oxide passivation. Nat Commun 2019, 10 (1), 16, DOI: 10.1038/s41467-018-07951-y.

(192) Babayigit, A.; Ethirajan, A.; Muller, M.; Conings, B. Toxicity of organometal halide perovskite solar cells. Nature materials 2016, 15 (3), 247-251.

(193) Du, K. z.; Meng, W.; Wang, X.; Yan, Y.; Mitzi, D. B. Bandgap engineering of lead-free double perovskite $Cs_2AgBiBr_6$ through trivalent metal alloying. Angewandte Chemie International Edition 2017, 56 (28), 8158-8162.

(194) Park, B. W.; Philippe, B.; Zhang, X.; Rensmo, H.; Boschloo, G.; Johansson, E. M. J. Bismuth based hybrid perovskites $A_3Bi_2I_9$ (A: methylammonium or cesium) for solar cell application. Advanced materials 2015, 27 (43), 6806-6813.

(195) Saparov, B.; Hong, F.; Sun, J.-P.; Duan, H.-S.; Meng, W.; Cameron, S.; Hill, I. G.; Yan, Y.; Mitzi, D. B. Thin-film preparation and characterization of $Cs_3Sb_2I_9$: a lead-free layered perovskite semiconductor. Chemistry of Materials 2015, 27 (16), 5622-5632.

(196) Boopathi, K. M.; Karuppuswamy, P.; Singh, A.; Hanmandlu, C.; Lin, L.; Abbas, S. A.; Chang, C. C.; Wang, P. C.; Li, G.; Chu, C. W. Solution-processable antimony-based light-absorbing materials beyond lead halide perovskites. J. Mater. Chem. A 2017, 5 (39), 20843-20850, DOI: 10.1039/c7ta06679a.

(197) Wang, B.; Li, N.; Yang, L.; Dall'Agnese, C.; Jena, A. K.; Sasaki, S. I.; Miyasaka, T.; Tamiaki, H.; Wang, X. F. Chlorophyll Derivative-Sensitized TiO_2 Electron Transport Layer for Record Efficiency of $Cs_2AgBiBr_6$ Double Perovskite Solar Cells. J Am Chem Soc 2021, 143, 2207-2211, DOI: 10.1021/jacs.0c12786.

(198) Chen, M.; Ju, M.-G.; Carl, A. D.; Zong, Y.; Grimm, R. L.; Gu, J.; Zeng, X. C.; Zhou, Y.; Padture, N. P. Cesium Titanium(IV) Bromide Thin Films Based Stable Lead-free Perovskite Solar Cells. Joule 2018, 2, 558-570, DOI: 10.1016/j.joule.2018.01.009.

(199) Kitagawa, S.; Noro, S. Coordination polymers: Infinite systems. ChemInform 2004, 35 (47), no-no.

(200) Robotti, N. The discovery of X-ray diffraction. Rendiconti Lincei 2012, 24, 7-18, DOI: 10.1007/s12210-012-0205-1.

(201) Swinehart, D. F. The beer-lambert law. Journal of chemical education 1962, 39, 333.

(202) Bardeen, J.; Blatt, F. J.; Hall, L. H. Proc. Atlantic City Photoconductivity Conf., 1954. 1956.

(203) Lefebvre, J.; Galli, F.; Bianchi, C. L.; Patience, G. S.; Boffito, D. C. Experimental methods in chemical engineering: X-ray photoelectron spectroscopy-XPS. The Canadian Journal of Chemical Engineering 2019, 97, 2588-2593, DOI: 10.1002/cjce.23530.

(204) Raman, C. V.; Krishnan, K. S. A new type of secondary radiation. Nature 1928, 121 (3048), 501-502.

(205) Sherman, C. P., In Handbook of Instrumental Techniques for Analytical Chemistry, chapter 15; Settle, F., Ed. Prentice-Hall Inc., New Jersey: 1997.

(206) Chalmers, J. M.; Edwards, H. G. M.; Hargreaves, M. D. Infrared and Raman spectroscopy in forensic science, John Wiley & Sons: 2012.

(207) Bumbrah, G. S.; Sharma, R. M. Raman spectroscopy–Basic principle, instrumentation and selected applications for the characterization of drugs of abuse. Egyptian Journal of Forensic Sciences 2016, 6, 209-215.

(208) Adam, N. K. Use of the term ‘Young's Equation’for contact angles. Nature 1957, 180, 809-810.

(209) Guy, O. J.; Walker, K.-A. D. Graphene Functionalization for Biosensor Applications. 2016, 85-141, DOI: 10.1016/b978-0-12-802993-0.00004-6.

(210) Wang, L.; Lee, C.-Y.; Schmuki, P. Solar water splitting: preserving the beneficial small feature size in porous α-Fe_2O_3 photoelectrodes during annealing. Journal of Materials Chemistry A 2013, 1, 212-215.

(211) Ghorai, U. K.; Das, S.; Saha, S.; Mazumder, N.; Sen, D.; Chattopadhyay, K. K. Efficient and persistent cold cathode emission from CuPc nanotubes: a joint experimental and simulation investigation. Dalton Trans 2014, 43, 9260-6, DOI: 10.1039/c4dt00300d.

(212) Yu, H.; Zhang, B.; Bulin, C.; Li, R.; Xing, R. High-efficient Synthesis of Graphene Oxide Based on Improved Hummers Method. Sci Rep 2016, 6, 36143, DOI: 10.1038/srep36143.

(213) El-Nahass, M. M.; Zeyada, H. M.; Aziz, M. S.; El-Ghamaz, N. A. Structural and optical properties of thermally evaporated zinc phthalocyanine thin films. Optical Materials 2004, 27, 491-498, DOI: 10.1016/j.optmat.2004.04.010.

(214) Gaffo, L.; Cordeiro, M. R.; Freitas, A. R.; Moreira, W. C.; Girotto, E. M.; Zucolotto, V. The effects of temperature on the molecular orientation of zinc phthalocyanine films. Journal of Materials Science 2010, 45, 1366-1370.

(215) Roy, D.; Das, N. M.; Shakti, N.; Gupta, P. S. Comparative study of optical, structural and electrical properties of zinc phthalocyanine Langmuir–Blodgett thin film on annealing. RSC Adv. 2014, 4, 42514-42522, DOI: 10.1039/c4ra05417b.

(216) Derouiche, H. Optimization of the properties of bulk heterojunctions obtained by coevaporation of Zn-phthalocyanine/perylene. Dyes and Pigments 2004, 63, 277-289, DOI: 10.1016/j.dyepig.2004.03.002.

(217) Li, S.; Wang, D.; Wang, Z.; Wang, Z.; Chen, M.; Liu, X. Laser-induced fabrication of single crystal zinc hydroxyl dodecylsulfate nano-sheets with excellent fluorescence emission. RSC advances 2015, 5, 63233-63239.

(218) Chen, X.; Liu, J.; Jing, X.; Wang, J.; Song, D.; Liu, L. Self-assembly of ZnO nanosheets into flower-like architectures and their gas sensing properties. Materials Letters 2013, 112, 23-25.

(219) Inamdar, A. I.; Mujawar, S. H.; Ganesan, V.; Patil, P. S. Surfactant-mediated growth of nanostructured zinc oxide thin films via electrodeposition and their photoelectrochemical performance. Nanotechnology 2008, 19, 325706.

(220) Chunder, A.; Pal, T.; Khondaker, S. I.; Zhai, L. Reduced graphene oxide/copper phthalocyanine composite and its optoelectrical properties. The Journal of Physical Chemistry C 2010, 114, 15129-15135.

(221) Zhang, M.; Shao, C.; Guo, Z.; Zhang, Z.; Mu, J.; Cao, T.; Liu, Y. Hierarchical nanostructures of copper (II) phthalocyanine on electrospun TiO_2 nanofibers: controllable solvothermal-fabrication and enhanced visible photocatalytic properties. ACS applied materials & interfaces 2011, 3, 369-377.

(222) Rahim, A.; Muhammad, N.; Nishan, U.; Khan, U. S.; Rehman, F.; Kubota, L. T.; Gushikem, Y. Copper phthalocyanine modified SiO_2/C electrode as a biomimetic electrocatalyst for 4-aminophenol in the development of an amperometric sensor. RSC advances 2015, 5, 87043-87050.

(223) Cho, N.-S.; Kim, K.-H.; Hahn, C.-S. Symmetry and Spectra of Complexes of Azo-Substituted Copper Phthalocyanine. Journal of the Korean Chemical Society 1972, 16, 378-384.

(224) Hashimoto, T.; Choe, Y.-K.; Nakano, H.; Hirao, K. Theoretical study of the Q and B bands of free-base, magnesium, and zinc porphyrins, and their derivatives. The Journal of Physical Chemistry A 1999, 103, 1894-1904.

(225) Ghorai, U. K.; Mazumder, N.; Mamgain, H.; Roy, R.; Saha, S.; Chattopadhyay, K. K. Raman spectroscopic observation of gradual polymorphic transition and phonon modes in CuPc nanorod. The Journal of Physical Chemistry C 2017, 121, 6323-6328.

(226) Kaniyoor, A.; Ramaprabhu, S. A Raman spectroscopic investigation of graphite oxide derived graphene. Aip Advances 2012, 2, 032183.

(227) Hessein, A.; El-Moneim, A. A. Developing Cost Effective Graphene Conductive Coating and its Application as Counter Electrode for CdS Quantum Dot Sensitized Solar Cell. Proc. World Congr. New Technol.(NewTech 2015) 2015, 307 (1).

(228) Tien, H. N.; Luan, V. H.; Hoa, L. T.; Khoa, N. T.; Hahn, S. H.; Chung, J. S.; Shin, E. W.; Hur, S. H. One-pot synthesis of a reduced graphene oxide–zinc oxide sphere composite and its use as a visible light photocatalyst. Chemical Engineering Journal 2013, 229, 126-133, DOI: 10.1016/j.cej.2013.05.110.

(229) Wang, Y.; Zhou, A.; Jiang, Y.; Chen, X.; He, J. Tetraamino-zinc phthalocyanine covalently bound to benzoic acid-functionalized graphene composites for highly efficient visible light photocatalytic activities. RSC Advances 2015, 5, 37823-37829.

(230) Sun, P.; Zhang, W.; Hu, X.; Yuan, L.; Huang, Y. Synthesis of hierarchical MoS_2 and its electrochemical performance as an anode material for lithium-ion batteries. Journal of Materials Chemistry A 2014, 2, 3498-3504.

(231) Lu, Y.; Yao, X.; Yin, J.; Peng, G.; Cui, P.; Xu, X. MoS_2 nanoflowers consisting of nanosheets with a controllable interlayer distance as high-performance lithium ion battery anodes. RSC Advances 2015, 5, 7938-7943.

(232) Rasamani, K. D.; Alimohammadi, F.; Sun, Y. Interlayer-expanded MoS_2. Materials Today 2017, 20, 83-91.

(233) Zheng, X.; Zhu, Y.; Sun, Y.; Jiao, Q. Hydrothermal synthesis of MoS_2 with different morphology and its performance in thermal battery. Journal of Power Sources 2018, 395, 318-327.

(234) Zhang, X.; Yang, F.; Cui, S.; Wei, W.; Chen, W.; Mi, L. Consecutive reaction to construct hierarchical nanocrystalline CuS “branch” with tunable catalysis properties. Scientific reports 2016, 6, 1-11.

(235) Huang, H.; Lan, Z.; Li, W.; Mo, W.; Zhao, L.; Zhang, J. A novel and low-cost CuPc@ C catalyst derived from the compounds of sunflower straw and copper phthalocyanine pigment for oxygen reduction reaction. RSC Advances 2021, 11, 15590-15597.

(236) Wang, Z.; Wei, R.; Liu, X. Dielectric properties of copper phthalocyanine nanocomposites incorporated with graphene oxide. Journal of Materials Science: Materials in Electronics 2017, 28, 7437-7448.

(237) Ramakrishnan, S.; Karuppannan, M.; Vinothkannan, M.; Ramachandran, K.; Kwon, O. J.; Yoo, D. J. Ultrafine Pt nanoparticles stabilized by MoS_2/N-doped reduced graphene oxide as a durable electrocatalyst for alcohol oxidation and oxygen reduction reactions. ACS applied materials & interfaces 2019, 11, 12504-12515.

(238) Shen, C.; Wang, L.; Zhou, A.; Zhang, H.; Chen, Z.; Hu, Q.; Qin, G. MoS_2-decorated Ti_3C_2 MXene nanosheet as anode material in lithium-ion batteries. Journal of The Electrochemical Society 2017, 164 (12), A2654.

(239) Das, B.; Samanta, M.; Sarkar, P.; Ghorai, U. K.; Mallik, A.; Chattopadhyay, K. K. Copper (II) Phthalocyanine (CuPc) Based Optoelectronic Memory Device with Multilevel

Resistive Switching for Neuromorphic Application. Advanced Electronic Materials 2021, 7, 2001079, DOI: 10.1002/aelm.202001079.

(240) Qin, J.; Xi, C.; Zhang, R.; Liu, T.; Zou, P.; Wu, D.; Guo, Q.; Mao, J.; Xin, H.; Yang, J. Activating edge-Mo of 2H-MoS_2 via coordination with pyridinic N–C for pH-universal hydrogen evolution electrocatalysis. ACS Catalysis 2021, 11, 4486-4497.

(241) Chaudhary, N.; Khanuja, M.; Islam, S. S. Broadband photodetector based on 3D architect of MoS_2-PANI hybrid structure for high photoresponsive properties. Polymer 2019, 165, 168-173, DOI: 10.1016/j.polymer.2019.01.028.

(242) Sahatiya, P.; Jones, S. S.; Badhulika, S. Direct, large area growth of few-layered MoS_2 nanostructures on various flexible substrates: growth kinetics and its effect on photodetection studies. Flexible and Printed Electronics 2018, 3, 015002, DOI: 10.1088/2058-8585/aaa4a5.

(243) Siwinska-Ciesielczyk, K.; Kurc, B.; Rymarowicz, D.; Kubiak, A.; Piasecki, A.; Moszynski, D.; Jesionowski, T. Crystallization of TiO_2-MoS_2 Hybrid Material under Hydrothermal Treatment and Its Electrochemical Performance. Materials (Basel) 2020, 13, DOI: 10.3390/ma13122706.

(244) Li, M.; Wang, D.; Li, J.; Pan, Z.; Ma, H.; Jiang, Y.; Tian, Z. Facile hydrothermal synthesis of MoS_2 nano-sheets with controllable structures and enhanced catalytic performance for anthracene hydrogenation. RSC Advances 2016, 6, 71534-71542, DOI: 10.1039/c6ra16084k.

(245) Zhao, B.; Wang, Z.; Gao, Y.; Chen, L.; Lu, M.; Jiao, Z.; Jiang, Y.; Ding, Y.; Cheng, L. Hydrothermal synthesis of layer-controlled MoS_2/graphene composite aerogels for lithium-ion battery anode materials. Applied Surface Science 2016, 390, 209-215, DOI: 10.1016/j.apsusc.2016.08.078.

(246) Ahmad, M.; Ahmed, E.; Hong, Z. L.; Ahmed, W.; Elhissi, A.; Khalid, N. R. Photocatalytic, sonocatalytic and sonophotocatalytic degradation of Rhodamine B using ZnO/CNTs composites photocatalysts. Ultrason Sonochem 2014, 21, 761-73, DOI: 10.1016/j.ultsonch.2013.08.014.

(247) Merouani, S.; Hamdaoui, O.; Saoudi, F.; Chiha, M. Sonochemical degradation of Rhodamine B in aqueous phase: Effects of additives. Chemical Engineering Journal 2010, 158, 550-557, DOI: 10.1016/j.cej.2010.01.048.

(248) Xu, P.; Shen, X.; Luo, L.; Shi, Z.; Liu, Z.; Chen, Z.; Zhu, M.; Zhang, L. Preparation of TiO_2/Bi_2WO_6 nanostructured heterojunctions on carbon fibers as a weaveable visible-light photocatalyst/photoelectrode. Environmental Science: Nano 2018, 5, 327-337.

(249) Sarkar, D.; Chattopadhyay, K. K. Branch density-controlled synthesis of hierarchical TiO_2 nanobelt and tunable three-step electron transfer for enhanced photocatalytic property. ACS Appl Mater Interfaces 2014, 6, 10044-59, DOI: 10.1021/am502379q.

(250) Deng, D.; Martin, S. T.; Ramanathan, S. Synthesis and characterization of one-dimensional flat ZnO nanotower arrays as high-efficiency adsorbents for the photocatalytic remediation of water pollutants. Nanoscale 2010, 2, 2685-91, DOI: 10.1039/c0nr00537a.

(251) Maiti, U. N.; Maiti, S.; Chattopadhyay, K. K. An ambient condition, one pot route for large scale production of ultrafine (<15 nm) ZnO nanowires from commercial zinc exhibiting excellent recyclable catalytic performance: Approach extendable to CuO nanostructures. CrystEngComm 2012, 14, 640-647, DOI: 10.1039/c1ce05917c.

(252) Liu, B.; Khare, A.; Aydil, E. S. TiO_2-B/anatase core-shell heterojunction nanowires for photocatalysis. ACS Appl Mater Interfaces 2011, 3, 4444-50, DOI: 10.1021/am201123u.

(253) Wan, Y.; Cong, T.; Liang, Q.; Li, Z.; Xu, S.; Peng, Y.; Lu, D. Facile in-situ solvothermal method to synthesize ZnPc–MWCNTs composites with enhanced visible light photocatalytic activity. Ceramics International 2016, 42, 2425-2430, DOI:10.1016/j.ceramint.2015.10.042.

(254) Markovic, D.; Saponjic, Z.; Radoicic, M.; Radetic, T.; Vodnik, V.; Potkonjak, B.; Radetic, M. Sonophotocatalytic degradation of dye C.I. Acid Orange 7 by TiO_2 and Ag nanoparticles immobilized on corona pretreated polypropylene non-woven fabric. Ultrason Sonochem 2015, 24, 221-9, DOI: 10.1016/j.ultsonch.2014.11.017.

(255) Singh, P.; Vishnu, M. C.; Sharma, K. K.; Singh, R.; Madhav, S.; Tiwary, D.; Mishra, P. K. Comparative study of dye degradation using TiO_2-activated carbon nanocomposites as catalysts in photocatalytic, sonocatalytic, and photosonocatalytic reactor. Desalination and Water Treatment 2015, 57, 20552-20564, DOI: 10.1080/19443994.2015.1108871.

(256) Wang, H.; Niu, J.; Long, X.; He, Y. Sonophotocatalytic degradation of methyl orange by nano-sized Ag/TiO_2 particles in aqueous solutions. Ultrason Sonochem 2008, 15, 386-392, DOI: 10.1016/j.ultsonch.2007.09.011.

(257) Cui, P.; Chen, Y.; Chen, G. Degradation of Low Concentration Methyl Orange in Aqueous Solution through Sonophotocatalysis with Simultaneous Recovery of Photocatalyst by Ceramic Membrane Microfiltration. Industrial & Engineering Chemistry Research 2011, 50, 3947-3954, DOI: 10.1021/ie100832q.

(258) Pang, Y. L.; Abdullah, A. Z. Fe^{3+} doped TiO_2 nanotubes for combined adsorption–sonocatalytic degradation of real textile wastewater. Applied Catalysis B: Environmental 2013, 129, 473-481, DOI: 10.1016/j.apcatb.2012.09.051.

(259) Wang, J.; Ma, T.; Zhang, Z.; Zhang, X.; Jiang, Y.; Dong, D.; Zhang, P.; Li, Y. Investigation on the sonocatalytic degradation of parathion in the presence of nanometer rutile titanium dioxide (TiO_2) catalyst. J Hazard Mater 2006, 137, 972-80, DOI: 10.1016/j.jhazmat.2006.03.022.

(260) Hayati, F.; Isari, A. A.; Anvaripour, B.; Fattahi, M.; Kakavandi, B. Ultrasound-assisted photocatalytic degradation of sulfadiazine using MgO@CNT heterojunction composite: Effective factors, pathway and biodegradability studies. Chemical Engineering Journal 2020, 381, 122636, DOI: 10.1016/j.cej.2019.122636.

(261) Dinesh, G. K.; Anandan, S.; Sivasankar, T. Sonophotocatalytic treatment of Bismarck Brown G dye and real textile effluent using synthesized novel Fe(0)-doped TiO_2 catalyst. RSC Advances 2015, 5, 10440-10451, DOI: 10.1039/c4ra07685k.

(262) Sivasankar, T.; Moholkar, V. S. Physical insights into the sonochemical degradation of recalcitrant organic pollutants with cavitation bubble dynamics. Ultrason Sonochem 2009, 16, 769-81, DOI: 10.1016/j.ultsonch.2009.02.009.

(263) Bejarano-Perez, N. J.; Suarez-Herrera, M. F. Sonophotocatalytic degradation of congo red and methyl orange in the presence of TiO_2 as a catalyst. Ultrason Sonochem 2007, 14, 589-595, DOI: 10.1016/j.ultsonch.2006.09.011.

(264) Shirgaonkar, I. Z.; Pandit, A. B. Sonophotochemical destruction of aqueous solution of 2, 4, 6-trichlorophenol. Ultrasonics Sonochemistry 1998, 5, 53-61.

(265) Li, L.; Zhang, M.; Zhao, Z.; Sun, B.; Zhang, X. Visible/near-IR-light-driven TNFePc/BiOCl organic–inorganic heterostructures with enhanced photocatalytic activity. Dalton Transactions 2016, 45, 9497-9505, DOI: 10.1039/c6dt01091a.

(266) Liang, Q.; Zhang, M.; Zhang, Z.; Liu, C.; Xu, S.; Li, Z. Zinc phthalocyanine coupled with UIO-66 (NH_2) via a facile condensation process for enhanced visible-light-driven photocatalysis. Journal of Alloys and Compounds 2017, 690, 123-130, DOI: 10.1016/j.jallcom.2016.08.087.

(267) Wang, H.; Zhao, L.; Liu, X.; Xu, J.; Hou, W.; Wang, J.; He, E.; Zhang, R.; Zhang, H. Novel hydrogen bonding composite based on copper phthalocyanine/perylene diimide derivatives p-n heterojunction with improved photocatalytic activity. Dyes and Pigments 2017, 137, 322-328, DOI: 10.1016/j.dyepig.2016.11.014.

(268) Guo, Z.; Mu, J.; Chen, B. 3D flower-like iron phthalocyanine hierarchical microstructures: solvothermal-fabrication and high visible light photocatalytic properties. Ceramics International 2015, 41, 4916-4922, DOI: 10.1016/j.ceramint.2014.12.053.

(269) Wang, Z.; Chen, H.; Tang, P.; Mao, W.; Zhang, F.; Qian, G.; Fan, X. Hydrothermal in situ preparation of the copper phthalocyanine tetrasulfonate modified titanium dioxide photocatalyst. Colloids and Surfaces A: Physicochemical and Engineering Aspects 2006, 289, 207-211, DOI: 10.1016/j.colsurfa.2006.04.049.

(270) Babu, S. G.; Ramalingam, V.; Neppolian, B.; Dionysiou, D. D.; Ashokkumar, M. Diffused sunlight driven highly synergistic pathway for complete mineralization of organic contaminants using reduced graphene oxide supported photocatalyst. J Hazard Mater 2015, 291, 83-92, DOI: 10.1016/j.jhazmat.2015.02.071.

(271) Vinoth, R.; Karthik, P.; Devan, K.; Neppolian, B.; Ashokkumar, M. TiO_2-NiO p-n nanocomposite with enhanced sonophotocatalytic activity under diffused sunlight. Ultrason Sonochem 2017, 35 (Pt B), 655-663, DOI: 10.1016/j.ultsonch.2016.03.005.

(272) Wang, S.; Gong, Q.; Liang, J. Sonophotocatalytic degradation of methyl orange by carbon nanotube/TiO_2 in aqueous solutions. Ultrason Sonochem 2009, 16, 205-8, DOI: 10.1016/j.ultsonch.2008.08.002.

(273) Ghows, N.; Entezari, M. H. Kinetic investigation on sono-degradation of Reactive Black 5 with core-shell nanocrystal. Ultrason Sonochem 2013, 20, 386-94, DOI: 10.1016/j.ultsonch.2012.06.013.

(274) Paul, K. K.; Giri, P. K. Role of Surface Plasmons and Hot Electrons on the Multi-Step Photocatalytic Decay by Defect Enriched Ag@TiO_2 Nanorods under Visible Light. The Journal of Physical Chemistry C 2017, 121, 20016-20030, DOI: 10.1021/acs.jpcc.7b05328.

(275) Lei, Z. H. U.; Ghosh, T.; Chong-Yeon, P.; Ze-Da, M.; Won-Chun, O. H. Enhanced sonocatalytic degradation of rhodamine B by graphene-TiO_2 composites synthesized by an ultrasonic-assisted method. Chinese Journal of Catalysis 2012, 33, 1276-1283.

(276) Di, J.; Xia, J.; Ge, Y.; Xu, L.; Xu, H.; Chen, J.; He, M.; Li, H. Facile fabrication and enhanced visible light photocatalytic activity of few-layer MoS(2) coupled BiOBr microspheres. Dalton Trans 2014, 43, 15429-38, DOI: 10.1039/c4dt01652a.

(277) Fu, M.; Jiao, Q.; Zhao, Y. One-step vapor diffusion synthesis of uniform CdS quantum dots/reduced graphene oxide composites as efficient visible-light photocatalysts. RSC Advances 2014, 4, 23242, DOI: 10.1039/c4ra02000f.

(278) Shamsunnahar, S. M.; Nagai, M. Nitrogen doping of ash-free coal and effect of ash components on properties and oxygen reduction reaction in fuel cell. Fuel 2014, 126, 134-142, DOI: 10.1016/j.fuel.2014.02.049.

(279) Senthilkumar, N.; Venkatachalam, V.; Kandiban, M.; Vigneshwaran, P.; Jayavel, R.; Vetha Potheher, I. Studies on electrochemical properties of hetarolite ($ZnMn_2O_4$) nanostructure for supercapacitor application. Physica E: Low-dimensional Systems and Nanostructures 2019, 106, 121-126, DOI: 10.1016/j.physe.2018.10.027.

(280) Li, H. B.; Yu, M. H.; Wang, F. X.; Liu, P.; Liang, Y.; Xiao, J.; Wang, C. X.; Tong, Y. X.; Yang, G. W. Amorphous nickel hydroxide nanospheres with ultrahigh capacitance and energy density as electrochemical pseudocapacitor materials. Nature communications 2013, 4, 1894.

(281) Howli, P.; Das, S.; Sarkar, S.; Samanta, M.; Panigrahi, K.; Das, N. S.; Chattopadhyay, K. K. Co_3O_4 Nanowires on Flexible Carbon Fabric as a Binder-Free Electrode for All Solid-State Symmetric Supercapacitor. ACS Omega 2017, 2, 4216-4226, DOI: 10.1021/acsomega.7b00702.

(282) Lvovich, V. F. Impedance spectroscopy: applications to electrochemical and dielectric phenomena, John Wiley & Sons: 2012.

(283) Maity, S.; Samanta, M.; Sen, A.; Chattopadhyay, K. K. Investigation of electrochemical performances of ceramic oxide $CaCu_3Ti_4O_{12}$ nanostructures. Journal of Solid State Chemistry 2019, 269, 600-607, DOI: 10.1016/j.jssc.2018.10.016.

(284) Cole, K. S.; Cole, R. H. Dispersion and Absorption in Dielectrics I. Alternating Current Characteristics. The Journal of Chemical Physics 1941, 9, 341-351, DOI: 10.1063/1.1750906.

(285) Nandy, S.; Mallick, S.; Ghosh, P. K.; Das, G. C.; Mukherjee, S.; Mitra, M. K.; Chattopadhyay, K. K. Impedance spectroscopic studies of nickel nanocluster in silica matrix synthesized by sol–gel method. Journal of Alloys and Compounds 2008, 453, 1-6, DOI: 10.1016/j.jallcom.2006.11.061.

(286) Chen, T.; Fan, Y.; Wang, G.; Yang, Q.; Yang, R. Rationally designed hierarchical $ZnCo_2O_4$/polypyrrole nanostructures for high-performance supercapacitor electrodes. RSC Advances 2015, 5, 74523-74530, DOI: 10.1039/c5ra14808a.

(287) Saha, S.; Jana, M.; Khanra, P.; Samanta, P.; Koo, H.; Murmu, N. C.; Kuila, T. Band Gap Engineering of Boron Nitride by Graphene and Its Application as Positive Electrode Material in Asymmetric Supercapacitor Device. ACS Appl Mater Interfaces 2015, 7, 14211-22, DOI: 10.1021/acsami.5b03562.

(288) Xia, H.; Li, B.; Lu, L. 1.8 V symmetric supercapacitors developed using nanocrystalline Ru films as electrodes. RSC Advances 2014, 4, 11111-11114.

(289) Nie, G.; Zhang, Z.; Wang, T.; Wang, C.; Kou, Z. Electrospun One-Dimensional Electrocatalysts for Oxygen Reduction Reaction: Insights into Structure-Activity Relationship. ACS Appl Mater Interfaces 2021, 13, 37961-37978, DOI: 10.1021/acsami.1c08798.

(290) Jaramillo, T. F.; Jørgensen, K. P.; Bonde, J.; Nielsen, J. H.; Horch, S.; Chorkendorff, I. Identification of active edge sites for electrochemical H_2 evolution from MoS_2 nanocatalysts. science 2007, 317, 100-102.

(291) Huang, Y.; Cui, F.; Zhao, Y.; Bao, J.; Lian, J.; Xu, Y.; Liu, T.; Li, H. Controllable synthesis of ultrathin $NiCo_2O_4$ nanosheets incorporated onto composite nanotubes for efficient oxygen reduction. Chemistry–An Asian Journal 2017, 12, 2426-2433.

(292) Zhao, K.; Gu, W.; Zhao, L.; Zhang, C.; Peng, W.; Xian, Y. MoS_2/Nitrogen-doped graphene as efficient electrocatalyst for oxygen reduction reaction. Electrochimica Acta 2015, 169, 142-149.

(293) Lin, L.; Yang, Z. K.; Jiang, Y.-F.; Xu, A.-W. Nonprecious Bimetallic (Fe,Mo)–N/C Catalyst for Efficient Oxygen Reduction Reaction. ACS Catalysis 2016, 6, 4449-4454, DOI: 10.1021/acscatal.6b00535.

(294) Liu, Y.; Dong, P.; Li, M.; Wu, H.; Zhang, C.; Han, L.; Zhang, Y. Cobalt Nanoparticles Encapsulated in Nitrogen-Doped Carbon Nanotube as Bifunctional-Catalyst for Rechargeable Zn-Air Batteries. Frontiers in Materials 2019, 6, 85, DOI: 10.3389/fmats.2019.00085.

(295) Wen, X.; Qi, H.; Cheng, Y.; Zhang, Q.; Hou, C.; Guan, J. Cu Nanoparticles Embedded in N-Doped Carbon Materials for Oxygen Reduction Reaction. Chinese Journal of Chemistry 2020, 38, 941-946, DOI: 10.1002/cjoc.202000073.

(296) Oh, J.; Yuan, H. C.; Branz, H. M. An 18.2%-efficient black-silicon solar cell achieved through control of carrier recombination in nanostructures. Nat Nanotechnol 2012, 7, 743-8, DOI: 10.1038/nnano.2012.166.

(297) Lastra, G.; Balderrama, V. S.; Resendiz, L.; Pallares, J.; Garduno, S. I.; Cabrera, V.; Marsal, L. F.; Estrada, M. High-Performance Inverted Polymer Solar Cells: Study and Analysis of Different Cathode Buffer Layers. IEEE Journal of Photovoltaics 2018, 8, 505-511, DOI: 10.1109/jphotov.2017.2782568.

(298) Taibi, I.; Belghachi, A.; Abid, H. Effect of trapping and temperature on the performance of P3HT:PCBM organic solar cells. Optik 2016, 127, 8592-8599, DOI: 10.1016/j.ijleo.2016.06.067.

(299) Tavakoli, M. M.; Tavakoli, R.; Prochowicz, D.; Yadav, P.; Saliba, M. Surface modification of a hole transporting layer for an efficient perovskite solar cell with an enhanced fill factor and stability. Molecular Systems Design & Engineering 2018, 3, 717-722, DOI: 10.1039/c8me00036k.

(300) Gong, X.; Sun, Q.; Liu, S.; Liao, P.; Shen, Y.; Gratzel, C.; Zakeeruddin, S. M.; Gratzel, M.; Wang, M. Highly Efficient Perovskite Solar Cells with Gradient Bilayer Electron Transport Materials. Nano Lett 2018, 18, 3969-3977, DOI: 10.1021/acs.nanolett.8b01440.

(301) Li, X.; Yang, J.; Jiang, Q.; Lai, H.; Li, S.; Xin, J.; Chu, W.; Hou, J. Low-Temperature Solution-Processed ZnSe Electron Transport Layer for Efficient Planar Perovskite Solar Cells with Negligible Hysteresis and Improved Photostability. ACS Nano 2018, 12, 5605-5614, DOI: 10.1021/acsnano.8b01351.

(302) Voznyy, O. Black and stable: A path to all-inorganic halide perovskite solar cells. Joule 2018, 2, 1215-1216.

(303) Jiang, Y.; Yuan, J.; Ni, Y.; Yang, J.; Wang, Y.; Jiu, T.; Yuan, M.; Chen, J. Reduced-dimensional α-$CsPbX_3$ perovskites for efficient and stable photovoltaics. Joule 2018, 2, 1356-1368.

(304) Wang, Y.; Zhang, T.; Kan, M.; Li, Y.; Wang, T.; Zhao, Y. Efficient α-$CsPbI_3$ photovoltaics with surface terminated organic cations. Joule 2018, 2, 2065-2075.

(305) Ju, M.-G.; Chen, M.; Zhou, Y.; Dai, J.; Ma, L.; Padture, N. P.; Zeng, X. C. Toward eco-friendly and stable perovskite materials for photovoltaics. Joule 2018, 2, 1231-1241.

(306) Hauch, J. A.; Schilinsky, P.; Choulis, S. A.; Childers, R.; Biele, M.; Brabec, C. J. Flexible organic P3HT:PCBM bulk-heterojunction modules with more than 1 year outdoor lifetime. Solar Energy Materials and Solar Cells 2008, 92, 727-731, DOI: 10.1016/j.solmat.2008.01.004.

(307) Koster, L. J. A.; Smits, E. C. P.; Mihailetchi, V. D.; Blom, P. W. M. Device model for the operation of polymer/fullerene bulk heterojunction solar cells. Physical Review B 2005, 72, 085205, DOI: 10.1103/PhysRevB.72.085205.

(308) Li, G.; Zhu, R.; Yang, Y. Polymer solar cells. Nature Photonics 2012, 6, 153-161, DOI: 10.1038/nphoton.2012.11.

(309) Sharma, N.; Gupta, S. K.; Singh Negi, C. M. Influence of active layer thickness on photovoltaic performance of PTB7:PC70BM bulk heterojunction solar cell. Superlattices and Microstructures 2019, 135, 106278, DOI: 10.1016/j.spmi.2019.106278.

(310) Scharber, M. C.; Mühlbacher, D.; Koppe, M.; Denk, P.; Waldauf, C.; Heeger, A. J.; Brabec, C. J. Design rules for donors in bulk-heterojunction solar cells—Towards 10% energy-conversion efficiency. Advanced materials 2006, 18, 789-794.

(311) Rong, X.; Tian, H.; Bi, W.; Jin, H.; Zhang, T.; Guo, D.; Zhao, K. Impact of metal electrode work function of $CH_3NH_3PbI_3$/p-Si planar heterojunction perovskite solar cells. Solar Energy 2017, 158, 424-431, DOI: 10.1016/j.solener.2017.08.050.

(312) Mandoc, M. M.; Koster, L. J. A.; Blom, P. W. M. Optimum charge carrier mobility in organic solar cells. Applied Physics Letters 2007, 90, 133504, DOI: 10.1063/1.2711534.

(313) Mazzio, K. A.; Luscombe, C. K. The future of organic photovoltaics. Chem Soc Rev 2015, 44, 78-90, DOI: 10.1039/c4cs00227j.

(314) Bao, Z.; Dodabalapur, A.; Lovinger, A. J. Soluble and processable regioregular poly (3-hexylthiophene) for thin film field-effect transistor applications with high mobility. Applied physics letters 1996, 69, 4108-4110.

(315) Li, S.; Hamada, F.; Nishikubo, R.; Saeki, A. Quantifying the optimal thickness in polymer:fullerene solar cells from the analysis of charge transport dynamics and photoabsorption. Sustainable Energy & Fuels 2022, 6, 756-765, DOI: 10.1039/d1se01228b.

(316) Lattante, S. Electron and Hole Transport Layers: Their Use in Inverted Bulk Heterojunction Polymer Solar Cells. Electronics 2014, 3, 132-164, DOI: 10.3390/electronics3010132.

(317) Gupta, S. K.; Sharma, A.; Banerjee, S.; Gahlot, R.; Aggarwal, N.; Deepak; Garg, A. Understanding the role of thickness and morphology of the constituent layers on the performance of inverted organic solar cells. Solar Energy Materials and Solar Cells 2013, 116, 135-143, DOI: 10.1016/j.solmat.2013.03.027.

(318) Kuddus, A.; Rahman, M. F.; Ahmmed, S.; Hossain, J.; Ismail, A. B. M. Role of facile synthesized V_2O_5 as hole transport layer for CdS/CdTe heterojunction solar cell: Validation of simulation using experimental data. Superlattices and Microstructures 2019, 132, 106168, DOI: 10.1016/j.spmi.2019.106168.

(319) Li, W.; Li, W.; Feng, Y.; Yang, C. Numerical analysis of the back interface for high efficiency wide band gap chalcopyrite solar cells. Solar Energy 2019, 180, 207-215, DOI: 10.1016/j.solener.2019.01.018.

(320) Han, S.; Shin, W. S.; Seo, M.; Gupta, D.; Moon, S.-J.; Yoo, S. Improving performance of organic solar cells using amorphous tungsten oxides as an interfacial buffer layer on transparent anodes. Organic Electronics 2009, 10, 791-797, DOI: 10.1016/j.orgel.2009.03.016.

(321) Chang, W.; Tian, H.; Fang, G.; Guo, D.; Wang, Z.; Zhao, K. Simulation of innovative high efficiency perovskite solar cell with Bi-HTL: NiO and Si thin films. Solar Energy 2019, 186, 323-327, DOI: 10.1016/j.solener.2019.05.017.

(322) Hacène, S. B.; Benouaz, T. Influence of charge carrier mobility and surface recombination velocity on the characteristics of P3HT:PCBM organic solar cells. physica status solidi (a) 2014, 211, 862-868, DOI: 10.1002/pssa.201330320.

(323) Son, D.-Y.; Im, J.-H.; Kim, H.-S.; Park, N.-G. 11% Efficient Perovskite Solar Cell Based on ZnO Nanorods: An Effective Charge Collection System. The Journal of Physical Chemistry C 2014, 118, 16567-16573, DOI: 10.1021/jp412407j.

(324) Arulanantham, A. M. S.; Valanarasu, S.; Kathalingam, A.; Shkir, M.; Kim, H.-S. An investigation on SnS layers for solar cells fabrication with CdS, SnS_2 and ZnO window layers prepared by nebulizer spray method. Applied Physics A 2018, 124, DOI: 10.1007/s00339-018-2164-6.

(325) Wang, K.; Jin, Z.; Liang, L.; Bian, H.; Bai, D.; Wang, H.; Zhang, J.; Wang, Q.; Liu, S. All-inorganic cesium lead iodide perovskite solar cells with stabilized efficiency beyond 15%. Nature communications 2018, 9, 1-8.

(326) Khadka, D. B.; Shirai, Y.; Yanagida, M.; Miyano, K. Unraveling the impacts induced by organic and inorganic hole transport layers in inverted halide perovskite solar cells. ACS applied materials & interfaces 2019, 11, 7055-7065.

(327) Gong, X.; Sun, Q.; Liu, S.; Liao, P.; Shen, Y.; Grätzel, C.; Zakeeruddin, S. M.; Grätzel, M.; Wang, M. Highly efficient perovskite solar cells with gradient bilayer electron transport materials. Nano Letters 2018, 18, 3969-3977.

(328) Nie, W.; Tsai, H.; Asadpour, R.; Blancon, J.-C.; Neukirch, A. J.; Gupta, G.; Crochet, J. J.; Chhowalla, M.; Tretiak, S.; Alam, M. A. High-efficiency solution-processed perovskite solar cells with millimeter-scale grains. Science 2015, 347, 522-525.

(329) Jung, E. H.; Jeon, N. J.; Park, E. Y.; Moon, C. S.; Shin, T. J.; Yang, T.-Y.; Noh, J. H.; Seo, J. Efficient, stable and scalable perovskite solar cells using poly (3-hexylthiophene). Nature 2019, 567, 511-515.

(330) Feng, Y.; Chen, Q.; Dong, L.; Zhang, Z.; Li, C.; Yang, S.; Cai, S.; Xu, Z.-X. Carbon-chain length substituent effects on Cu (II) phthalocyanines as dopant-free hole-transport materials for perovskite solar cells. Solar Energy 2019, 184, 649-656.

(331) Ke, W.; Zhao, D.; Grice, C. R.; Cimaroli, A. J.; Fang, G.; Yan, Y. Efficient fully-vacuum-processed perovskite solar cells using copper phthalocyanine as hole selective layers. Journal of Materials Chemistry A 2015, 3, 23888-23894.

(332) Xu, L.; Chen, X.; Jin, J.; Liu, W.; Dong, B.; Bai, X.; Song, H.; Reiss, P. Inverted perovskite solar cells employing doped NiO hole transport layers: A review. Nano Energy 2019, 63, 103860.

(333) Chen, W.; Wu, Y.; Yue, Y.; Liu, J.; Zhang, W.; Yang, X.; Chen, H.; Bi, E.; Ashraful, I.; Grätzel, M. Efficient and stable large-area perovskite solar cells with inorganic charge extraction layers. Science 2015, 350, 944-948.

(334) Lu, H.; Ma, Y.; Gu, B.; Tian, W.; Li, L. Identifying the optimum thickness of electron transport layers for highly efficient perovskite planar solar cells. Journal of Materials Chemistry A 2015, 3, 16445-16452.

(335) Zhou, P.; Bu, T.; Shi, S.; Li, L.; Zhang, Y.; Ku, Z.; Peng, Y.; Zhong, J.; Cheng, Y.-B.; Huang, F. Efficient and stable mixed perovskite solar cells using P3HT as a hole transporting layer. Journal of Materials Chemistry C 2018, 6, 5733-5737.

(336) Guo, J.; Meng, X.; Zhu, H.; Sun, M.; Wang, Y.; Wang, W.; Xing, M.; Zhang, F. Boosting the performance and stability of perovskite solar cells with phthalocyanine-based dopant-free hole transporting materials through core metal and peripheral groups engineering. Organic Electronics 2019, 64, 71-78.

(337) Wittenauer, M. A.; Van Zandt, L. L. Surface conduction versus bulk conduction in pure stoichiometric NiO crystals. Philosophical Magazine B 1982, 46, 659-667.

(338) Stolterfoht, M.; Wolff, C. M.; Amir, Y.; Paulke, A.; Perdigón-Toro, L.; Caprioglio, P.; Neher, D. Approaching the fill factor Shockley–Queisser limit in stable, dopant-free triple cation perovskite solar cells. Energy & Environmental Science 2017, 10, 1530-1539.

(339) Wu, N.; Wu, Y.; Walter, D.; Shen, H.; Duong, T.; Grant, D.; Barugkin, C.; Fu, X.; Peng, J.; White, T. Identifying the cause of voltage and fill factor losses in perovskite solar cells by using luminescence measurements. Energy Technology 2017, 5, 1827-1835.

(340) Zhang, Y.; Wang, J.; Xu, J.; Chen, W.; Zhu, D.; Zheng, W.; Bao, X. Efficient inverted planar formamidinium lead iodide perovskite solar cells via a post improved perovskite layer. RSC Advances 2016, 6, 79952-79957, DOI: 10.1039/c6ra15210d.

(341) Liu, M.; Johnston, M. B.; Snaith, H. J. Efficient planar heterojunction perovskite solar cells by vapour deposition. Nature 2013, 501, 395-398, DOI: 10.1038/nature12509.

(342) Haque, F.; Yi, H.; Duan, L.; Zhang, Y.; Wright, M.; Conibeer, G.; Uddin, A. Optimisation of annealing temperature for low temperature processed inverted structure Caesium Formamidinium Lead Triiodide perovskite solar cells. Materials Science in Semiconductor Processing 2019, 102, 104580, DOI: 10.1016/j.mssp.2019.06.015.

(343) Zhang, M.; Zhang, F.; Wang, Y.; Zhu, L.; Hu, Y.; Lou, Z.; Hou, Y.; Teng, F. High-Performance Photodiode-Type Photodetectors Based on Polycrystalline Formamidinium Lead Iodide Perovskite Thin Films. Sci Rep 2018, 8, 11157, DOI: 10.1038/s41598-018-29147-6.

(344) Verma, D. K.; Kuntail, J.; Kumar, B.; Singh, A. K.; Shukla, N.; Kavita; Sinha, I.; Rastogi, R. B. Amino Borate-Functionalized Reduced Graphene Oxide Further Functionalized with Copper Phthalocyanine Nanotubes for Reducing Friction and Wear. ACS Applied Nano Materials 2020, 3, 5530-5541, DOI: 10.1021/acsanm.0c00812.

(345) Hu, Q.; Rezaee, E.; Shan, H.; Liu, P.; Xu, Z.-X. Graphene oxide/N-$CuMe_2Pc$ nanorod hybrid nanocomposite as efficient visible light photocatalyst for aqueous Cr(VI) reduction. Catalysis Today 2019, 335, 180-186, DOI: 10.1016/j.cattod.2018.11.004.

(346) Rajappa, S.; Shivarathri, P. G.; Aruna Kumari, M. L.; Swamygowda, D. K.; Devendrachari, M. C.; Kotresh, H. M. N. Mechanochemical route for tetra amino zinc phthalocyanine embedded PANI sensitized Fe_2O_3 heteroarchitecture for photodegradation of dyes under the influence of low power LED light source. Surfaces and Interfaces 2022, 29, 101720, DOI: 10.1016/j.surfin.2022.101720.

(347) Ramachandran, R.; Hu, Q.; Rajavel, K.; Zhu, P.; Zhao, C.; Wang, F.; Xu, Z.-X. Non-peripheral octamethyl-substituted copper (II) phthalocyanine nanorods with MXene sheets: An excellent electrode material for symmetric supercapacitor with enhanced electrochemical performance. Journal of Power Sources 2020, 471, 228472, DOI: 10.1016/j.jpowsour.2020.228472.

(348) Gorduk, O.; Gorduk, S.; Gencten, M.; Sahin, M.; Sahin, Y. One-step electrochemical preparation of ternary phthalocyanine/acid-activated multiwalled carbon nanotube/polypyrrole-based electrodes and their supercapacitor applications. International Journal of Energy Research 2020, 44, 9093-9111, DOI: 10.1002/er.5634.

(349) Lu, C.; Guo, F.; Yan, Q.; Zhang, Z.; Li, D.; Wang, L.; Zhou, Y. Hydrothermal synthesis of type II ZnIn2S4/BiPO4 heterojunction photocatalyst with dandelion-like microflower structure for enhanced photocatalytic degradation of tetracycline under simulated solar light. Journal of Alloys and Compounds 2019, 811, 151976, DOI: 10.1016/j.jallcom.2019.151976.

(350) Ren, X.; Wu, K.; Qin, Z.; Zhao, X.; Yang, H. The construction of type II heterojunction of Bi_2WO_6/BiOBr photocatalyst with improved photocatalytic performance. Journal of Alloys and Compounds 2019, 788, 102-109, DOI: 10.1016/j.jallcom.2019.02.211.

(351) Wu, S.; Zhao, H. J.; Li, C. F.; Liu, J.; Dong, W.; Zhao, H.; Wang, C.; Liu, Y.; Hu, Z. Y.; Chen, L.; Li, Y.; Su, B. L. Type II heterojunction in hierarchically porous zinc oxide/graphitic carbon nitride microspheres promoting photocatalytic activity. J Colloid Interface Sci 2019, 538, 99-107, DOI: 10.1016/j.jcis.2018.11.076.

(352) Samaniego-Benitez, J. E.; Lartundo-Rojas, L.; García-García, A.; Calderón, H. A.; Mantilla, A. One-step synthesis and photocatalytic behavior for H_2 production from water of ZnS/MoS_2 composite material. Catalysis Today 2021, 360, 99-105, DOI: 10.1016/j.cattod.2019.08.011.

(353) Tiwari, A.; Gautam, A.; Sk, S.; Gavali, D. S.; Thapa, R.; Pal, U. Controlled Loading of MoS_2 on Hierarchical Porous TiO_2 for Enhanced Photocatalytic Hydrogen Evolution. The Journal of Physical Chemistry C 2021, 125, 11950-11962, DOI: 10.1021/acs.jpcc.1c01922.

(354) Samanta, M.; Ahmed, S. I.; Chattopadhyay, K. K.; Bose, C. Role of various transport layer and electrode materials in enhancing performance of stable environment-friendly Cs_2TiBr_6 solar cell. Optik 2020, 217, 164805, DOI: 10.1016/j.ijleo.2020.164805.

(355) Meza'al, S. K.; Hassan, N. K. Cs_2TiBr Solar Cell Performance Enhancement by Different Absorber Layer Thickness. Journal of university of Anbar for Pure science 2021, 15.

(356) Ahmed, S.; Jannat, F.; Khan, M. A. K.; Alim, M. A. Numerical development of eco-friendly Cs_2TiBr_6 based perovskite solar cell with all-inorganic charge transport materials via SCAPS-1D. Optik 2021, 225, 165765, DOI: 10.1016/j.ijleo.2020.165765.

(357) Khan, M. A. K.; Urmi, S. S.; Ferdous, T. T.; Azam, S.; Alim, M. A. Highly efficient Cesium Titanium (IV) Bromide perovskite solar cell and its point defect investigation: A computational study. Superlattices and Microstructures 2021, 156, 106946, DOI: 10.1016/j.spmi.2021.106946.

(358) Chakraborty, K.; Choudhury, M. G.; Paul, S. Life Cycle Assessment of a Lead-Free Cesium Titanium (IV) Single and Mixed Halide Perovskite Solar Cell Based 1 m² PV Module. IEEE Transactions on Device and Materials Reliability 2021, 21, 465-471, DOI: 10.1109/tdmr.2021.3106340.

(359) Yang, X.; Wang, W.; Ran, R.; Zhou, W.; Shao, Z. Recent advances in $Cs_2AgBiBr_6$-based halide double perovskites as lead-free and inorganic light absorbers for perovskite solar cells. Energy & Fuels 2020, 34, 10513-10528.

(360) Garcia-Espejo, G.; Rodriguez-Padron, D.; Luque, R.; Camacho, L.; de Miguel, G. Mechanochemical synthesis of three double perovskites: $Cs_2AgBiBr_6$, $(CH_3NH_3)_2TlBiBr_6$ and $Cs_2AgSbBr_6$. Nanoscale 2019, 11, 16650-16657, DOI: 10.1039/c9nr06092h.

(361) Lei, H.; Hardy, D.; Gao, F. Lead-Free Double Perovskite $Cs_2AgBiBr_6$: Fundamentals, Applications, and Perspectives. Advanced Functional Materials 2021, 31, 2105898, DOI: 10.1002/adfm.202105898.

(362) Wei, F.; Deng, Z.; Sun, S.; Hartono, N. T. P.; Seng, H. L.; Buonassisi, T.; Bristowe, P. D.; Cheetham, A. K. Enhanced visible light absorption for lead-free double perovskite $Cs_2AgSbBr_6$. Chem Commun (Camb) 2019, 55, 3721-3724, DOI: 10.1039/c9cc01134j.

(363) Li, Z.; Kavanagh, S. R.; Napari, M.; Palgrave, R. G.; Abdi-Jalebi, M.; Andaji-Garmaroudi, Z.; Davies, D. W.; Laitinen, M.; Julin, J.; Isaacs, M. A.; Friend, R. H.; Scanlon, D. O.; Walsh, A.; Hoye, R. L. Z. Bandgap lowering in mixed alloys of $Cs_2Ag(Sb_xBi_{1-x})Br_6$ double perovskite thin films. Journal of Materials Chemistry A 2020, 8, 21780-21788, DOI: 10.1039/d0ta07145e.